

MODEL DEVELOPMENT AND SIMULATION OF THE RESPONSE OF
SHAPE MEMORY POLYMERS

A Dissertation

by

PRITHA BHUTNATH GHOSH

Submitted to the Office of Graduate Studies of
Texas A&M University
in partial fulfillment of the requirements for the degree of

DOCTOR OF PHILOSOPHY

Approved by:

Co-Chairs of Committee,	Arun R. Srinivasa Junuthula N. Reddy
Committee Members,	Jay R. Walton Anastasia H. Muliana
Department Head,	Jerald A. Caton

December 2012

Major Subject: Mechanical Engineering

Copyright 2012 Pritha Bhutnath Ghosh

ABSTRACT

The aim of this work is to develop and validate a continuum model for the simulation of the thermomechanical response of a shape memory polymer(SMP). Rather than integral type viscoelastic model, the approach here is based on the idea of two inter-penetrating networks, one which is permanent and the other which is transient together with rate equations for the time evolution of the transient network. We find that the activation stress for network breakage and formation of the material controls the gross features of the response of the model, and exhibits a “thermal Bauschinger effect”. The model developed here is similar to a thermoviscoelastic model, and is developed with an eye towards ease of numerical solutions to boundary value problems. The primary hypothesis of this model is that the hysteresis of temperature dependent activation-stress plays a lead role in controlling its main response features. Validation of this hypothesis is carried out for the uniaxial response from the experimental data available in the literature for two different SMP samples: shape memory polyurethane and Veriflex, to show the control of the evolution of the temperature sensitive activation stress on the response.

We extend the validated 1D model to a three dimensional small strain continuum SMP model and carry out a systematic parameter optimization method for the identification of the activation stress coefficients, with different weights given to different features of the response to match the parameters with experimental data. A comprehensive parametric study is carried out, that varies each of the model material and loading parameters, and observes their effect on design-relevant response characteristics of the model undergoing a thermomechanical cycle. We develop “response charts” for the response characteristics: shape fixity, shape recovery and maximum stress rise during cooling, to give the designer an idea of how the simultaneous variation of two of the most influential material parameters changes a specific response parameter.

To exemplify the efficacy of the model in practical applications, a thermoviscoelastic extension of a beam theory model will be developed. This SMP beam theory will account for activation stress governed inelastic response of a SMP beam. An example of a three point bend test is simulated using the beam theory model. The numerical solution is implemented by using an operator split technique that utilizes

an elastic predictor and dissipative corrector. This algorithm is validated by using a three-point bending experiment for three different material cases: elastic, plastic and thermoplastic response. Time step convergence and mesh density convergence studies are carried out for the thermoviscoelastic FEM model. We implement and study this model for a SMP beam undergoing three-point bending strain recovery, stress recovery and cyclic thermomechanical loading.

Finally we develop a thermodynamically consistent finite continuum model to simulate the thermomechanical response of SMPs. The SMP is modelled as a isotropic viscoplastic material where thermal changes govern the evolution of the activation stress of the material. The response of the SMP in a thermomechanical cycle is modelled as a combination of a rubbery and a glassy element in series. Using these assumptions, we propose a specific form for the Helmholtz potential and the rate of dissipation. We use the technique of upper triangular decomposition for developing the constitutive equations of the finite strain SMP model. The resulting model is implemented in an ODE solver in MATLAB, and solved for a simple shear problem. We study the response of the SMP model for shear deformation as well as cyclic shear deformation at different initial temperatures. Finally, we implement the thermomechanical cycle under shear deformations and study the behaviour of the model.

DEDICATION

To my father.

ACKNOWLEDGMENTS

I would like to thank Professor Srinivasa and Professor Reddy for providing me with the opportunity to work on this NSF project. Professor Srinivasa provided some interesting problems to tackle within this dissertation, and his ideas and insights have widened the scope of this work. Professor Reddy's meticulous attention to detail and pertinent suggestions have helped improve the quality of this work. I thank them for their inspiring teaching styles and the courses that they have offered. I appreciate their time and guidance through the course of this dissertation.

I am thankful to Dr. Creasy for providing me with his laboratory facilities and access to the Instron machine, that aided in the polymer synthesis and preliminary tests. He has been very generous with his time and support in trouble shooting the bottlenecks that we faced during the use of the machine. I am grateful that he agreed to act as a substitute for my final defense and read my dissertation in detail.

I thank Professor Walton for serving on my committee and for asking many insightful questions during the proposal and the final defense that helped address finer issues. I also thank Dr. Muliana for serving on my committee.

A special mention of my supervisor at the Utilities and Energy Management plant, Micky Wong, for providing me with the opportunity to work as a Graduate Assistant, thus ensuring financial assistance at a crucial time during the progress of this dissertation.

I thank the workshop of the Mechanical Engineering department for providing the necessary tools for cutting samples and fabrication of grips and supports for the experiments.

I appreciate the help and the fun times I have had with my colleagues Srikrishna Doraiswamy, Ashwin Rao and Jayavel Arumugam. They have been generous with their time and provided their support when I needed them. I wish the best for each of them. I also appreciate the helpful comments from Gene Cha, Shreyas Balachandran, Jayadurga Iyer during meetings and laboratory interactions.

My stay at College Station was made memorable by many friends and roommates over the last couple of years. Thanks to all of them for the good times and support, whether near or far away: Anjana Talapatra, Abhilasha Katariya, Sneha Shah, Purvee Parekh, Vinita Bashetti, Shriram Srinivasan, Nikhil Joshi, Mandar Kulkarni,

Guruprakash Thirumalaisamy, Anand Govindasamy, Shubhangi Maindale, Madhuri Murali and so many more.

I am grateful to my family for their support in the last few years, especially to my mother and my brother for taking care of many issues so I could continue this pursuit without major difficulties. I appreciate the care and concern of my sister-in-law Renu Gupta, and her constant cheering and motivational talks. A special thank you to my brother Somnath Ghosh for his unfaltering support and ominous threats for the timely completion of this work!

My father has taught me everything I know, through his words and his silence. He had faith in me and supported my decision to pursue a PhD. As the days unfold, I understand the love and the wisdom behind many of his decisions and I feel blessed to have known him.

Finally, I would like to thank Saradhi Koneru, my husband, who acted as the sounding board and the critic of many crucial aspects of this work. His quiet support and care have made things worthwhile. I cherish his love and companionship, and look forward to a new phase of togetherness ahead.

I am grateful to have been associated with so many nice people with different working styles in the past few years. This dissertation and the journey it has entailed have added to my experiences.

TABLE OF CONTENTS

	Page
ABSTRACT	ii
DEDICATION	iv
ACKNOWLEDGMENTS	v
TABLE OF CONTENTS	vii
LIST OF FIGURES	xi
LIST OF TABLES	xv
1. INTRODUCTION, LITERATURE REVIEW AND MOTIVATION	1
1.1 Shape Memory Polymers: Behavior, Morphology and Classification .	1
1.2 Review of Application Areas of SMPs	4
1.3 Review of Characterization Methods of SMP Behavior and Macro- scopic Experiments	7
1.4 Review of SMP Models	10
1.5 Motivation and Problem Formulation	14
1.6 Objective and Scope	17
1.7 Structure of the Dissertation	19
2. TWO NETWORK THEORY BASED ONE DIMENSIONAL MODEL FOR SMPS*	21
2.1 Introduction	21
2.2 The Thermomechanical Cycle and Morphology Changes	22
2.3 Development of a Two-network One Dimensional Model	24
2.4 Normalizing Variables	30
2.5 Non-dimensional Set of System Equations	31
2.6 Simulation of the SMP Response	32
2.6.1 Implementation of the System Equations	32
2.6.2 Simulation Specifications of the Thermomechanical Cycle . . .	33
2.7 Temperature Dependence Form of Material Parameters	34
2.7.1 The Activation Stress Parameter	34
2.7.2 The Effect of Thermal Expansion	39

2.8	Results of Validation and Prediction of 1D Model using Referred Experimental Data	42
2.8.1	Shape Memory Polyurethane	42
2.8.2	Shape Memory Epoxy Resin	44
2.9	Conclusions from the 1D Model	46
3.	SMALL STRAIN THREE DIMENSIONAL MODEL WITH PARAMETRIC ANALYSIS AND ERROR OPTIMIZATION	47
3.1	Introduction	47
3.2	Development of the Three Dimensional Model	47
3.3	Non-dimensionalization of the Model Equations	54
3.4	Comparison to the 1D SMP Model	56
3.5	Implementation of the Small Strain 3D Model	59
3.6	Error Optimization: Identification of Activation Stress Coefficients	62
3.6.1	Results of “fminsearch” Solver	66
3.6.2	Results of “fmincon” Solver	67
3.7	Thermomechanical Cycle Results	68
3.7.1	Unconstrained Shape Recovery	68
3.7.2	Constrained Stress Recovery	71
3.8	Parametric Study of the SMP Model with respect to Material Parameters	74
3.8.1	Material Parameters	76
3.8.2	Activation Stress Coefficients	80
3.9	Sensitivity Analysis	83
3.10	Parametric Study of the SMP Model with respect to Control Parameters	86
3.10.1	Maximum Strain	86
3.10.2	Deformation Temperature	86
3.10.3	Heating Rate	87
3.10.4	Cooling Rate	87
3.11	Summary	89
4.	BEAM THEORY MODEL USING ELASTIC-PREDICTOR PLASTIC-CORRECTOR	90
4.1	Introduction	90
4.2	Development of Finite Element Model for SMP	91
4.2.1	Thermomechanical Three-point Flexural Cycle	91
4.2.2	Displacement Field and Strains	93
4.2.3	Constitutive Equations of the SMP Model	94
4.2.4	Weak Form	96
4.2.5	Finite Element Formulation	99
4.2.6	Non-dimensionalization of the Model Equations	104

4.3	Elastic Predictor - Dissipative Corrector Algorithm	106
4.4	Analysis of the Implementation	109
4.4.1	Elastic, Plastic and Thermoplastic Material Cases	109
4.4.2	Time Step Convergence	111
4.4.3	Mesh Convergence	112
4.5	SMP Beam Theory Model undergoing a Thermomechanical Cycle . .	113
4.5.1	Experimental Parameters for Thermomechanical Flexural Cycle	113
4.5.2	Thermomechanical Three-point Bending: Strain Recovery . .	116
4.5.3	Thermomechanical Three-point Bending: Stress recovery . . .	123
4.6	Summary	126
5.	FINITE STRAIN MODEL USING QR DECOMPOSITION	127
5.1	Introduction	127
5.2	Kinematics	128
5.3	Constitutive Theory for Finite Deformation	131
5.4	QR Decomposition	136
5.5	Non-dimensionalization of System Equations	142
5.6	Implementation of the Finite Strain Model	143
5.7	Results for Shear Deformation	144
5.7.1	Isothermal Shear Deformation at Different Temperatures . . .	144
5.7.2	Rate Dependent Strain Softening Behavior	147
5.7.3	Cyclic Isothermal Shear Deformation	148
5.7.4	Thermomechanical Shear Cycle: Stress Recovery	149
5.7.5	Thermomechanical Shear Cycle: Shape Recovery	154
5.8	Concluding Remarks	154
6.	DESIGN OF MULTI-STATE AND SMART-BIAS COMPONENTS USING SMA AND SMP COMPOSITES*	156
6.1	Introduction	156
6.2	Smart tools: Development Details	159
6.2.1	MSMS Fabrication: General Considerations	159
6.2.2	Tuning the Glass Transition Temperature of SMP	160
6.2.3	Fabrication Details	162
6.3	SMA and SMP based Multi-state and Smart-bias Components	168
6.3.1	Three-state Configurations	168
6.3.2	Three-state Configurations with a Discontinuous SMP matrix and SMA Reinforcement	170
6.3.3	SMA Spring inside SMP Tube: Automatic Thermal Cycling Mechanism	171

6.3.4	Shape-set SMA Reinforcement in SMP Matrix: Automatic Thermal Cycling Mechanism	173
6.4	Conclusions	174
7.	CONCLUSIONS	176
7.1	Conclusions on the 1D and Small Strain 3D Model	176
7.2	Conclusions on the Beam Theory Model	177
7.3	Conclusions on the Finite Strain Model	178
7.4	Recommendations for Future Work	179
	REFERENCES	184
	APPENDIX A.	193

LIST OF FIGURES

	Page
1.1 Parent tree structure for shape memory polymers	1
1.2 The processes and corresponding material responses involved in a thermomechanical cycle to observe the shape memory effect	2
1.3 Characterization Methods for shape memory polymers based on permanent netpoints and temporary netpoints [1]	3
1.4 The processes and corresponding material responses involved in a shape recovery and stress recovery thermomechanical cycle	5
1.5 Examples of property dependent applications of SMPs.	6
1.6 Examples of small strain applications of SMPs	6
2.1 Processes and response in a thermomechanical cycle	22
2.2 Change in morphology in the SMP material during a thermomechanical cycle	24
2.3 The proposed mechanical model for the SMP	25
2.4 Variation of activation stress with temperature in a thermomechanical cycle	35
2.5 Variation of thermal strain with temperature	39
2.6 Plastic, thermal and elastic strain and their combination to produce the total strain in the complete cycle	41
2.7 Comparison of the experimental data of polyurethane by Tobushi et al [2] with the prediction of the model developed here for $\epsilon_{max} = 4\%$	42
2.8 Comparison of the experimental data of polyurethane by Tobushi et al [2] with the prediction of the model developed here for maximum applied strain of 2.4%	43
2.9 Comparison of the experimental data of polyurethane by Tobushi et al [2] with the prediction of the model developed here for maximum applied strain of 10%	44
2.10 Comparison of the experimental data of epoxy by Liu et al [3] with the prediction of the model developed here under tension of 9.1%	45
2.11 Comparison of the experimental data of epoxy by Liu et al [3] with the prediction of the model developed here under compression of 9.1%	45
2.12 Comparison of the experimental data of epoxy by Liu et al [3] with the prediction of the model developed here in the undeformed case	45
3.1 “fminsearch” function values (top) and model versus data for optimum values (bottom)	66
3.2 “fmincon” function values (top) and model versus data for optimum values (bottom)	67

3.3	3D Model results versus data for the unconstrained shape recovery thermomechanical cycle on polyurethane	68
3.4	Evolution of inelastic strain in 3.4b by controlling the difference between the activation stress and the inelastic flow potential in 3.4a for the 3D and 1D model	69
3.5	All strains for unconstrained shape recovery thermomechanical cycle on polyurethane	70
3.6	Stress strain temperature process controls for the constrained stress recovery thermomechanical cycle on polyurethane	72
3.7	3D model results versus data for the constrained stress recovery thermomechanical cycle on polyurethane	73
3.8	Glassy modulus effect on the response for values around experimental data range	76
3.9	Rubbery modulus effect on the response for values around experimental data range	77
3.10	Glassy thermal expansion effect on the response for values around experimental data range	78
3.11	Rubbery thermal expansion effect on the response for values around experimental data range	79
3.12	Viscosity effect on the response for values around experimental data range	79
3.13	Activation stress coefficient y_1 effect on the response	80
3.14	Activation stress coefficient y_2 effect on the response	81
3.15	Activation stress coefficient y_3 effect on the response	81
3.16	Activation stress coefficient y_4 effect on the response	82
3.17	Activation stress coefficient y_5 effect on the response	83
3.18	Response surface maps	85
3.19	Effect of maximum strain applied on the response for values around experimental data range	86
3.20	Effect of deformation temperature on the response for values around experimental data range	87
3.21	Effect of heating rate on the response for values around experimental data range	88
3.22	Effect of cooling rate on the response for values around experimental data range	88
4.1	Processes and response in a flexural thermomechanical cycle	92
4.2	Kinematics of deformation of the Euler-Bernoulli beam theory	93
4.3	The Euler-Bernoulli finite element with primary degrees of freedom	96

4.4	Loading and boundary conditions along the beam for three point bending experiment, and displacement and strain computations across the cross section of the beam	103
4.5	Elastic predictor dissipative corrector concept	107
4.6	Inelastic strains evolution in the beam for chosen time steps, for the plastic and thermoplastic cases	110
4.7	Displacement of beam for various time steps	111
4.8	Displacement of beam for various mesh refinements, as shown in color bar	112
4.9	Control variables of a thermomechanical cycle	113
4.10	Control variables of the thermomechanical cycle from the code	117
4.11	Displacement and reaction forces of the load point of beam undergoing the thermomechanical cycle	118
4.12	Configuration of the beam through the four ranges of the thermomechanical cycle	119
4.13	Inelastic strain evolution in the beam through the four ranges of the strain recovery thermomechanical cycle	120
4.14	Total strain, inelastic strain and thermal strain at center of the beam through the four ranges of the thermomechanical cycle	121
4.15	Strain recovery for three different unloading cases	122
4.16	Results for three cycles of thermomechanical loading. Cycle 1: blue, Cycle 2: green, Cycle 3: red	122
4.17	Displacement and reaction forces at the center of the beam undergoing the thermomechanical cycle	123
4.18	Inelastic strain evolution in the beam through the four ranges of the stress recovery thermomechanical cycle	124
4.19	Total strain, inelastic strain and thermal strain at the center of the beam through the four ranges of the thermomechanical cycle	125
5.1	Schematic to illustrate current natural configuration of the material .	128
5.2	Response for shear deformation at different temperatures	146
5.3	Results of the response for shear deformation at low and glass transition temperature, with respective activation stresses	147
5.4	Rate dependent strain softening behavior for low and high temperatures	148
5.5	Results of the response for cyclic shear deformation at low and high temperature	149
5.6	Results for shear deformation thermomechanical cycle - stress recovery	151

5.7	Comparison of the model response with the data for shear deformation thermomechanical cycle for stress recovery. The model is evaluated for the identified parameters in the experiment in Figure 5.3	152
5.8	Results for shear deformation thermomechanical cycle - shape recovery	154
6.1	Fabrication methodology for a multifunctional smart material system	160
6.2	SMA vs SMP modulus comparison on a temperature scale with particular emphasis of critical transformation temperatures of SMA and SMP	161
6.3	Samples prepared with volume ratios and glass transition temperatures corresponding to those enlisted in Table 6.2	164
6.4	Fixture to shape set SMA springs	164
6.5	SMA and SMP composite sample preparation	167
6.6	Three-state configurations obtained with SMA and SMP	168
6.7	Thermally activated two - stage alarm system	169
6.8	Discontinuous SMP and SMA composite showing two stage shape recovery	170
6.9	Photographs of the actual sample showing the behavior described in Figure 6.8	171
6.10	Smart valve	172
6.11	Smart tent	173
7.1	Experimental setup for shear and three-point flexure tests	182
A.1	Glassy modulus effect on the response for order of magnitude	195
A.2	Rubbery modulus effect on the response for order of magnitude	197
A.3	Glassy thermal expansion effect on the response for order of magnitude	199
A.4	Rubbery thermal expansion effect on the response for order of magnitude	201
A.5	Viscosity effect on the response for order of magnitude	203
A.6	Activation stress coefficient y_1 effect on the response	205
A.7	Activation stress coefficient y_2 effect on the response	207
A.8	Activation stress coefficient y_3 effect on the response	209
A.9	Activation stress coefficient y_4 effect on the response	211
A.10	Activation stress coefficient y_5 effect on the response	213

LIST OF TABLES

	Page
1.1 Selected list of available experimental data	8
1.2 Classification of few models in the current literature that deal with the macroscopic responses of pure SMPs	11
2.1 Dimensional quantities and corresponding non-dimensional quantities	31
2.2 Parameter values for normalization and their significance in the samples	31
2.3 Process inputs with respect to time	33
2.4 Specifications of the processes obtained from experimental data of polyurethane and epoxy resin	34
2.5 Comparison of the strain responses and thermal strains, of shape mem- ory polyurethane at various applied strain (ϵ_{max}) levels	41
3.1 Dimensional quantities and corresponding non-dimensional quantities for the small strain model	54
3.2 Initial conditions and final optimum results of activation stress coeffi- cients from the “fminsearch” solver	66
3.3 Initial conditions, parameter space and final results of activation stress coefficients from “fmincon” solver	67
3.4 Chosen response parameters in a thermomechanical cycle	74
3.5 Experimental values of material parameters in the SMP model	75
3.6 Sensitivity of a particular response property to each of the material parameters	84
4.1 Dimensional quantities and corresponding non-dimensional quantities for the beam theory model	104
4.2 Control parameters for the three cases: elastic, plastic and thermoplastic	109
4.3 Displacements along the beam nodes for the three cases: elastic, plas- tic and thermoplastic at the final time step	110
4.4 Control parameters for the strain recovery thermodynamic cycle . . .	114
4.5 Control parameters for the stress recovery thermodynamic cycle . . .	115
5.1 Comparison of the small strain model and finite strain model kine- matics and constitutive approach	130
5.2 Dimensional quantities and corresponding non-dimensional quantities for the finite strain model	142
6.1 Comparison of the properties of NiTi shape memory alloys (SMAs) and shape memory polymers (SMPs) [4]	157

6.2	Chemical volume ratios for preparing samples with different glass transition temperatures	163
7.1	Details for INSTRON settings during a thermomechanical cycle . . .	183
A.1	Parameter value changing details for (1) Order of magnitude and (2) $\pm 20\%$ range around actual value	193
A.2	Glassy modulus parametric analysis: order of magnitude	194
A.3	Glassy modulus parametric analysis: around experimental data . . .	194
A.4	Rubbery modulus parametric analysis: order of magnitude	196
A.5	Rubbery modulus parametric analysis: around experimental data . .	196
A.6	Glassy thermal expansion parametric analysis: order of magnitude . .	198
A.7	Glassy thermal expansion: around experimental data	198
A.8	Rubbery thermal expansion parametric analysis: order of magnitude .	200
A.9	Rubbery thermal expansion: around experimental data	200
A.10	Glassy viscosity parametric analysis: order of magnitude	202
A.11	Glassy viscosity parametric analysis: around experimental data . . .	202
A.12	Activation stress coefficient y_1 : order of magnitude	204
A.13	Activation stress coefficient y_1 : around experimental data	204
A.14	Activation stress coefficient y_2 : order of magnitude	206
A.15	Activation stress coefficient y_2 : around experimental data	206
A.16	Activation stress coefficient y_3 : order of magnitude	208
A.17	Activation stress coefficient y_3 : around experimental data	208
A.18	Activation stress coefficient y_4 : order of magnitude	210
A.19	Activation stress coefficient y_4 : around experimental data	210
A.20	Activation stress coefficient y_5 : order of magnitude	212
A.21	Activation stress coefficient y_5 : around experimental data	212

1. INTRODUCTION, LITERATURE REVIEW AND MOTIVATION

1.1 Shape Memory Polymers: Behavior, Morphology and Classification

Stimuli-responsive polymers undergo relatively large, abrupt, and physical or chemical changes in response to small external changes in stimuli [5]. Smart materials refer to a subset of these materials that can (1) recognize the stimulus in its surrounding environment as a signal and respond reversibly, and (2) be able to judge the magnitude of the signal and react with an optimal or useful response by either changing its physical or mechanical properties [6, 7].

As shown in Figure 1.1, the stimulus can be physical or chemical with a variety

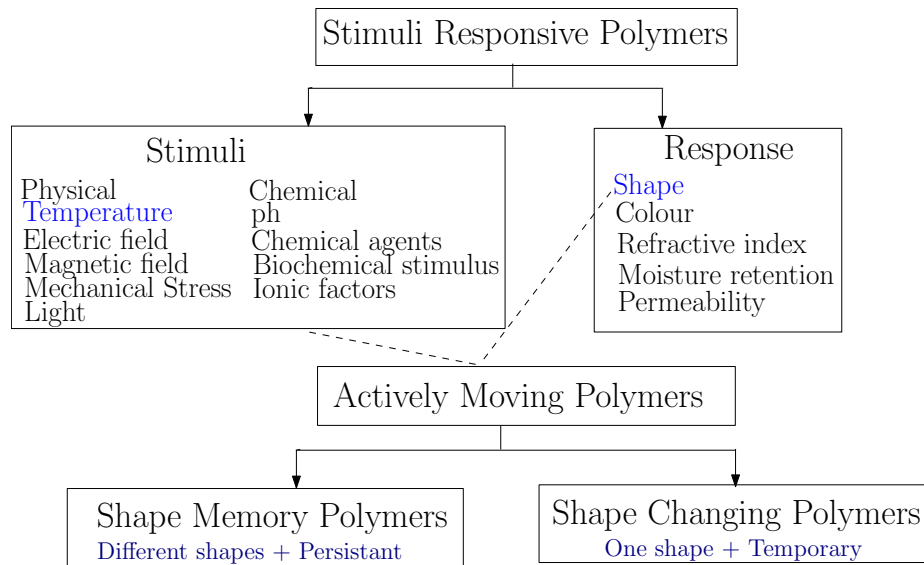


Figure 1.1: Parent tree structure for shape memory polymers

of possibilities. The response can manifest itself depending on the morphological changes involved. We are interested in a subset of these possibilities, where the stimulus is thermal and the response is restricted to shape change and these are known as actively moving polymers. These can be categorized as (1) shape changing polymers that change their shape gradually, as long as they are exposed to the stimulus. Removal of the stimulus initiates return of original shape, and (2) shape memory

polymers where the stimulus is used to program the polymer, and then deformed to a temporary shape. Even after removal of stimulus and deformation load, the polymer shows memory of the temporary shape. On the reapplication of the stimulus, the polymer shows memory of the permanent shape.

In this work we will focus on thermally responsive shape memory polymers

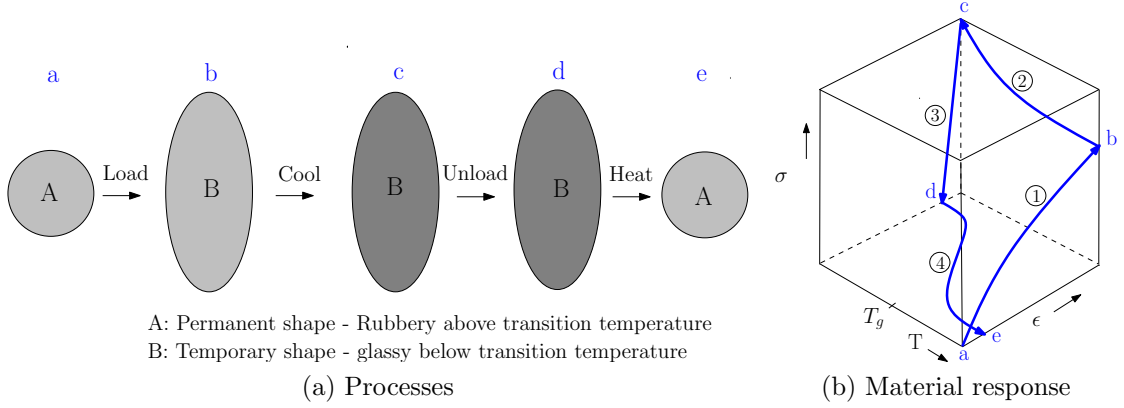


Figure 1.2: The processes and corresponding material responses involved in a thermomechanical cycle to observe the shape memory effect

(SMPs) and study their behavior in detail. As shown in Figure 1.2, they “lock-in” a deformed shape in response to a thermal signal and, subsequently, “unlock” the deformed shape and revert to their original “undeformed” shape when subject to another thermal signal. The thermal signal stimulates structural changes of the SMPs at a certain temperature, called the transition temperature. This transition temperature could correspond to T_g glass-transition (for amorphous polymers) or the T_m melting temperature (for polymers with crystalline phases), which gives rise to different kinds of shape-memory behavior [8]. SMPs can be easily deformed (with response similar to an elastomeric rubber, with modulus of magnitude 10-50MPa) to give a temporary shape at low-working temperatures below their transition temperature (0-90°C). Here the SMP is glassy (with modulus of 500-1000MPa) and holds on to this shape at low temperatures. Upon heating above their transition temperature, they return to their original structure, where it is rubbery again. Thus a SMP exhibits a change of shape and modulus while undergoing the shape memory effect,

		Reversible netpoints determining temporary shape	
		Switching domain (T_g)	Switching domain (T_m)
Netpoint determining permanent shape	Chemical Crosslinks	A-I Chemically crosslinked amorphous polymer networks <i>Example: Crosslinked Polystyrene</i>	A-II Chemically crosslinked semicrystalline polymer networks <i>Example: Crosslinked Polycyclooctene</i>
	Hard Domain T_m	B-I Thermoplastics with crystalline hard domain and amorphous switching domain <i>Example: Copolyesterurethane</i>	B-II Thermoplastics with crystalline hard domain and switching domain <i>Example: Polyetherurethane</i>
	Hard Domain T_g	C-I Thermoplastics with amorphous hard domain and switching domain <i>Example: Butanedoil</i>	C-II Thermoplastics with amorphous hard domain and crystalline switching domain <i>Example: Block polymers from styrene and butadiene</i>

Figure 1.3: Characterization Methods for shape memory polymers based on permanent netpoints and temporary netpoints [1]

and either or both of these effects can be used for design purposes.

On the morphological level, Kelch and Lendlien [8] observe that SMPs consist of at least two components: switching domains and permanent networks. The switching domains act as a molecular switch with a well-defined T_m or T_g , and enable the fixation of the temporary shape. These domains form a temporary-network, which can be made to persist over long periods of time by suitably lowering the temperature, below transition. The permanent network that determines the permanent shape of the SMP consists of physical netpoints associated with a high thermal transition temperature or covalent netpoints. Classification of thermally induced SMPs could be defined by identifying unique characteristics, such as morphology (amorphous or semicrystalline), nature of crosslinks (chemical vs physical), or the underlying mechanism responsible for the shape memory effect. The nature of the netpoints, which determine the permanent and the temporary shape respectively, could be used to categorize SMPs as shown in the Figure (1.3) which is reproduced from the work of Wagermaier, Kratz, et al. [1].

1.2 Review of Application Areas of SMPs

SMPs have been the subject of intense interest for designers in the last decade, because of their ability to change their mechanical properties in response to external non-mechanical stimuli, thus rendering them useful as sensors and actuators in a variety of applications. The fields of application for SMPs are diverse, ranging from packaging, electronics, textiles, to biomedical and aerospace applications [9]. These materials have the potential to revolutionize the design of a wide variety of devices ranging from human exoskeletons for people with disabilities to morphing wings and blades for aircrafts.

The central characteristics of a SMP response that concern an application-designer include the following:

Shape Fixity measures the extent to which the SMP is able to hold on to its temporary shape while unloading. Refer to Figure 1.4a,1.4b.

Shape Recovery measures the extent to which the SMP returns to its original shape at the end of the cycle. Refer to Figure 1.4a,1.4b.

Stress Recovery measures the stress needed to restrain the SMP at fixed dimensions while the specimen attempts to undergo shape recovery upon applying stimulus. Refer to Figure 1.4c,1.4d.

Depending on where the application lies, SMPs are designed or analysed to enhance the particular parameter driving the application. Refer to Figure 1.5. For example, if the application were a SMP repair patch, which is used to patch up dented bodies of vehicles, it would involve being deformed to conform to the body of the vehicle and frozen at that shape [10]. The first property - shape fixity would be of crucial importance here, and the patch would be designed to show excellent shape fixity. On the other hand, if the SMP is being used as a stent, where it is inserted into the body in its least invasive shape, and on reaching the target area, it recovers to its original permanent shape [11], the second property - shape recovery parameter is of most importance. Design for the third property - the stress recovery parameter comes to the fore in actuator applications, where the SMP may be used to hold open a valve, push a button, or in biomedical applications such as implants to compete against compressive forces of body tissues.

As observed in the recent paper by Xie [14], since SMPs exhibit large recoverable strain, applications of SMPs have primarily been advertised and concentrated in this area. However for a SMP to be useful, it is not necessary for it to exhibit large strain

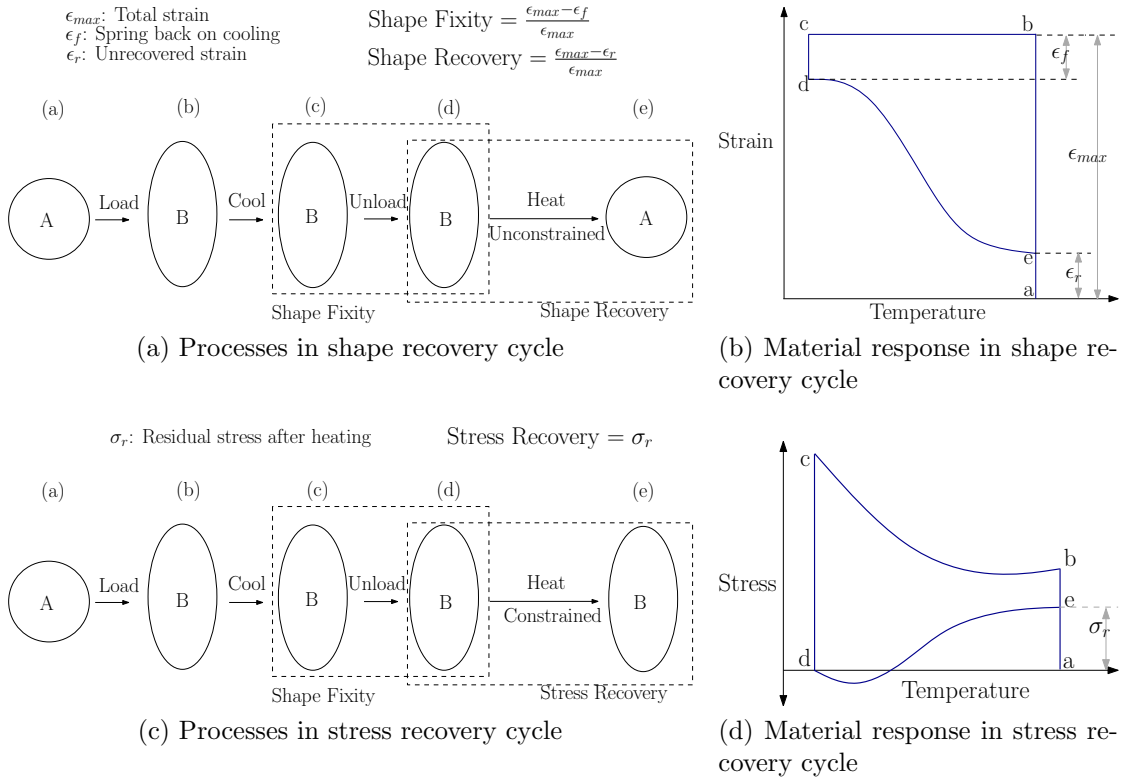


Figure 1.4: The processes and corresponding material responses involved in a shape recovery (top) and stress recovery (bottom) thermomechanical cycle

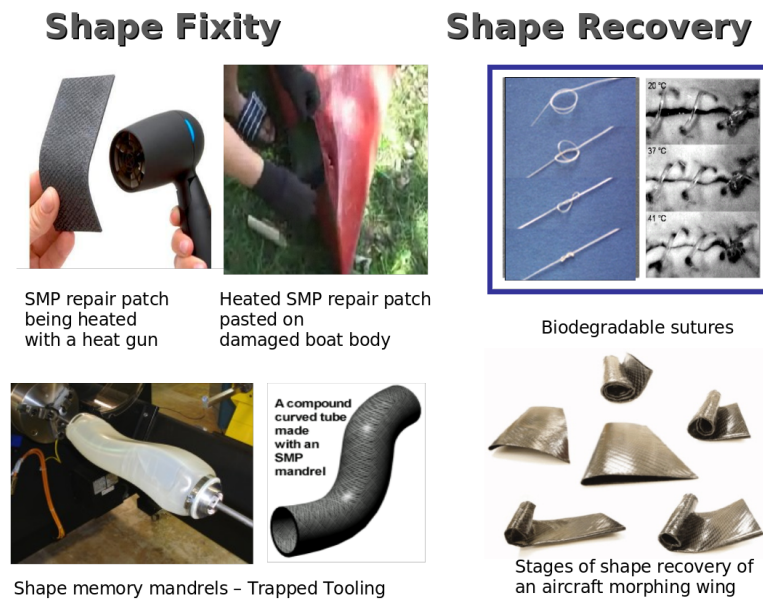


Figure 1.5: Examples of property dependent applications of SMPs.

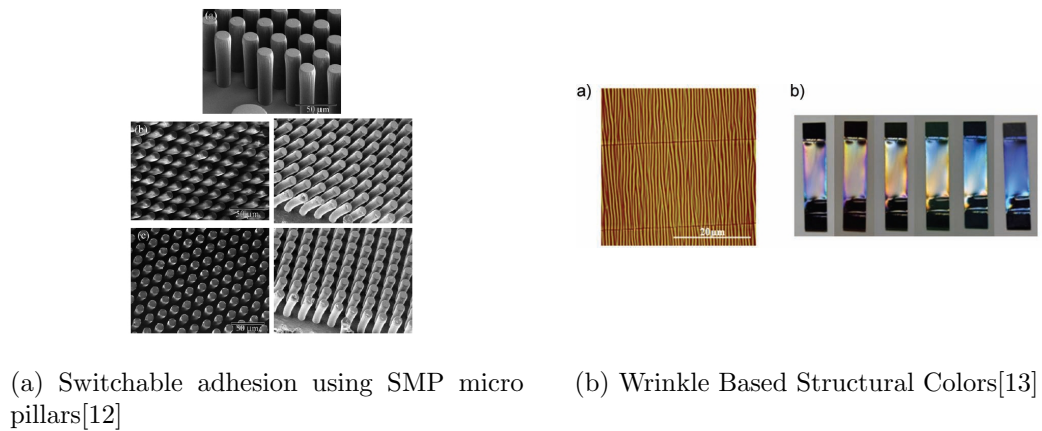


Figure 1.6: Examples of small strain applications of SMPs

behaviour. Several real world applications of shape memory polymers involve small strain changes. Examples of this include the following: Reddy et al. [12] used small strain deformations to create gecko inspired thermo-reversible adhesive pads. Lizards can reversibly adhere to surfaces because of the surface topography of their pads, that are covered with fine structures of particular dimensions and geometry. The switching between adhesive and non-adhesive states is mainly due to the tip direction of the fine structures. The smart adhesive pads uses the same principle, where the change in the tip direction in the adhesive pad is caused by fine SMP pillars, as shown in Figure 1.6a. The thermally actuated SMP pillars are tilted in deformed state. This small strain deformation can still produce adhesive stress of $3N/mm^2$ by the pad surface. Different attempts in making a gecko inspired reversible adhesion systems have been conducted by Xie et al. [15] and Kim et al. [16]. Other small strain applications have shown up in the creation of localized surface wrinkles based structural colors [13], as shown in Figure 1.6b. SMP is used as the wrinkle substrate, and surface wrinkling is created when a rigid thin film supported on the SMP and compressed laterally beyond a critical strain. Strains as low as 2.6% are sufficient to generate wrinkles [14].

1.3 Review of Characterization Methods of SMP Behavior and Macroscopic Experiments

Tailored characterization methods to obtain a complete description of the measurements of the shape memory behavior are thermomechanical tensile or bending experiments. A few of the most heavily cited experimental data on SMP characterization in recent literature that is relevant to our work, along with the information on the type of experiments, the cases considered and data available are listed in Table 1.1. The obtained shape-memory properties are strongly influenced by temperature dependent test parameters like deformation and fixation temperature or applied heating and cooling rate.

Apart from the mechanical characterization experiments, it is important to understand which material properties of the SMP govern the shape memory behavior. Experiments to conduct these studies are more challenging, as they involve synthesizing chemically tunable samples that exhibit different material properties, and only a handful of researchers address this in the literature. Buckley et al. [21] studied the effect of crosslink density on the shape recovery response of polytetrahydrofu-

Table 1.1: Selected list of available experimental data

Author	Material	Experiment Specs
Tobushi et al. 1997 [2] Citation hits by google scholar: 49	Base: Polyurethane Source: Mitsubishi Series: MS5510	Load: Uniaxial tension Levels: 2.4%, 4% and 10% strain Cases: (a) unconstrained free strain recovery (b) stress recovery under full constraint and then unloading
Liu et al. 2003 [17] Citation hits by google scholar: 30	Base: Epoxy resin Source: CTD Series: DP7AR	Load: 3-point Flexure Levels: 10%, 25%, 50%, and 100% strain, and 25% strain for temperature rate at 1, 3, 5°C/min Cases: (a) unconstrained free strain recovery
Liu et al. 2006 [3] Citation hits by google scholar: 83	Base: Epoxy resin Source: CRG Series: Veriflex	Load: Uniaxial tension and compression Levels: $\pm 9\%$ strain Cases: (a) unconstrained free strain recovery (b) stress recovery under full constraint at the pre-deformation strain (c) stress recovery under full constraint at low temperature un- loading strain
Baer et al. 2007 [18] Citation hits by google scholar: 26	Base: Polyurethane Source: Mitsubishi Series: MP5510	Load: Uniaxial tension Levels: 20 and 100% strains, at 37 and 80°C Cases: (a) isothermal free strain recovery (b) constrained stress recovery
Khan et al. 2008 [19] Citation hits by google scholar: 6	Base: Epoxy resin Source: CRG Series: Veriflex	Load: Shear Levels: Applied shear rate was 0.01/s with maximum shear strain limited to approxi- mately 60% Cases: (a) constrained stress recovery
Tobushi et al. 2008 [20] Citation hits by google scholar: 6	Base: Polyurethane Source: Mitsubishi Series: MM6520	Load: 3-point Flexure Levels: 2.4%, 4% and 10% strain Cases: (a) unconstrained free strain recovery (b) stress recovery under full constraint and then unloading

thane/polycaprolactone glycol. The rubbery modulus was increased by increasing the crosslink density, and this resulted in the increase of the temperature of maximum shape recovery rate and the shape recovery rate. Buckley also observes that the some parameters that are important to the SMP behaviour are the initial temperature, the temperature range and the rubbery modulus. Yakacki et al. [22] studied the shape recovery response of the polymer stents (SMP formed by photopolymerization of tert-butyl acrylate and poly(ethylene glycol) dimethacrylate) at body temperature, as a function of T_g , crosslink density, geometrical perforation, and θ_{high} . Gunes et al. [23] studied the effects of thermal expansion on shape memory performance of shape memory polyurethanes. Some important observations from this work include (1) the shape recovery process and the thermal expansion behavior counteract each other. A relatively low value of thermal expansion strain in comparison to recovered strain is desired for proper shape memory actions of SMP, (2) large thermal expansion strains comparable to the strains imposed on specimens in the stretching step might decrease the value of recovered strain, (3) the thermal expansion effect may be much more crucial for SMPs with low recoverable strains (8-10%) and with high trigger temperatures.

Macroscopic applications of SMPs include utensils for handicapped patients, bandages or casts for patients with motion disabilities [6], morphing wing structures, SMP repair patches for dented vehicle fenders, reformable mandrels [10]. As can be seen on studying these applications from their references, the SMP sample is subjected to bending load. Although uniaxial characterization experiments can be found abundantly in literature over the last decade, bending characterizations are less than a handful [17, 20], inspite of the fact that majority of the applications of SMPs involve bending and large displacements of beams and plates. The benefit of looking at bending experiments as opposed to uniaxial experiments are not restricted to application areas alone, but characterization problems themselves. For example, as Liu et al. [17] point out in their paper, in tension or compression, thermal stresses arise from constrained thermal expansion or contraction, leading to difficulties in separating the various mechanisms during deformation. Upon cooling, the applied stress can increase at a fixed strain, while in the flexural deformation the thermal contraction is not as severely constrained. Other advantages are that large displacements studies can be achieved in flexure at much more modest strain levels. A drawback is that the stress and strain are nonuniform and therefore more difficult

to analyze. Liu et al. [17] carried out several cases of thermomechanical cycle for a SMP epoxy sample, DP7AR in a three point bending setup, specifically the maximum initial temperature, applied deformation, heating/cooling rate and load rate. They noticed that the primary factors affecting shape recovery response of the SMPs are the initial high temperature at which the sample is deformed and the applied stress/strain level. They also observed that higher cooling rates during constant hold under cooling, necessitate lower temperatures for complete shape fixity, but raise the peak recovery stress. Also, lower heating rates during recovery increase the peak recovery stress. Tobushi et al. [20] carried out modified thermomechanical cycle on a polyurethane SMP sample in three point bending setup. They carry out various case studies to observe relationships between irrecoverable strain rate and holding time or holding temperature.

1.4 Review of SMP Models

Establishing appropriate models to simulate the shape memory processes and to predict the shape memory properties should be helpful for the development and application of SMPs. Constitutive models are critical for predicting the deformation and recovery of SMPs under a range of different constraints, in a way that is accessible to designers of components and applications that use these materials, but are scant in the literature [3]. In a recent review, Wagermaier et al. [1] state that the majority of research activities of the last decade on SMPs were focused on the experimental characterization of the shape memory effect and its principal physical understanding. However, they also note that only a few studies concentrated on the development of constitutive theories that describe the thermomechanical properties of SMPs at the macroscopic level. The key issue in the design of SMP based devices is a thorough understanding of the constitutive response of these materials under complex force and temperature protocols and the identification of the parameters that will serve to characterize the response of these materials and will allow for a detailed comparison of their properties [24]. Models for the shape fixity and recovery behavior have been developed by Tobushi et al. [25, 2, 26, 20], Abrahamson et al. [27], Takahashi et al. [28], Lee et al. [29], Lin and Chen [30], Bhattacharyya and Tobushi [31], Hong et al. [32], Liu et al. [3], Diani et al. [33]. Compared to the vast literature on experimental data on SMPs and SMP composites, the literature on SMP models is still growing only modestly.

The approaches in modeling techniques that have developed over the last decade

Table 1.2: Classification of few models in the current literature that deal with the macroscopic responses of pure SMPs

	Rheological		Phenomenological
	Ad-hoc	Thermodynamic Concepts	
Rate Type	Tobushi et al. [25, 2, 26, 20] Lin and Chen [30], Bhattacharya [31], Abrahamson [27]	Ghosh & Srinivasa [34], Diani [33]	Liu and Gall [3], Qi et al. [35]
History Dependent	Hong Yu [32]	—	Barot et al. [36], Chen et al. [37], Kim et al. [38]

from 1997 to 2010 can be classified into rheological and phenomenological approaches as shown in Table 1.2. Initial rheological modeling attempts mainly focused on capturing the shape recovery characteristics qualitatively. The more recent advances on the morphological studies encouraged thermodynamically motivated phenomenological models over the last five years. However in the attempt to encompass all the physical aspects of the material, the resulting phenomenological models are complicated and there is no assistance available to an application designer who can use simple models to predict the SMP responses even approximately.

The model developed by Tobushi et al [2] takes irreversible deformation and thermal strains of shape memory polyurethanes into account. Tobushi and coworkers have added a friction element into the standard linear viscoelastic model to simulate the behaviors of shape memory polyurethanes. They have carried out a series of creep tests of shape memory polyurethanes at different temperatures. They propose that if the strain exceeds particular threshold strain, irreversible deformation occurs. Also, the temperature change that would cause thermal expansion is accounted for by simply adding a coefficient of thermal expansion to terms involving the rate of strain, without any thermodynamic considerations as seen in Eq. (4) in Tobushi et al [2]. As a result, their model can be shown to be thermodynamically inconsistent even for pure thermoelasticity.

The model proposed by Lin and Chen [30] employs two Maxwell elements con-

nected in parallel to describe the shape memory properties of shape memory polyurethane. Their modeling results and experimental data show some deviation, which the authors ascribe to the polydispersed glass transition temperature of the studied samples. The model can qualitatively explain the occurrence of shape memory behaviors. However, since the dampers in the model are both viscous, there is no truly irrecoverable strain at the end of the process. Furthermore, the model was not developed using thermodynamical principles.

Abrahamson et al. [27] utilize a friction element in their model to account for the irrecoverable strain at the end of the cycle, that progresses from fully stuck to fully free over a finite range of strain. It was found that the stress-strain curve predicted by the model and that obtained by experiment agreed well. However, Abrahamson's model does not take the thermal expansion of the material, which is a crucial parameter to the material response, into consideration during the change of temperature.

A more recent work is the three-dimensional small-strain internal state variable constitutive model for uniaxial experiments by Liu et al. [3]. The model uses two internal variables to account for the micromechanical structures: frozen fraction describing the volume fraction of the frozen phase, and stored strain describing the strain that is stored (memorized) in the material during freezing. The entropic strain energy is gradually stored during cooling and released during reheating as free recovery strain or constrained recovery stress. The model was validated for uniaxial experiments carried out inhouse by the authors, for various loading conditions and strain levels.

Diani et al. [33] developed a three dimensional thermoviscoelastic constitutive model formulated in finite strains. This model was based on the viscoelastic properties of crosslinked SMP networks and was thermodynamically motivated. The deformation gradient is split into elastic and viscous parts, and the stress is split into entropic (following the Neo-Hookean model) and internal energy (defined in terms of Hencky strain measure) parts. The conditions on the evolution of the viscous part of the deformation gradient when the material is completely rubber or completely glassy is specified. The mechanical dissipation equation is obtained from the Clausius Duhem inequality, and the evolution of the deformation gradients for temperatures ranging between above glass transition temperature to below glass transition, are defined to satisfy the mechanical dissipation equation.

Following a similar approach to Liu's work, Chen and Lagoudas [37] developed a

three-dimensional constitutive model which can account for the non-linear material response to large deformations. This model, proposed on the framework of thermoelectricity, incorporates the concepts of stored strain and a frozen volume fraction. The constitutive equation proposed by this model, in its general form, can be interpreted as a rule of mixtures with contributions due to deformations in the frozen and active phase as well as a contribution due to deformations which are frozen upon cooling. The linearized version of this model for small deformation as a subsequent work was validated using data generated by Liu et al., however the large deformation model was not validated due to lack of sufficient data in the literature.

Barot and Rao [39] and Barot, Rao and Rajagopal [36] have developed models for SMPs undergoing shape setting through partial crystallization using a thermodynamical approach developed by Rajagopal and Srinivasa [40] using the maximum rate of dissipation criterion.

Although the attempts at modeling the SMP response have increased dramatically in the last decade, there have only been a handful of attempts at implementing the SMP models in a finite element setup to study the response for different load configurations or sample geometries, as listed below:

Qi et al. [35] proposed a volume fraction evolution model based on their experimental findings on SMP, where they used the concept of the first order phase transition for the deformation from the rubbery state to viscoplastic glassy state. This model was implemented in a user material subroutine (UMAT) in the finite element software package ABAQUS. The model was tested for isothermal uniaxial compressions at different temperatures and strain rates, and the response showed similar trends to experimental data. It was also tested for free recovery and constraint recovery cases, and the model trend agreed with experimental data only for the former case.

Nuygen et al. [41] incorporated a nonlinear Adam Gibbs model of structural relaxation and a modified Eyring model of viscous flow into a finite deformation thermoviscoelastic framework, which involved a fictive temperature concept and a nonlinear formulation of the Adam Gibbs model. This model was implemented numerically in a finite element setup, where the internal variables were computed by applying a backwards Euler scheme, and the predictor corrector integration scheme. The boundary value problem was that of a cylindrical SMP plug subjected to uniaxial thermomechanical compression. The model was tested for unconstrained strain

recovery and constrained stress recovery cycles.

Reese et al. [42] propose a large strain model, in a macromechanical as well a micromechanical format, employing the rule of mixtures for the energy parts of the rubbery and the glassy phase. They have implemented both the models in the finite element software “FEAP”, to investigate the thermomechanical response of a three dimensional cylindrical system, followed by a more realistic stent structure.

Srivasatava et al. [43] proposed a large deformation constitutive theory, using a “multimechanism” generalization of the classical Kroner Lee multiplicative decomposition of the deformation gradient. They implemented the model in a user material subroutine (UMAT) in ABAQUS/Standard for thermomechanical loading of a ring shaped structure, a flat diamond-lattice-shaped structure and compared it with experimental data. Finally they studied the model response in a cylindrical diamond-lattice-shaped structure approximating a SMP stent.

Diani et al. [44] proposed a model combining a generalized Maxwell model with the WLF equation, with specified parameters. Since both the generalized Maxwell model and the WLF equation are available in the ABAQUS/Standard, the model was implemented directly using these built-in features, and studied for various cases. These include the torsion shape recovery of a thin rectangular bar for various heating rates.

Baghani et al. [45] modified the model presented by Liu et al. [3] and presented the evolution law for internal variables for cooling and heating. They implemented the constitutive model within a user material subroutine (UMAT) in ABAQUS/Standard, and simulated the torsion of a rectangular bar and a circular tube, and compared the results with experimental data.

1.5 Motivation and Problem Formulation

Our approach, while similar in the use of thermodynamical ideas to that of Barot et al., differs from these models in the following ways: (1) we are focused on shape setting through glass transition and not through a real phase change, making our modeling task much simpler, (2) their approach is based on a history integral as seen from Eq. (34) in Barot et al. [36]. This leads to considerable complications in solving boundary value problems. Our approach is based on a much simpler rate type constitutive equations using a thermoplasticity like approach, leading to simple ODEs for homogeneous deformations and coupled PDEs and ODEs for general boundary

value problems. A Helmholtz potential based approach will be adopted [40] for the development of the constitutive equations for continuum model, using the maximum rate of dissipation criterion for the evolution of inelastic strain. The primary hypothesis of this model is that the hysteresis of temperature dependent activation-stress plays a lead role in controlling its main response features. This hypothesis will be validated and its implications on the model predictive capabilities as well as on the morphological understanding of the behavior of SMPs will be studied.

Most works in the literature use the continuum models of SMPs and incorporate it in a finite element setup for the applications of the SMP by writing a user-defined routine in FEM packages. Apart from issues with implementing complex non-linear 3D continuum models, this is computationally expensive and/or masks parametric design and control features that should be transparent and easily available to the designer. The loading conditions in the thermomechanical cycle studied are mainly uniaxial loading or torsion loading. While applications of shape memory materials utilize rods, plates or shells (for example: locking mechanisms, morphing air foils, repair patches, handicap casts, mandrels), there is a major stumbling block in the design of devices that use these materials i.e the non-availability of smart structural models such as beams, plates and shells that will allow designers to quickly evaluate alternative designs and carry out feasibility studies. Euler Bernoulli, Timoshenko, and other beam theories have been extended to formulate plate theories within general elastic and plastic regimes. This has lead to the development of specialized discrete elements that are utilized within a finite element framework to simulate complex geometries subject to complex loading conditions giving rise to various deformation modes. Analogous to this, the development of a SMP beam theory as a first step will establish the necessary background needed to develop specialized discrete elements that can be utilized to represent shape memory behavior (with the necessary degrees of freedom and temperature dependence) for structures. This will enable us to represent the shape memory behavior in a computationally efficient manner, that can be utilized for design exploration and optimization. There is thus a need to develop a unified framework for the simplistic modeling (both theoretical and computational) of such components which is capable of simultaneously accounting for the special geometry of these components as well as multiple field dependent behaviors i.e include deformations coupled with hysteretic and thermal phenomena. This acts as the motivation to develop a thermoviscoplastic beam theory

model for SMPs.

The particular problems that we are addressing in this work, shall target three important questions in the field and present solutions for them:

1. Is it possible to develop a simple model for SMPs with as few constitutive parameters as possible, such that it will capture the behavior of these polymers? The initial modeling attempts in the literature in the 1990s were rheological models but they lacked in physical correlation of the morphological changes in the SMP, and were ad hoc in their development without any thermodynamical considerations. Phenomenological models with thermodynamic concepts and phase evolution theories are now growing in the recent literature in the 2000s, and are developed with insights from the microstructural behavior of the SMPs but it is extremely difficult for an application engineer to work with these models and simulate responses of SMPs with 2D or 3D geometries or complex loading patterns. Most of these large strain models are linearized to small strain for validations, or the 3D models are reduced to 1D for actual simulation/validation. The validations are mostly qualitative. A strict error analysis of the results with experimental data is lacking. Would a thermodynamically consistent rheological model with physical motivation be able to address these shortcomings?
2. The primary hypothesis of this work shall explore the possibility of interpreting SMP responses as yield stress governed materials. Is it possible to control the gross responses of the SMP by controlling only this single variable of the model, which can give designers an approximate simulation and prediction of SMP responses for different loading conditions? Can this thermal hysteresis of the yield-stress be motivated as the underlying physical concept that controls the response of these polymers? Once this is sufficiently analyzed, it can act as a further motivation to explore cyclic thermomechanical responses of SMPs.
3. The last decade has seen an intense exploration of the uniaxial responses of the SMPs. As this area gets saturated, and attempts increases in the morphological investigations of the polymers, an area that has gotten ignored in the process is that of application oriented model development of SMPs. We shall address this area and show the efficacy of the model developed here by extending it to a beam theory model. The numerical implementation developed will be such

that this should keep the parameter controls and their evolution transparent to the designer, and make it sufficiently computationally inexpensive to carry out simulations for different load configurations and load levels. This will also act as a first step for the development of a complete beam, plate, shell theory for smart materials.

4. SMPs are capable of exhibiting large and complicated deformations. Most of the existing constitutive models of SMPs that are extensively referred to have been limited to one-dimensional small deformations [25, 3] or else the existing finite deformation models are reduced to linearized small strain models for validation purposes[46]. More importantly, these finite deformation models are motivated by non-linear responses of SMPs, but are studied for only uniaxial responses. Instead, we use the insights from the small strain model and develop a finite deformation model for the SMPs. We study the non-linear behavior of the model for shear deformations, that include isothermal, cyclic and thermomechanical loading cases.

1.6 Objective and Scope

The primary objective of this dissertation is the development and prediction of the thermomechanical response of SMP for different loading configurations. Specifically, the aims of this study are as follows:

1. A thermodynamically consistent 1D model and a corresponding small strain 3D model will be developed that can simulate the gross response of a SMP undergoing a thermomechanical cycle. The validation of the model will include the following targets:
 - (a) Validation of the activation stress hypothesis as the controlling parameter for the SMP response. The estimated parameters will be used for prediction of the SMP response under different loading conditions for the experimental data obtained for uniaxial loading conditions on two different SMP samples: polyurethane and Veriflex[2, 3].
 - (b) Estimation of yield stress coefficients from the error optimization of the model response.

- (c) Quantification of the effect of thermal expansion. Its implications shall be compared with the observations made by Gunes et. al. [23].
 - (d) Parametric study of the model parameters and a sensitivity analysis of the chosen response variables.
2. A beam theory model will be developed using the small strain 3D model, and a simple numerical implementation in the form of the operator-split approach will be used to analyse the beam theory model. This will include different recovery cases for thermodynamical cycle for a three point bend experiment on a SMP beam.
 3. A thermodynamically consistent finite strain 3D model will be developed from insights gained from the small strain model. This model will be able to simulate the gross responses of the SMP undergoing a shear thermomechanical cycle compared with experimental observations [19].
 4. Prescription of method to develop a SMA-SMP based multifunctional smart material system, that allows for the combined material system to have different tunable characteristics in different temperature ranges. This will include design guidelines and device ideas for proof of concept of these working systems.

Given the lack of experimental data on the actual polymer temperature versus that of the ambient atmosphere, and the extremely slow deformation rates, we will assume that the temperature of the polymer is the same as that of the surrounding atmosphere. Thus, we shall not be dealing with the heat equation in this work, rather we shall take temperature changes to the material as a defined input. Explicit history dependence of the material response, and moisture absorption capabilities of the material is outside the scope of this work. The material properties of the material like modulus and viscosity depend on heating and cooling processes which affects the material behavior, but instead of interpreting this dependence as being functions of temperature, as abundantly done in the literature, we look at the properties as two values corresponding to the rubbery and glassy phases, and switch between these values as the temperature dependent activation-stress moves from the rubbery to glassy phase and back.

1.7 Structure of the Dissertation

The structure of the dissertation is as follows:

1. Chapter 1 presents the research topic, with relevant literature survey and background information on shape memory polymers, including their behavior, applications, characterization methods, experimental studies and model development techniques. We propose the problem and the scope of the dissertation.
2. In Chapter 2, we demonstrate a Helmholtz potential based approach for the development of a 1D model for a SMP undergoing a thermomechanical cycle. We also propose the hypothesis of the activation stress as the primary controlling factor of the response of SMPs. We validate this hypothesis for the thermomechanical of SMPs for shape memory polyurethane and shape memory epoxy resin.
3. In Chapter 3, we extend the Helmholtz potential based 1D model developed in Chapter 2 to a small strain 3D version. We also establishing a systematic method to compute the coefficients of activation stress equation using an error optimization technique between the model results and the experimental data. We conduct an extensive parametric study of the model material parameters and loading conditions, and present a sensitivity analysis to the designer for SMP applications.
4. In Chapter 4, we develop an Euler Bernoulli beam theory for the small strain SMP model developed in Chapter 3. The boundary value problem that the SMP model is subjected to is a three point bending experiment. The implementation consists of developing a time stepping algorithm for the elastic predictor dissipative corrector loop. The beam theory model is subjected to validation and convergence studies, and finally implemented for a three point bend thermomechanical cycle.
5. In Chapter 5, we use the insights from the small strain model in Chapter 3 to develop a thermodynamically consistent finite deformation continuum model to simulate the thermomechanical response of SMPs. The SMP is modeled as a isotropic thermoviscoelastic material where thermal changes govern the evolution of the activation stress of the material. For the development of the

finite strain model, we follow the general technique of upper triangular or QR decomposition. The response of the model is studied for shear deformation for various temperature conditions, shear rates, cyclic loading and thermomechanical cycles.

6. In Chapter 6, we discuss a method for developing SMA-SMP multifunctional smart material system, that allow for the material system to have different tunable characteristics in different temperature ranges. Guidelines to form such smart systems have been established by estimating the volume fractions of the individual constituents. Various ideas for “smart-bias” tools/devices have been proposed, such that they can operate under three different temperature regimes, with one material constituent being passive and the other active at a given temperature.
7. We close in Chapter 7 with some final remarks on the different aspects of the work in this dissertation, and a discussion on future research directions.

2. TWO NETWORK THEORY BASED ONE DIMENSIONAL MODEL FOR SMPS*

2.1 Introduction

This chapter deals with the development of a two-network thermodynamically consistent model in a state-space form and shows that most of the gross features of a SMP depend on the yield-stress of the material. It is demonstrated that a systematic application of fundamental thermodynamic principles coupled with a suitable choice for the Helmholtz potential and suitable kinetic equations for the inelastic variables will allow the development of a complete simulation of the behavior of a class of shape memory polymeric materials. A number of significant features of the response can be deduced by a careful observation of the available experimental data.

- 1.) There is a hysteresis in the activation stress function of the material during heating and cooling.
- 2.) The yield stress of the material evolves differently depending on the extent to which the material has been strained.
- 3.) The thermal expansion behavior of the material significantly enhances the stress rise in the material during cooling due to contraction, but opposes the strain recovery by heating due to expansion. The contrasting behavior of the thermal expansion during cooling and heating makes the material response very sensitive to the coefficient of thermal expansion of the material.

The model that we propose takes into account these three phenomena. Given the lack of experimental data on the actual polymer temperature versus that of the ambient atmosphere, and the extremely slow deformation rates, we will assume that the temperature of the polymer is the same as that of the surrounding atmosphere. Thus, we shall not be dealing with the heat equation in this work, rather we shall take temperature changes to the material as a defined input. The solution of the system equations for a simple thermomechanical cycle shall be simulated in MATLAB. The results of the simulation are in qualitative and quantitative agreement with experiments performed on two different shape memory polymer samples: polyurethane

*Reprinted with permission from P. Ghosh and A. R. Srinivasa, "A Two-network Thermomechanical Model of a Shape Memory Polymer", *International Journal of Engineering Science*, vol. 49, no. 9, pp. 823–838, Copyright [2011] by Elsevier Limited

and epoxy resin. We find that modeling the hysteresis of the activation stress of the material during temperature changes is the key to the results.

2.2 The Thermomechanical Cycle and Morphology Changes

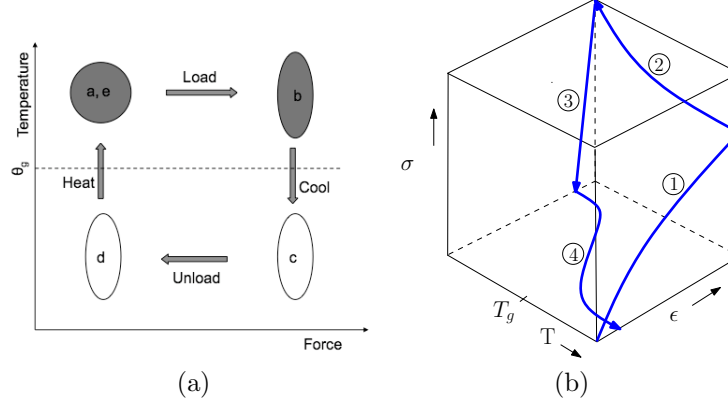


Figure 2.1: (a) The processes taking place in a thermomechanical cycle (b) Typical response data for a SMP sample undergoing a thermomechanical cycle. The curve 1 indicates the high temperature deformation. Curve 2 is the shape fixing process at constant strain, under cooling. Curve 3 is the relaxation of the stress at constant low temperature. Curve 4 is the strain recovery process under no load condition through heating.

The experiment carried out to observe the shape memory behavior of a SMP is a thermomechanical cycle as illustrated in Figure (2.1).

1. *Initial conditions: At (a):* The material is considered stress free above the glass transition temperature $\theta_g = \theta_g + 20^\circ\text{C}$. All strains are measured from this state. This current shape is recognized as the “permanent shape” of the material.
2. *Process ①: From (a) to (b): High temperature stretching:* The temperature is held fixed at θ_{max} and the strain is increased steadily at a constant prescribed rate g_1 to give the temporary shape to the material, and then the strain is held constant for a time $0 < t < t_1$.
3. *Process ②: From (b) to (c): Cooling and fixing the temporary shape:* The strain is fixed at g_1 and the temperature is lowered to $\theta_{min} = \theta_g - 20^\circ\text{C}$ at a predetermined

rate ' $-f_1$ '.

4. *Process ③: From (c) to (d): Relaxing the stress:* Now the temperature is fixed at θ_{min} and the stress is gradually relaxed to zero at a predetermined rate ' $-g_2$ '. During this process, material is observed to still be in its temporary shape.
5. *Process ④: From (d) to (e): Recovering the original shape:* Now the body is heated at rate ' f_1 ' in a stress-free state back to the original temperature to recover the original shape. The strain slowly relaxes and the material is back to its original shape.

The typical material response for the thermomechanical tests is shown in Figure (2.1-Right). The thermomechanical cycle also involves strain and stress-relaxing rate, and cooling and heating rates, which is not evident in these graphs. In the following work, we have extracted information from the above experimental data and plotted them against time.

To model the shape memory phenomenon, we borrow ideas from the two-network theory for polymeric materials dating back to Tobolsky and Andrews [47] and Tobolsky, Prettyman and Dillon [48] and introduce just two networks; one of which is a permanent-network responsible for permanent shape retention and recovery while the other network is a temporary-network which can be made to persist over long periods of time by suitably lowering the temperature. This latter network is responsible for the shape fixity properties of the polymer at low temperatures. Furthermore the interactions between the two networks are related to the shape fixity and shape recovery parameters. Changes in morphology of an SMP during a thermomechanical cycle: (Figure (2.2))

1. State (a) to (b): As the polymer is stretched, the permanent network, i.e polymer chains with permanent nodes (shown as black circles) in the figure, deforms due to the partial uncoiling of the polymeric chains between the cross-links. When two chains come close enough they stick together momentarily and form temporary nodes (shown as grey circles) before breaking off (shown as white jagged circles) continuously at high temperature, because of the electrostatic attraction between the individual chains. The connections between these temporary nodes form the temporary network.
2. State (b) to (c): Material is cooled, mobility of the chains decreases and the temporary nodes that are formed hold parts of the chains immobile exhibiting

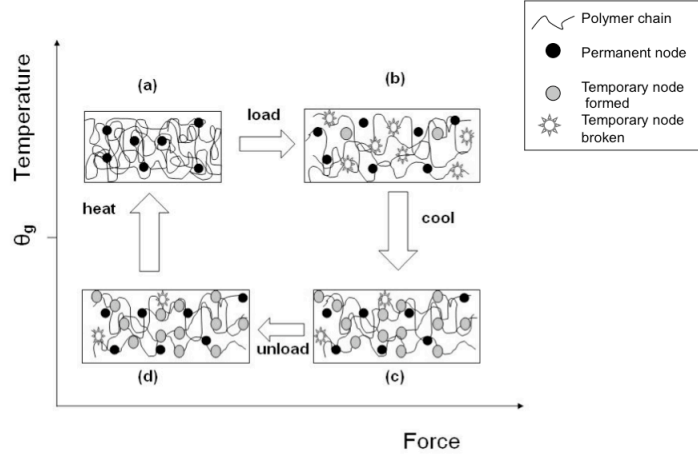


Figure 2.2: Change in morphology in a two-network model of the material during a thermomechanical cycle. Network 1: Permanent network consisting of polymer chains with permanent nodes, and network 2: Temporary network consisting of connections between the temporary nodes

“stickiness” and makes the polymer glassy.

3. State (c) to (d): On unloading of the material, the permanent network will have a tendency to coil back to its initial configuration. However, the temporary nodes “lock-in” the deformed state of the permanent network here as they are extant at low temperatures.
4. State (d) to (a): Subsequent heating increases the mobility of the chains, and the rate of breaking and reforming of temporary nodes starts rising once again. This “unlocks” the permanent network which now take over and recoil the polymer back to its original state.

2.3 Development of a Two-network One Dimensional Model

Rajaogopal and Wineman [49] developed a constitutive theory for the response of materials based on the two-network theory of Tobolsky and Andrews[47]. In this work, we follow their approach and present a thermodynamically consistent

rheological model for shape memory polymers.

It is clear from the morphological discussion in section (2.2) that the model simulating this kind of response should have:

1. Two viscoelastic components: A rubbery one which is apparent at high temperatures for the permanent network and a glassy one which is apparent at low temperatures for the temporary network,
2. activation behavior which is temperature sensitive so that it allows strains to be “locked-in” at low temperatures and “unlocked” at high temperatures,

The model shown in Figure (2.3) represents a mechanical visualization of a model that has all the necessary features to model for the SMP response in a thermomechanical cycle. In Figure (2.3), E_1 and E_2 denote the modulus of the rubbery

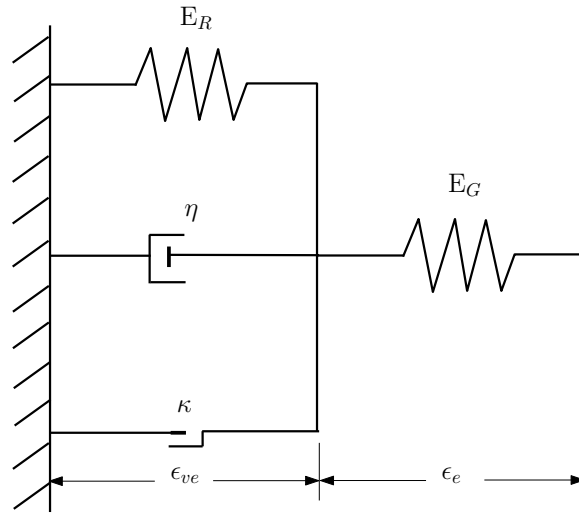


Figure 2.3: The proposed mechanical model for the SMP. The spring E_1 together with the viscous dashpot η represents the rubbery response of the material, the spring E_2 represents that glassy response and the frictional element k represents the locking behavior.

and glassy springs respectively, η is the viscosity of the viscous dashpot, and k is the activation stress of the friction dashpot of the model. The rubbery spring in the model represents the non-linear rubbery response of the material, at temperatures

beyond the glass transition. The glassy spring represents the glassy response at temperatures below the glass transition (when the rubbery spring is “locked”) and the stress is relaxed. To elaborate, the dashpot is a frictional dashpot that is temperature sensitive. Below the glass transition, the frictional dashpot locks, and prevents the rubbery network from deforming further, leading to a “locked in” strain. On the other hand, at high temperature, the dashpot ceases to operate i.e., its resistance vanishes, and the material behaves like an elastic rubber.

In this work, we will use the finite strain measure $\epsilon = (\lambda - 1)$, where λ is the stretch ratio, and all our stress measures will be with respect to the reference configuration. In other words, we are using a referential description for the 1D response in this work. We assign the stress σ_1 , which is a first Piola-Kirchhoff stress, as the non-linear rubbery response and, stress σ_2 as the dissipative response. ϵ_{ve} is the strain of the dampers in parallel, representing the locked in shape of the polymer, while ϵ_e is the strain of the glassy spring. To the mechanical strain ϵ_1 shown in the figure we shall have to add the thermal strain of the material so that we now have the total strain ϵ of the material. Thus, taking α to be the thermal expansion of the material, the elastic strain is given as:

$$\epsilon_e = \epsilon - \epsilon_{ve} - \alpha(\theta - \theta_{high}) \quad (2.1)$$

In the above equation α is not a constant, but is actually a function of temperature, and θ is the absolute temperature of the SMP sample (assumed to be uniform), and the form $\alpha(\theta - \theta_{high})$ is written for convenience. For this development, we shall be dealing with the temperature dependence of the thermal expansion of shape memory polyurethanes[23], and the thermal strains directly in the case of epoxy resin[3]. Consider a one-dimensional continuum, i.e., a wire, made of shape memory polymer, lying along the X-axis of a co-ordinate system and is heated above its glass-transition temperature so that it is in its rubbery state. A preliminary list of state variables is given by $S = (\sigma, \epsilon, \epsilon_{ve}, \theta)$. The foundation of the thermodynamical approach presented here is that, the non-dissipative properties of the material are derivable from a single potential, namely the Helmholtz potential for the continuum, while the dissipative properties are explored through the manifestation of the second law of thermodynamics, using the role of the rate of mechanical dissipation as a mechanism for entropy generation[40].

We begin with the equation of state in terms of the internal energy as below, following Callen [50]:

$$u = \hat{u}(\epsilon, \epsilon_{ve}, \zeta) \quad (2.2)$$

where u is the internal energy per unit reference length of the system, ζ is the entropy of the 1-D continuum per unit reference length. In terms of Eq. (2.2), the absolute temperature θ is given by $\theta = \frac{\partial u}{\partial \zeta}$.

The energy conservation equation in the absence of body forces can be written as:

$$\rho_r \frac{du}{dt} = \sigma \frac{d\epsilon}{dt} - \frac{dq}{dX} + r \quad (2.3)$$

where q is the axial heat flux and r is the lateral rate of heat transfer per unit reference length.

The Helmholtz potential being the legendre transform of the internal energy with respect to the entropy, it is related to the energy through

$$\psi = u - \theta \zeta \quad (2.4)$$

The entropy ζ now becomes a function of Helmholtz free energy as below:

$$\zeta = -\frac{\partial \psi}{\partial \theta} \quad (2.5)$$

Now, we can take the time derivative of the internal energy function in Eq. (2.4):

$$\frac{du}{dt} = \frac{d}{dt} \hat{\psi}(\epsilon, \epsilon_{ve}, \theta) - \frac{\partial \psi}{\partial \theta} \frac{d\theta}{dt} - \theta \frac{d}{dt} \frac{\partial \psi}{\partial \theta} \quad (2.6)$$

We reduce the energy conservation equation in terms of the Helmholtz potential by substituting equations (2.4), (2.5), (2.6) into Eq. (2.3) and arrive at the *heat equation*:

$$\theta \dot{\zeta} = \left\{ \sigma \dot{\epsilon} - \left(\frac{\partial \psi}{\partial \epsilon} \dot{\epsilon} + \frac{\partial \psi}{\partial \epsilon_{ve}} \dot{\epsilon}_{ve} \right) \right\} - \frac{dq}{dX} + r \quad (2.7)$$

The terms in the equation above are:

$$\text{Rate of heating} = \{ \text{Rate of heating due to mechanical effects} \} + \text{axial heat flow} + \text{latent heat}$$

The terms within the curly brackets in Eq. (2.7) is representative of the thermomechanical coupling. The first term inside the curly brackets represents the mechanical

power (or deformation power) supplied to the wire, while the second two terms represent the rate of decrease in recoverable mechanical work. The sum of these terms represents the net mechanical power dissipated by the system. We hence introduce the rate of dissipation ξ through

$$\sigma\dot{\epsilon} - \left(\frac{\partial\psi}{\partial\epsilon}\dot{\epsilon} + \frac{\partial\psi}{\partial\epsilon_{ve}}\dot{\epsilon}_{ve} \right) := \xi \quad (2.8)$$

where $\xi \geq 0$ as effected by the second law of thermodynamics. The terms in the equation above are:

$$\text{Supply of mechanical power} - \text{Rate of recoverable mechanical work} = \text{Net mechanical power dissipated}$$

The above identity is referred to as the dissipation relation or the reduced energy relation. This identity can also be equated in the following manner, which represents the *reduced energy-rate of dissipation relation* for the system:

$$\sigma\dot{\epsilon} - (\dot{\psi}|_{\theta fixed}) = \xi \quad (2.9)$$

We now have to characterize the material response by relating the energy storage elements in the proposed model to the Helmholtz potential and the dissipated elements in the model to the rate of dissipation function in the Eq. 2.9.

The Helmholtz potential ψ function depends on the state variables $(\epsilon, \epsilon_{ve}, \theta)$ and is assumed to be of the form*:

$$\psi = a\epsilon_{ve}^2 - b\epsilon_{ve}^4 + \frac{1}{2}E_2(\epsilon - \epsilon_{ve} - \alpha(\theta - \theta_{high}))^2 \quad (2.10)$$

The above form is not expected to be valid for arbitrary strains but only for strains upto 10 - 15%. The rate of dissipation will also be a function of the state variables $(\epsilon, \epsilon_{ve}, \theta)$, and will depend on how the mechanical work is dissipated due to internal viscous and frictional effects. The rate of dissipation depends upon the visocelastic strain rate and is assumed to have the following simple form

$$\xi = \eta\dot{\epsilon}_{ve}^2 + k|\dot{\epsilon}_{ve}| \quad (2.11)$$

*since we are not interested in the heat flux problem, we have suppressed the purely temperature dependent part of the Helmholtz potential.

The first term represents the rate of dissipation through the viscous damper modeled as a viscous effects, while the second term accounts for the rate of dissipation through the frictional effects.

Substituting Eq. (2.10) in Eq. (2.8) results in the following:

$$\sigma \cdot \dot{\epsilon} - (E_2(\epsilon - \epsilon_{ve} - \alpha(\theta - \theta_{high})))\epsilon - (2a\epsilon_{ve} - 4b\epsilon_{ve}^3 - E_2(\epsilon - \epsilon_{ve} - \alpha(\theta - \theta_{high})))\dot{\epsilon}_{ve} = \hat{\xi}(\dot{\epsilon}_{ve}) \quad (2.12)$$

Based on the assumption that the material possesses instantaneous hyperelastic response, the total stress σ is given by:

$$\sigma = \frac{\partial \psi}{\partial \epsilon} = E_2(\epsilon - \epsilon_{ve} - \alpha(\theta - \theta_{high})) \quad (2.13)$$

In the light of the Eq. (2.13), Eq. (2.12) reduces to

$$\hat{\xi}(\dot{\epsilon}_{ve}) = -(2a\epsilon_{ve} - 4b\epsilon_{ve}^3 - E_2(\epsilon - \epsilon_{ve} - \alpha(\theta - \theta_{high})))\dot{\epsilon}_{ve} \quad (2.14)$$

Using the stress in Eq. (2.13), the above equation can be reduced further as below, and this is used as the constraint for the system

$$\hat{\xi}(\dot{\epsilon}_{ve}) = (\sigma - (2a\epsilon_{ve} - 4b\epsilon_{ve}^3))\dot{\epsilon}_{ve} \quad (2.15)$$

We are thus led to the development of a kinetic equation for ϵ_{ve} which will satisfy the above equation. Now we shall use the *maximum rate of dissipation criterion* [51], which states that the system will evolve such that the actual value of $\dot{\epsilon}_{ve}$ is that which maximizes ξ subject to the constraint Eq. (2.15). Hence by using the standard method of calculus of constrained maximization as explained in Segel [52], we extremize ξ subject to the constraint Eq. (2.15) using the method of Lagrange multipliers:

Thus the value of $\dot{\epsilon}_{ve}$ that extremizes ξ is:

$$\dot{\epsilon}_{ve} = \frac{1}{\eta}(\sigma - (2a\epsilon_{ve} - 4b\epsilon_{ve}^3) + k(\text{sgn}(\dot{\epsilon}_{ve}))) \quad (2.16)$$

The dissipative response of the rubbery network is described by means of this kinetic equation. As can be seen from the model figure, the change in amount of stretch

of the rubbery spring, is related to the rate of change of ϵ_{ve} and this in turn is determined by the nature of the frictional dashpot. Notice that the above expression holds only when $\dot{\epsilon}_{ve} \neq 0$, which occurs only when $\sigma_2 > \hat{k}$, i.e only when the stress in the friction damper is greater than the activation-stress, the damper will have a velocity. Otherwise if $\sigma_2 \leq \hat{k}$, then $\dot{\epsilon}_{ve}$ will have to remain zero, because the stress in the friction damper has not yet exceeded its activation-stress, hence the damper remains locked.

The second law of thermodynamics requires that the dissipation of the system considered always be non-negative, which is automatically satisfied by the above consideration. The cases that arise from this lead us to three threshold conditions which are stated as the *kinetic equation* of the model:

$$\dot{\epsilon}_{ve} = \begin{cases} 0, & |(\sigma - (2a\epsilon_{ve} - 4b\epsilon_{ve}^3))| \leq \hat{k}; \\ \frac{1}{\eta}(\sigma - (2a\epsilon_{ve} - 4b\epsilon_{ve}^3) - \hat{k}), & (\sigma - (2a\epsilon_{ve} - 4b\epsilon_{ve}^3)) > \hat{k}; \\ \frac{1}{\eta}(\sigma - (2a\epsilon_{ve} - 4b\epsilon_{ve}^3) + \hat{k}), & (\sigma - (2a\epsilon_{ve} - 4b\epsilon_{ve}^3)) < -\hat{k} \end{cases} \quad (2.17)$$

The above set of cases can be written in a compact form as

$$\dot{\epsilon}_{ve} = \frac{1}{\eta} \{ \langle \sigma - (2a\epsilon_{ve} - 4b\epsilon_{ve}^3) - \hat{k} \rangle - \langle -\sigma + (2a\epsilon_{ve} - 4b\epsilon_{ve}^3) - \hat{k} \rangle \} \quad (2.18)$$

where $\langle x \rangle = \frac{1}{2}(x + \|x\|)$.

The state of the material is represented by the variables $S = (\sigma, \epsilon, \epsilon_{ve}, \theta)$. Equations (2.13) and (2.17) represent two constitutive equations for the response of the material. The remaining two equations needed to solve for this four-variable system can be specified in the control equation of stress/strain input and the input function of the temperature θ .

2.4 Normalizing Variables

We will now normalize the equations with respect to pertinent experimental values so that the material parameters identified for the validation case can be used to for prediction of different experimental variables.

- (1) The glass transition temperature θ_g .

- (2) The maximum strain applied ϵ_0 from experimental results.
- (3) The typical stress response at high temperature and constant applied strain, σ_0 , from experimental results.
- (4) The non-dimensionalization of the time, since this is connected with the kinetic response.

The parameters used to normalize the equations here are $C = \frac{\sigma_0}{\epsilon_0}$ and $\bar{\alpha} = \frac{\alpha\theta_0}{\epsilon_0}$. Note that $\bar{\alpha}$ is still a function of $\bar{\theta}$. Thereafter, the non-dimensional quantities are tabulated as in Table (2.1). Besides the above non-dimensional quantities, we take the values for the parameters enlisted in Table (2.2), which are decided based on normalizing the experimental data from Tobushi's[2] and Liu's[3]experimental data so that comparison of model and experimental data is sensible.

Table 2.1: Dimensional quantities and corresponding non-dimensional quantities

Dim	σ	ϵ	t	θ	a	b	E_2	η
Nondim	$\bar{\sigma} = \frac{\sigma}{\sigma_0}$	$\bar{\epsilon} = \frac{\epsilon}{\epsilon_0}$	$\bar{t} = \frac{t}{t_0}$	$\bar{\theta} = \frac{\theta}{\theta_g}$	$\bar{a} = \frac{2a}{C}$	$\bar{b} = \frac{4b\epsilon_0^2}{C}$	$\bar{E}_2 = \frac{E_2}{C}$	$\bar{\eta} = \frac{\eta}{t_0 C}$

Table 2.2: Parameter values for normalization and their significance in the samples

Param	ϵ_{max} for tests on Polyurethane			ϵ_{max} for tests on Epoxy resin			Significance
	2.4%	4%	10%	9.1%	-9.1%	0%	
σ_0 Mpa	0.796	1.251	2.069	0.85	-0.8	0	Experimental value of stress at constant θ_{high} and applied constant ϵ_{max}
ϵ_0	0.023	0.040	0.096	0.091	-0.091	0	Experimental applied constant ϵ_{max}
θ_g K		328			343		Glass-transition temperature of sample
t_0 sec		100			100		Glass-transition temperature of sample

2.5 Non-dimensional Set of System Equations

We view the SMP as a dynamical system i.e., one whose state changes are given by a suitable differential equation. We have obtained the system of model equations

for the material in state evolution form.

Force or Strain Control:

$$A(\bar{t})\dot{\bar{\sigma}} + B(\bar{t})\dot{\bar{\epsilon}} = g(\bar{t}) \quad (2.19)$$

State Equation:

Eq.(2.13) can be rewritten in rate form as follows:

$$\dot{\bar{\sigma}} - \bar{E}_2\dot{\bar{\epsilon}} + \bar{E}_2\dot{\epsilon}_{ve} + \bar{E}_2\left(\frac{d\bar{\alpha}}{d\bar{\theta}}\left(\bar{\theta} - \frac{\theta_{high}}{\theta_g}\right) + \bar{\alpha}\right)\dot{\bar{\theta}} = 0 \quad (2.20)$$

Kinetic Equation:

$$\dot{\epsilon}_{ve} = \begin{cases} 0, & |(\bar{\sigma} - (\bar{a} + \bar{b}\epsilon_{ve}^{-2})\epsilon_{ve}^{-})| \leq \bar{k}; \\ \frac{1}{\bar{\eta}}(\bar{\sigma} - (\bar{a} + \bar{b}\epsilon_{ve}^{-2})\epsilon_{ve}^{-} - \bar{k}), & (\bar{\sigma} - (\bar{a} + \bar{b}\epsilon_{ve}^{-2})\epsilon_{ve}^{-}) > \bar{k}; \\ \frac{1}{\bar{\eta}}(\bar{\sigma} - (\bar{a} + \bar{b}\epsilon_{ve}^{-2})\epsilon_{ve}^{-} + \bar{k}), & (\bar{\sigma} - (\bar{a} + \bar{b}\epsilon_{ve}^{-2})\epsilon_{ve}^{-}) < -\bar{k} \end{cases} \quad (2.21)$$

Temperature Specification:

$$\dot{\bar{\theta}} = f(\bar{t}) \quad (2.22)$$

2.6 Simulation of the SMP Response

2.6.1 Implementation of the System Equations

The state evolution form derived in the previous section will translate as follows to be fed into a suitable manner into MATLAB:

$$\dot{S} = f(S, t) \quad (2.23)$$

where S represents the variables that model the current state of the system and f is a function of the state variables and time. We will include the activation-stress as another variable for convenience in solving these equations in an numerical solver, details of this are discussed in Sec. (2.7.1). Thus, we can proceed to feed the equations (2.19) to (2.22) in the form $A_{(x,\theta,t)}\dot{x} = p_{(x,\theta,t)} + Q_{(x,\theta,t)}x$, which is solved by the ODE45 solver in MATLAB.

$$\begin{aligned}
& \begin{bmatrix} A(\bar{t}) & B(\bar{t}) & 0 & 0 & 0 \\ 0 & 0 & 1 & 0 & 0 \\ 1 & -\bar{E}_2 & \bar{E}_2(\frac{d\bar{\alpha}}{d\bar{\theta}}(\bar{\theta} - \frac{\theta_{high}}{\theta_g}) + \bar{\alpha}) & \bar{E}_2 & 0 \\ 0 & 0 & 0 & 1 & 0 \\ 0 & 0 & -\frac{d\hat{k}}{d\theta} & 0 & 1 \end{bmatrix} \begin{bmatrix} \dot{\bar{\sigma}} \\ \dot{\bar{\epsilon}} \\ \dot{\bar{\theta}} \\ \dot{\epsilon}_{ve}^- \\ \dot{\bar{k}} \end{bmatrix} \\
& = \begin{bmatrix} g(\bar{t}) \\ f(\bar{t}) \\ 0 \\ 0 \\ 0 \end{bmatrix} + \begin{bmatrix} 0 & 0 & 0 & 0 & 0 \\ 0 & 0 & 0 & 0 & 0 \\ 0 & 0 & 0 & 0 & 0 \\ \frac{1}{\bar{\eta}}a^2 & 0 & 0 & -\frac{1}{\bar{\eta}}(\bar{a} + \bar{b}\epsilon_{ve}^{-2})a^2 & -\frac{1}{\bar{\eta}}a^3 \\ 0 & 0 & 0 & 0 & 0 \end{bmatrix} \begin{bmatrix} \bar{\sigma} \\ \bar{\epsilon} \\ \bar{\theta} \\ \epsilon_{ve}^- \\ \bar{k} \end{bmatrix}
\end{aligned} \tag{2.24}$$

where,

$$a = \begin{cases} 0, & |(\bar{\sigma} - (\bar{a} + \bar{b}\epsilon_{ve}^{-2})\epsilon_{ve}^-)| \leq \bar{k}; \\ 1, & (\bar{\sigma} - (\bar{a} + \bar{b}\epsilon_{ve}^{-2})\epsilon_{ve}^-) > \bar{k}; \\ -1, & (\bar{\sigma} - (\bar{a} + \bar{b}\epsilon_{ve}^{-2})\epsilon_{ve}^-) < -\bar{k} \end{cases} \tag{2.25}$$

2.6.2 Simulation Specifications of the Thermomechanical Cycle

Since we are dealing with rate equations to describe the system, we have extracted the experimental data from Tobushi's and Liu's work with respect to time, which are then used in the governing equations as shown below.

Initial conditions: In terms of the state variables as shown in the section above, $\{\bar{\sigma}, \bar{\epsilon}, \bar{\theta}, \epsilon_{ve}^-, \bar{k}\} = \{0, 0, \theta_{high}, 0, 0\}$.

Table 2.3: Process inputs with respect to time

Process	Stress/ Strain rate input $g(\bar{t})$	Stress Control: $A(\bar{t})$	Strain Con- trol: $B(\bar{t})$	Temperature rate i/p i.e $f(\bar{t})$
a-b : $0 < t < t_1$	$g_1(\bar{t})$	0	1	0
b-c : $t_1 < t < t_2$	0	0	1	$-f_1(\bar{t})$
c-d : $t_1 < t < t_2$	$-g_2(\bar{t})$	1	0	0
d-e : $t_3 < t < t_4$	0	1	0	$f_1(\bar{t})$

For this the specifications of the processes are obtained from experimental data of Polyurethane[2] and Epoxy resin[33] as tabulated in Tables 2.3 and 2.4.

Table 2.4: Specifications of the processes obtained from experimental data of polyurethane and epoxy resin

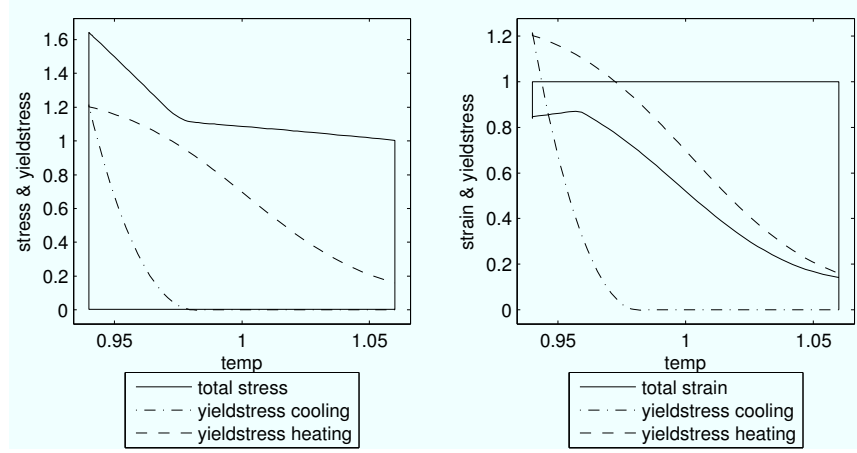
Process Specification	For Polyurethane	For Epoxy resin
Strain-rate	5-50% per minute	0.03-3% per minute
Loading and unloading hold-time	120 minutes	127 minutes
Heating and cooling rate	± 4 K/min	± 1 K/min
Total rise or drop in temperature	40 K	85 K

2.7 Temperature Dependence Form of Material Parameters

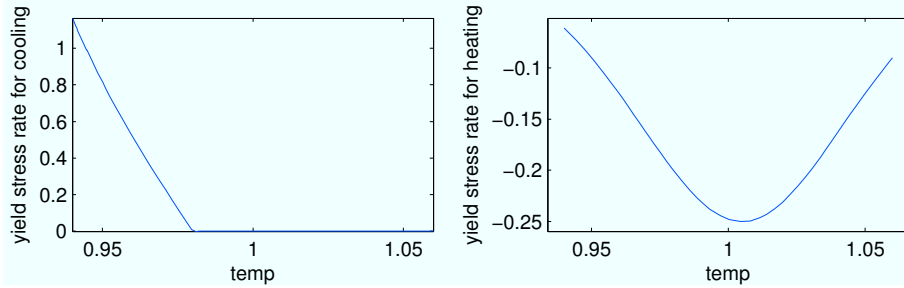
2.7.1 The Activation Stress Parameter

The key to the SMP response is the idea of “change in geometry on demand”. This kind of response requires two things: a signal to commence the change and energy to do it. The signal is represented by the activation threshold value which depends upon temperature and strain. The energy for change is the LHS of the energy dissipation equation 2.9. The variation of the activation stress controls the response of the SMP. The activation-stress of the material has a sensitive dependence on temperature, and the material yields differently depending on not just the current value of the temperature but also on whether the temperature of the material dropped or increased from the previous time-step. Thus there is a hysteresis of the activation-stress from the cooling to the heating cycle, which gives the different trends of the stress-rise during cooling and the strain-recovery during heating. The unrecovered strain at the end of the cycle is also explained by this hysteresis, because of the inelastic yielding of the material in the thermomechanical cycle. These considerations suggest that the activation-stress rate has the following functional form, and thus the activation-stress varies as shown in Figure (2.4).

$$\dot{\bar{k}} = \hat{f}(\bar{\theta}, \bar{\epsilon}, \text{sgn}(\frac{d\bar{\theta}}{dt})) \frac{d\bar{\theta}}{dt} \quad (2.26)$$



(a) (Left) The stress response mimics the activation-stress trend during cooling, which is negligible until $\theta = 0.98$, after which it steadily rises to reach a maximum of 1.65. (Right) The strain response mimics the activation-stress trend during heating. There is unrecovered strain at the end of the process, along with activation-stress in the material. This remnant of the activation-stress will affect the response of the material in the next test-cycle performed on the material.



(b) (Left) The rate of activation-stress during cooling is negligible until $\theta = 0.98$, after which the rate of activation-stress rises steadily, effecting in the rise of stress shown in 2.4a-Left. This rate of activation-stress along with thermal expansion of the material helps control the peak rise of the activation-stress and thus in the stress response of the material towards the end of the cooling process. (Right) The rate of activation stress during heating is decreasing steadily until $\theta = 0.95$, to take into account the increasing thermal strain, and result in the negligible recovery in the strain during the beginning of heating process, as shown in 2.4a-Right. The activation-stress rate is increasing after $\theta = 1.01$, to give a gentler decrease in the activation-stress and correspondingly in the strain recovery response as seen in 2.4a-Right, and to also control the unrecovered strain at the end of the process at $\theta = 1.06$.

Figure 2.4: Variation of (a)activation-stress with temperature in a thermomechanical cycle and (b)activation-stress rate with temperature during cooling and heating processes, for experimental data of polyurethane with maximum strain of 4%.

The factors that become important in this setup are as follows:

$\bar{\theta}_{high}$ **and** $\bar{\theta}_{low}$: The value of the activation stress is kept at a low minimum k_{min} , almost zero, so that in the initial range of high temperature stretching, the instantaneous rise in stress in the dry-friction damper overcomes its activation-stress and hence the inelastic strain starts rising in the dampers. Once the stress reaches a constant value, there is no more sliding of the dry-friction damper, and hence the inelastic strain gets “locked-in” after the initial rise. On the other hand, at low temperature towards the end of the cooling range, the activation stress of the dashpots reaches its maximum limit for that particular temperature. The stress in the dashpot network, even though in compression in the stress-relaxation range, its magnitude never exceeds the activation-stress and hence the friction dashpot helps “lock” the inelastic strain for this range as well.

$\bar{\theta}$: A typical observation regarding polymeric materials that thermally transition between a rubbery and glassy phase is that the number of secondary nodes formed at lower temperature is significantly higher than those formed at high temperature, and this number is a function of temperature [53]. Therefore the resistance provided by the temporary nodes in the polymer at low temperature will be significantly higher than that at high temperature, and is a function of temperature. Thus the activation-stress of the material is temperature dependent and changes during heating or cooling of the material during a thermomechanical cycle. During cooling, the stress of the material rises. This is effected mainly by allowing stress in the dashpots to rise by varying the activation stress of the material. The stress in the dashpots overcomes the activation-stress and hence the friction dashpot slips further. The rate of activation-stress of the material \dot{k} here is prescribed to be zero till almost above glass-transition, and starts rising rapidly only at lower temperatures below glass-transition[54]. Because of this, the rise in stress can be controlled carefully, and kept constant till temperature drops to θ_g , and then the stress is made to rise in desired fashion at lower temperatures. Thus a sigmoidal function \hat{f}_1 is used which asymptotes between k_{min} and k_{max} .

$\frac{d\bar{\theta}}{dt}$: In this work we propose that the resistance provided by the networks during the cooling process at constant deformation is different than that during heating

at no load. During cooling at constant deformation, the resistance provided by the temporary network consists only of the temporary nodes formed during cooling. No additional temporary nodes are formed, as the permanent network polymer chain mobility is decreasing. However, during heating at no load condition, the resistance provided by the temporary network consists not only of the temporary nodes formed at low temperature, but also new temporary nodes that are formed as the permanent network polymer chains recoil to new configurations during heating. Therefore there is a hysteresis in the resistance provided by the temporary network during the cooling and heating regime of the thermomechanical cycle. The activation stress controls the way the inelastic strain evolves. Having the same function of rate of activation-stress during heating, as specified for cooling f_1 in the above point, leads to unsatisfactory strain recovery from the model. Also, complete recovery of the activation-stress implies complete recovery of the inelastic strain at the end of heating, which will not mimic the residual strain recovery at the end of the cycle. For finer control on the response curves of stress and strain during cooling and heating respectively, it becomes obvious that different trends of activation stress \bar{k}_1 and \bar{k}_2 (see Figure (2.4a)) are needed depending on whether the material is cooled or heated, i.e whether $\text{sign}(\frac{d\bar{\theta}}{dt}) < \text{ or } > 0$. Thus Eq. (2.26) will depend on three cases as follows:

$$\dot{k} = \begin{cases} 0, & \text{if } \frac{d\bar{\theta}}{dt} = 0; \\ \hat{f}_1(\bar{\theta}, \bar{\epsilon}) \frac{d\bar{\theta}}{dt}, & \text{if } \text{sgn}(\frac{d\bar{\theta}}{dt}) = -ve; \\ \hat{f}_2(\bar{\theta}, \bar{\epsilon}) \frac{d\bar{\theta}}{dt}, & \text{if } \text{sgn}(\frac{d\bar{\theta}}{dt}) = +ve; \end{cases} \quad (2.27)$$

This hypothesis suggests that the *material yields differently depending on not just the current value of the temperature but also on whether the temperature of the material dropped or increased from the previous time-step*. \hat{f}_2 is adjusted so that desired shape recovery is obtained and is reduced to a value that will give ideal residual shape recovery response. This adjustment was done by extracting a Gaussian curve-fit to get an approximate idea of the functional form that will fit data for all three strain levels for validation. The residual activation-stress at the end of heating range will affect the next cycle of loading, and will account

for the thermal hardening of the material under cyclic loading. Thus the stress and strain response during cooling and heating respectively, can be controlled by adjusting \hat{f}_1 and \hat{f}_2 . This can be witnessed in Figure (2.4b). For example, the initial constant strain response during heating is maintained by keeping \bar{k}_{max} high enough at the end of the cooling cycle, so that the activation stress takes a while before it becomes comparable to the stress in the dampers. Only then the the inelastic strain gets “unlocked”, and strain recovery begins.

$\bar{\epsilon}$: Another typical observation made for polymer materials is that as the material is deformed, the polymer chains uncoil and stretch out. As the polymer chains are stretched, the chain mobility decreases, thus increasing the chain entanglements and formation of temporary nodes. Therefore, the resistance provided by the temporary nodes increases as the polymer is deformed to higher strain levels. It becomes evident that the rate of activation stress of the material being dependent on $\bar{\theta}$ and $sgn(\frac{d\bar{\theta}}{dt})$, it has the same trend regardless of the strain level. However the strain recovery of polyurethane during heating for the three different strain levels we are working with for validation, have different trends (Refer Sec. 2.8). It is also evident in the compression and tension experiments of epoxy resin, that the strain level implies different yield tendencies of the material. Although the maximum stress rise during cooling and the thermal strain Opposing Factor during heating (refer to Sec. (2.7.2) contribute in the strain recovery characteristics at different strain levels, the changes accounted for are not satisfactory. Thus, the activation stress rate needs to take into account the strain level the material is at, to affect the strain recovery differently at different strain levels. Note that the rate activation stress is only a linear function of the strain, and this dependence will disappear for the activation-stress, and hence not cause any inconsistencies with the assumptions for the rate of dissipation function. Thus we have the rate of activation stress as $\dot{\bar{k}} = \hat{f}_1(\bar{\theta}, \bar{\epsilon}) \frac{d\bar{\theta}}{dt}$ for cooling and $\dot{\bar{k}} = \hat{f}_2(\bar{\theta}, \bar{\epsilon}) \frac{d\bar{\theta}}{dt}$ for heating.

Taking all these factors into consideration, the final equations of rate of activation stress have the following form:

$$\begin{aligned} f_1 &= a\epsilon + \delta_1 b(\sinh(-c\pi(\theta - \theta_1))) \\ f_2 &= -d\epsilon - \delta_2 e(1 - (f \tanh(m\theta + n))^2) \end{aligned}$$

where, $m = 2/(\theta_{max} - \theta_2)$, $n = 1 - m\theta_{max}$

and, a, b, c, d, e, f are constants depending on material type and applied ϵ_{max} , θ_1 and θ_2 are limiting values of θ until which there is no rise/fall in the stress/strain during the cooling/heating cycle. This is determined from the experimental data, for example, refer to the experimental data for maximum applied strain of 4% in Figure 2.4, where these values will be $\theta_1 = 0.98$ (value of θ until which there is no stress rise in the cooling process) and $\theta_2 = 0.95$ (value of θ until which there is no strain recovery in the heating process), and

$$\delta_1 = \begin{cases} 1, & \forall \theta \leq \theta_1; \\ 0, & \forall \theta > \theta_1; \end{cases} \quad (2.28)$$

$$\delta_2 = \begin{cases} 0, & \forall \theta < \theta_2; \\ 1, & \forall \theta \geq \theta_2; \end{cases} \quad (2.29)$$

The rate of activation-stress specified by the above equations for the experimental data is as shown in Figure (2.4b).

2.7.2 The Effect of Thermal Expansion

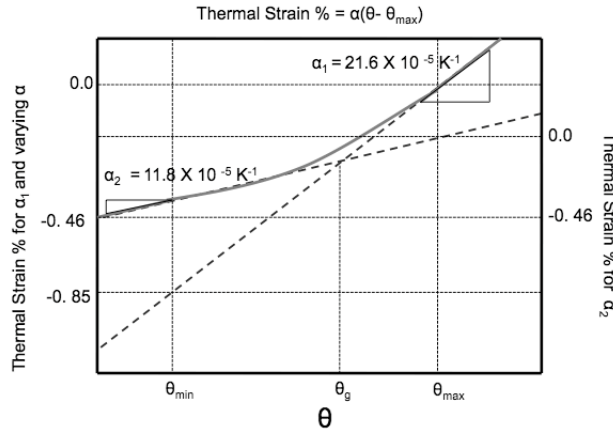


Figure 2.5: Variation of thermal strain with temperature. Take note of (a) Thermal strain for constant high temp value α_1 , axis on LHS and associated unaccounted thermal strain, (b) Thermal strain for constant low temp value α_2 , axis on RHS and associated unaccounted thermal strain, (c) Thermal strain for varying values of α , axis on LHS

The thermal expansion of the material is dependent on temperature. Let us consider the typical shape memory polyurethane thermal response as shown in Figure (2.5). The average thermal expansion coefficient in the rubbery state ($\alpha_1 = 21.6 \times 10^{-5} K^{-1}$) is about two times of that in the glassy state ($\alpha_2 = 11.8 \times 10^{-5} K^{-1}$)[23]. All thermal strains being measured with reference to the high temperature, the thermal strains at lower temperatures, are the largest. The thermal behavior of the material although aids in the cooling process, it counteracts the recovery behavior during the heating process (refer to Figure (2.6)). This counteraction is what causes the total strain to rise at the initial period of heating, and this can be controlled by the thermal strain completely. The material response is very sensitive to the thermal expansion coefficient, and the final rise of stress at the end of cooling range and the rise of strain during the start of heating range are affected severely by it. Therefore, a more accurate specification of the thermal expansion gives closer results to the actual experimental data. Note however that the thermal strains of the material is dependent on the temperature alone, and this role of thermal expansion in the strain recovery process reduces with increasing strain levels, because the total amount of strain to be recovered is rising while the amount gained back by the thermal expansion remains the same at all strain levels. Hence, for the polyurethane experiments, at low strain levels, the thermal strain accounts for almost 20% of the total strain as shown in the contributing factor C. F. values in Table. (2.5), but at high strain levels its effect is only 4%. This implies that at increasing strain levels, 96% of the recovery will have to be dictated by the yielding of the material and not the thermal expansion. Also, as discussed previously, the strain recovery process and the thermal expansion process during heating counteract each other, as see in Figure (2.6). This implies that a relatively low value of thermal expansion in comparison to recovered strain is desired for improved shape memory effect. This is measured in terms of opposing factor O.F, as shown in Table. (2.5), lower O.Fs being desirable.

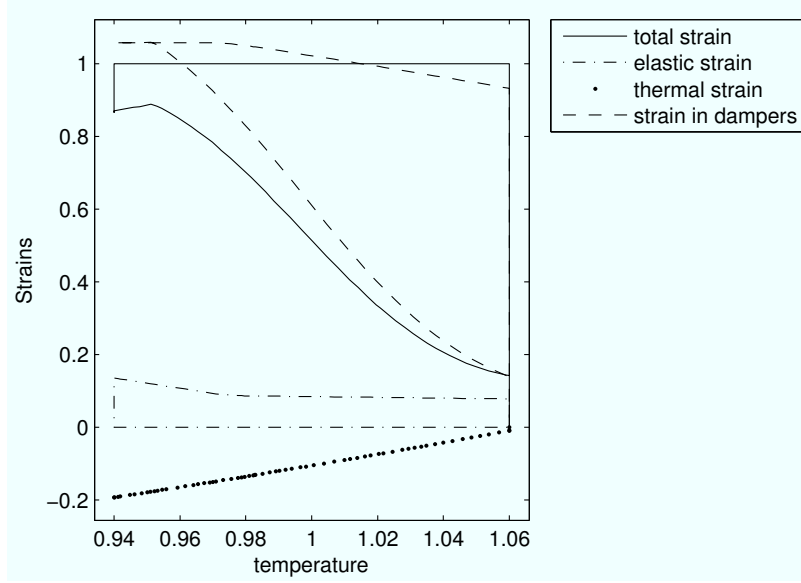


Figure 2.6: Plots of viscoelastic, thermal and elastic strain and their combination to produce the total strain in the complete cycle. Notice that the thermal strain is opposite to the damper strain during recovery, and the effect is pronounced at the beginning of recovery

Table 2.5: Comparison of the strain responses and thermal strains, of shape memory polyurethane at various applied strain (ϵ_{max}) levels

ϵ_{max} (%)	Shape fixity F (%)	Shape recovery R (%)	$C.F = \frac{\epsilon_{th}}{\epsilon_{max}}(\%)$	$O.F = \frac{C.F}{R}$
2.4	84.33	87.5	19.35	0.22
4	87.5	82.5	11.61	0.14
10	83	94	4.64	0.04

2.8 Results of Validation and Prediction of 1D Model using Referred Experimental Data

With the development of a one-dimensional model complete, we will now compare the simulations with experimental data from two different polymers.

2.8.1 Shape Memory Polyurethane

We will compare our simulations with the experimental data provided by Tobushi et al. [2]. In their experiments, the polyurethane used had a glass transition of 328 K, the thickness of the specimen was about 70 μ m, the width was 5 mm, gauge length 25 mm and total length of 75mm. The activation-stress function was chosen such that the model gave reasonable results for all three strain levels. The simulation

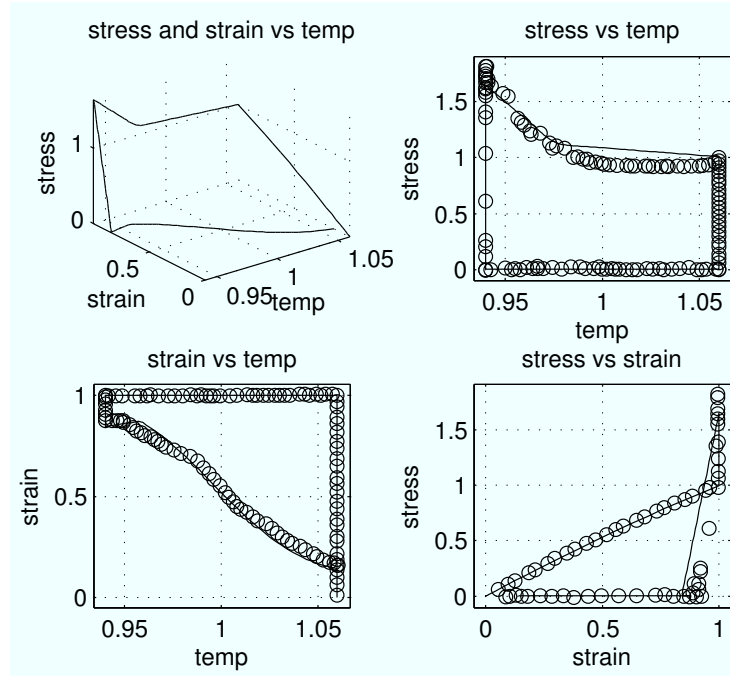


Figure 2.7: Comparison of the experimental data of polyurethane by Tobushi et al [2] with the prediction of the model developed here for $\epsilon_{max} = 4\%$

results shown in Figure (2.7) compare the results of the model and experimental data for $\epsilon_{max} = 4\%$. The parameters a, b and η are selected to control the stress

response of the model during the initial high-temperature stretching (process a-b). These values are used to predict for lower and higher strain levels, in Figures 2.8 and 2.9. The stress vs. strain graph will show how the non-linearity of the response comes into play. For higher strains this can be seen in Figure (2.9). The activation-stress functions are chosen to control the stress-rise during cooling (process b-c) and the strain recovery during heating (process d-e) as discussed in Section 2.7.1. The parameter E_2 is selected to control the strain response i.e the shape fixity, during low temperature stress relaxation (process c-d). Using these parameter values we predict the SMP response for different strain levels of $\epsilon_{max} = 2.4\%$ and $\epsilon_{max} = 10\%$.

The activation-stress rate function chosen for this material response is depen-

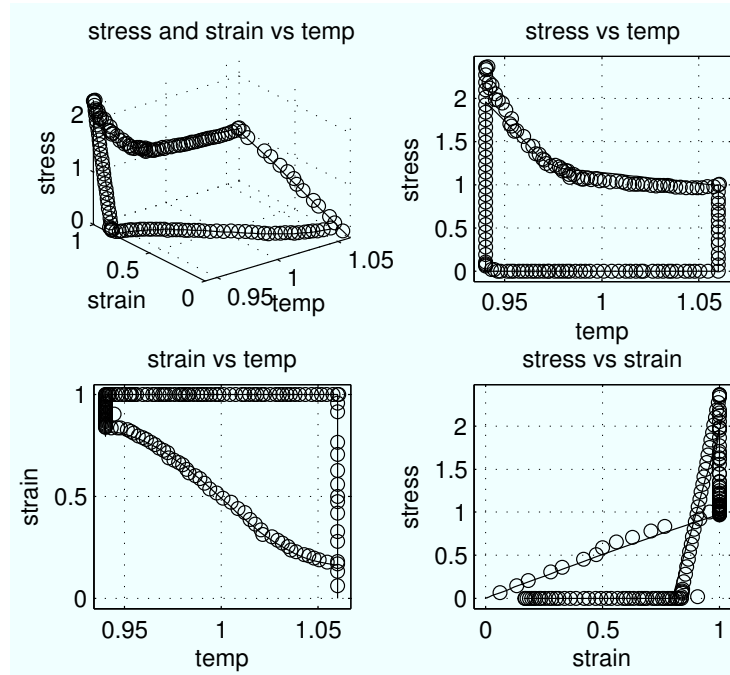


Figure 2.8: Comparison of the experimental data of polyurethane by Tobushi et al [2] with the prediction of the model developed here for maximum applied strain of 2.4%

dent on strain levels, and hence with change in the maximum strain applied in the thermomechanical cycle, the activation-stress changes slightly to accommodate the changing responses in the strain levels. The non-linear response becomes obvious

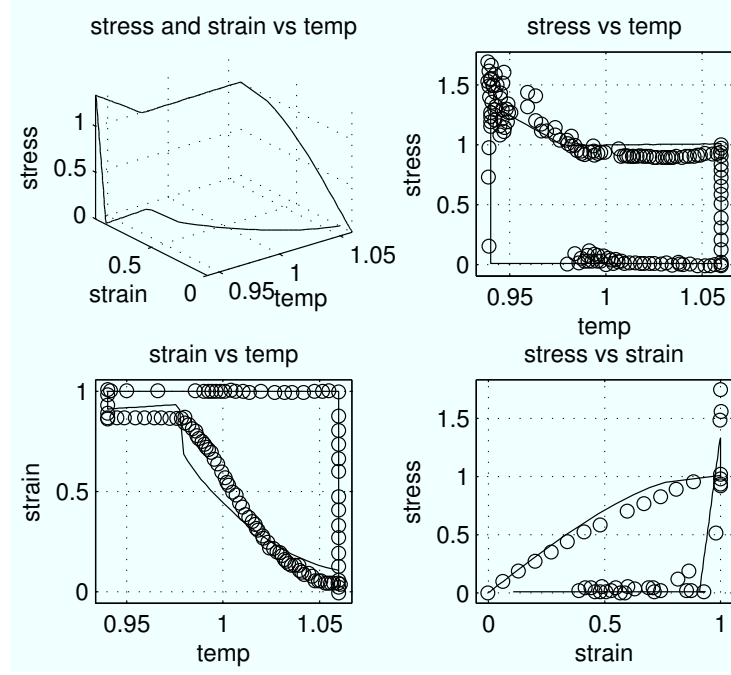


Figure 2.9: Comparison of the experimental data of polyurethane by Tobushi et al [2] with the prediction of the model developed here for maximum applied strain of 10%

at this higher strain level as can be seen in the stress vs. strain plot here. The parameters a and b were chosen to exhibit non-linearity in the model. The stress rise during cooling, for the chose activation-stress function, is not satisfactory and this consequently affects the strain recovery during heating.

2.8.2 Shape Memory Epoxy Resin

The second sample that we will consider is that of Epoxy resin that was experimentally investigated by Liu et al. [3]. A thermal strain function $\bar{\epsilon}_{thermal} = \hat{f}(\bar{\theta})$ is fitted from experimental data, and used in the model in the rate form directly as below, rather than in terms of the conductivity $\bar{\alpha}$ previously. Using the parameter values for the validation of tension $\epsilon_{max} = 9\%$ in Figure 2.10, we predict the SMP response for compression $\epsilon_{max} = -9\%$ in Figure 2.11 and no load cases in Figure 2.12.

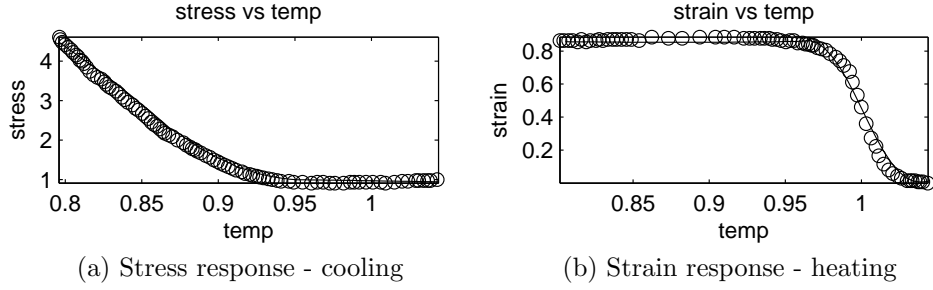


Figure 2.10: Comparison of the experimental data of epoxy by Liu et al [3] with the prediction of the model developed here under tension of 9.1%

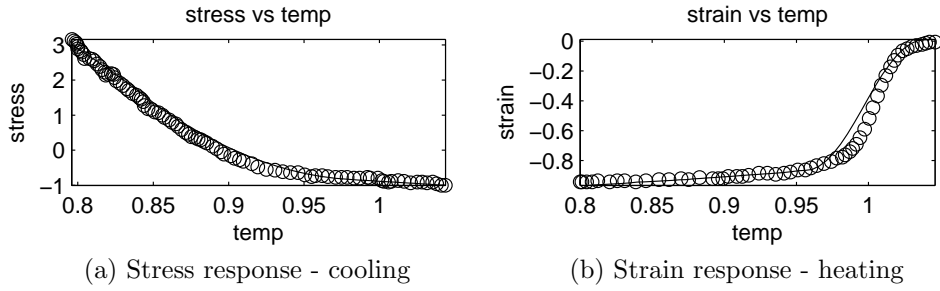


Figure 2.11: Comparison of the experimental data of epoxy by Liu et al [3] with the prediction of the model developed here under compression of 9.1%

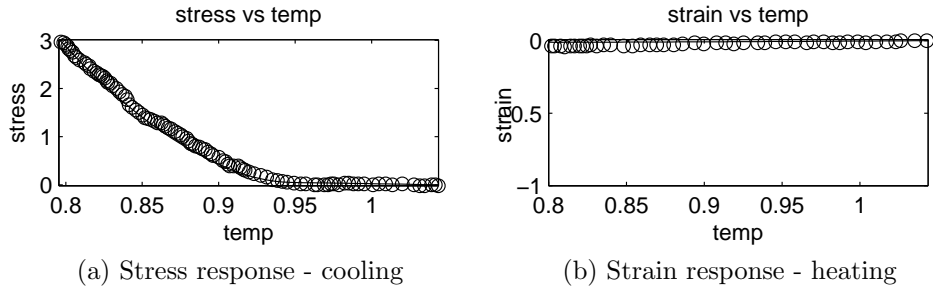


Figure 2.12: Comparison of the experimental data of epoxy by Liu et al [3] with the prediction of the model developed here in the undeformed case

2.9 Conclusions from the 1D Model

The activation-stress of the friction dashpot plays the lead role in controlling the response of the model during heating and cooling. Different functions of the activation-stress evolution during heating versus cooling processes give improved results in strain recovery. This suggests that there is a hysteresis in the activation stress of the material when it undergoes a heating-cooling cycle. The activation stress rate as a function of the strain of the material, affects the recovery behavior during heating, and simulates the significantly different strain recoveries at the different strain levels. This suggests that the yielding of the material is influenced by the extent to which it is loaded. For a detailed discussion of these findings, refer to the work by Ghosh and Srinivasa[34]. The hypothesis of the thermal hysteresis of the activation stress is thus validated for the 1D model, and proves to have reasonable predictive capacity as seen from the different cases predicted in the results section for two different polymer systems. We will use this hypothesis in the extension of the model to a three-dimensional setup.

3. SMALL STRAIN THREE DIMENSIONAL MODEL WITH PARAMETRIC ANALYSIS AND ERROR OPTIMIZATION

3.1 Introduction

The Helmholtz potential-based approach, proposed and developed as a 1D model (refer to Chapter 2) will be employed here for the development of the small strain 3D continuum model, using the maximum rate of dissipation criterion for the evolution of inelastic strain. The primary hypothesis of the model has been that the hysteresis of temperature dependent activation-stress plays a lead role in controlling its main response features. This hypothesis has been validated and its implications on the model predictive capabilities as well as on the morphological understanding of the behavior of SMPs were studied in the previous chapter. In this chapter, we will extend this approach to 3 dimensions (small strain) in a fairly simplistic way and further establish a method to compute the coefficients of the model using a systematic weighted error computation and minimization technique. We then move on to a detailed study of the effect of each material parameter on the response characteristics of the model. This helps conduct a sensitivity analysis of the parameters, where we can provide the designer with solutions such as the control of which particular material parameter will affect which response. Since the response of the SMPs is complicated, with two or more material parameters affecting a single response, we provide response surface maps for some of the response characteristics to give the designer a better understanding of the control of a particular response by varying two controlling material parameters simultaneously. Similar parametric study is done for some of the control parameters of the experiment such as the cooling rate ϵ_{max} and heating rate θ_{max} . This extensive study gives a fairly good idea of how the model works and few insights into the SMP behavior itself.

3.2 Development of the Three Dimensional Model

The experiment that we shall be considering in this work is a thermomechanical cycle on a shape memory polymer from the work carried out on a polyurethane sample by Tobushi et al. [2] as described in Chapter 2 Figure 2.1.

A detailed development of the Helmholtz potential-based 1D multi-network model was presented in Chapter 2. Here, we retain its important features for the develop-

ment a small strain 3D model. Consider a SMP sample at a temperature $\theta_h > \theta_g$. This will be considered as the reference configuration of the body, and all strain measurements will be made relative to this reference configuration. Let this body undergo a displacement $\mathbf{u}(x, t)$. The small strain $\boldsymbol{\epsilon} = \frac{1}{2}(\nabla \mathbf{u} + \nabla \mathbf{u}^T)$ of the body can be separated into deviatoric and volumetric parts as $\boldsymbol{\epsilon} = \boldsymbol{\gamma} + \frac{1}{3}e\mathbf{I}$ where, $\boldsymbol{\gamma}$ is the deviatoric strain, and $\frac{1}{3}e\mathbf{I}$, is the volumetric strain, where $e = \text{tr}\boldsymbol{\epsilon}$. The two network model for the SMP is made up of a permanent “backbone” network that is responsible for shape recovery and a temporary or transient network that is responsible for the shape fixing phenomena. We introduce the idea of viscoelastic strain $\boldsymbol{\epsilon}_{ve}$ that represents the “locked in” shape of the polymer i.e it corresponds to the strain of the temporary network. The elastic strain $\boldsymbol{\epsilon}_e = \boldsymbol{\epsilon} - \boldsymbol{\epsilon}_{ve} - \alpha(\theta - \theta_h)$ represents the strain of the permanent network. As the polymer is stretched, the permanent networks deform due to the partial uncoiling of the polymeric chains between cross-links. Thus $\boldsymbol{\epsilon}_e$ represents sliding and well as expansion or contraction behaviour of the permanent network chains. The temporary network on the other hand, is created whenever temporary nodes are formed between two chains sticking together momentarily. The temporary nodes are broken whenever two chains slide apart, thus breaking the temporary network. The temporary network is locked at glassy state, i.e at temperatures below glass transition. This behaviour is captured by the strain $\boldsymbol{\epsilon}_{ve}$. We assume that these temporary networks are formed only due to the sliding of chains over one another, and not during expansion or contraction. Therefore assuming viscoelastic incompressibility: $\text{tr}\boldsymbol{\epsilon}_{ve} = 0$, the viscoelastic strain is purely deviatoric $\boldsymbol{\epsilon}_{ve} = \boldsymbol{\gamma}_{ve}$.

Based on the 1D model of the SMP, which had Helmholtz potential of the form,

$$\psi_{1D} = \frac{1}{2}E_G(\epsilon - \epsilon_{ve} - \alpha(\theta - \theta_h))^2 + \frac{1}{2}E_R\epsilon_{ve}^2 \quad (3.1)$$

We begin the thermodynamical modelling of the response of the material by assuming that the Helmholtz potential is the sum of the strain energy of the glassy or temporary network and that of the permanent network

$$\psi = \psi_{\text{permanent}} + \psi_{\text{transient}}$$

$$= \frac{1}{2} \mathbf{C}_G (\boldsymbol{\epsilon} - \boldsymbol{\epsilon}_{ve} - \alpha(\theta - \theta_h) \mathbf{I}) \cdot (\boldsymbol{\epsilon} - \boldsymbol{\epsilon}_{ve} - \alpha(\theta - \theta_h) \mathbf{I}) + \frac{1}{2} \mathbf{C}_R \boldsymbol{\epsilon}_{ve} \cdot \boldsymbol{\epsilon}_{ve} + f(\theta) \quad (3.2)$$

For the purposes of the current study, we assume that glassy and rubbery moduli are isotropic. The glassy and the rubbery stiffness matrices are given as

$$\mathbf{C}_G = k_G \mathbf{I} \otimes \mathbf{I} + 2\mu_G (\mathbf{I} - \frac{1}{3} \mathbf{I} \otimes \mathbf{I}) \quad (3.3)$$

$$= (k_G - \frac{2\mu_G}{3}) \mathbf{I} \otimes \mathbf{I} + 2\mu_G \mathbb{I}$$

$$\mathbf{C}_R = k_R \mathbf{I} \otimes \mathbf{I} + 2\mu_R (\mathbb{I} - \frac{1}{3} \mathbf{I} \otimes \mathbf{I}) \quad (3.4)$$

$$= (k_R - \frac{2\mu_R}{3}) \mathbf{I} \otimes \mathbf{I} + 2\mu_R \mathbb{I}$$

where k_G is the glassy bulk modulus, k_R is the rubbery bulk modulus, μ_G is the glassy shear modulus, μ_R is the rubbery shear modulus, and α is the thermal expansion.

There are researchers in this field who propose the moduli of SMPs as anisotropic. Beblo et al. [55] have conducted experiments to investigate the strain induced anisotropic properties of SMP Veriflex. These observations have been made for large strain applications of 40% and 70%. They have observed decreased transverse stiffness and increased axial toughness when the material is subjected to high strain applications. The anisotropic behavior shows up while heating the polymer across the T_g , and the constant, isotropic stiffness values above and below T_g that is generally considered in the literature, have been discouraged by researchers in this area. Hypotheses regarding the morphological changes in the material that cause the observed anisotropic effects have been offered, but these ideas remain fairly new and complex in the SMP field. Behl et al. [9, 56] have commented on strain induced anisotropy, their primary focus being SMPs with carbon nanotubes and other light induced SMPs. It is proposed that on heating the SMP beyond the transition temperature, the orientation of the switching segments change from an oriented conformation to a random one. The mechanical property changes caused due to this shift from anisotropic characteristics to isotropic behavior. However, in view of the fact that these observations are crucial only in large deformation cases, and also that the data for designing or characterizing such behavior is limited, for the current

purposes we assume isotropy in the SMP response. However, the procedure that we follow here is such that it can be extended to anisotropic materials.

Thus, in terms of material properties, ψ becomes

$$\begin{aligned}
\psi &= \frac{1}{2} \left(\left(k_G - \frac{2\mu_G}{3} \right) \mathbf{I} \otimes \mathbf{I} + 2\mu_G \mathbb{I} \right) (\boldsymbol{\epsilon} - \boldsymbol{\epsilon}_{ve} - \alpha(\theta - \theta_h) \mathbf{I}) \cdot (\boldsymbol{\epsilon} - \boldsymbol{\epsilon}_{ve} - \alpha(\theta - \theta_h) \mathbf{I}) \\
&\quad + \frac{1}{2} \left(\left(k_R - \frac{2\mu_R}{3} \right) \mathbf{I} \otimes \mathbf{I} + 2\mu_R \mathbb{I} \right) \boldsymbol{\epsilon}_{ve} \cdot \boldsymbol{\epsilon}_{ve} \\
&= \frac{1}{2} \left(k_G - \frac{2\mu_G}{3} \right) \left(\text{tr} \boldsymbol{\epsilon} - 3\alpha(\theta - \theta_h) \right)^2 \\
&\quad + \mu_G \left(\boldsymbol{\epsilon} - \boldsymbol{\epsilon}_{ve} - \alpha(\theta - \theta_h) \mathbf{I} \right) \cdot \left(\boldsymbol{\epsilon} - \boldsymbol{\epsilon}_{ve} - \alpha(\theta - \theta_h) \mathbf{I} \right) + \mu_R \boldsymbol{\epsilon}_{ve} \cdot \boldsymbol{\epsilon}_{ve}
\end{aligned} \tag{3.5}$$

As for the Helmholtz potential, we propose the following dissipation rate, similar to that of the 1D model of the SMP:

$$\begin{aligned}
\zeta &= \eta_R \dot{\boldsymbol{\epsilon}}_{ve}^2 + \eta_G \dot{\boldsymbol{\gamma}}_{ve} \cdot \dot{\boldsymbol{\gamma}}_{ve} + \kappa \|\dot{\boldsymbol{\epsilon}}_{ve}\| \\
&= \eta_G \dot{\boldsymbol{\epsilon}}_{ve} \cdot \dot{\boldsymbol{\epsilon}}_{ve} + \kappa \sqrt{\dot{\boldsymbol{\epsilon}}_{ve} \cdot \dot{\boldsymbol{\epsilon}}_{ve}}
\end{aligned} \tag{3.6}$$

We begin with the energy dissipation equation,

$$\boldsymbol{\sigma} \cdot \dot{\boldsymbol{\epsilon}} - \dot{\psi}|_{\theta=c} = \zeta \tag{3.7}$$

The stress in the material can be derived from the Helmholtz potential as follows:

$$\begin{aligned}
\boldsymbol{\sigma} &= \frac{\partial \psi}{\partial \boldsymbol{\epsilon}} \\
&= \left(k_G - \frac{2\mu_G}{3} \right) \left(\text{tr} \boldsymbol{\epsilon} - 3\alpha(\theta - \theta_h) \right) \mathbf{I} + 2\mu_G \left(\boldsymbol{\epsilon} - \boldsymbol{\epsilon}_{ve} - \alpha(\theta - \theta_h) \mathbf{I} \right)
\end{aligned} \tag{3.8}$$

Volumetric stress: (3.9)

$$\boldsymbol{\sigma}_v = \left(k_G - \frac{2\mu_G}{3} \right) \left(\text{tr} \boldsymbol{\epsilon} - 3\alpha(\theta - \theta_h) \right) \mathbf{I} \tag{3.10}$$

Deviatoric stress: (3.11)

$$\boldsymbol{\tau} = 2\mu_G \left(\boldsymbol{\epsilon} - \boldsymbol{\epsilon}_{ve} - \alpha(\theta - \theta_h) \mathbf{I} \right) \tag{3.12}$$

Thus, we derive $\boldsymbol{\sigma} \cdot \dot{\boldsymbol{\epsilon}}$ and $\dot{\psi}$ for the energy dissipation equation as follows:

$$\boldsymbol{\sigma} \cdot \dot{\boldsymbol{\epsilon}} = \left(k_G - \frac{2\mu_G}{3}\right) \left(\text{tr}\boldsymbol{\epsilon} - 3\alpha(\theta - \theta_h)\right) \text{tr}\dot{\boldsymbol{\epsilon}} + 2\mu_G \left(\boldsymbol{\epsilon} - \boldsymbol{\epsilon}_{ve} - \alpha(\theta - \theta_h)\mathbf{I}\right) \cdot \dot{\boldsymbol{\epsilon}} \quad (3.13)$$

and

$$\begin{aligned} \dot{\psi}|_{\theta=c} = & \left(k_G - \frac{2\mu_G}{3}\right) \left(\text{tr}\boldsymbol{\epsilon} - 3\alpha(\theta - \theta_h)\right) \left(\text{tr}\dot{\boldsymbol{\epsilon}}\right) \\ & + 2\mu_G \left(\boldsymbol{\epsilon} - \boldsymbol{\epsilon}_{ve} - \alpha(\theta - \theta_h)\mathbf{I}\right) \cdot \left(\dot{\boldsymbol{\epsilon}} - \dot{\boldsymbol{\epsilon}}_{ve}\right) + 2\mu_R \boldsymbol{\epsilon}_{ve} \cdot \dot{\boldsymbol{\epsilon}}_{ve} \end{aligned} \quad (3.14)$$

Subtracting Eq. (3.14) from Eq. (3.13), and substituting the answer into the energy dissipation equation, Eq. (3.7), we get the constraint that needs to be satisfied for the system in terms of the dissipation as below:

$$\zeta = 2\mu_G \left(\boldsymbol{\epsilon} - \boldsymbol{\epsilon}_{ve} - \alpha(\theta - \theta_h)\mathbf{I}\right) \cdot \dot{\boldsymbol{\epsilon}}_{ve} - 2\mu_R \boldsymbol{\epsilon}_{ve} \cdot \dot{\boldsymbol{\epsilon}}_{ve} \quad (3.15)$$

We now use the maximum rate of dissipation criterion to obtain the evolution equation for $\boldsymbol{\epsilon}_{ve}$. However, compared to the one dimensional case, the maximization is much more involved. We begin by first introducing function h as a function of the rate of dissipation $\zeta(\dot{\boldsymbol{\epsilon}}_{ve})$ and the constraint in Eq. 3.15, where λ is the Lagrange multiplier,

$$h = \zeta + \lambda \left(2\mu_G \left(\boldsymbol{\epsilon} - \boldsymbol{\epsilon}_{ve} - \alpha(\theta - \theta_h)\mathbf{I}\right) \cdot \dot{\boldsymbol{\epsilon}}_{ve} - 2\mu_R \boldsymbol{\epsilon}_{ve} \cdot \dot{\boldsymbol{\epsilon}}_{ve} - \zeta\right) \quad (3.16)$$

We now partially differentiate h with respect to the Lagrange multiplier λ and the independent variable that defines ζ , which is $\dot{\boldsymbol{\epsilon}}_{ve}$

$$\begin{aligned} \frac{\partial h}{\partial \lambda} &= 0 \\ \implies \zeta &= 2\mu_G \left(\boldsymbol{\epsilon} - \boldsymbol{\epsilon}_{ve} - \alpha(\theta - \theta_h)\mathbf{I}\right) \cdot \dot{\boldsymbol{\epsilon}}_{ve} - 2\mu_R \boldsymbol{\epsilon}_{ve} \cdot \dot{\boldsymbol{\epsilon}}_{ve} \end{aligned} \quad (3.17)$$

$$\begin{aligned} \frac{\partial h}{\partial \dot{\boldsymbol{\epsilon}}_{ve}} &= 0 \\ \implies \frac{\partial \zeta}{\partial \dot{\boldsymbol{\epsilon}}_{ve}} + \lambda \left(2\mu_R \boldsymbol{\epsilon}_{ve} - \frac{\partial \zeta}{\partial \dot{\boldsymbol{\epsilon}}_{ve}}\right) &= 0 \end{aligned} \quad (3.18)$$

Rearranging the terms in Eq. (3.18) and then taking a dot product of the rearranged equation with $\dot{\boldsymbol{\epsilon}}_{ve}$, should again give the LHS in the constraint form of ζ derived in

Eq. 3.15, as shown in the steps below

$$\frac{\lambda}{\lambda-1}(\tau - 2\mu_R \epsilon_{ve}) = \frac{\partial \zeta}{\partial \dot{\epsilon}_{ve}} \quad (3.19)$$

$$\begin{aligned} \frac{\lambda}{\lambda-1}(\tau - 2\mu_R \epsilon_{ve}) \cdot \dot{\epsilon}_{ve} &= \frac{\partial \zeta}{\partial \dot{\epsilon}_{ve}} \cdot \dot{\epsilon}_{ve} \\ \frac{\lambda}{\lambda-1} \zeta &= \frac{\partial \zeta}{\partial \dot{\epsilon}_{ve}} \cdot \dot{\epsilon}_{ve} \end{aligned} \quad (3.20)$$

Substituting the definition of ζ from Eq. (3.6)

$$\begin{aligned} \frac{\lambda}{\lambda-1}(\eta_G \dot{\epsilon}_{ve} \cdot \dot{\epsilon}_{ve} + \kappa \sqrt{\dot{\epsilon}_{ve} \cdot \dot{\epsilon}_{ve}}) &= 2\eta_G \dot{\epsilon}_{ve} \cdot \dot{\epsilon}_{ve} + \kappa \sqrt{\dot{\epsilon}_{ve} \cdot \dot{\epsilon}_{ve}} \\ \frac{\lambda}{\lambda-1} &= \frac{2\eta_G \dot{\epsilon}_{ve} \cdot \dot{\epsilon}_{ve} + \kappa \sqrt{\dot{\epsilon}_{ve} \cdot \dot{\epsilon}_{ve}}}{\eta_G \dot{\epsilon}_{ve} \cdot \dot{\epsilon}_{ve} + \kappa \sqrt{\dot{\epsilon}_{ve} \cdot \dot{\epsilon}_{ve}}} \end{aligned} \quad (3.21)$$

Substituting this result back into Eq. 3.19

$$\begin{aligned} 2\eta_G \dot{\epsilon}_{ve} + \kappa \frac{\dot{\epsilon}_{ve}}{\sqrt{\dot{\epsilon}_{ve} \cdot \dot{\epsilon}_{ve}}} &= \frac{2\eta_G \dot{\epsilon}_{ve} \cdot \dot{\epsilon}_{ve} + \kappa \sqrt{\dot{\epsilon}_{ve} \cdot \dot{\epsilon}_{ve}}}{\eta_G \dot{\epsilon}_{ve} \cdot \dot{\epsilon}_{ve} + \kappa \sqrt{\dot{\epsilon}_{ve} \cdot \dot{\epsilon}_{ve}}} (\tau - 2\mu_R \epsilon_{ve}) \\ &= \frac{2\eta_G \|\dot{\epsilon}_{ve}\|^2 + \kappa \|\dot{\epsilon}_{ve}\|}{\eta_G \|\dot{\epsilon}_{ve}\|^2 + \kappa \|\dot{\epsilon}_{ve}\|} (\tau - 2\mu_R \epsilon_{ve}) \end{aligned} \quad (3.22)$$

We note that we have $\dot{\epsilon}_{ve}$ in terms of its norm. We want to find the evolution equation $\dot{\epsilon}_{ve}$, and so we first proceed to find the value of the norm of $\dot{\epsilon}_{ve}$ as follows.

Taking the norm of both sides, we have

$$\begin{aligned} 2\eta_G \|\dot{\epsilon}_{ve}\| + \kappa \frac{\|\dot{\epsilon}_{ve}\|}{\|\dot{\epsilon}_{ve}\|} &= \frac{2\eta_G \|\dot{\epsilon}_{ve}\|^2 + \kappa \|\dot{\epsilon}_{ve}\|}{\eta_G \|\dot{\epsilon}_{ve}\|^2 + \kappa \|\dot{\epsilon}_{ve}\|} \|\tau - 2\mu_R \epsilon_{ve}\| \\ \eta_G \|\dot{\epsilon}_{ve}\| + \kappa &= \|\tau - 2\mu_R \epsilon_{ve}\| \quad \dots \eta, \kappa > 0 \\ \|\dot{\epsilon}_{ve}\| &= \frac{1}{\eta_G} \left(\|\tau - 2\mu_R \epsilon_{ve}\| - \kappa \right) \end{aligned} \quad (3.23)$$

$$\text{Let } \Phi = \tau - 2\mu_R \epsilon_{ve} \quad (3.24)$$

$$\phi = (\|\Phi\| - \kappa)$$

$$\text{Thus } \|\dot{\epsilon}_{ve}\| = \frac{1}{\eta_G} (\|\Phi\| - \kappa) = \frac{\phi}{\eta} \quad (3.25)$$

Depending on how the value of $\|\Phi\|$ compares with κ , Eq. (3.25) gives us the following conditions .

$$\begin{aligned}\|\Phi\| = \kappa &\implies \|\dot{\epsilon}_{ve}\| = 0 \\ \|\Phi\| > \kappa &\implies \|\dot{\epsilon}_{ve}\| \text{ is non - zero} \\ \|\Phi\| < \kappa &\implies \|\dot{\epsilon}_{ve}\| \text{ is set to zero}\end{aligned}\tag{3.26}$$

Now that we have the value of $\|\dot{\epsilon}_{ve}\|$, we proceed to determine ϵ_{ve} . Rearranging terms in Eq. (3.22):

$$(2\eta_G + \frac{1}{\|\dot{\epsilon}_{ve}\|})\dot{\epsilon}_{ve} = \frac{2\eta_G\|\dot{\epsilon}_{ve}\|^2 + \kappa\|\dot{\epsilon}_{ve}\|}{\eta_G\|\dot{\epsilon}_{ve}\|^2 + \kappa\|\dot{\epsilon}_{ve}\|}(\tau - 2\mu_R\epsilon_{ve})\tag{3.27}$$

$$\dot{\epsilon}_{ve} = \frac{\|\dot{\epsilon}_{ve}\|}{\eta_G\|\dot{\epsilon}_{ve}\| + \kappa}(\tau - 2\mu_R\epsilon_{ve})\tag{3.28}$$

Substituting Eq. (3.25) into this result

$$\epsilon_{ve} = \frac{1}{\eta_G}(\|\Phi\| - \kappa)\frac{\Phi}{\|\Phi\|}$$

Rewriting

$$\begin{aligned}\dot{\epsilon}_{ve} &= \frac{\phi}{\eta_G} \frac{\Phi}{\|\Phi\|} \\ \epsilon_{ve} &= \frac{1}{\eta_G}(\|\tau - 2\mu_R\epsilon_{ve}\| - \kappa)\frac{\tau - 2\mu_R\epsilon_{ve}}{\|\tau - 2\mu_R\epsilon_{ve}\|}\end{aligned}\tag{3.29}$$

As per Eq. (5.32), for the condition when $\|\dot{\epsilon}_{ve}\|$ is zero, we will have $\epsilon_{ve} = 0$, evident from Eq. (3.28). For the condition when $\|\dot{\epsilon}_{ve}\|$ is non-zero, we will have ϵ_{ve} take its final form as shown in Eq. (3.29). Thus the three cases of $\|\dot{\epsilon}_{ve}\|$, give ϵ_{ve} as the following two possibilities:

$$\epsilon_{ve} = \begin{cases} 0, & \forall \quad \|\tau - 2\mu_R\epsilon_{ve}\| \leq \kappa; \\ \frac{1}{\eta_G}(\|\tau - 2\mu_R\epsilon_{ve}\| - \kappa)\frac{\tau - 2\mu_R\epsilon_{ve}}{\|\tau - 2\mu_R\epsilon_{ve}\|}, & \forall \quad \|\tau - 2\mu_R\epsilon_{ve}\| > \kappa; \end{cases}\tag{3.30}$$

3-D state space rate type constitutive model for SMPs

1. State Variables: $\epsilon, \epsilon_{ve}, \theta, \sigma$

2. **Elastic Response:**

$$\boldsymbol{\sigma} = \left(k_G - \frac{2\mu_G}{3}\right) \left(\text{tr}\boldsymbol{\epsilon} - 3\alpha(\theta - \theta_h)\right) \mathbf{I} + 2\mu_G \left(\boldsymbol{\epsilon} - \boldsymbol{\epsilon}_{ve} - \alpha(\theta - \theta_h)\mathbf{I}\right)$$

3. **Flow Rule:** $\dot{\boldsymbol{\epsilon}}_{ve} = \frac{\phi}{\eta_G} \frac{\boldsymbol{\tau} - 2\mu_R \boldsymbol{\epsilon}_{ve}}{\|\boldsymbol{\tau} - 2\mu_R \boldsymbol{\epsilon}_{ve}\|}$

4. **Activation Conditions:**

$$\phi = \begin{cases} 0, & \forall \quad \|\boldsymbol{\tau} - 2\mu_R \boldsymbol{\epsilon}_{ve}\| \leq \kappa; \\ \|\boldsymbol{\tau} - 2\mu_R \boldsymbol{\epsilon}_{ve}\| - \kappa, & \forall \quad \|\boldsymbol{\tau} - 2\mu_R \boldsymbol{\epsilon}_{ve}\| > \kappa; \end{cases} \quad (3.31)$$

We shall now non-dimensionalize the equations as described next.

3.3 Non-dimensionalization of the Model Equations

Non-dimensionalizing Variables

We choose the following variables as the non-dimensional parameters, based either on their control on the SMP behavior (E_R, θ_g) as reported in the literature, or their influence as a loading parameter in the experiment (ϵ_0, t_0)

- (1) The typical rubbery modulus E_R , from experimental results $\sim 27\text{Mpa}$.
- (2) The maximum axial strain applied ϵ_0 from experimental results ~ 0.024 .
- (3) The glass transition temperature $\theta_g \sim 328$.
- (4) The non-dimensionalization of the time t_0 , since this is connected with the kinetic response.

The non-dimensional quantities using these variables are tabulated in Table 3.1.

Table 3.1: Dimensional quantities and corresponding non-dimensional quantities for the small strain model

Dim	$\boldsymbol{\sigma}$	$\boldsymbol{\epsilon}$	t	θ	α	η_G	$k_{G,R}, \mu_R$
Nondim	$\bar{\boldsymbol{\sigma}} = \frac{\boldsymbol{\sigma}}{E_R \epsilon_0}$	$\bar{\boldsymbol{\epsilon}} = \frac{\boldsymbol{\epsilon}}{\epsilon_0}$	$\bar{t} = \frac{t}{t_0}$	$\bar{\theta} = \frac{\theta}{\theta_g}$	$\bar{\alpha} = \frac{\alpha \theta_g}{\epsilon_0}$	$\bar{\eta}_G = \frac{\eta_G}{E_R t_0}$	$\bar{\bullet} = \frac{\bullet}{E_R}$

In the current form, the constitutive equation and the kinetic equation have six dimensional parameters: $k_R, k_G, \alpha, \eta_G, \mu_R, \mu_G$.

Non-dimensional Equations

Thus we begin with the rate form of the constitutive equation:

$$\begin{aligned}
\dot{\boldsymbol{\sigma}} &= \left(\bar{k}_G - \frac{2\bar{\mu}_G}{3}\right) \left(\text{tr}\dot{\boldsymbol{\epsilon}} - 3\left(\frac{\partial\alpha}{\partial\theta}(\theta - \theta_h) + \alpha\right)\dot{\theta}\right) \mathbf{I} + 2\bar{\mu}_G \left(\dot{\boldsymbol{\epsilon}} - \dot{\boldsymbol{\epsilon}}_{ve} - \left(\frac{\partial\alpha}{\partial\theta}(\theta - \theta_h) + \alpha\right)\dot{\theta}\mathbf{I}\right) \\
\dot{\boldsymbol{\sigma}} \frac{E_R \epsilon_0}{t_0} &= \left(\bar{k}_G E_R - \frac{2\bar{\mu}_G E_R}{3}\right) \frac{\epsilon_0}{t_0} \left(\text{tr}\dot{\boldsymbol{\epsilon}} - 3\left(\frac{\partial\bar{\alpha}}{\partial\bar{\theta}}(\bar{\theta} - \bar{\theta}_h)\theta_g + \frac{\bar{\alpha}}{\theta_g}\right)\dot{\bar{\theta}}\theta_g\right) \mathbf{I} \\
&\quad + 2\bar{\mu}_G E_R \frac{\epsilon_0}{t_0} \left(\dot{\boldsymbol{\epsilon}} - \dot{\boldsymbol{\epsilon}}_{ve} - \left(\frac{\partial\bar{\alpha}}{\partial\bar{\theta}}(\bar{\theta} - \bar{\theta}_h)\theta_g + \frac{\bar{\alpha}}{\theta_g}\right)\dot{\bar{\theta}}\theta_g\mathbf{I}\right) \\
\dot{\boldsymbol{\sigma}} &= \left(\bar{k}_G - \frac{2\bar{\mu}_G}{3}\right) \left(\text{tr}\dot{\boldsymbol{\epsilon}} - 3\left(\frac{\partial\bar{\alpha}}{\partial\bar{\theta}}(\bar{\theta} - \bar{\theta}_h) + \bar{\alpha}\right)\dot{\bar{\theta}}\right) \mathbf{I} + 2\bar{\mu}_G \left(\dot{\boldsymbol{\epsilon}} - \dot{\boldsymbol{\epsilon}}_{ve} - \left(\frac{\partial\bar{\alpha}}{\partial\bar{\theta}}(\bar{\theta} - \bar{\theta}_h) + \bar{\alpha}\right)\dot{\bar{\theta}}\mathbf{I}\right)
\end{aligned} \tag{3.32}$$

Similarly for the kinetic equation:

$$\begin{aligned}
\dot{\boldsymbol{\epsilon}}_{ve} &= \frac{1}{\eta_G} (||\boldsymbol{\Phi}|| - \kappa) \frac{\boldsymbol{\Phi}}{||\boldsymbol{\Phi}||} \\
\dot{\boldsymbol{\epsilon}}_{ve} \frac{\epsilon_0}{t_0} &= \frac{1}{\bar{\eta}_G E_R t_0} E_R \epsilon_0 (||\bar{\boldsymbol{\Phi}}|| - \bar{\kappa}) \frac{\bar{\boldsymbol{\Phi}}}{||\bar{\boldsymbol{\Phi}}||} \\
\dot{\epsilon}_{ve} &= \frac{1}{\bar{\eta}_G} (||\bar{\boldsymbol{\Phi}}|| - \bar{\kappa}) \frac{\bar{\boldsymbol{\Phi}}}{||\bar{\boldsymbol{\Phi}}||}
\end{aligned} \tag{3.33}$$

where

$$\bar{\boldsymbol{\Phi}} = \bar{\boldsymbol{\tau}} - 2\bar{\mu}_R \boldsymbol{\epsilon}_{ve}^-$$

Thus we now have the constitutive equation and the kinetic equation in non-dimensional form in Eq. (3.32) and Eq. (3.33). There are six non-dimensional parameters of the equations: $\bar{k}_R, \bar{k}_G, \bar{\alpha}, \bar{\eta}, \bar{\mu}_R$

$$\bar{\mathbf{C}}_G = \left(\bar{k}_G - \frac{2\bar{\mu}_G}{3}\right) \mathbf{I} \otimes \mathbf{I} + 2\bar{\mu}_G \mathbb{I} \tag{3.34}$$

$$\bar{\mathbf{C}}_R = \left(\bar{k}_R - \frac{2\bar{\mu}_R}{3}\right) \mathbf{I} \otimes \mathbf{I} + 2\bar{\mu}_R \mathbb{I} \tag{3.35}$$

We will implement all the equations in the form of differential equations, so that

we can use a differential solver for the computations. Thus for the implementation, we need to find the rate form of the state variables as follows.

Rate form for the elastic law:

$$\begin{aligned}
[\dot{\boldsymbol{\sigma}}] &= (\bar{k}_G - \frac{2\bar{\mu}_G}{3}) \left(\text{tr} \dot{\boldsymbol{\epsilon}} - 3 \left(\frac{\partial \bar{\alpha}}{\partial \bar{\theta}} (\bar{\theta} - \bar{\theta}_h) + \bar{\alpha} \right) \dot{\bar{\theta}} \right) \mathbf{I} + 2\bar{\mu}_G \left(\dot{\boldsymbol{\epsilon}} - \dot{\boldsymbol{\epsilon}}_{ve} - \left(\frac{\partial \bar{\alpha}}{\partial \bar{\theta}} (\bar{\theta} - \bar{\theta}_h) + \bar{\alpha} \right) \dot{\bar{\theta}} \mathbf{I} \right) \\
&= (\bar{\mathbf{C}}_G) \left[\dot{\boldsymbol{\epsilon}} - \left(\frac{\partial \bar{\alpha}}{\partial \bar{\theta}} (\bar{\theta} - \bar{\theta}_h) + \bar{\alpha} \right) \dot{\bar{\theta}} \mathbf{I} \right] - 2\bar{\mu}_G [\dot{\boldsymbol{\epsilon}}_{ve}] \\
&= (\bar{\mathbf{C}}_G) \left[\dot{\boldsymbol{\epsilon}} - (\bar{\mathbf{C}}_\alpha) \dot{\bar{\theta}} \mathbf{I} \right] - 2\bar{\mu}_G [\dot{\boldsymbol{\epsilon}}_{ve}]
\end{aligned} \tag{3.36}$$

Rate form for the activation stress:

$$\dot{\bar{\kappa}} = \hat{f}(\bar{\theta}, \bar{\epsilon}, \text{sgn}(\dot{\bar{\theta}})) \dot{\bar{\theta}} \tag{3.37}$$

Rate form for the thermal conductivity:

$$\dot{\bar{\alpha}} = \frac{\partial \bar{\alpha}}{\partial \bar{\theta}} \dot{\bar{\theta}} \tag{3.38}$$

Rate form for the inelastic strain:

$$\begin{aligned}
[\dot{\boldsymbol{\epsilon}}_{ve}] &= \frac{1}{\bar{\eta}_G} (||\bar{\boldsymbol{\Phi}}|| - \bar{\kappa}) \frac{[\bar{\boldsymbol{\Phi}}]}{||\bar{\boldsymbol{\Phi}}||} \\
[\bar{\boldsymbol{\Phi}}] &= [\bar{\boldsymbol{\tau}}] - 2\bar{\mu}_R [\boldsymbol{\epsilon}_{ve}^-]
\end{aligned} \tag{3.39}$$

3.4 Comparison to the 1D SMP Model

The original 1D model was

$$\dot{\boldsymbol{\epsilon}}_{1D} = \left(\frac{1}{\bar{E}_G} \right) \dot{\boldsymbol{\sigma}}_{1D} + \dot{\boldsymbol{\epsilon}}_{ev1D} + (\bar{\mathbf{C}}_\alpha) \dot{\bar{\theta}} \tag{3.40}$$

$$\dot{\boldsymbol{\epsilon}}_{ev1D} = \frac{1}{\bar{\eta}} \left(\bar{\boldsymbol{\sigma}}_{1D} - \bar{\mathbf{E}}_R \bar{\boldsymbol{\epsilon}}_{ev1D} - \bar{\sigma}_y \right) \tag{3.41}$$

$$\tag{3.42}$$

The 3D model is as follows

$$[\dot{\boldsymbol{\sigma}}] = (\bar{\mathbf{C}}_G) \left[\dot{\boldsymbol{\epsilon}} - (\bar{\mathbf{C}}_\alpha) \dot{\bar{\theta}} \mathbf{I} \right] - 2\bar{\mu}_G [\dot{\boldsymbol{\epsilon}}_{ve}] \tag{3.43}$$

$$[\dot{\bar{\epsilon}}_{ve}] = \frac{1}{\bar{\eta}_G} \left\langle ||[\bar{\tau}] - 2\bar{\mu}_R[\bar{\epsilon}_{ve}]|| - \bar{\kappa} \right\rangle \frac{[\bar{\tau}] - 2\bar{\mu}_R[\bar{\epsilon}_{ve}]}{||[\bar{\tau}] - 2\bar{\mu}_R[\bar{\epsilon}_{ve}]||}$$

$\langle \rangle$ are Macauley brackets.

Thus,

$$[\dot{\bar{\epsilon}}] = \left(\bar{\mathbf{C}}_{\mathbf{G}}^{-1} \right) \left[[\dot{\bar{\sigma}}] + 2\bar{\mu}_G[\dot{\bar{\epsilon}}_{ve}] \right] + (\bar{C}_\alpha) \dot{\bar{\theta}} [\mathbf{I}]$$

Consider uniaxial stress applied to the sample. Thus we have $\bar{\sigma}_{11} = f$

$$\begin{aligned} \dot{\bar{\epsilon}}_{11} &= \left(\bar{\mathbf{C}}_{\mathbf{G}_{11}}^{-1} \right) \left[[\dot{\bar{\sigma}}_{11}] + 2\bar{\mu}_G[\dot{\bar{\epsilon}}_{ev11}] \right] + \left(\bar{\mathbf{C}}_{\mathbf{G}_{12}}^{-1} \right) \left[[\dot{\bar{\sigma}}_{22}] + 2\bar{\mu}_G[\dot{\bar{\epsilon}}_{ev22}] \right] \\ &\quad + \left(\bar{\mathbf{C}}_{\mathbf{G}_{13}}^{-1} \right) \left[[\dot{\bar{\sigma}}_{33}] + 2\bar{\mu}_G[\dot{\bar{\epsilon}}_{ev33}] \right] + (\bar{C}_\alpha) \dot{\bar{\theta}} \end{aligned} \quad (3.44)$$

Now $\bar{\sigma}_{22}, \bar{\sigma}_{33} = 0$ and $\dot{\bar{\epsilon}}_{ev22}, \dot{\bar{\epsilon}}_{ev33} = -\frac{1}{2}\dot{\bar{\epsilon}}_{ev11}$ Thus,

$$\begin{aligned} \dot{\bar{\epsilon}}_{11} &= \left(\bar{\mathbf{C}}_{\mathbf{G}_{11}}^{-1} \right) [\dot{\bar{\sigma}}_{11}] + \left(2\bar{\mathbf{C}}_{\mathbf{G}_{11}}^{-1} - \bar{\mathbf{C}}_{\mathbf{G}_{12}}^{-1} - \bar{\mathbf{C}}_{\mathbf{G}_{13}}^{-1} \right) \bar{\mu}_G [\dot{\bar{\epsilon}}_{ev11}] + (\bar{C}_\alpha) \dot{\bar{\theta}} \\ &= \left(\frac{1}{\bar{E}_G} \right) [\dot{\bar{\sigma}}_{11}] + \left(2\frac{1}{\bar{E}_G} + \frac{\nu_G}{\bar{E}_G} + \frac{\nu_G}{\bar{E}_G} \right) \bar{\mu}_G [\dot{\bar{\epsilon}}_{ev11}] + (\bar{C}_\alpha) \dot{\bar{\theta}} \\ &= \left(\frac{1}{\bar{E}_G} \right) [\dot{\bar{\sigma}}_{11}] + \left(\frac{2(1+\nu)}{\bar{E}_G} \right) \bar{\mu}_G [\dot{\bar{\epsilon}}_{ev11}] + (\bar{C}_\alpha) \dot{\bar{\theta}} \\ &= \left(\frac{1}{\bar{E}_G} \right) [\dot{\bar{\sigma}}_{11}] + \left(\frac{\bar{\mu}_G}{\bar{\mu}_G} \right) [\dot{\bar{\epsilon}}_{ev11}] + (\bar{C}_\alpha) \dot{\bar{\theta}} \\ &= \left(\frac{1}{\bar{E}_G} \right) [\dot{\bar{\sigma}}_{11}] + [\dot{\bar{\epsilon}}_{ev11}] + (\bar{C}_\alpha) \dot{\bar{\theta}} \end{aligned} \quad (3.45)$$

This resembles the strain of the 1D model in Eq. (3.40)

Now consider the inelastic strain evolution in the 3D model for the uniaxial loading:

$$[\dot{\bar{\epsilon}}_{ve}] = \frac{1}{\bar{\eta}_G} \left(||[\bar{\tau}] - 2\bar{\mu}_R[\bar{\epsilon}_{ve}]|| - \bar{\kappa} \right) \frac{[\bar{\tau}] - 2\bar{\mu}_R[\bar{\epsilon}_{ve}]}{||[\bar{\tau}] - 2\bar{\mu}_R[\bar{\epsilon}_{ve}]||} \quad (3.46)$$

Therefore,

$$\begin{aligned} \dot{\bar{\epsilon}}_{ev11} &= \frac{1}{\bar{\eta}_G} \left(||[\bar{\tau}] - 2\bar{\mu}_R[\bar{\epsilon}_{ve}]|| - \bar{\kappa} \right) \frac{\bar{\tau}_{11} - 2\bar{\mu}_R\bar{\epsilon}_{ev11}}{||[\bar{\tau}] - 2\bar{\mu}_R[\bar{\epsilon}_{ve}]||} \\ &= \frac{1}{\bar{\eta}_G} \left(||[\bar{\tau}] - 2\bar{\mu}_R[\bar{\epsilon}_{ve}]|| - \bar{\kappa} \right) \frac{2(\bar{\sigma}_{11} - 3\bar{\mu}_R\bar{\epsilon}_{ev11})}{3||[\bar{\tau}] - 2\bar{\mu}_R[\bar{\epsilon}_{ve}]||} \end{aligned} \quad (3.47)$$

Now we compare the activation stress for 3D and 1D model:

$$\begin{aligned}
||[\bar{\boldsymbol{\tau}}] - 2\bar{\mu}_R[\bar{\boldsymbol{\epsilon}}_{ve}]|| &= \sqrt{(\bar{\boldsymbol{\tau}}_{11} - 2\bar{\mu}_R\bar{\boldsymbol{\epsilon}}_{ev11})^2 + (\bar{\boldsymbol{\tau}}_{22} - 2\bar{\mu}_R\bar{\boldsymbol{\epsilon}}_{ev22})^2 + (\bar{\boldsymbol{\tau}}_{33} - 2\bar{\mu}_R\bar{\boldsymbol{\epsilon}}_{ev33})^2} \\
&= \sqrt{\left(\frac{2}{3}\bar{\boldsymbol{\sigma}}_{11} - 2\bar{\mu}_R\bar{\boldsymbol{\epsilon}}_{ev11}\right)^2 + \left(-\frac{1}{3}\bar{\boldsymbol{\sigma}}_{11} + \bar{\mu}_R\bar{\boldsymbol{\epsilon}}_{ev11}\right)^2 + \left(-\frac{1}{3}\bar{\boldsymbol{\sigma}}_{11} + \bar{\mu}_R\bar{\boldsymbol{\epsilon}}_{ev11}\right)^2} \\
&= \sqrt{\left(\frac{2}{3}\bar{\boldsymbol{\sigma}}_{11} - 2\bar{\mu}_R\bar{\boldsymbol{\epsilon}}_{ev11}\right)^2 + \frac{1}{4}\left(\frac{2}{3}\bar{\boldsymbol{\sigma}}_{11} - 2\bar{\mu}_R\bar{\boldsymbol{\epsilon}}_{ev11}\right)^2 + \frac{1}{4}\left(\frac{2}{3}\bar{\boldsymbol{\sigma}}_{11} - 2\bar{\mu}_R\bar{\boldsymbol{\epsilon}}_{ev11}\right)^2} \\
&= \sqrt{\frac{3}{2}\left(\frac{2}{3}\bar{\boldsymbol{\sigma}}_{11} - 2\bar{\mu}_R\bar{\boldsymbol{\epsilon}}_{ev11}\right)^2} \\
&= \sqrt{\frac{3}{2}}\left(\frac{2}{3}\bar{\boldsymbol{\sigma}}_{11} - 2\bar{\mu}_R\bar{\boldsymbol{\epsilon}}_{ev11}\right) \\
&= \sqrt{\frac{2}{3}}(\bar{\boldsymbol{\sigma}}_{11} - 3\bar{\mu}_R\bar{\boldsymbol{\epsilon}}_{ev11}) \tag{3.48}
\end{aligned}$$

Substituting above result into Eq. (3.47), we get,

$$\begin{aligned}
\dot{\boldsymbol{\epsilon}}_{ev11} &= \frac{1}{\bar{\eta}_G} \left(\sqrt{\frac{2}{3}}(\bar{\boldsymbol{\sigma}}_{11} - 3\bar{\mu}_R\bar{\boldsymbol{\epsilon}}_{ev11}) - \bar{\kappa}_{3D} \right) \frac{2}{3} \frac{(\bar{\boldsymbol{\sigma}}_{11} - 3\bar{\mu}_R\bar{\boldsymbol{\epsilon}}_{ev11})}{\sqrt{\frac{2}{3}}(\bar{\boldsymbol{\sigma}}_{11} - 3\bar{\mu}_R\bar{\boldsymbol{\epsilon}}_{ev11})} \\
&= \frac{1}{\bar{\eta}_G} \left(\sqrt{\frac{2}{3}}(\dot{\bar{\boldsymbol{\sigma}}}_{11} - 3\bar{\mu}_R\dot{\bar{\boldsymbol{\epsilon}}}_{ev11}) - \sqrt{\frac{2}{3}}\bar{\kappa}_{1D} \right) \frac{2}{3} \frac{(\bar{\boldsymbol{\sigma}}_{11} - 3\bar{\mu}_R\bar{\boldsymbol{\epsilon}}_{ev11})}{\sqrt{\frac{2}{3}}(\bar{\boldsymbol{\sigma}}_{11} - 3\bar{\mu}_R\bar{\boldsymbol{\epsilon}}_{ev11})} \\
&= \frac{2}{3\bar{\eta}_G} \left((\bar{\boldsymbol{\sigma}}_{11} - 3\bar{\mu}_R\bar{\boldsymbol{\epsilon}}_{ev11}) - \bar{\kappa}_{1D} \right) \frac{(\bar{\boldsymbol{\sigma}}_{11} - 3\bar{\mu}_R\bar{\boldsymbol{\epsilon}}_{ev11})}{(\bar{\boldsymbol{\sigma}}_{11} - 3\bar{\mu}_R\bar{\boldsymbol{\epsilon}}_{ev11})} \\
&= \frac{2}{3\bar{\eta}_G} \left(\bar{\boldsymbol{\sigma}}_{11} - 3\bar{\mu}_R\bar{\boldsymbol{\epsilon}}_{ev11} - \bar{\kappa}_{1D} \right) \\
&= \frac{2}{3\bar{\eta}_G} \left(\bar{\boldsymbol{\sigma}}_{11} - 3\frac{\bar{E}_R}{2(1+\nu_R)}\bar{\boldsymbol{\epsilon}}_{ev11} - \bar{\kappa}_{1D} \right) \quad \dots \nu_R \approx 0.5 \\
&= \frac{2}{3\bar{\eta}_G} \left(\bar{\boldsymbol{\sigma}}_{11} - \bar{E}_R\bar{\boldsymbol{\epsilon}}_{ev11} - \bar{\kappa}_{1D} \right) \tag{3.49}
\end{aligned}$$

Thus the activation stress may be different for 3D and 1D as seen in Eq. 3.48, but it will result in the same viscoelastic strain for both 1D and 3D model, because of the assignment of $\eta_{3D} = \frac{2}{3}\eta_{1D}$ and $\kappa_{3D} = \sqrt{\frac{2}{3}}\kappa_{1D}$ in Eq. 3.49.

3.5 Implementation of the Small Strain 3D Model

For homogeneous deformations, the control equation will look as follows:

$$\begin{aligned} (\mathbb{A})[\dot{\bar{\sigma}}] + (\mathbb{B})[\dot{\bar{\epsilon}}] &= [f(\bar{t})] \\ [\dot{\bar{\theta}}] &= [g(\bar{t})] \end{aligned} \tag{3.50}$$

where,

$(\mathbb{A}(\bar{t}))$: 6X6 matrix representing the combination of components of stress that are known

$(\mathbb{B}(\bar{t}))$: 6X6 matrix representing the combination of the components of strains that are known

$[f(\bar{t})]$: 6 term column vector representing the way in which these known components change with time

$[g(\bar{t})]$: 1 term vector representing the way in which temperature changes with time

Given the loading scheme as described by Eq. (3.50), and given the initial condition of $\bar{\sigma}$, $\bar{\epsilon}$, $\bar{\epsilon}_{ve}$, $\bar{\theta}$, and \bar{t} , we find $\dot{\bar{\sigma}}$ and $\dot{\bar{\epsilon}}$ over the whole time range by the following steps:

The state evolution form derived above will translate as follows to be fed into a suitable manner into MATLAB:

$$\dot{S} = f(S, t) \tag{3.51}$$

where S represents the variables that model the current state of the system and f is a function of the state variables and time. Thus, we can proceed to feed the equations (3.50) to (3.39) in the form $A_{(x,\theta,t)}\dot{x} = p_{(x,\theta,t)} + Q_{(x,\theta,t)}x$, which is solved by the ODE45 solver in MATLAB. The algorithm is presented in Algorithm 1.

Let

$i_{11} = [1]$, $i_{61} = [1 \ 1 \ 1 \ 0 \ 0 \ 0]^T$, $i_{66} = 6 \times 6$ identity matrix

$z_{11} = [0]$, $z_{16} = 1 \times 6$ zero matrix, $z_{61} = 6 \times 1$ zero matrix, $z_{66} = 6 \times 6$ zero matrix

$x = [\sigma_{6X1}; \epsilon_{6X1}; \theta; \kappa; \alpha]$

$x_{init} = [\sigma_{6X1} = 0; \epsilon_{6X1} = 0; \theta_h; \kappa; \alpha_r]$, $\epsilon_{6X1}^p = 0$

Algorithm 1 State space model

```

1: function  $\dot{x} = \text{ODESOLVER}(t, x_{init})$ 
2:   Calculate  $\bar{\mathbf{C}}_{\mathbf{G}}, \bar{\mathbf{C}}_{\mathbf{R}}, \bar{C}_{\alpha} = (\frac{\partial \bar{\alpha}}{\partial \bar{\theta}}(\bar{\theta} - \bar{\theta}_h) + \bar{\alpha})$ 
3:   Calculate  $\bar{\Phi} = \bar{\tau} - 2\bar{\mu}_R \bar{\epsilon}_{ve}$ 
4:   if  $\|\bar{\Phi}\| \leq \bar{\kappa}$  then
5:      $a = 0$ 
6:   else  $\|\bar{\Phi}\| > \bar{\kappa}$ 
7:      $a = \|\bar{\Phi}\| - \bar{\kappa}$ 
8:   end if
9:    $\dot{\epsilon}_{ve} = \frac{a\bar{\Phi}}{\bar{\eta}\|\bar{\Phi}\|}$ 
10:  Solve ODE system:

```

$$\begin{bmatrix} \mathbb{A}(\bar{t}) & \mathbb{B}(\bar{t}) & z_{61} & z_{61} & z_{61} \\ i_{66} & -\bar{\mathbf{C}}_{\mathbf{G}} & \bar{C}_{\alpha} \bar{\mathbf{C}}_{\mathbf{G}} i_{61} & z_{61} & z_{61} \\ z_{16} & z_{16} & i_{11} & z_{11} & z_{11} \\ z_{16} & z_{16} & -\hat{\kappa} & i_{11} & z_{11} \\ z_{16} & z_{16} & -d\hat{\alpha}/d\theta & z_{11} & i_{11} \end{bmatrix} \begin{bmatrix} \dot{\bar{\sigma}} \\ \dot{\bar{\epsilon}} \\ \dot{\bar{\theta}} \\ \dot{\bar{\kappa}} \\ \dot{\bar{\alpha}} \end{bmatrix} = \begin{bmatrix} f(\bar{t}) \\ -2\bar{\mu}_G \dot{\epsilon}_{ve} \\ g(\bar{t}) \\ z_{11} \\ z_{11} \end{bmatrix}$$

$$[P]_{15 \times 15} [\dot{x}]_{15 \times 1} = [r]_{15 \times 1} \quad (3.52)$$

```

11: end function

```

$[P]_{15 \times 15}[\dot{x}]_{15 \times 1} = [r]_{15 \times 1}$ looks as follows for uniaxial experiment:

$$\begin{bmatrix}
a(t) & 0 & 0 & 0 & 0 & 0 \\
0 & 1 & 0 & 0 & 0 & 0 \\
0 & 0 & 1 & 0 & 0 & 0 \\
0 & 0 & 0 & 1 & 0 & 0 \\
0 & 0 & 0 & 0 & 1 & 0 \\
0 & 0 & 0 & 0 & 0 & 1
\end{bmatrix}
\begin{bmatrix}
b(t) & 0 & 0 & 0 & 0 & 0 \\
0 & 0 & 0 & 0 & 0 & 0 \\
0 & 0 & 0 & 0 & 0 & 0 \\
0 & 0 & 0 & 0 & 0 & 0 \\
0 & 0 & 0 & 0 & 0 & 0 \\
0 & 0 & 0 & 0 & 0 & 0
\end{bmatrix}
-
\begin{bmatrix}
\bar{k}_G + \frac{4\bar{\mu}_G}{3} & \bar{k}_G - \frac{2\bar{\mu}_G}{3} & \bar{k}_G - \frac{2\bar{\mu}_G}{3} & 0 & 0 & 0 \\
\bar{k}_G - \frac{2\bar{\mu}_G}{3} & \bar{k}_G + \frac{4\bar{\mu}_G}{3} & \bar{k}_G - \frac{2\bar{\mu}_G}{3} & 0 & 0 & 0 \\
\bar{k}_G - \frac{2\bar{\mu}_G}{3} & \bar{k}_G - \frac{2\bar{\mu}_G}{3} & \bar{k}_G + \frac{4\bar{\mu}_G}{3} & 0 & 0 & 0 \\
0 & 0 & 0 & 2\bar{\mu}_G & 0 & 0 \\
0 & 0 & 0 & 0 & 2\bar{\mu}_G & 0 \\
0 & 0 & 0 & 0 & 0 & 2\bar{\mu}_G
\end{bmatrix}
\begin{bmatrix}
\bar{C}_\alpha(3\bar{k}_G - \frac{8\bar{\mu}_G}{3}) \\
\bar{C}_\alpha(3\bar{k}_G - \frac{8\bar{\mu}_G}{3}) \\
\bar{C}_\alpha(3\bar{k}_G - \frac{8\bar{\mu}_G}{3}) \\
0 \\
0 \\
0
\end{bmatrix}
=
\begin{bmatrix}
\dot{\sigma}_{11} & \dot{\sigma}_{22} & \dot{\sigma}_{33} & \dot{\sigma}_{12} & \dot{\sigma}_{13} & \dot{\sigma}_{23} \\
\dot{\epsilon}_{11} & \dot{\epsilon}_{22} & \dot{\epsilon}_{33} & \dot{\epsilon}_{12} & \dot{\epsilon}_{13} & \dot{\epsilon}_{23} \\
\dot{\theta} & \dot{\kappa} & \dot{\alpha} & & &
\end{bmatrix}
=
\begin{bmatrix}
f(\dot{t}) \\
0 \\
0 \\
0 \\
0 \\
0 \\
-2\bar{\mu}_G\dot{\epsilon}_{ev11} \\
-2\bar{\mu}_G\dot{\epsilon}_{ev22} \\
-2\bar{\mu}_G\dot{\epsilon}_{ev33} \\
-2\bar{\mu}_G\dot{\epsilon}_{ev12} \\
-2\bar{\mu}_G\dot{\epsilon}_{ev13} \\
-2\bar{\mu}_G\dot{\epsilon}_{ev23} \\
g(\dot{t}) \\
0 \\
0
\end{bmatrix}$$

3.6 Error Optimization: Identification of Activation Stress Coefficients

The hysteresis of the activation stress is key in controlling the response of the SMP model. Details of the activation stress dependence on temperature, and its functional form, can be found in the original proposition by Ghosh and Srinivasa[34]. In this work, we present an optimization method to determine the coefficients of the activation stress function. The activation stress function remains the same as proposed in the previous chapter 2:

Form of the Activation Stress Rate Function

$$\dot{\kappa} = f(\theta, \text{sign}(\dot{\theta}), \epsilon) \dot{\theta} \quad (3.53)$$

$$f_{cool} = y_1 e_v + (\sinh(-y_2(\theta - \theta_1))) \delta_1 \quad (3.54)$$

$$f_{heat} = -y_3 e_v - y_4 (1 - (y_5 \tanh(m\theta + n))^2) \delta_2 \quad (3.55)$$

where, where, e_v is the von mises strain corresponding to the strain $(\epsilon - \epsilon_{ve} - \alpha(\theta - \theta_h)\mathbf{I})$. e_v is the scalar strain value selected in 3D context, such that it is affected by pure thermal strains or pure mechanical processes. Also, $m = 2/(\theta_{max} - \theta_2)$, $n = 1 - m\theta_{max}$. θ_1 and θ_2 are limiting values of θ until which there is no rise/fall in the stress/strain during the cooling/heating cycle.

$$\delta_1 = \begin{cases} 1, & \forall \theta \leq \theta_1; \\ 0, & \forall \theta > \theta_1; \end{cases} \quad \delta_2 = \begin{cases} 0, & \forall \theta < \theta_2; \\ 1, & \forall \theta \geq \theta_2; \end{cases}$$

Optimization Parameters

For range 1 (Strain Control): y_1, y_2

For range 2 (Stress Control): y_3, y_4, y_5

Defining Error Region

We use the parametric analysis to narrow down exactly which response regimes are affected by the activation stress coefficients. This helps in reducing the error area that needs to be optimized to a smaller pertinent region.

Let $r1$ = range of stress response that is affected by y_1, y_2 as observed from 3.8.2

and $r2$ = range of strain response that is affected by y_3, y_4, y_5 as observed from 3.8.2

Defining the Objective Function

$$\text{For range 1 (Strain Control): } f_1 = \frac{\text{L2 norm}(\sigma_{model} - \sigma_{data}) \Big|_{r1}}{\text{L2 norm}(\sigma_{data}) \Big|_{r1}}$$

$$\text{For range 2 (Stress Control): } f_2 = \frac{\text{L2 norm}(\epsilon_{model} - \epsilon_{data}) \Big|_{r2}}{\text{L2 norm}(\epsilon_{data}) \Big|_{r2}}$$

Notice from the parametric analysis in Section 3.8.2, y_1, y_2 affect the strain response in range 2 as well. This happens because of the stress rise in range 1 (which is controlled by y_1, y_2) acts as the initial condition for range 2. However, we restrict f_1 to only the stress response in range 1. The code is split up so that the optimum results of stress and strain in range 1 are passed over as the initial condition for range 2. The stress rise in range 1 due to y_1, y_2 affects the strain response in range 2, and this shall be handled by the optimization of f_2 alone. In other words, y_3, y_4, y_5 will be determined to get better solutions in range 2, only after fixing the optimum values of y_1, y_2 that give better solutions in range 1.

Optimization Algorithm

Since the inbuilt optimization functions `fminsearch` / `fmincon` of MATLAB are used in this work, the primary concern of the optimization algorithm is that, unlike the usual implementation of these functions, where the optimization parameters are directly involved in the objective function, the optimization algorithm of the current work consists of parameters that belong to a different implicit function $\left(\frac{d\kappa}{d\theta}\right)$ of the model, and that the objective function only compares the output of the model (stress/strain response) and an input data set (experimental data). The algorithm has been generated to obtain an optimization routine that can be referred to in Algorithm 2.

Defining the Parameter Space

The initial guesses and the definition of the parameter space is crucial for `fmincon`. In this work we first determine the parameter space by using the `fminsearch` solver, starting with a random initial guess as shown in Table 3.2. The function values for each iteration step and the final results for the optimum values of the coefficients are shown in Figures 3.1a, 3.1b and 3.1c, 3.1d. On obtaining the optimum coefficient values from the `fminsearch` solver, we use these values to set up a parameter space

(lower and upper bound) for the coefficients for the fmincon solver as you can see in Table 3.3. We use the fmincon solver to get optimum values of y_1 , y_2 , y_3 , y_4 , y_5 . The function values for each iteration step and the final results for the optimum values of the coefficients are shown in Figures 3.2a,3.2b and 3.2c,3.2d.

Notice that fminsearch does give reduced objective function values, however, when we take a look at the model output and the experimental data, we see that the trend of the model output is physically incorrect. Since fminsearch is looking for values in an unrestricted manner, with the aim of only reducing the objective function value, it may lead to problems like these. In order to get physically realistic values, a suitable parametric space has to be defined, so that the trends of the responses are kept intact in the process of reducing the objective function value. On specifying a suitable parametric space, fmincon gives physically realistic answers. For example, although fminsearch returns $y_4 = -0.1601$, we realize this is causing the wavy unrealistic shape recovery response in the model. Therefore we set the parametric space for y_4 to a non-negative space, i.e lower bound $lb = 0$ and upper bound $ub = 0.6$. This dictates to fmincon a better searching region that can return a smooth gradual response of the shape recovery, which is physically realistic.

Note that the difference between the model and the data for range 2 has increased from 9.91% in the last iteration of the fminsearch solver to 12.63% in the last iteration of the fmincon solver. Decision on which values are finally chosen is left to the designer, depending on not just the final value of the objective function but also on which trend of the response and range of the response is critical for the application in which the SMP will be used.

Algorithm 2 Optimization for parameter identification in a thermomechanical cycle

```
1: Specifying initial values for the parameters  $y_1, y_2$  to be optimized in range 1
2: function OPTIMIZATION SOLVER(minimize  $f_1$ )                                 $\triangleright$  fminsearch/fmincon
3:   Specify upper and lower bound of  $y_1, y_2$  for fmincon solver
4:   TolFun = 1e-6, Alg = int-point, MaxFunEvals = 3000, MaxIter = 120
5:   function MODEL SOLVER(Calculate  $f_1$  for each trial value of  $y_1, y_2$ )
6:     Extract experimental time, stress, strain data for strain control range 1
7:     Obtain material parameters and their non-dimensional values
8:     Obtain control parameters ( $y_1, y_2$  to evaluate activation stress)
9:     Set initial condition  $x_{init}=[\sigma_{6X1}=0; \epsilon_{6X1}=0; \theta_h; \kappa=0; \alpha_r; \epsilon_{6X1}^p=0]$ 
10:    Pass data from Line 6 to 9 to state space model. Refer Algorithm 1
11:    Use solutions of model to determine minimization function  $f_1$ 
12:    Assign solution of ode solver to base workspace
13:  end function
14:  Assign optimized parameter values  $y_1, y_2$  to base workspace
15: end function
16: Specifying initial values for the parameters  $y_3, y_4, y_5$  to be optimized in range 2
17: function OPTIMIZATION SOLVER(minimize  $f_2$ )                                 $\triangleright$  fminsearch/fmincon
18:   Specify upper and lower bound of  $y_3, y_4, y_5$  for fmincon
19:   TolFun = 1e-6, Alg = int-point, MaxFunEvals = 3000, MaxIter = 120
20:   function MODEL SOLVER(Calculate  $f_2$  for each trial value of  $y_3, y_4, y_5$ )
21:     Extract experimental time, stress, strain data for stress control range 2
22:     Obtain material parameters and their non-dimensional values
23:     Obtain control parameters ( $y_3, y_4, y_5$  to evaluate the activation stress)
24:     Initial condition is set as solution of last time step from strain controlled range 1 from
    base workspace. Thus  $x_{init}=x_{straincontrol}(t=end)$ 
25:     Pass data from Line 21 to 24 to state space model. Refer Algorithm 1
26:     Use solutions of model to determine minimization function  $f_2$ 
27:     Assign solution of ode solver to base workspace
28:   end function
29:   Assign optimized parameter values  $y_3, y_4, y_5$  to base workspace
30: end function
```

3.6.1 Results of “fminsearch” Solver

Table 3.2: Initial conditions and final optimum results of activation stress coefficients from the “fminsearch” solver

fminsearch	f1 value	f2 value	y1	y2	y3	y4	y5
initial	0.381496	0.6117	1.0000	10.0000	0.2038	0.4657	0.8374
optim	0.0689	0.0991	0.0482	27.8625	-0.3815	-0.1601	1.9749

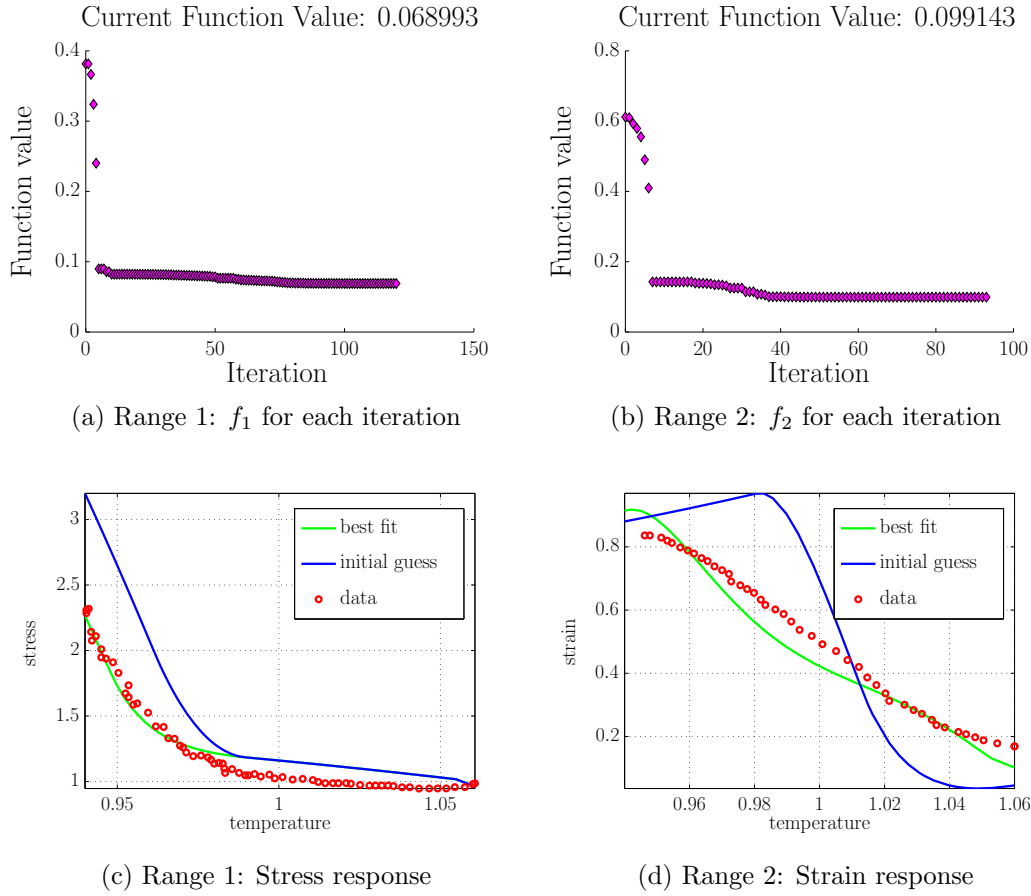


Figure 3.1: “fminsearch” function values (top) and model versus data for optimum values (bottom)

3.6.2 Results of “fmincon” Solver

Table 3.3: Initial conditions, parameter space and final results of activation stress coefficients from “fmincon” solver

fmincon	f1 value	f2 value	y1	y2	y3	y4	y5
initial	0.4153	0.6192	1.000	10.000	-0.204	0.466	0.837
lb	-	-	0.001	10.000	-0.850	0.000	0.000
ub	-	-	2.500	30.000	0.350	0.600	2.000
optim	0.068	0.1263	0.076	23.357	-0.192	0.029	0.548

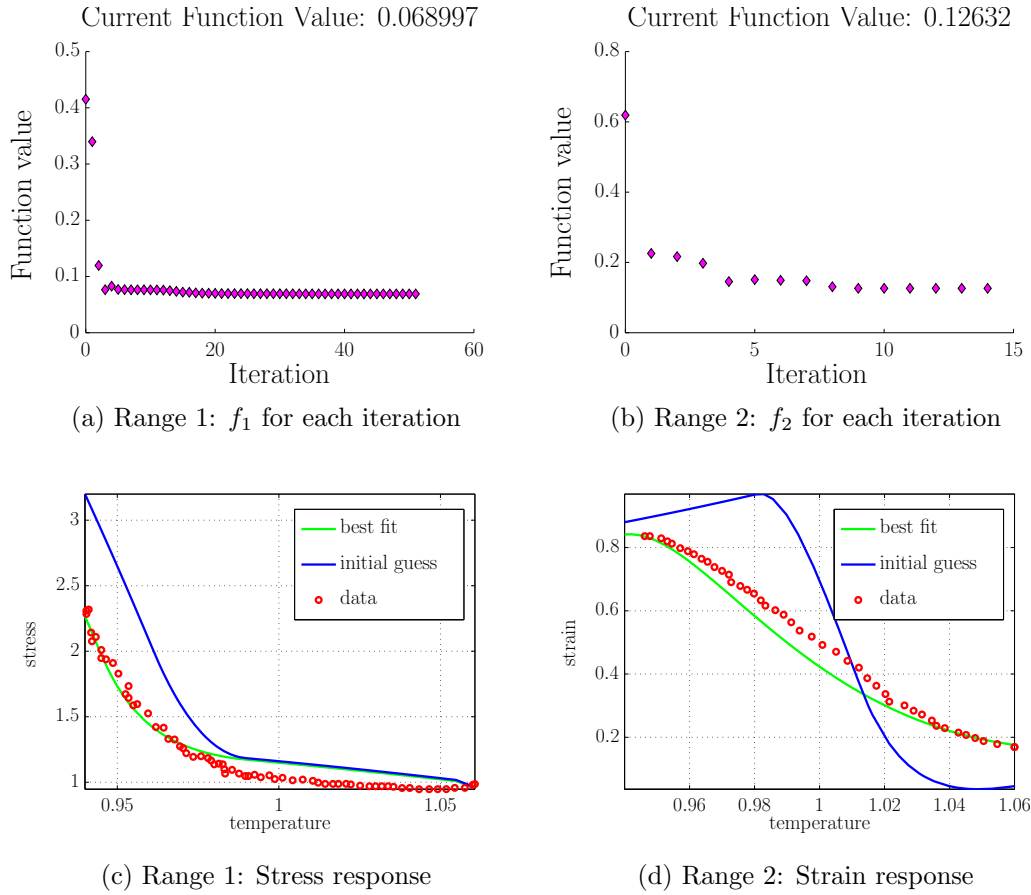


Figure 3.2: “fmincon” function values (top) and model versus data for optimum values (bottom)

3.7 Thermomechanical Cycle Results

3.7.1 Unconstrained Shape Recovery

We use the insights from the parametric analysis in Section 3.8 and the optimum results obtained from the error minimization in Section 3.6 to validate the model for uniaxial tensile loading on polyurethane, as shown in Figure 3.3. Similar validation can be carried out for other cases using the insights from the parametric analysis for the material parameters, and using the method of error minimization to obtain the activation stress coefficients.

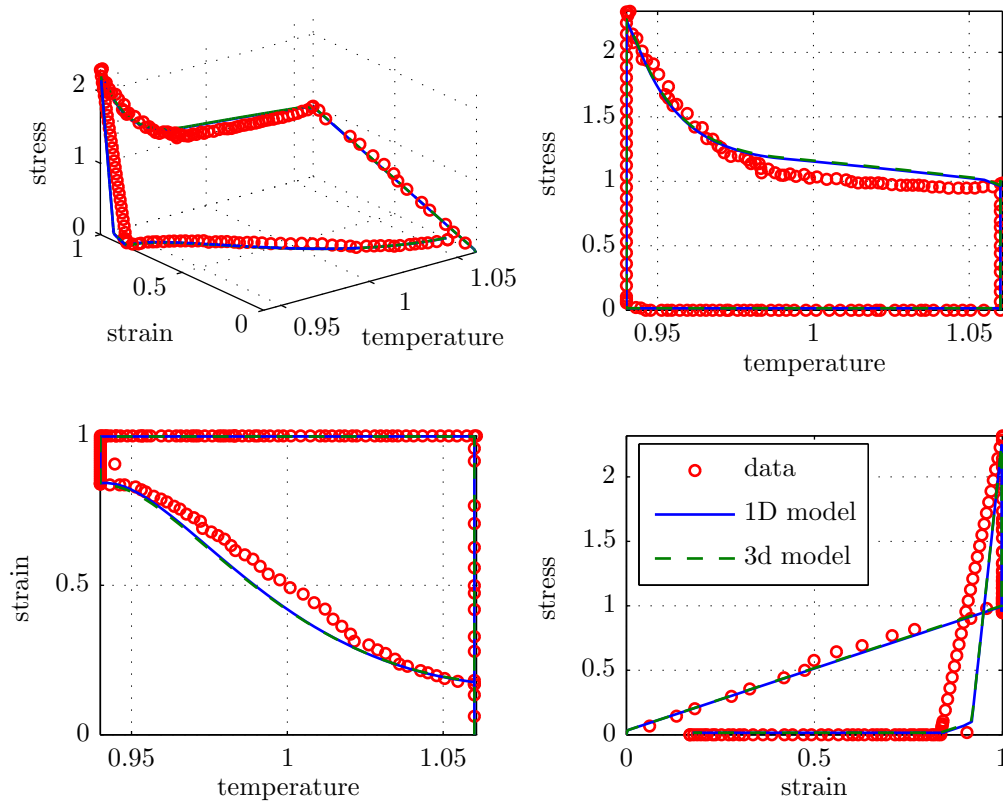
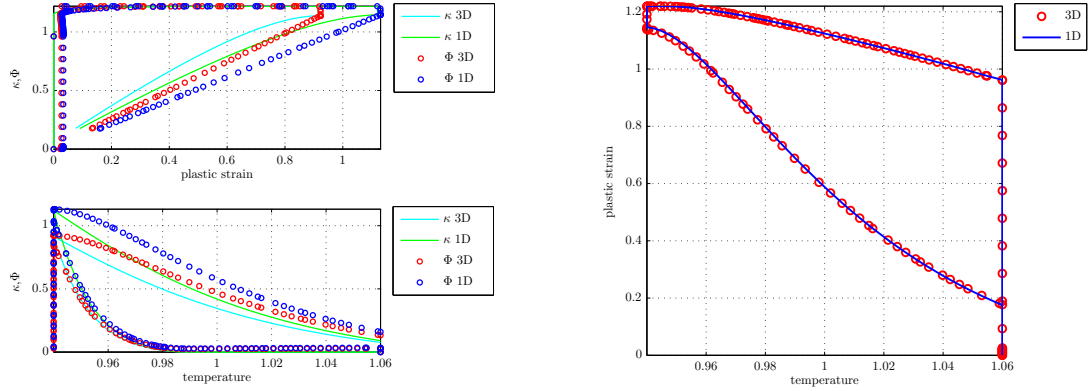


Figure 3.3: 3D Model results versus data for the unconstrained shape recovery thermomechanical cycle on polyurethane

The activation stress evolution and the corresponding flow potential is plotted in Figure 3.4 to observe how the activation stress controls the evolution of the flow potential. The difference between these two dictates the rate of inelastic strain as can be seen from the figures. Notice how this difference gives the same inelastic strain for both 1D and 3D model, because of the assignment of $\eta_{3D} = \frac{2}{3}\eta_{1D}$ as derived in Section 3.4. Observe the hysteresis of the activation stress and the flow potential in the heating and cooling ranges, which gives the two different inelastic strain evolutions.



(a) Activation stress and inelastic flow potential evolution for the thermomechanical cycle (b) Plastic strain evolution for the unconstrained shape recovery thermomechanical cycle

Figure 3.4: Evolution of inelastic strain in 3.4b by controlling the difference between the activation stress and the inelastic flow potential in 3.4a for the 3D and 1D model

The three strains that are competing with each other in this model are the total strain, the inelastic strain and the thermal strain. In the time graph shown in Figure 3.5, this comparison shows how the elastic strain evolves as $\epsilon_e = \epsilon - \epsilon_{ve} - \alpha(\theta - \theta_h)$, for the strain control region ($t = 0$ to 72) and stress control region ($t = 72$ to 151). Thus it becomes evident how $\sigma = C_G \epsilon_e$ evolves in the strain control region i.e stress increases when the material is cooled, and how the material shows spring back i.e decrease in strain during unloading.

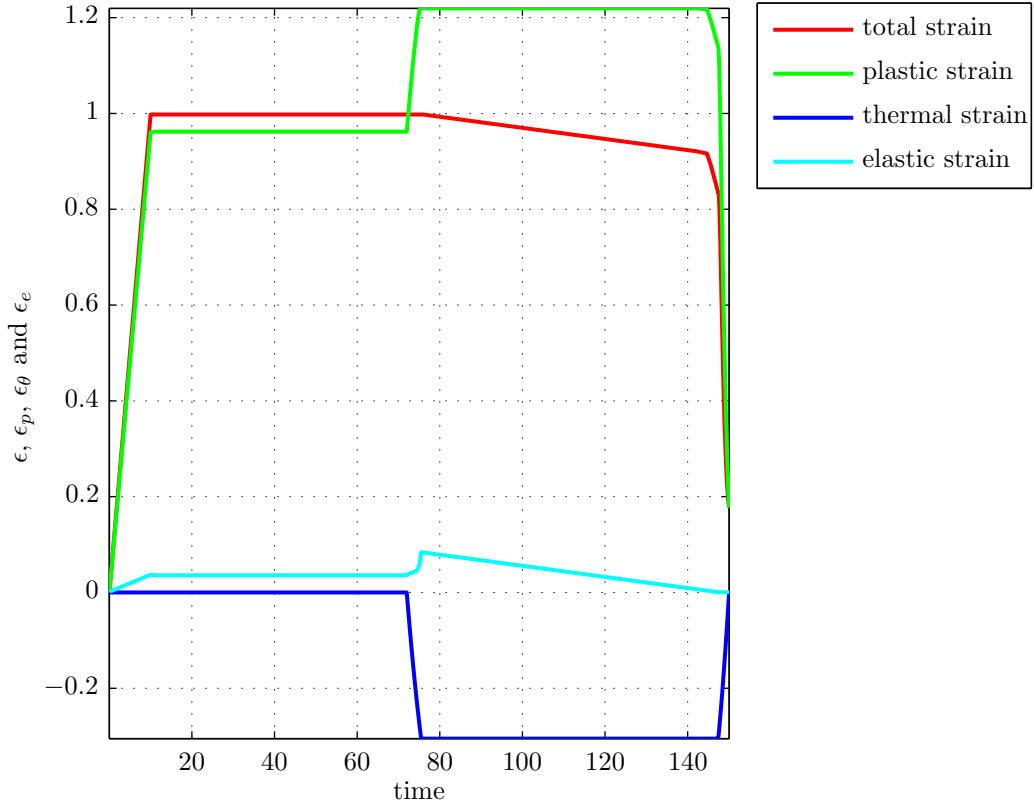


Figure 3.5: All strains for unconstrained shape recovery thermomechanical cycle on polyurethane

3.7.2 Constrained Stress Recovery

Using Experimental Specified Parameters

This thermomechanical experiment, carried out by Tobushi et al., consists of six processes enlisted below and shown in Figure 3.6.

- Strain loading to 2.4% and holding at constant strain at high temperature (7200s)
- Cooling to below T_g at constant strain constraint (360s)
- Unloading to zero load at low temperature (7200s)
- Holding at no load until 1% strain rise is observed (600s)
- Heating to above T_g at constant strain constraint (360s)
- Unloading to zero load at high temperature (7200s)

We implement this constrained stress recovery cycle and observe the model response in this section. As seen by the model results in Figure 3.7, the model is able to depict the material response up to process 3. It is unable to capture two of the six process responses:

(Process 4) Holding at no load until 1% strain rise is observed: model is unable to show a strain spring back at no load, it shows spring back during unloading at process 3 only.

(Process 5) Heating to above T_g at constant strain constraint: the stress response initially shows a dip which is not captured by the model. It is possible that the thermal effects are controlling the response at this stage, as well the recovery time plays a significant role.

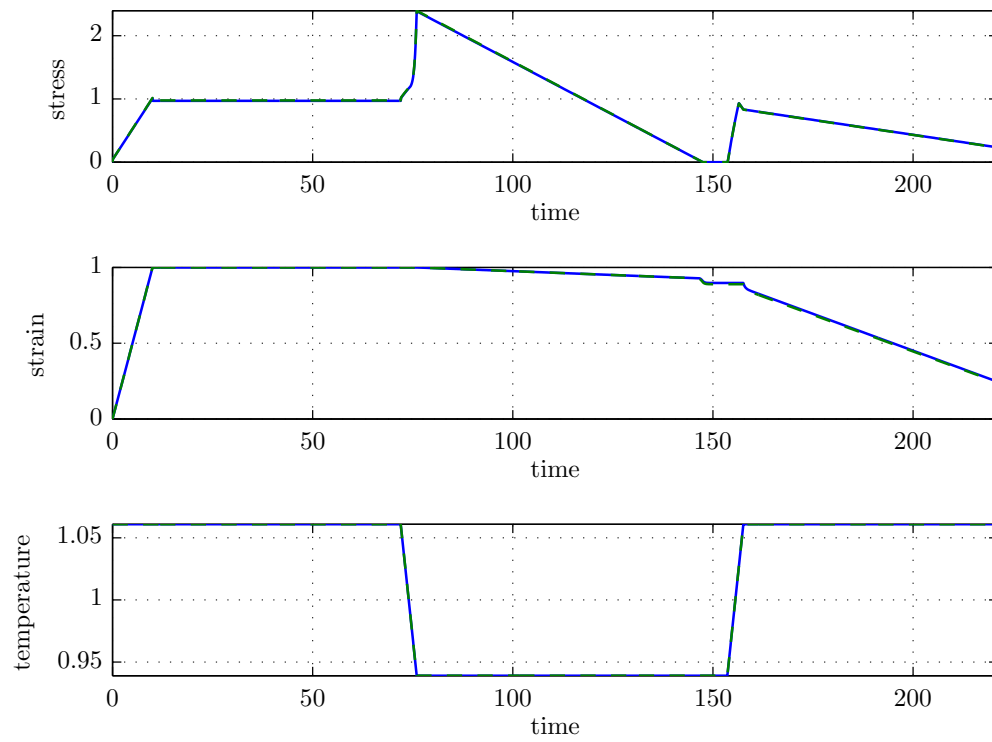


Figure 3.6: Stress strain temperature process controls for the constrained stress recovery thermomechanical cycle on polyurethane

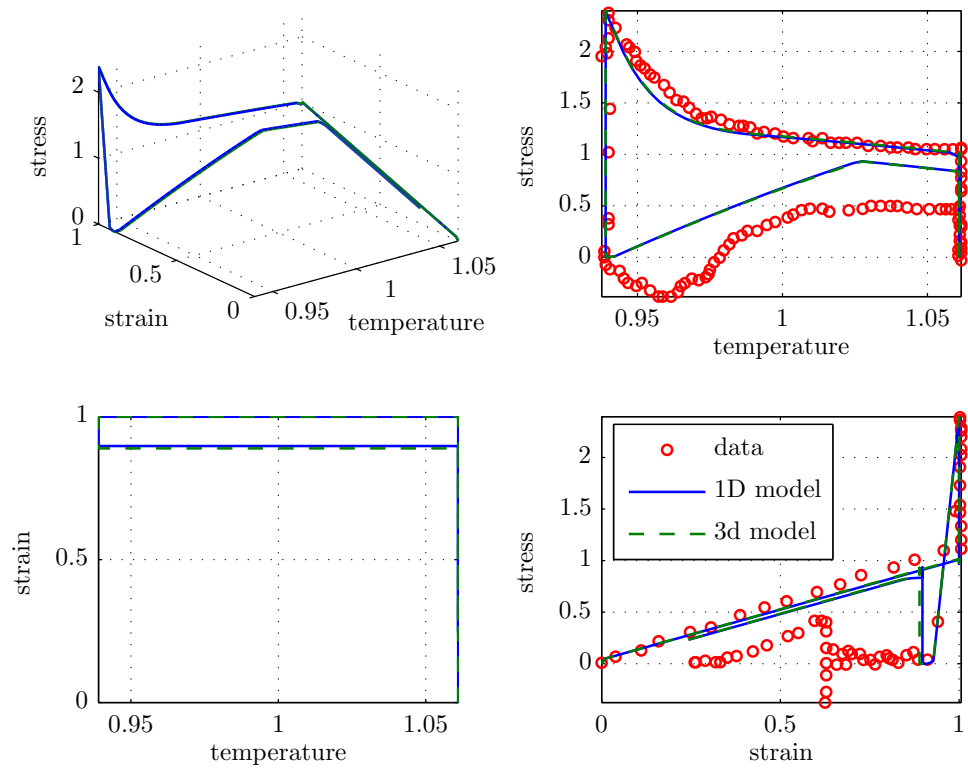


Figure 3.7: 3D model results versus data for the constrained stress recovery thermo-mechanical cycle on polyurethane

3.8 Parametric Study of the SMP Model with respect to Material Parameters

Response Parameters

The response parameters that are chosen for the parametric study from the response of SMP through a thermomechanical cycle are listed in Table 3.4. When designing a SMP application, two or more of these response parameters (depending on the application) are the phenomenological details that are of interest to the application designer. In this work, we attempt to connect this to the constitutive parameters, because that will be of interest to the materials designer.

Table 3.4: Chosen response parameters in a thermomechanical cycle

Range 1 (Strain Control)	Range 2 (Stress Control)
σ_b : Stress at the end of loading	ϵ_{cd} : Spring back on unloading
σ_{Tg} : Value of stress during cooling at T_g	ϵ_{Tg} : Value of strain during heating at T_g
σ_c : Maximum stress rise at end of cooling	ϵ_{ea} : Unrecoverable strain at the end of cycle

Material Parameters

Material properties that will be varied in order to observe the effect of their change on the chosen response parameters: E_G , E_R , α_G , α_R , η_G , η_R . Apart from this, coefficients of the activation stress function will be varied in order to observe the effect of their change on the response parameters

- $y1, y2$: activation Stress coefficients in the cooling function
- $y3, y4, y5$: activation Stress coefficients in the heating function

Protocol for the Analysis

We will be focussing on the thermomechanical cycle for uniaxial loading on the SMP sample that was carried out by Tobushi et al. [2]. The actual experimental values of the material parameters for the shape memory polyurethane sample as

Table 3.5: Experimental values of material parameters in the SMP model

	Modulus E	Thermal Expansion α	Viscosity η
Glassy	907 MPa	11.6×10^{-5} per K	116000 Mpas
Rubbery	27.6 MPa	11.6×10^{-5} per K	2030 Mpas

described in their work are as listed in Table 3.5. For each of the material parameters/activation stress coefficients, we vary the value of one of these properties, keeping all the others constant at the actual experimental value provided. We conduct a two step parametric analysis for each of these material properties and activation stress coefficients:

1. Order of magnitude: We vary each material parameter/activation stress coefficient over a order of magnitude of 10^{-2} to 10^{+2} around the actual experimental value, and make a note of the response parameters that get affected.
2. Around experimental value: We then vary the same material parameter/activation stress coefficient within a range of -20% to $+20\%$ around the actual experimental value, and observe the effect on the response parameters.

The tables containing the values of the parametric studies and the graphs generated for the order of magnitude study are enlisted in Appendix A. Here we will only present the graphs generated for the parametric study around the experimental value of the parameter. Some comments have been made based on the observations and analysis of these two studies for each of the parameter studies.

A note for the time factor used in the implementation: The time zones for the experiment as specified by Tobushi are

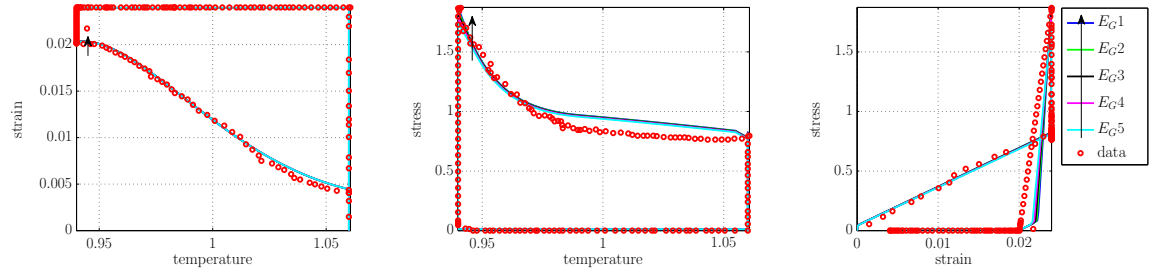
- Strain loading to 2.4% at high temperature + Holding strain constant = 7200s
- Cooling to below T_g at constant strain constraint = 360s
- Unloading to zero load at low temperature = 7200s

- Heating to above T_g under no load (stress free) configuration = 360s

Note that the experimental value for $\eta_G = 116000\text{MPas}$. In the code run however, we have set the time scale factor $t_{exp} = 100s$ thus factoring the experiment time by 100 to reduce the code run time on the machine. Now, care has to be taken that the viscosity value present in the model constitutive equations, η_G , is factored by the same amount, or else the creep and relaxation behaviors will be exaggerated and misrepresented. Therefore for all the runs, we use $\eta_G = \frac{116000(\text{MPas})}{t_{exp}(s)}$ and $t_{exp} = 100s$. The whole experiment is now interpreted in a new time scale t_{exp} , so the units of η_G should be interpreted as $\eta_G = 1160(\text{MPat}_{exp})$.

3.8.1 Material Parameters

Glassy Modulus



(a) Increasing values of E_G decrease the spring back during unloading ϵ_{cd} , while ϵ_{ea} is not affected
 (b) Increasing values of E_G increase the stress rise on cooling σ_c slightly
 (c) No additional effect observed

Figure 3.8: Glassy modulus effect on the response for values around experimental data range

Observations:

As the material becomes more glassy, the stress rise on cooling becomes higher and the tendency to spring back on unloading at glassy state becomes lower. Changing the glassy modulus by order of magnitudes above or below, has shown that five of the six model response parameters are affected by the glassy modulus (refer to Appendix A, Table A.2), with pronounce effect on the stress rise on cooling σ_c and shape fixity ϵ_{cd} (refer to Appendix A, Figure A.1). We look out for these response characteristics

by changing the glassy modulus only by $\pm 20\%$ range around the actual experimental value of glassy modulus, but these effects on σ_c and ϵ_{cd} are minimal as can be seen in the Figure 3.8. Effects on the other parameters are negligible (refer Appendix A, Table A.3).

Rubbery Modulus

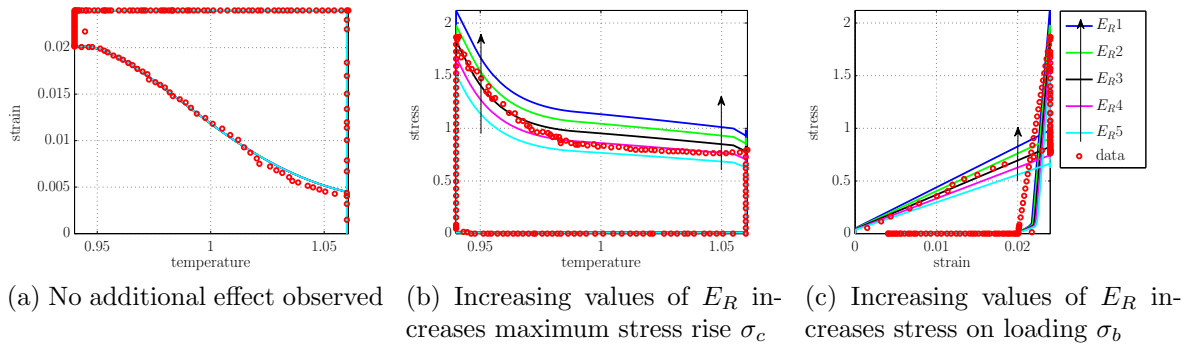


Figure 3.9: Rubbery modulus effect on the response for values around experimental data range

Observations:

As seen from Figure 3.9c, when the material becomes more rubbery, stress rise on loading σ_b at rubbery state is higher. This also results in a proportional rise in the maximum stress developed in the material during cooling as seen in Figure 3.9b. Yakacki et al. [22] proposed an increase in crosslinking, which is directly related to a polymers rubbery modulus, will provide more restorative forces and may enable accelerated viscoelastic recovery. In the current analysis, we can comment on the restorative forces developed in the material only, and these results agree with observations made by Yakacki. Spring back at glassy state and recovery at the end of the cycle is not affected severely. Since E_R is the non-dimensionalizing parameter in this model, as well as the parameter selected for determining the relaxation time, this parameter has significant control over most parameters of the response (Refer to Appendix A, Table A.4). Table A.5 and the Figure 3.9 shows that increasing values of the rubbery modulus results in significant increase in the stress rise response on loading, σ_b , significant increase in the maximum stress rise response after cooling, σ_c

and increase in the shape fixity ϵ_{cd} .

Glassy Thermal Expansion

Observations:

Refer to Figure 3.10. As expected, the effect of glassy thermal expansion is evident at lower temperatures. Glassy thermal expansion coefficient shows a pronounced effect on the stress rise during cooling and spring back on unloading. Increasing values of the glassy thermal expansion results in increase of the trend of stress rise σ_{Tg} and significant increase in the maximum stress rise response on cooling, σ_c . This change in σ_c affects the spring back during unloading. The model shows increasing spring back tendencies during unloading at low temperatures, with increasing values of the glassy thermal expansion. Effects on the other parameters is not significant.

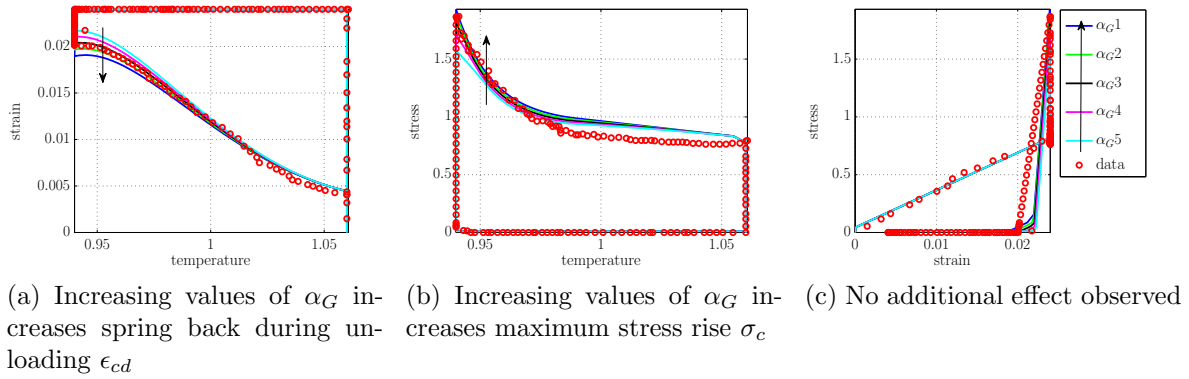
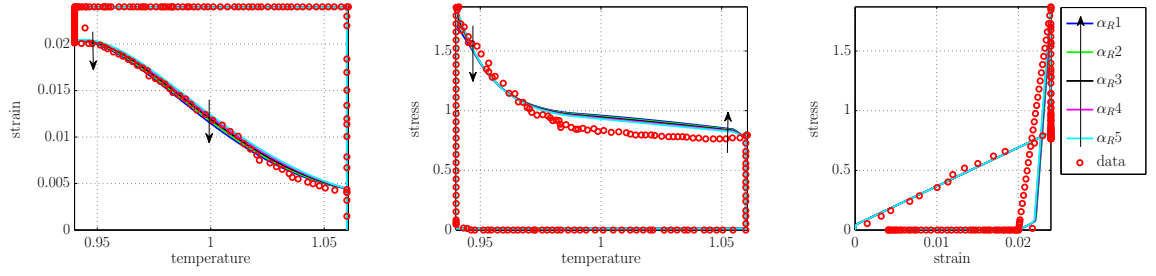


Figure 3.10: Glassy thermal expansion effect on the response for values around experimental data range

Rubbery Thermal Expansion

Observations:

Refer to Figure 3.11. Increasing values of the rubbery thermal expansion results in slight decrease of the maximum stress rise response after cooling, σ_c and slight decrease in the shape fixity ϵ_{cd} . Note that the rubbery thermal expansion affects the same parameters as the glassy thermal expansion coefficient, but the effects are opposite. Effects on the other parameters is not significant.



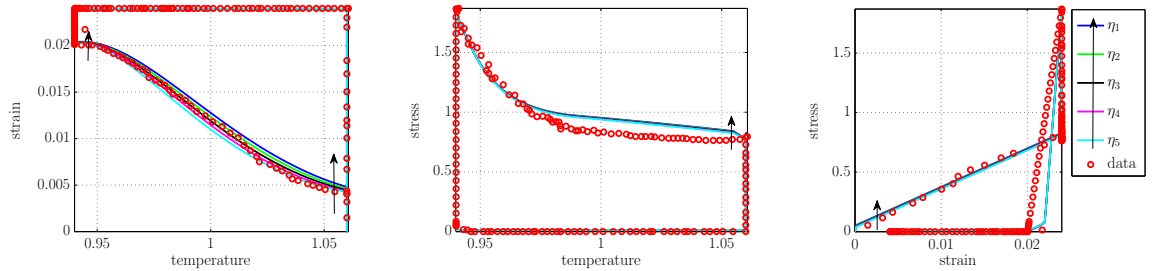
(a) Increasing α_R decreases spring back on unloading ϵ_{cd} (b) Increasing values of α_R increases maximum stress rise σ_c (c) No additional effect observed

Figure 3.11: Rubbery thermal expansion effect on the response for values around experimental data range

Glassy Viscosity

Observations:

From Appendix A, Table A.10 it comes to light that the viscosity has significant control over the stress rise during loading and the shape fixity, which is typical of creep and relaxation phenomena in a viscoelastic model. Thus the effect of changing the glassy viscosity by an order of magnitude is significant on three response parameters. It affects the trend of the strain recovery response during heating. Increasing values of the viscosity results in the increase in the strain at the end of cycle ϵ_{ea} . However, these effects are not so pronounced when the viscosity is changed only by $\pm 20\%$, as seen in Appendix A, Table A.11 and the graphs in Figure 3.12.



(a) Increasing values of η affect strain recovery characteristics (b) Increasing values of η affects the stress rise trend at beginning of cooling (c) Increasing values of η affects the stress rise trend at beginning of loading

Figure 3.12: Viscosity effect on the response for values around experimental data range

3.8.2 Activation Stress Coefficients

Activation Stress Coefficient y_1

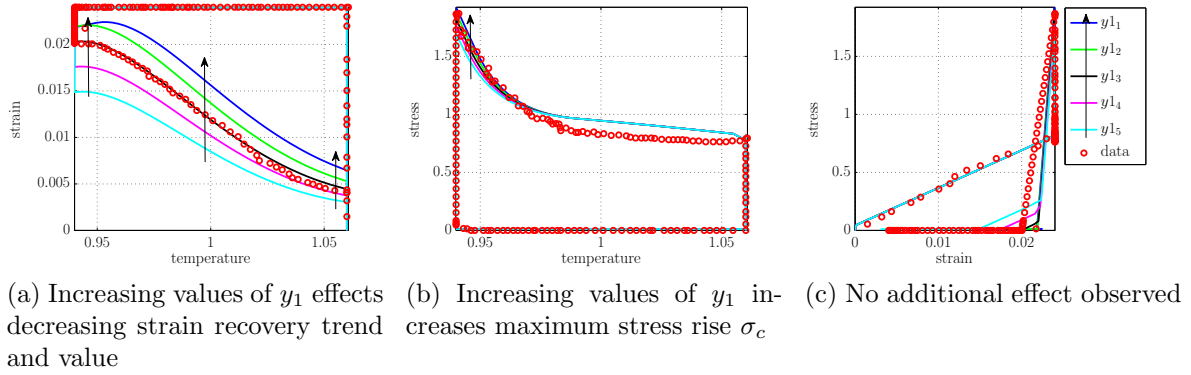


Figure 3.13: Activation stress coefficient y_1 effect on the response

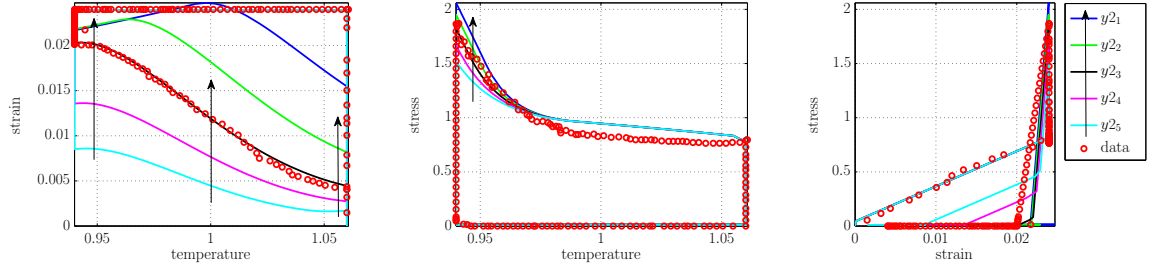
Observations:

Refer to Figure 3.13. The activation stress coefficient y_1 significantly affects the shape recovery trend on heating. Increasing values of y_1 effects the increase of the maximum stress rise response after cooling, σ_c . This results smaller spring back tendencies on unloading, and eventually in the decreasing trend of shape recovery or, in the decrease in the values of ϵ_{Tg} and in the increase in the strain recovery at the end of the cycle. Effects on the other parameters is not significant.

Activation Stress Coefficient y_2

Observations:

Refer to Figure 3.14. The effect of activation stress coefficient y_2 is similar to y_1 , but significantly higher. It primarily affects not just the value of shape recovery at the end of the cycle, but more importantly the shape recovery trend on heating, even though this coefficient shows up only in the cooling part of the cycle. This is because increasing values of y_2 effects the increase of the maximum stress rise response after cooling, σ_c significantly. Since this acts as the initial condition for the unloading and heating range, the response parameters in this second range get affected. This eventually results in the decreasing trend of shape recovery or, in the increase in the

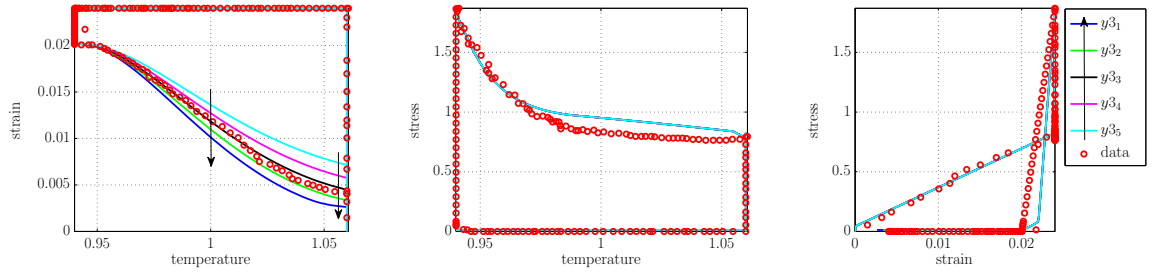


(a) Increasing values of y_2 increases strain recovery trend and value, ϵ_{Tg} and ϵ_{ea} (b) Increasing values of y_2 increases maximum stress rise σ_c (c) No additional effect observed

Figure 3.14: Activation stress coefficient y_2 effect on the response

values of ϵ_{Tg} and in the increase in the strain recovery at the end of the cycle ϵ_{ea} .

Activation Stress Coefficient y_3



(a) Increasing values of y_3 increases strain recovery trend and value, ϵ_{Tg} and ϵ_{ea} (b) No additional effect observed (c) No additional effect observed

Figure 3.15: Activation stress coefficient y_3 effect on the response

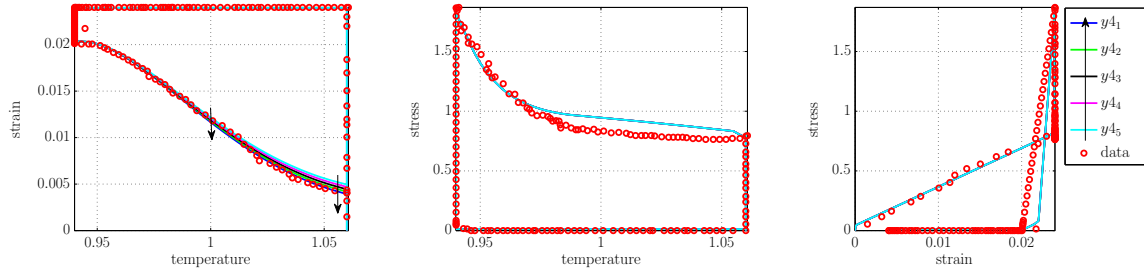
Observations:

Refer to Figure 3.15. The activation stress coefficient y_3 significantly affects the shape recovery trend on heating. Increasing values of y_3 results in the increasing trend of shape recovery or, in the decrease in the values of ϵ_{Tg} and in the significant decrease in the strain at the end of the cycle ϵ_{ea} . It does not have any other effect on the other parameters.

Activation Stress Coefficient y_4

Observations:

Refer to Figure 3.16. The activation stress coefficient y_4 affects the shape recovery trend on heating slightly. Increasing values of y_4 results in the increasing trend of shape recovery or, in the decrease in the values of ϵ_{Tg} and in the decrease in the strain recovery at the end of the cycle ϵ_{ea} . It does not have any other effect on the other parameters.



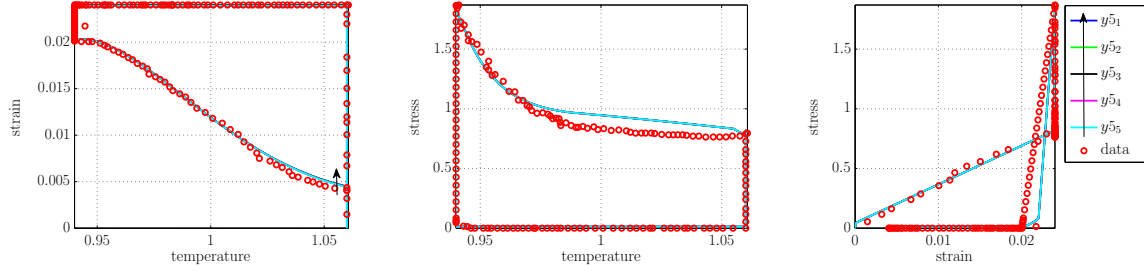
(a) Increasing values of y_4 slightly increases strain recovery trend and value, ϵ_{Tg} and ϵ_{ea} (b) No additional effect observed (c) No additional effect observed

Figure 3.16: Activation stress coefficient y_4 effect on the response

Activation Stress Coefficient y_5

Observations:

Refer to Figure 3.17. The activation stress coefficient y_5 affects the shape recovery trend on heating. Increasing values of y_5 results very slightly in the decreasing trend of shape recovery or, in the increase in the values of ϵ_{Tg} and in the increase in the strain recovery at the end of the cycle ϵ_{ea} . It does not have any other effect on the other parameters.



(a) Increasing values of y_5 very slightly decreases strain recovery trend and value, ϵ_{Tg} and ϵ_{ea} (b) No additional effect observed (c) No additional effect observed

Figure 3.17: Activation stress coefficient y_5 effect on the response

3.9 Sensitivity Analysis

The Table 3.6 is derived from all the parametric analysis (around experimental data range), and we enlist the effect of change in the response of the material with respect to the material parameters. To calculate the sensitivity of each response parameter, we first compute the logarithm of the response

$$\ln param = \frac{\Delta param}{param} = \frac{(param^{var+20\%} - param^{var-20\%})}{(param^{expvar})}.$$

For example for the sensitivity of the response parameter σ_b with respect to the material parameter E_G , we first compute the logarithm of σ_b as

$$\ln \sigma_b = \frac{\Delta \sigma_b}{\sigma_b} = \frac{(\sigma_b^{E_G^{exp}+20\%} - \sigma_b^{E_G^{exp}-20\%})}{\sigma_b^{E_G^{exp}}},$$

and the logarithm of the material parameter E_G as

$$\ln E_G = \frac{\Delta E_G}{E_G} = \frac{(E_g^{exp+20\%} - E_g^{exp-20\%})}{E_g^{exp}}.$$

The sensitivity of each response parameter with respect to a particular material parameter is determined by dividing their corresponding logarithms. For example, the sensitivity of σ_b with respect to E_G is given by $\frac{\ln \sigma_b}{\ln E_G}$. These values have been computed and presented in Table 3.6. The maximum value in any column will give an idea of which material variable has maximum control on that particular response parameter. Thus the Table 3.6 shows how sensitive a particular response parameter is to any of the material parameters. For example, the shape fixity response parameter

ϵ_{cd} does not depend much on E_G , and is sensitive only by a small fraction to α_G , but it is sensitive to y_1 and y_2 .

Table 3.6: Sensitivity of a particular response property to each of the material parameters

Material	Affected Response Property					
Parameter	σ_b	σ_{Tg}	σ_c	ϵ_{cd}	ϵ_{Tg}	ϵ_{ea}
E_G	0.041116	0.03859	0.175751	-0.03648	0.001648	0.000534
E_R	0.962056	0.962736	0.831967	0.033672	-0.00193	-0.00029
η_G	0.052342	0.040464	0.000888	-0.11262	0.386203	-0.06997
α_G	0	0.099929	0.494241	1.90404	-0.13933	-0.00067
α_R	0	0.077597	-0.20701	0.041836	-0.19562	0.000501
y_1	0	0	0.308941	-4.76861	1.519462	-0.43661
y_2	0	0	0.743927	-9.00851	4.403135	-1.76431
y_3	0	0	0	2.61E-05	-0.78519	0.580071
y_4	0	0	0	2.6E-05	-0.11714	0.13142
y_5	0	0	0	5.5E-05	0.004765	-0.01262

The Table 3.6 is useful from a synthesis aspect, because one can deduce the physical properties that need to be changed in order to observe a particular kind of response. On the other hand, it is also useful to the designer, since it reports how much a particular response parameter can be controlled by each of the material parameters. From a designer's point of view, it now becomes clear that

- E_R controls the response parameters σ_b , σ_{Tg} , σ_c in the strain control region
- σ_c can be controlled primarily by E_R and y_2 , and partially by α_G and y_1
- It should be noted that σ_c value affects the strain responses in range 2 i.e stress control regime of the thermomechanical cycle, since it is the initial condition for this part of the cycle.
- Shape fixity ϵ_{cd} is affected primarily by y_1 , y_2 , because of their effect on σ_c , but it can be controlled individually through α_G
- ϵ_{Tg} is affected primarily by y_1 , y_2 , because of their effect on σ_c , but it can be controlled individually through y_3

- Shape recovery ϵ_{ea} is affected primarily by y_2 , because of its effect on σ_c , but it can be controlled individually through y_3

Response Surface Map

We notice that the parameter y_2 is the common influencing parameter for each of these responses. The remaining three "uncommon" parameters E_R , y_1 and y_3 separately affect the three responses.

1. Although the parametric analysis suggests response properties being directly proportional to the material properties, increasing or decreasing monotonically (example Figure 3.18a), the response surface maps give a visual idea of the dependence, which may be complicated (example Figure 3.18b, 3.18c).
2. For a particular set of all the material parameters, and fixing y_2 to a certain value, we will obtain corresponding response values of σ_C , ϵ_{cd} and ϵ_{ea} . Of these response values, if two of the responses lie in an acceptable range, but the third is not within acceptable range, then the corresponding uncommon parameter of the response can be varied to get a desirable answer, without affecting the other two responses.
3. Plotting the three response parameters against the common parameter y_2 , and using the physically acceptable ranges for the responses, we can determine the physically acceptable range for y_2 . This helps in recognizing whether the error optimization code is giving a physically acceptable result.

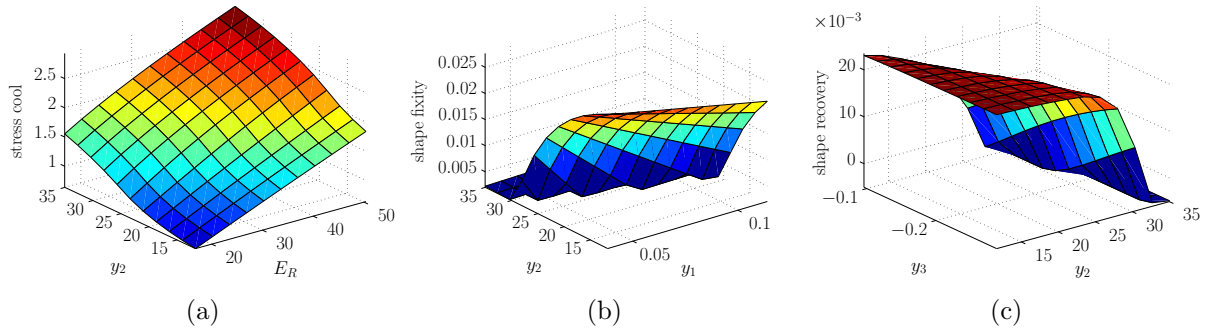


Figure 3.18: Response surface maps

3.10 Parametric Study of the SMP Model with respect to Control Parameters

The following parametric study involves varying certain loading conditions in the thermomechanical cycle, which have been known to affect the response of SMPs in the literature. We choose the following loading parameters of significance: maximum strain applied, deformation temperature, cooling rate and heating rate.

3.10.1 Maximum Strain

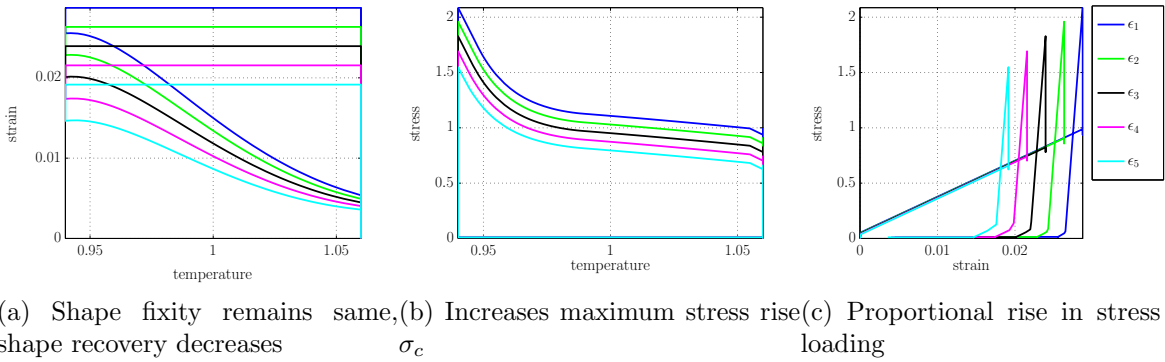


Figure 3.19: Effect of maximum strain applied on the response for values around experimental data range

Observations:

Refer to Figure 3.19. As we increase the applied maximum strain, it increases the stress rise in the material proportionally during loading. The amount of stress rise only during cooling remains the same, although the maximum stress rise at the end of cooling increases proportionally. Shape fixity is not affected by the applied strain. With increasing applied strain, the final strain at the end of the cycle increases, but the shape recovery is decreases very gradually.

3.10.2 Deformation Temperature

Observations:

Refer to Figure 3.20. Heating the material to a higher temperature affects the stress rise during cooling and therefore the shape fixity slightly, compared to its effect on

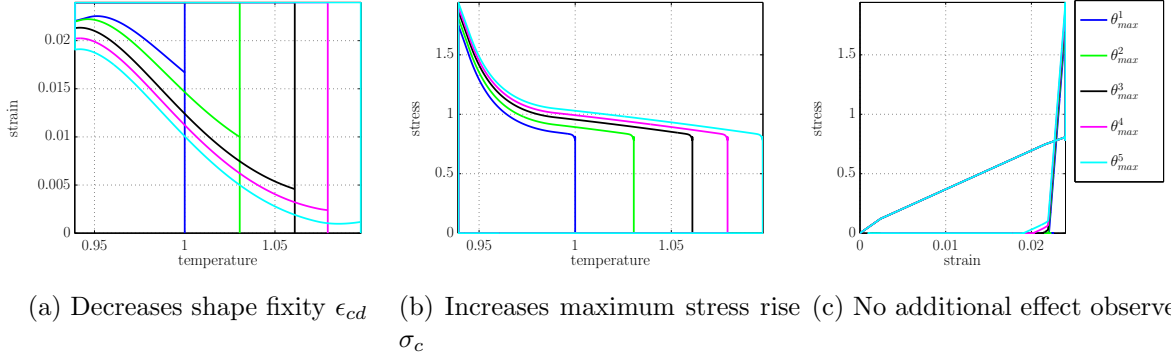


Figure 3.20: Effect of deformation temperature on the response for values around experimental data range

the shape recovery. As the deformation temperature is increased, the stress rise in the material increases, as it is cooling over a larger $\Delta\theta$. This reflects in the shape fixity behavior directly, and we see greater spring back with larger stress in the material. On heating the material at the end of the cycle to greater temperatures, better shape recovery is observed.

3.10.3 Heating Rate

Observations:

Refer to Figure 3.21. Varying the heating rate of the material affects the shape recovery characteristics severely. Heating the material gradually as opposed to ramping it suddenly gives more recovery of the strain at the end of the cycle.

3.10.4 Cooling Rate

Observations:

Refer to Figure 3.22. Varying the cooling rate of the material affects the trend rise in the material and correspondingly the shape fixity slightly. Effects on other response parameters are minimal.

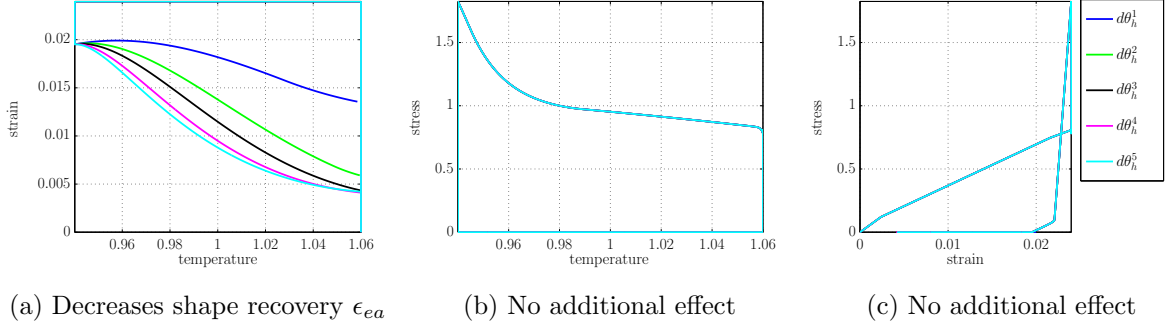


Figure 3.21: Effect of heating rate on the response for values around experimental data range

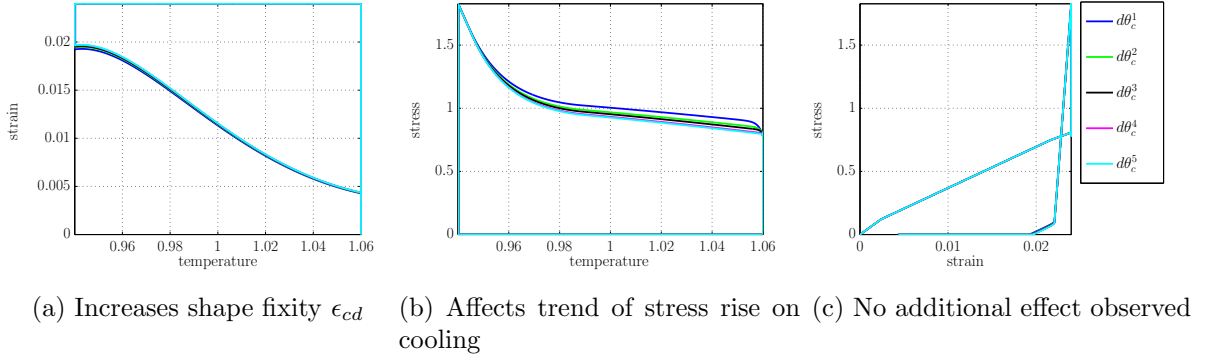


Figure 3.22: Effect of cooling rate on the response for values around experimental data range

3.11 Summary

The approach used in the development of the 1D model with the hysteresis of the activation stress through a temperature cycle, as proposed initially by Ghosh and Srinivasa [34], is extended in this chapter to a small strain 3D model. The details of a systematic optimization method to compute the coefficients of the activation stress function are presented. This gives significantly improved results when compared to using an ad hoc estimation of the coefficients in the previous chapter for the 1D model. Then this model is used to carry out an extensive parametric study for all material parameters and some chosen loading conditions of the experiment. The material parametric study gives an idea of how the trends of the response characteristics get affected by the material parameters. The sensitivity analysis of the material parameters has made it clear to the designer the quantitative control of each material parameter on the chosen response parameters. The crucial material parameters that governed the SMP response were the rubbery modulus and some of the coefficients of the activation stress function while cooling and heating. This also showed how the activation stress hysteresis function controls the response of the SMP. The sensitivity analysis also showed that behavior of SMPs are complex, where each response parameter is affected by two or more material parameters simultaneously. This was presented visually in the form of response surface maps, by varying two most influencing material parameters simultaneously and observing its effect on the response parameter. Finally, a parametric study for appropriate loading conditions was carried out, and we see that the model response is concurrent with the experimental results reported in the literature. Thus, the model is studied under different loading and thermal conditions, in addition to providing a comprehensive analysis of the material properties that characterize the SMP response.

4. BEAM THEORY MODEL USING ELASTIC-PREDICTOR PLASTIC-CORRECTOR

4.1 Introduction

Due to unique thermomechanical properties and the process-controllable behavior, SMPs have found numerous macroscopic applications as discussed in Chapter 1 Section 1.3. In most of these applications the SMP sample is subjected to bending load. The benefit of looking at bending experiments as opposed to uniaxial experiments are not restricted to application areas alone, but characterization problems themselves. For example, as Liu et al. [17] point out in their paper, in tension or compression, thermal stresses arise from constrained thermal expansion or contraction, leading to difficulties in separating the various mechanisms during deformation. Upon cooling, the applied stress can increase at a fixed strain, while in the flexural deformation the thermal contraction is not as severely constrained. Other advantages are that large displacements studies can be achieved in flexure at much more modest strain levels. A drawback is that the stress and strain are nonuniform and therefore more difficult to analyze. There have only been a handful of attempts at implementing the SMP models in a finite element setup to study the response for different load configurations or sample geometries as discussed in Chapter 1 Section 1.4. The typical approach with implementing complex non-linear 3D continuum models, is that it is computationally expensive and/or masks parametric design and control features that should be transparent and easily available to the designer as discussed in detail in Chapter 1 Section 1.5.

This chapter will focus on the development of an Euler Bernoulli beam theory for the small strain model developed in the previous Chapter 3. The boundary value problem that the SMP model is subjected to is a three point bending experiment. The first section begins with the statement of assumptions regarding the displacement and strains for theory development. This is followed by the derivation of the weak form from the principle of virtual work, in terms of the generalized displacements, where the constitutive equations of the small strain SMP model are used for the stress and plastic strain terms. Finally the Hermite cubic interpolation functions are used and the set of resulting algebraic equations are written in matrix form to set up the finite element model. The non-dimensional forms of the finite element model

and the constitutive equations are presented which are used in the implementation. The implementation consists of developing a time stepping algorithm for the elastic predictor dissipative corrector loop, where the elastic displacements are computed in the finite element numerical algorithm, and these are used to compute the elastic and plastic strain in the dissipative corrector loop, followed by a displacement convergence criteria within the time step. The key idea is that the elastic predictor is based on the solution to a beam theory boundary value problem while the dissipative corrector is entirely local (and hence can be parallelized) and is applied by considering the beam as a two or three dimensional body[57, 58]. This enables a very rapid solution of the problem yet maintaining fidelity of the distribution of inelastic strains across the cross-section. Within the iterative dissipative corrector loop, Simo et al. [58] have observed that only a few local sub-iterations are required to obtain good results, and the additional computational cost involved in this technique is more than offset by the drastic reduction in the required element data base. Thus the finite element displacements have to be computed only for a 1D beam, while the local iterative loop will be solved for a 2D cross-section of the beam. In this work, the algorithm is tested and studied for a three point bending experiment for three different material cases: elastic, plastic and thermoplastic beam. Time step convergence and mesh density convergence is carried out for the viscoplastic FEM code. Finally, we implement this model for a SMP undergoing three-point bending thermomechanical cycle and study its behavior. We will study both strain recovery and stress recovery cases for the thermomechanical cycle.

4.2 Development of Finite Element Model for SMP

4.2.1 Thermomechanical Three-point Flexural Cycle

A typical three-point flexure thermomechanical cycle for SMPs can be described as follows. Refer to Figure 4.1a and 4.1b for the processes. Process 1 involves deforming the SMP material at a high temperature above T_g . Process 2 is a shape fixing procedure where the SMP is cooled while maintaining the deformed shape. The stress needed to maintain the shape gradually reduces as the material is cooled. Process 3 is the unloading process, where the constraint load is unloaded to a certain prescribed level(or fully unloaded as shown in the figure) and the temporary shape is mostly retained at low temperature, after some amount of spring back. Finally,

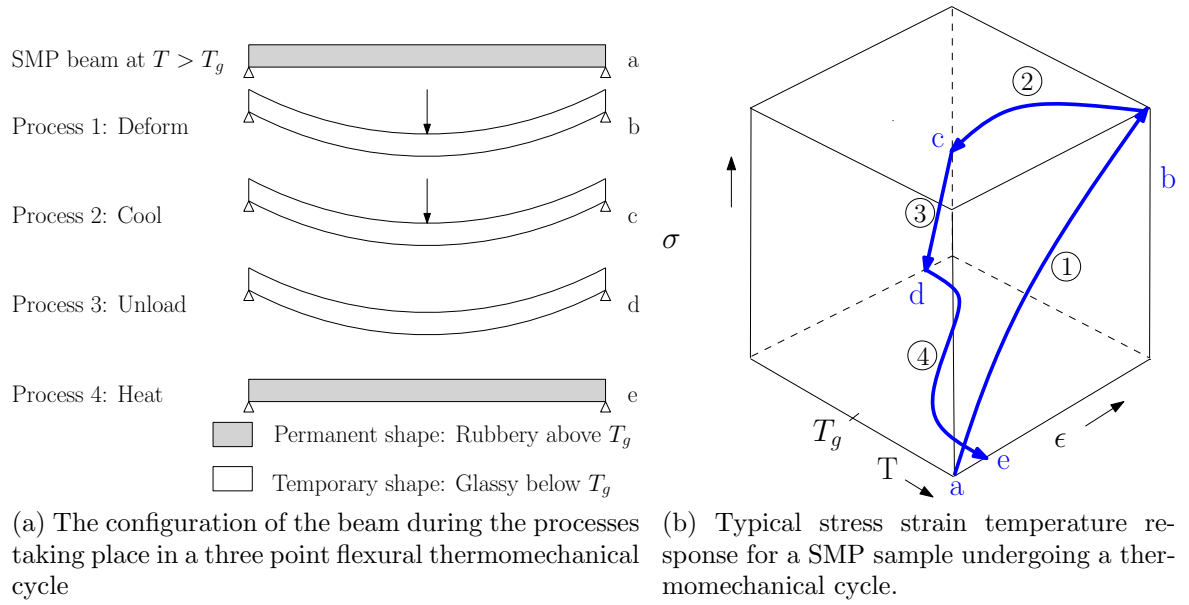


Figure 4.1: Thermomechanical flexural cycle: The curve 1 indicates the high temperature deformation. Curve 2 is the shape fixing process at constant strain, under cooling. Curve 3 is the relaxation of the stress at constant low temperature. Curve 4 is the strain recovery process under no load condition through heating.

process 4 includes the SMP beam being subject to a prescribed constant constraint load and heated beyond T_g .

4.2.2 Displacement Field and Strains

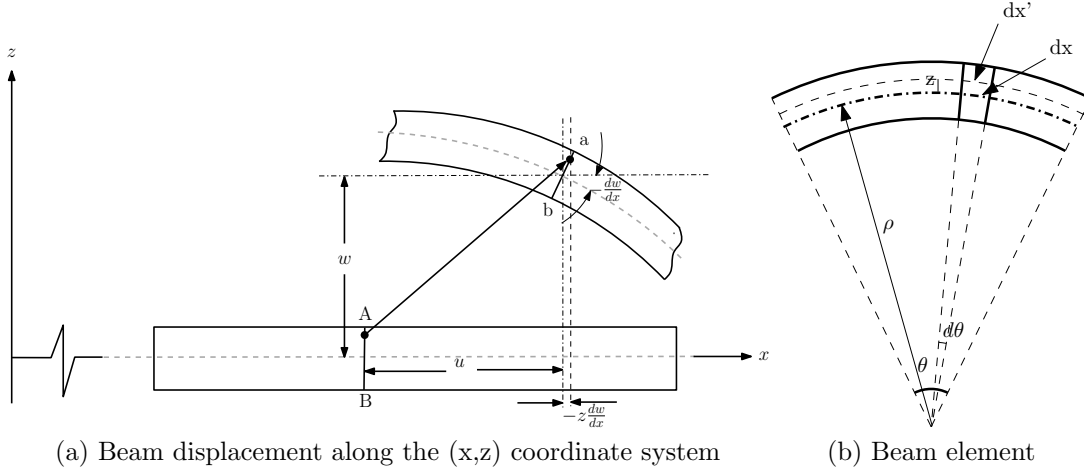


Figure 4.2: Kinematics of deformation of the Euler-Bernoulli beam theory

Following the general outline of the procedure presented by Reddy, 2004 [59], we employ the assumptions of Euler - Bernoulli beam theory (shown in Figure 4.2), where the bending of beams with small strains and rotations can be derived as below.

$$u_1 = -z \frac{dw}{dx}, \quad u_2 = 0, \quad u_3 = w(x) \quad (4.1)$$

where (u_1, u_2, u_3) are the total displacements of a material point occupying the location (x, y, z) in the undeformed body [usually denoted with capital letters: (X, Y, Z)], and u and w denote the axial and transverse displacements of a point on the x-axis, which is taken along the geometric centroid of the cross section of the beam. Note that since we are solving the problem of a three point bending load, an additional assumption has been made: transverse loads only cause transverse displacement and curvature of the section, i.e., $u = 0$. Hence the displacement field $u_1 = -z \frac{dw}{dx}$.

Using the Green-Lagrange strain tensor components, we can write

$$E_{ij} = \epsilon_{ij} = \frac{1}{2} \left(\frac{\partial u_i}{\partial x_j} + \frac{\partial u_j}{\partial x_i} \right) + \frac{1}{2} \frac{\partial u_m}{\partial x_i} \frac{\partial u_m}{\partial x_j} \quad (4.2)$$

where sum on repeated subscripts is implied. In explicit form

$$\begin{aligned} \epsilon_{11} = \epsilon_{xx} &= \frac{\partial u_1}{\partial x_1} + \frac{1}{2} \left[\left(\frac{\partial u_1}{\partial x_1} \right)^2 + \left(\frac{\partial u_3}{\partial x_1} \right)^2 \right] \\ &= -z \frac{\partial^2 w}{\partial x^2} + \frac{1}{2} \left(\frac{\partial w}{\partial x} \right)^2 \\ &= \frac{1}{2} \left(\frac{\partial w}{\partial x} \right)^2 - z \frac{\partial^2 w}{\partial x^2} \end{aligned} \quad (4.3)$$

In view of the small strain assumption, the first term in the square brackets is neglected, i.e., $\frac{\partial u_1}{\partial x_1} = O(2)$ and hence $\left(\frac{\partial u_1}{\partial x_1} \right)^2 = O(22) \approx 0$. The second term, $\frac{\partial u_3}{\partial x_1}$, denotes the rotation of a line perpendicular to the beam axis. Even when the strains are small, because of the slenderness, beams can undergo moderate to large rotations. Hence we retain the square of the rotation $\frac{\partial u_3}{\partial x_1}$ in the strain component ϵ_{11} . Thus we begin with the following expression for strain:

$$\epsilon_{xx} = -z \frac{\partial^2 w}{\partial x^2} \quad (4.4)$$

4.2.3 Constitutive Equations of the SMP Model

Now consider the shape memory polymer constitutive equations that were developed in Chapter 3. We assume that the SMP is made up of a permanent “backbone” network that is responsible for shape recovery and a temporary or transient network that is responsible for the shape setting phenomena. We begin the experiment at a temperature $\theta > \theta_g$. This will be considered as the reference configuration of the body, and all strain measurements will be made relative to this reference configuration. Let the SMP undergo a displacement $u(x, t)$. The strains in the networks are $\boldsymbol{\varepsilon}$ for the permanent network and $\boldsymbol{\varepsilon}_t$ for the temporary network. It is convenient to introduce the inelastic strain $\boldsymbol{\varepsilon}_{ve} = \boldsymbol{\varepsilon} - \boldsymbol{\varepsilon}_t$ and use it as a primary variable. As described in Chapter 3, the shape memory effect is governed by the strain and temperature dependent activation of network breaking and reformation. This effect is modeled as:

$$[\boldsymbol{\sigma}] = \left(\mathbf{C}_G\right) \left[\boldsymbol{\varepsilon} - \alpha(\theta - \theta_h)\mathbf{I}\right] - 2\mu_G[\boldsymbol{\varepsilon}_{ve}] \quad (4.5)$$

$$[\dot{\boldsymbol{\varepsilon}}_{ve}] = \begin{cases} 0, & \text{if } \|\boldsymbol{\tau} - 2\mu_R\boldsymbol{\varepsilon}_{ve}\| \leq \kappa; \\ \frac{1}{\eta_G}(\|\boldsymbol{\tau} - 2\mu_R\boldsymbol{\varepsilon}_{ve}\| - \kappa) \frac{[\boldsymbol{\tau} - 2\mu_R\boldsymbol{\varepsilon}_{ve}]}{\|\boldsymbol{\tau} - 2\mu_R\boldsymbol{\varepsilon}_{ve}\|}, & \text{if } \|\boldsymbol{\tau} - 2\mu_R\boldsymbol{\varepsilon}_{ve}\| > \kappa; \end{cases} \quad (4.6)$$

where, the deviatoric stress is given as $\boldsymbol{\tau} = 2\mu_G[\boldsymbol{\varepsilon} - \boldsymbol{\varepsilon}_{ve} - \alpha(\theta - \theta_h)\mathbf{I}]$ and the isotropic glassy stiffness that is assumed is given as $\mathbf{C}_G = (k_G - \frac{2\mu_G}{3})\mathbf{I} \otimes \mathbf{I} + 2\mu_G\mathbb{I}$. Also, κ is the network activation threshold, and the hysteresis of the activation stress is key in controlling the response of the SMP model. Thus the thermodynamic driving force $\boldsymbol{\tau} - 2\mu_R\boldsymbol{\varepsilon}_{ve}$ competes with the network activation threshold κ , resulting in the evolution of the inelastic strain $\boldsymbol{\varepsilon}_{ve}$. Apart from these, k_G is the glassy bulk modulus, k_R is the rubbery bulk modulus, μ_G is the glassy shear modulus, μ_R is the rubbery shear modulus, α is the thermal expansion coefficient, and η_G is the glassy viscosity.

The activation stress of the material κ is sensitive to temperature, and the material yields differently depending the current value of the temperature, the amount of strain the material is subjected to, and on whether the temperature of the material dropped or increased from the previous time-step. Thus there is a hysteresis of the activation stress from the cooling to the heating cycle, which gives the different trends of the stress-rise during cooling and the strain-recovery during heating. These considerations suggest that the rate of activation stress has the following functional form

$$\dot{\kappa} = f(\bar{\theta}, \text{sign}(\dot{\bar{\theta}}), \bar{\epsilon})\dot{\bar{\theta}}$$

$$f_{cool} = y_1(e_v + \sinh(-y_2(\theta - \theta_1)))\delta_1$$

$$f_{heat} = (-y_3e_v - y_4(1 - (y_5 \tanh(m\theta + n))^2))\delta_2$$

where, e_v is the von mises strain corresponding to the strain $(\mathbf{e}_e - \alpha(\theta - \theta_h)\mathbf{I})$. e_v is the scalar strain value selected in 3D context, such that it is affected by pure thermal strains or pure mechanical processes. Also, $m = 2/(\theta_{max} - \theta_2)$, $n = 1 - m\theta_{max}$. Here θ_1 and θ_2 are limiting values of θ until which there is no rise/fall in the stress/strain

during the cooling/heating cycle.

$$\delta_1 = \begin{cases} 1, & \forall \theta \leq \theta_1; \\ 0, & \forall \theta > \theta_1; \end{cases} \quad \delta_2 = \begin{cases} 0, & \forall \theta < \theta_2; \\ 1, & \forall \theta \geq \theta_2; \end{cases}$$

Since we are primarily interested in the moment M_{xx} generated in the beam, let us compute only the axial stresses from the constitutive equation 4.5.

$$\begin{aligned} \sigma_{11} &= (k_G + \frac{4}{3}\mu_G)\epsilon_{xx} - 2\mu_G\epsilon_{xx}^{ve} - 3k_G\alpha(\theta - \theta_h) \\ &= (k_G + \frac{4}{3}\mu_G)\left[-z\frac{\partial^2 w}{\partial x^2}\right] - 2\mu_G\epsilon_{xx}^{ve} - 3k_G\alpha(\theta - \theta_h) \end{aligned} \quad (4.7)$$

4.2.4 Weak Form

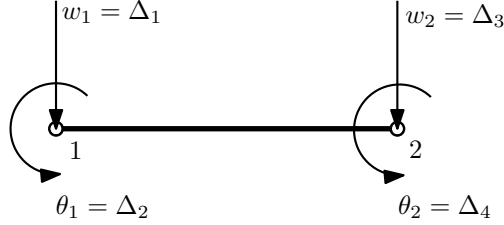


Figure 4.3: The Euler-Bernoulli finite element with primary degrees of freedom

The weak form is derived from the principle of virtual displacements which states that if a body is in equilibrium, the total virtual work done by actual internal as well as external forces in moving through their respective virtual displacements is zero. The analytical form of the principle over a typical element $\Omega^e = (x_a, x_b)$ shown in Figure 4.3, is as follows

$$\delta W^e = \delta W_I^e + \delta W_E^e = 0 \quad (4.8)$$

where δW_I^e is the virtual strain energy stored in the element due to actual stresses σ_{ij} in moving through the virtual strains $\delta\epsilon_{ij}$, and δW_E^e is the work done by external applied loads in moving through their respective virtual displacements.

The internal and external virtual work expressions for a Euler Bernoulli beam

element are

$$\delta W_I^e = \int_{V_e} \delta \epsilon_{ij} \sigma_{ij} dV \quad (4.9)$$

$$= \int_{x_a}^{x_b} \int_{A_e} \left(-z \frac{\partial^2 \delta w}{\partial x^2} \right) \sigma_{11} dA dx \quad (4.10)$$

$$= \int_{x_a}^{x_b} \left(-\frac{\partial^2 \delta w}{\partial x^2} M_{xx} \right) dx \quad (4.11)$$

$$\delta W_E^e = - \left[\int_{x_a}^{x_b} q \delta w dx + \sum_{i=1}^4 Q_i^e \delta \Delta_i^e \right] \quad (4.12)$$

where V_e and A_e are the element volume and cross sectional area, respectively, $q(x)$ is the distributed transverse loads measured per unit length, Q_i^e are the generalized nodal forces, and $\delta \Delta_i^e$ are the virtual generalized nodal displacements of the element.

The virtual work statement in Eq 4.8 becomes

$$0 = \int_{x_a}^{x_b} \left(-\frac{\partial^2 \delta w}{\partial x^2} M_{xx} \right) dx - \int_{x_a}^{x_b} q \delta w dx - \sum_{i=1}^4 Q_i^e \delta \Delta_i^e \quad (4.13)$$

The virtual statement Eq 4.13 is equivalent to the following weak form:

$$0 = \int_{x_a}^{x_b} \left(-\frac{\partial^2 \delta w}{\partial x^2} M_{xx} - q \delta w \right) dx - Q_1^e \delta \Delta_1^e - Q_2^e \delta \Delta_2^e - Q_3^e \delta \Delta_3^e - Q_4^e \delta \Delta_4^e \quad (4.14)$$

Integration by parts of the expressions in Eq. 4.14 to relieve δw of any differentiation, results in

$$\begin{aligned} 0 = & - \int_{x_a}^{x_b} \left(\frac{\partial^2 M_{xx}}{\partial x^2} + q \right) \delta w dx - \left[M_{xx} \frac{d\delta w}{dx} \right]_{x_a}^{x_b} + \left[\frac{dM_{xx}}{dx} \delta w \right]_{x_a}^{x_b} \\ & - Q_1^e \delta \Delta_1^e - Q_2^e \delta \Delta_2^e - Q_3^e \delta \Delta_3^e - Q_4^e \delta \Delta_4^e \end{aligned} \quad (4.15)$$

The governing equations of equilibrium, i.e the Euler Lagrange equation is

$$\delta w : \quad -\frac{d^2 M_{xx}}{dx^2} = q(x) \quad (4.16)$$

Consider the balance of forces and momentums around any point of the beam:

$$\frac{d^2 M}{dx^2} + q(x) = 0 \quad (4.17)$$

where M is the bending moment and V is the shear force

$$M(x) = \int_A z \sigma_{xx} dx, \quad V(x) = \frac{dM}{dx}$$

The above equations are the same as Eq 4.16. The weak form of Eq 4.16 is

$$0 = \int_{x_a}^{x_b} \left(-\frac{\partial^2 v}{\partial x^2} M_{xx} - qv \right) dx - \left[M_{xx} \frac{dv}{dx} \right]_{x_a}^{x_b} + \left[\frac{dM_{xx}}{dx} v \right]_{x_a}^{x_b} \quad (4.18)$$

where v is the weight function.

We evaluate the momentum in a SMP beam of height $2c$ and width b , with moment of inertia $I = \frac{2bc^3}{3}$ using the form of stress from Eq. 4.7:

$$\begin{aligned} M_{xx} &= \int_A z \sigma_{11}(x, z) dA \\ &= b \int_{-c}^c z \sigma_{11}(x, z) dz \\ &= b(k_G + \frac{4}{3}\mu_G) \int_{-c}^c \left[-z^2 \frac{\partial^2 w}{\partial x^2} \right] dz - 2b\mu_G \int_{-c}^c z \epsilon_{11}^{ve} dz - 3bk_G \alpha \int_{-c}^c z(\theta - \theta_h) dz \\ &= -\frac{2bc^3}{3} (k_G + \frac{4}{3}\mu_G) \left[\frac{\partial^2 w}{\partial x^2} \right] - 2b\mu_G \int_{-c}^c z \epsilon_{11}^{ve} dz - 3bk_G \alpha \int_{-c}^c z(\theta - \theta_h) dz \\ &= -I \left\{ (k_G + \frac{4}{3}\mu_G) \left[\frac{\partial^2 w}{\partial x^2} \right] + \frac{3\mu_G}{c^3} \int_{-c}^c z \epsilon_{11}^{ve} dz + \frac{9k_G \alpha}{2c^3} \int_{-c}^c z(\theta - \theta_h) dz \right\} \\ &= -I(k_G + \frac{4}{3}\mu_G) \left[\frac{\partial^2 w}{\partial x^2} \right] - M_{xx}^{ve} - M_{xx}^T \end{aligned} \quad (4.19)$$

where the moment generated due to inelastic strain M_{xx}^{ve} and the moment generated due to thermal differences M_{xx}^T are as follows

$$M_{xx}^{ve} = 2b\mu_G \int_{-c}^c z \epsilon_{11}^{ve} dz \quad (4.20)$$

$$M_{xx}^T = 3bk_G \alpha \int_{-c}^c z(\theta - \theta_h) dz \quad (4.21)$$

Using the above result, we now apply the balance equations in Eq. (4.17)

$$I(k_G + \frac{4}{3}\mu_G) \left[\frac{\partial^4 w}{\partial x^4} \right] + \frac{d^2 M_{xx}^{ve}}{dx^2} + \frac{d^2 M_{xx}^T}{dx^2} - q(x) = 0 \quad (4.22)$$

The virtual work statements Eq 4.14 can be expressed in terms of the generalized displacement (w) with the help of the form momentum in Eq 4.22.

$$\begin{aligned} 0 = \int_{x_a}^{x_b} & \left(I(k_G + \frac{4}{3}\mu_G) \frac{d^2 \delta w}{dx^2} \frac{d^2 w}{dx^2} + (M_{xx}^{ve} + M_{xx}^T) \frac{d^2 \delta w}{dx^2} - q \delta w \right) dx \\ & - Q_1 \delta w(x_a) - Q_2 \delta \theta(x_b) - Q_3 \delta w(x_b) - Q_4 \delta \theta(x_a) \end{aligned} \quad (4.23)$$

where (Q_1, Q_3) denote shear forces and (Q_2, Q_4) are the bending moments at nodes 1 and 2.

4.2.5 Finite Element Formulation

Since we are concerned with the transverse displacement and its derivative, we will choose the Hermite cubic interpolation functions for approximation. Therefore, the transverse deflection $w(x)$ is approximated as

$$w(x) = \sum_{j=1}^4 \bar{\Delta}_j \phi_j(x) \quad (4.24)$$

where ϕ_j are the Hermite cubic interpolation functions. Also $(\theta_x = -dw/dx)$,

$$\bar{\Delta}_1 = w(x_a), \quad \bar{\Delta}_2 = \theta_x(x_a), \quad \bar{\Delta}_3 = w(x_b), \quad \bar{\Delta}_4 = \theta_x(x_b) \quad (4.25)$$

and we replace the weight function $v = \delta w$ with

$$\delta w(x) = \phi_i(x) \quad (4.26)$$

Substituting all the relationships from Eq 4.24 to 4.26 in the weak form obtained in Eq 4.23, we obtain

$$\begin{aligned} 0 = \int_{x_e}^{x_e+1} & \left(I(k_G + \frac{4}{3}\mu_G) \frac{d^2 \phi_i}{dx^2} \frac{d^2 \phi_j}{dx^2} \bar{\Delta}_j + (M_{xx}^{ve} + M_{xx}^T) \frac{d^2 \phi_i}{dx^2} - q \phi_i \right) dx \\ & - Q_1(x_a) - Q_2(x_a) - Q_3(x_b) - Q_4(x_b) \end{aligned} \quad (4.27)$$

Therefore this equation can be rewritten as

$$0 = \sum_{j=1}^4 K_{ij} \bar{\Delta}_j - F_i \quad (4.28)$$

where

$$K_{ij} = \int_{x_e}^{x_e+1} I(k_G + \frac{4}{3}\mu_G) \frac{d^2\phi_i}{dx^2} \frac{d^2\phi_j}{dx^2} dx \quad (4.29)$$

$$F_i = \int_{x_e}^{x_e+1} (-(M_i^{ve} + M_i^T) \frac{d^2\phi_i}{dx^2} + q\phi_i) dx + Q_i \quad (4.30)$$

Now we write out the Hermite cubic functions that have to be substituted in the above equations to get the explicit form of the above equations.

$$\begin{aligned} \phi_1 &= 1 - 3\left(\frac{\bar{x}}{h}\right)^2 + 2\left(\frac{\bar{x}}{h}\right)^3 \\ \phi_2 &= -\bar{x}\left(1 - \frac{\bar{x}}{h}\right)^2 \\ \phi_3 &= 3\left(\frac{\bar{x}}{h}\right)^2 - 2\left(\frac{\bar{x}}{h}\right)^3 \\ \phi_4 &= -\bar{x}\left[\left(\frac{\bar{x}}{h}\right)^2 - \left(\frac{\bar{x}}{h}\right)\right] \end{aligned} \quad (4.31)$$

where $h = x_b - x_a$ is the element length and \bar{x} is the local coordinate.

The first derivatives of ϕ with respect to \bar{x} are

$$\frac{d\phi_1}{d\bar{x}} = -\frac{6\bar{x}}{h^2}\left(1 - \frac{\bar{x}}{h}\right) \quad (4.32)$$

$$\begin{aligned} \frac{d\phi_2}{d\bar{x}} &= -\left[1 + 3\left(\frac{\bar{x}}{h}\right)^2 - 4\frac{\bar{x}}{h}\right] \\ \frac{d\phi_3}{d\bar{x}} &= \frac{6\bar{x}}{h^2}\left(1 - \frac{\bar{x}}{h}\right) \end{aligned} \quad (4.33)$$

$$\frac{d\phi_4}{d\bar{x}} = -\frac{\bar{x}}{h}\left(3\frac{\bar{x}}{h} - 2\right)$$

The second derivatives of ϕ with respect to \bar{x} are

$$\frac{d^2\phi_1}{d\bar{x}^2} = -\frac{6}{h^2} \left(1 - 2\frac{\bar{x}}{h}\right) \quad (4.34)$$

$$\begin{aligned} \frac{d^2\phi_2}{d\bar{x}^2} &= -\frac{2}{h} \left(3\frac{\bar{x}}{h} - 2\right) \\ \frac{d^2\phi_3}{d\bar{x}^2} &= \frac{6}{h^2} \left(1 - 2\frac{\bar{x}}{h}\right) \\ \frac{d^2\phi_4}{d\bar{x}^2} &= -\frac{2}{h} \left(3\frac{\bar{x}}{h} - 1\right) \end{aligned} \quad (4.35)$$

The coefficients given by Eq 4.29 and 4.30 can be calculated using the interpolations functions and their derivatives from Eq 4.31 to 4.34.

$$\begin{aligned} K_{11} &= \int_0^h I(k_G + \frac{4}{3}\mu_G) \frac{d^2\phi_1}{d\bar{x}^2} \frac{d^2\phi_1}{d\bar{x}^2} dx \\ &= I(k_G + \frac{4}{3}\mu_G) \int_0^h \frac{6}{h^2} \left(1 - 2\frac{\bar{x}}{h}\right) \times \frac{6}{h^2} \left(1 - 2\frac{\bar{x}}{h}\right) dx \\ &= I(k_G + \frac{4}{3}\mu_G) \int_0^h \frac{36}{h^4} \left(1 - 4\frac{\bar{x}}{h} + 4\frac{\bar{x}^2}{h^2}\right) dx \\ &= 36I(k_G + \frac{4}{3}\mu_G) \left[\frac{\bar{x}}{h^4} - 4\frac{\bar{x}^2}{2h^5} + 4\frac{\bar{x}^3}{3h^6} \right]_0^h \\ &= 36I(\bar{k}_G + \frac{4}{3}\bar{\mu}_G) \left(\frac{1}{h^3} - 2\frac{1}{h^3} + 4\frac{1}{3h^3} \right) \\ &= \frac{12I}{h^3} (k_G + \frac{4}{3}\mu_G) \end{aligned} \quad (4.36)$$

Similarly we calculate the remaining coefficients of K_{ij}

$$[K^e] = \frac{2(k_G + \frac{4}{3}\mu_G)I}{h^3} \begin{bmatrix} 6 & -3h & -6 & -3h \\ -3h & 2h^2 & 3h & h^2 \\ -6 & 3h & -6 & 3h \\ -3h & h^2 & 3h & 2h^2 \end{bmatrix} \quad (4.37)$$

For the coefficients of the force matrix, consider q constant over an element, and $(M^{ve} + M^T)$ varying :

$$\begin{aligned}
F_1 &= \int_0^h (-(M^{ve} + M^T) \frac{d^2 \phi_1}{dx^2} + q \phi_1) dx + Q_1(0) \\
&= \int_0^h (M^{ve} + M^T) \frac{6}{h^2} \left(1 - 2 \frac{\bar{x}}{h}\right) + q \left(1 - 3 \left(\frac{\bar{x}}{h}\right)^2 + 2 \left(\frac{\bar{x}}{h}\right)^3\right) dx + Q_1(0) \\
&= \left[(M^{ve} + M^T) \left(-\frac{6\bar{x}}{h^2} + \frac{12\bar{x}^2}{2h^3} \right) \right]_0^h + q \left[\bar{x} - \frac{\bar{x}^3}{h^2} + \frac{\bar{x}^4}{2h^3} \right]_0^h + Q_1(0) \\
&= \frac{qh}{2} + Q_1(0)
\end{aligned} \tag{4.38}$$

$$\begin{aligned}
F_2 &= \int_0^h (-(M^{ve} + M^T) \frac{d^2 \phi_2}{dx^2} + q \phi_2) dx + Q_2(0) \\
&= \int_0^h (M^{ve} + M^T) \frac{2}{h} \left(3 \frac{\bar{x}}{h} - 2\right) - q \bar{x} \left(1 - \frac{\bar{x}}{h}\right)^2 dx + Q_2(0) \\
&= \left[(M^{ve} + M^T) \left(\frac{3\bar{x}^2}{h^2} - \frac{4\bar{x}}{h} \right) \right]_0^h - q \left[\frac{\bar{x}^2}{2} - \frac{2\bar{x}^3}{3h} + \frac{\bar{x}^4}{4h^2} \right]_0^h + Q_2(0) \\
&= -(M_h^{ve} + M_h^T) - \frac{qh^2}{12} + Q_2(0)
\end{aligned} \tag{4.39}$$

$$\begin{aligned}
F_3 &= \int_0^h (-(M^{ve} + M^T) \frac{d^2 \phi_3}{dx^2} + q \phi_3) dx + Q_3(h) \\
&= \int_0^h -(M^{ve} + M^T) \frac{6}{h^2} \left(1 - 2 \frac{\bar{x}}{h}\right) + q \left(3 \left(\frac{\bar{x}}{h}\right)^2 - 2 \left(\frac{\bar{x}}{h}\right)^3\right) dx + Q_3(h) \\
&= \left[-(M^{ve} + M^T) \left(\frac{6\bar{x}}{h^2} - \frac{6\bar{x}^2}{h^3} \right) \right]_0^h + q_e \left[\frac{\bar{x}^3}{h^2} + \frac{\bar{x}^4}{2h^3} \right]_0^h + Q_3(h) \\
&= \frac{qh}{2} + Q_3(h)
\end{aligned} \tag{4.40}$$

$$\begin{aligned}
F_4 &= \int_0^h (-(M^{ve} + M^T) \frac{d^2 \phi_4}{dx^2} + q \phi_4) dx + Q_4(h) \\
&= \int_0^h (M^{ve} + M^T) \frac{2}{h} \left(3 \frac{\bar{x}}{h} - 1\right) - q \bar{x} \left\{ \left(\frac{\bar{x}}{h}\right)^2 - \left(\frac{\bar{x}}{h}\right) \right\} dx + Q_4(h)
\end{aligned}$$

$$\begin{aligned}
&= \left[(M^{ve} + M^T) \left(\frac{3\bar{x}^2}{h^2} - \frac{2\bar{x}}{h} \right) \right]_0^h - q_e \left[\frac{\bar{x}^4}{4h^2} - \frac{\bar{x}^3}{3h} \right]_0^h + Q_4(h) \\
&= (M_h^{ve} + M_h^T) + \frac{qh^2}{12} + Q_4(h)
\end{aligned} \tag{4.41}$$

The resulting algebraic equations from Eq 4.37 to 4.41 are written in matrix form

$$\mathbf{K}^e \mathbf{\Delta}^e = \mathbf{F}^e$$

$$\frac{2(k_G + \frac{4}{3}\mu_G)I}{h^3} \begin{bmatrix} 6 & -3h & -6 & -3h \\ -3h & 2h^2 & 3h & h^2 \\ -6 & 3h & -6 & 3h \\ -3h & h^2 & 3h & 2h^2 \end{bmatrix} \begin{bmatrix} \Delta_1 \\ \Delta_2 \\ \Delta_3 \\ \Delta_4 \end{bmatrix} = \frac{qh}{12} \begin{bmatrix} 6 \\ -h \\ 6 \\ h \end{bmatrix} + \begin{bmatrix} Q_1(0) \\ -(M_h^{ve} + M_h^T) + Q_2(0) \\ Q_3(h) \\ (M_h^{ve} + M_h^T) + Q_4(h) \end{bmatrix} \tag{4.42}$$

For the current problem, we solve for a 3 point bending problem, i.e a simply supported beam with a central load,, and assume $q = 0, M^T = 0, Q_i = 0$. The problem reduces to

$$\frac{2(k_G + \frac{4}{3}\mu_G)I}{h^3} \begin{bmatrix} 6 & -3h & -6 & -3h \\ -3h & 2h^2 & 3h & h^2 \\ -6 & 3h & -6 & 3h \\ -3h & h^2 & 3h & 2h^2 \end{bmatrix} \begin{bmatrix} \Delta_1 \\ \Delta_2 \\ \Delta_3 \\ \Delta_4 \end{bmatrix} = \begin{bmatrix} 0 \\ -(M_h^{ve} + M_h^T) \\ 0 \\ (M_h^{ve} + M_h^T) \end{bmatrix} \tag{4.43}$$

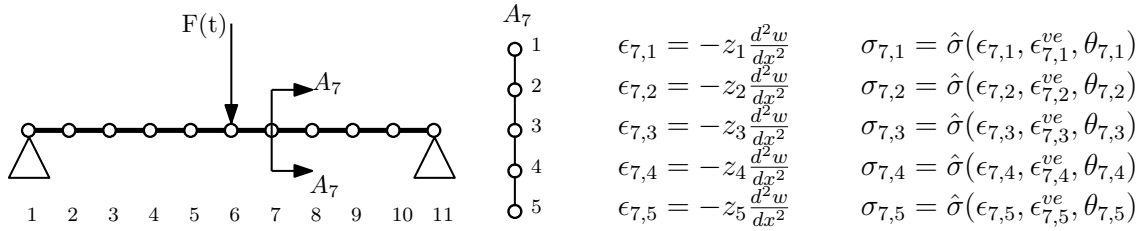


Figure 4.4: Loading and boundary conditions along the beam for three point bending experiment, and displacement and strain computations across the cross section of the beam

For implementation purposes, we will focus on the simulation of the center line of the beam. For this purpose, we start with a 1D beam for the elastic displacement

solutions along the centreline of the beam, as shown in Figure 4.4 . The corresponding strains, stresses and plastic strain solutions are computed across the cross section A-A as shown in Figure 4.4, for node 7 along the length of the beam.

4.2.6 Non-dimensionalization of the Model Equations

Non-dimensionalizing Variables

The following are the non-dimensionalization parameters chosen for this problem:

- (1) The typical rubbery modulus E_R .
- (2) The length of the beam L .
- (3) The glass transition temperature θ_g .
- (4) The non-dimensionalization of the time t_0 , since this is connected with the kinetic response. The SMP has two time scales, the glassy and the rubbery, and in this work the rubbery relaxation time is chosen to make sure any fluid-like (larger time scale) behavior is captured. Thus, we use the relaxation time $t_0 = \frac{\eta_R}{E_R}$ as the non-dimensionalization parameter.

The non-dimensional terms are written as $(\bar{\bullet})$ in Table 4.1. Notice that the strain ϵ is computed from the results of the FEM displacement solutions as $\epsilon = CoordY \frac{d^2 \bar{\Delta}_{1,3}}{dx^2}$. Since we set up the FEM matrices in their non-dimensional form, and obtain non-dimensional displacement solutions $\bar{\Delta}$, the strains computed from these are already normalized with respect to the displacements. So we will write the strain terms as $\bar{\epsilon}$.

Table 4.1: Dimensional quantities and corresponding non-dimensional quantities for the beam theory model

Dim	σ	L	t	θ	α	η_G	$k_G, \mu_{R,G}$
Nondim	$\bar{\sigma} = \frac{\sigma}{E_R}$	$\bar{L} = \frac{L}{L}$	$\bar{t} = \frac{t}{t_0}$	$\bar{\theta} = \frac{\theta}{\theta_g}$	$\bar{\alpha} = \alpha \theta_g$	$\bar{\eta}_G = \frac{\eta_G}{E_R t_0}$	$\bar{\bullet} = \frac{\bullet}{E_R}$

Non-dimensional Equations

Let H be the height and b be the width of the beam. The non-dimensional form of it will be $\bar{H} = \frac{H}{L}$. Thus, the non-dimensional half-height will follow as $\bar{c} = \frac{\bar{H}}{2}$

and non-dimensional width $\bar{b} = \frac{b}{L}$. The non-dimensional element size will be $\bar{h} = \frac{\bar{L}}{NumNodes - 1}$. The non-dimensional displacement solutions will be substituted as $\bar{\Delta} = \frac{\Delta}{L}$. We will non-dimensionalize the four equations in the FEM matrix equations and the two constitutive equations. For the FEM matrix equations:

$$\frac{2(\frac{k_G}{E_R} + \frac{4}{3}\frac{\mu_G}{E_R})\bar{I}}{L\bar{h}^3} \begin{bmatrix} 6 & -3\bar{h} & -6 & -3\bar{h} \\ -3\bar{h} & 2\bar{h}^2 & 3\bar{h} & \bar{h}^2 \\ -6 & 3\bar{h} & -6 & 3\bar{h} \\ -3\bar{h} & \bar{h}^2 & 3\bar{h} & 2\bar{h}^2 \end{bmatrix} \begin{bmatrix} \bar{\Delta}_1 \\ \bar{\Delta}_2 \\ \bar{\Delta}_3 \\ \bar{\Delta}_4 \end{bmatrix} = \begin{bmatrix} 0 \\ -\frac{(M_h^{ve} + M_h^T)}{E_R} \\ 0 \\ \frac{(M_h^{ve} + M_h^T)}{E_R} \end{bmatrix} \quad (4.44)$$

$$\frac{(M_h^{ve} + M_h^T)}{E_R} = (2\bar{b}\frac{\mu_G}{E_R} \int_{-\bar{c}}^{\bar{c}} z\bar{\epsilon}_{11}^{ve} dz + 3\bar{b}\frac{k_G}{E_R}\alpha\theta_g \int_{-\bar{c}}^{\bar{c}} z(\frac{\theta}{\theta_G} - \frac{\theta_h}{\theta_G}) dz) \quad (4.45)$$

$$\frac{(M_h^{ve} + M_h^T)}{E_R} = (2\bar{b}\frac{\mu_G}{E_R} \int_{-\bar{c}}^{\bar{c}} z\bar{\epsilon}_{11}^{ve} dz + 3\bar{b}\frac{k_G}{E_R}\alpha\theta_g \int_{-\bar{c}}^{\bar{c}} z(\frac{\theta}{\theta_G} - \frac{\theta_h}{\theta_G}) dz) \quad (4.46)$$

Thus, the non-dimensional form of the FEM equations are:

$$\frac{2(\bar{k}_G + \frac{4}{3}\bar{\mu}_G)\bar{I}}{L\bar{h}^3} \begin{bmatrix} 6 & -3\bar{h} & -6 & -3\bar{h} \\ -3\bar{h} & 2\bar{h}^2 & 3\bar{h} & \bar{h}^2 \\ -6 & 3\bar{h} & -6 & 3\bar{h} \\ -3\bar{h} & \bar{h}^2 & 3\bar{h} & 2\bar{h}^2 \end{bmatrix} \begin{bmatrix} \bar{\Delta}_1 \\ \bar{\Delta}_2 \\ \bar{\Delta}_3 \\ \bar{\Delta}_4 \end{bmatrix} = \begin{bmatrix} 0 \\ -(\bar{M}_h^{ve} + \bar{M}_h^T) \\ 0 \\ (\bar{M}_h^{ve} + \bar{M}_h^T) \end{bmatrix} \quad (4.47)$$

$$(\bar{M}_h^{ve} + \bar{M}_h^T) = (2\bar{b}\bar{\mu}_G \int_{-\bar{c}}^{\bar{c}} z\bar{\epsilon}_{11}^{ve} dz + 3\bar{b}\bar{k}_G\bar{\alpha} \int_{-\bar{c}}^{\bar{c}} z(\bar{\theta} - \bar{\theta}_h) dz) \quad (4.48)$$

$$(\bar{M}_h^{ve} + \bar{M}_h^T) = (2\bar{b}\bar{\mu}_G \int_{-\bar{c}}^{\bar{c}} z\bar{\epsilon}_{11}^{ve} dz + 3\bar{b}\bar{k}_G\bar{\alpha} \int_{-\bar{c}}^{\bar{c}} z(\bar{\theta} - \bar{\theta}_h) dz) \quad (4.49)$$

For the stress constitutive equation:

$$\frac{\sigma_{11}}{E_R} = (\frac{k_G}{E_R} + \frac{4}{3}\frac{\mu_G}{E_R})\bar{\epsilon}_{11} - 2\frac{\mu_G}{E_R}\bar{\epsilon}_{11}^{ve} - 3\frac{k_G}{E_R}\alpha\theta_g(\frac{\theta}{\theta_G} - \frac{\theta_h}{\theta_G})$$

Thus, $\bar{\sigma}_{11} = (\bar{k}_G + \frac{4}{3}\bar{\mu}_G)\bar{\epsilon}_{11} - 2\bar{\mu}_G\bar{\epsilon}_{11}^{ve} - 3\bar{k}_G\bar{\alpha}(\bar{\theta} - \bar{\theta}_h)$ (4.50)

For the plastic evolution equation:

$$\begin{aligned} \frac{d\bar{\epsilon}_{ve}}{d(t/t_0)} &= \frac{1}{\eta_G/(E_R t_0)} \left(\|\tau/E_R - 2(\mu_R/E_R)\bar{\epsilon}_{ve}\| - \kappa/E_R \right) \frac{\tau/E_R - 2(\mu_R/E_R)\bar{\epsilon}_{ve}}{\|\tau/E_R - 2(\mu_R/E_R)\bar{\epsilon}_{ve}\|} \\ \text{Thus, } \frac{d\bar{\epsilon}_{ve}}{d\bar{t}} &= \frac{1}{\bar{\eta}_G} \left(\|\bar{\tau} - 2\bar{\mu}_R\bar{\epsilon}_{ve}\| - \bar{\kappa} \right) \frac{\bar{\tau} - 2\bar{\mu}_R\bar{\epsilon}_{ve}}{\|\bar{\tau} - 2\bar{\mu}_R\bar{\epsilon}_{ve}\|} \end{aligned} \quad (4.51)$$

Non-dimensional System Equations for the Beam Theory Model

1. FEM displacement and slope equations:

$$\frac{2(\bar{k}_G + \frac{4}{3}\bar{\mu}_G)\bar{I}}{L\bar{h}^3} \begin{bmatrix} 6 & -3\bar{h} & -6 & -3\bar{h} \\ -3\bar{h} & 2\bar{h}^2 & 3\bar{h} & \bar{h}^2 \\ -6 & 3\bar{h} & -6 & 3\bar{h} \\ -3\bar{h} & \bar{h}^2 & 3\bar{h} & 2\bar{h}^2 \end{bmatrix} \begin{bmatrix} \bar{\Delta}_1 \\ \bar{\Delta}_2 \\ \bar{\Delta}_3 \\ \bar{\Delta}_4 \end{bmatrix} = \begin{bmatrix} 0 \\ -(\bar{M}_{ve} + \bar{M}_t) \\ 0 \\ (\bar{M}_{ve} + \bar{M}_t) \end{bmatrix}$$

where $\bar{M}_{ve} = 2\bar{b}\bar{\mu}_G \int_{-\bar{c}}^{\bar{c}} z \bar{\epsilon}_{11}^{ve} dz$
and, $\bar{M}_t = 3\bar{b}\bar{k}_G \bar{\alpha} \int_{-\bar{c}}^{\bar{c}} z (\bar{\theta} - \bar{\theta}_h) dz$

2. Stress constitutive equation:

$$\bar{\sigma}_{11} = (\bar{k}_G + \frac{4}{3}\bar{\mu}_G)\bar{\epsilon}_{11} - 2\bar{\mu}_G\bar{\epsilon}_{11}^{ve} - 3\bar{k}_G\bar{\alpha}(\bar{\theta} - \bar{\theta}_h)$$

3. Plastic strain evolution equation:

$$\dot{\bar{\epsilon}}_{ve} = \frac{1}{\bar{\eta}_G} \left(\|\bar{\tau} - 2\bar{\mu}_R\bar{\epsilon}_{ve}\| - \bar{\kappa} \right) \frac{\bar{\tau} - 2\bar{\mu}_R\bar{\epsilon}_{ve}}{\|\bar{\tau} - 2\bar{\mu}_R\bar{\epsilon}_{ve}\|}$$

4.3 Elastic Predictor - Dissipative Corrector Algorithm

The time stepping algorithm follows the elastic-predictor dissipative-corrector iterative scheme. The key idea is that for the elastic predictor we utilize beam theory whereas for the dissipative corrector, we solve the problem as though it were a two dimensional continuum. The general idea of this scheme is shown in Figure 4.5, where n is the time loop increment and k is the iteration loop increment within each time loop. The time stepping algorithm for the elastic-predictor dissipative-corrector loop consists of computing the elastic displacements using the finite element numerical algorithm, known as the elastic predictor. These are used to iteratively compute the elastic and inelastic strain in the dissipative corrector loop, followed by

a convergence criteria within the time step. The dissipative corrector is executed only if the elastic trial state variables violate dissipative admissibility. After updating the state variables, a displacement convergence criteria is used to keep the current time step solution within a tolerance limit of the previous time step. If the results of the current iteration converge then the iteration is terminated and next time increment is applied. Refer to details of this algorithm in 3.

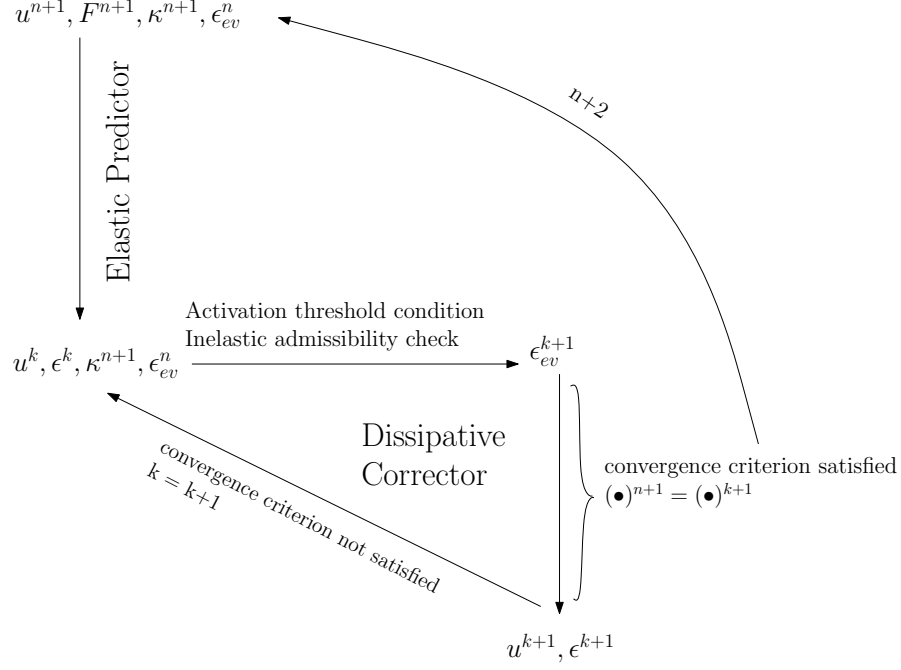


Figure 4.5: For each time step, the elastic predictor loop computes a preliminary estimate of displacement u^{n+1} , using loading condition F^{n+1} of current time step, and inelastic strains ϵ_{ve}^n of previous time step. The iterative dissipative corrector then computes consequent elastic strains ϵ^k based on the current iteration displacement solution u^k ($= u^{n+1}$ for the first iteration of each time step). Elastic strain ϵ^k and the previous time step's inelastic strain ϵ_{ve}^n is used to compute the updated inelastic strain ϵ_{ve}^{k+1} . This is used to update the iteration displacement u^{k+1} , and compared with the previous iteration displacement u^k to meet a convergence criterion. After convergence is satisfied, the displacement, strain and inelastic strain for the current time step are updated using the converged solution. Refer to the Algorithm 3 for details.

Algorithm 3 Elastic predictor - dissipative corrector loop

```

1: Input: Geometry, Material, Control parameters
2: Initialize Variables for  $n = 1$ 
3: for  $n = 2 : \Delta t : \text{MaxTimeSteps}$  do
4:   Update  $F^n, \theta_n, \kappa_n$ , Constraint matrix
5:    $\varepsilon_{ve_n}^{trial} = \varepsilon_{ve_{n-1}}$  ▷ Initial guess for current time step
6:   function  $[\Delta_n] = \text{FEM DRIVER}(F^n, \varepsilon_{ve_n}^{trial})$  ▷ Predicted displacement
7:   end function
8:    $\varepsilon^{init} = f(\Delta_n)$  ▷ Predicted strain
9:   set iteration count  $k = 2$  ▷ Reset corrector iteration count
10:  while  $k < \text{MaxIterationCount}$  do ▷ Corrector loop begins
11:    function  $[\varepsilon_{ve}^k] = \text{INELASTICITY DRIVER}(\varepsilon^{init}, \varepsilon_{ve_n}^{trial}, \theta_n, \kappa_n)$ 
12:     $\tau_{ij}^{trial} = 2\bar{\mu}_G(\varepsilon_{ij}^{init} - \varepsilon_{ve_{ij}}^{trial} - \bar{\alpha}_n(\bar{\theta}_n - \bar{\theta}_h)\text{I}_{ij})$  ▷ Trial deviatoric stress
13:     $\Phi_{ij}^{trial} = \tau_{ij}^{trial} - 2\bar{\mu}_R\varepsilon_{ve_{ij}}^{trial}$  ▷ Trial flow potential
14:    if  $\Phi_{ij}^{trial} \leq \bar{\kappa}_n$  then ▷ Activation threshold not reached
15:      Set  $\varepsilon_{ve_{ij}}^k = \varepsilon_{ve_{ij}}^{trial}$ 
16:    else ▷ Activation threshold reached
17:       $\varepsilon_{ve_{ij}}^k = \varepsilon_{ve_{ij}}^{trial} + \frac{\Delta t}{\bar{\eta}}(\Phi_{ij}^{trial} - \bar{\kappa}_n)\frac{\Phi_{ij}^{trial}}{\|\Phi_{ij}^{trial}\|}$  ▷ Update inelastic strain
18:    end if
19:     $\sigma_{ij}^k = \left(\bar{k}_G + \frac{4}{3}\mu_G\right)\varepsilon_{ij}^{init} - 2\bar{\mu}_G\varepsilon_{ve_{ij}}^k - 3\bar{k}_G\bar{\alpha}_n(\bar{\theta}_n - \bar{\theta}_h)\text{I}_{ij}$  ▷ Update stress
20:    end function
21:    function  $[\Delta^k] = \text{FEM DRIVER}(F^n, \varepsilon_{ve}^k)$  ▷ Corrected displacement
22:    end function
23:     $\varepsilon^k = f(\Delta^k)$ ; ▷ Corrected strain
24:    if L2 norm  $\|\Delta^k - \Delta^{k-1}\|_0 > TOL$  then ▷ Tolerance check not satisfied
25:       $\varepsilon^{init} = \varepsilon^k$ ; ▷ Initial guess for next iteration
26:       $k \leftarrow k + 1$ ; ▷ Go to next iteration (line 10)
27:    else L2 norm  $\|\Delta^k - \Delta^{k-1}\|_0 \leq TOL$  ▷ Tolerance check satisfied
28:      Set  $\varepsilon_{ve_n} = \varepsilon_{ve}^k$ ; ▷ Update solution for current time step
29:      Set  $\Delta_n = \Delta^k$ ; ▷ Update solution for current time step
30:      Break loop; ▷ Go to next time step (line 3)
31:    end if
32:  end while ▷ Corrector loop ends
33: end for

```

4.4 Analysis of the Implementation

4.4.1 Elastic, Plastic and Thermoplastic Material Cases

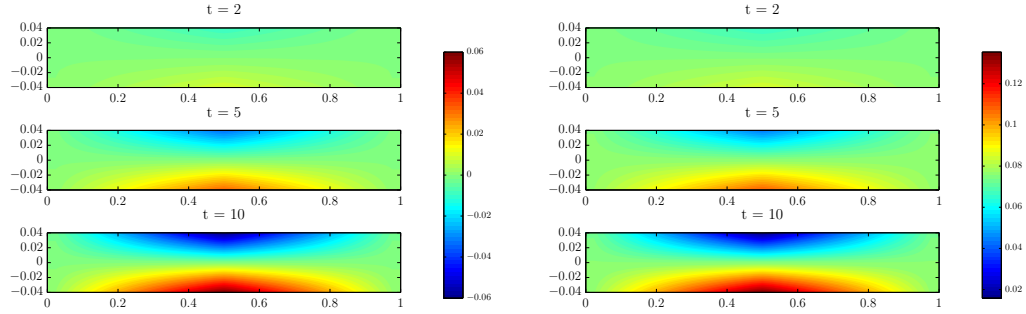
Table 4.2: Control parameters for the three cases: elastic, plastic and thermoplastic

	Ideal Elastic	FEM Elastic	FEM Plastic	FEM Thermoplastic
Force	$f(t)$	$f(t)$	$f(t)$	$f(t)$
θ_{max}	1	1	1	1
θ_{init}	1	1	1	0.04
$\theta(t)$	θ_{init}	θ_{init}	θ_{init}	$0.1\theta_{init}t$
$\kappa(t)$	NA	1000	0.02	$0.01(4 - \theta(t))$

In this section, we will implement the algorithm developed in Section 4.3, for a three-point bending test and examine the material behavior for three cases of activation stress and thermal loading conditions: elastic, plastic and thermoplastic beam. The beam will be subjected to the same linear time incremental load in all three cases and the initial temperature is kept constant at the maximum temperature for elastic and plastic cases. Only the activation stress is changed for the elastic and plastic cases, where for the plastic case it is a function of temperature. For the thermoplastic case, the initial temperature is started at a lower temperature than the maximum, thus creating a thermal difference. The activation stress is a function of temperature similar to the plastic case. These loading conditions for the three cases can be compared in the Table 4.2. The resulting displacements are tabulated in Table 4.3, and the plastic strain across cross-section along length of beam for the plastic and thermoplastic cases are plotted in the graphs of Figures 4.6.

Table 4.3: Displacements along the beam nodes for the three cases: elastic, plastic and thermoplastic at the final time step

Ideal Elastic	FEM Elastic	FEM Plastic	FEM Thermoplastic
0.000000000	0.000000000	0.000000000	0.000000000
-0.041862558	-0.0418625584	-0.043416971	-0.043559292
-0.074064526	-0.0740645263	-0.076669513	-0.076896843
-0.086945314	-0.0869453135	-0.089789395	-0.090044747
-0.074064526	-0.0740645263	-0.076341620	-0.076567984
-0.041862558	-0.0418625584	-0.043079984	-0.043220132
0.000000000	0.000000000	0.000000000	0.000000000



(a) Plastic: Inelastic strains increase with increasing load. Inelastic strains evolve from the support points towards the point of loading along the length of beam. They are highest at the outer fibres, and zero at the centreline of the beam, as seen from values in the colorbar shown alongside the figure

(b) Thermoplastic: The inelastic strain evolution in the beam show the same trend as for the plastic case, except that the inelastic strain is no longer zero at the centreline. Inelastic strains have a finite value at the centreline depending on how the inelastic zone evolves with temperature, as seen from values in the colorbar shown alongside the figure

Figure 4.6: Inelastic strains evolution in the beam for chosen time steps, for the plastic and thermoplastic cases where the stresses developed in the beam overcome the activation stress κ . Note the comments made for each case under the graphs.

4.4.2 Time Step Convergence

Since the SMP model is viscoplastic, we expect the time step Δt to affect the results significantly for the numerical implementation of the elastic plastic loop. Δt shows up directly in the plastic strain equation. Also the predictor corrector loop proceeds with plastic strain solution of the previous time step as an initial guess for the current time step. If the time steps are large, the plastic strain solution will get affected, and consequently this as the initial guess will affect the displacement solutions as well. Therefore, it is important to select a time step that gives consistent solutions. This section studies the convergence of the displacement solutions for various time steps.

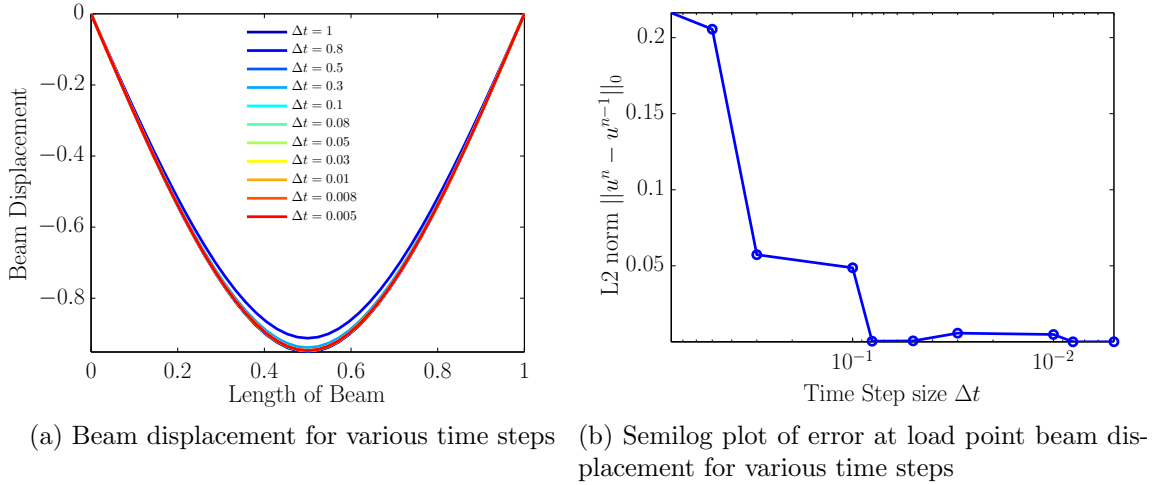


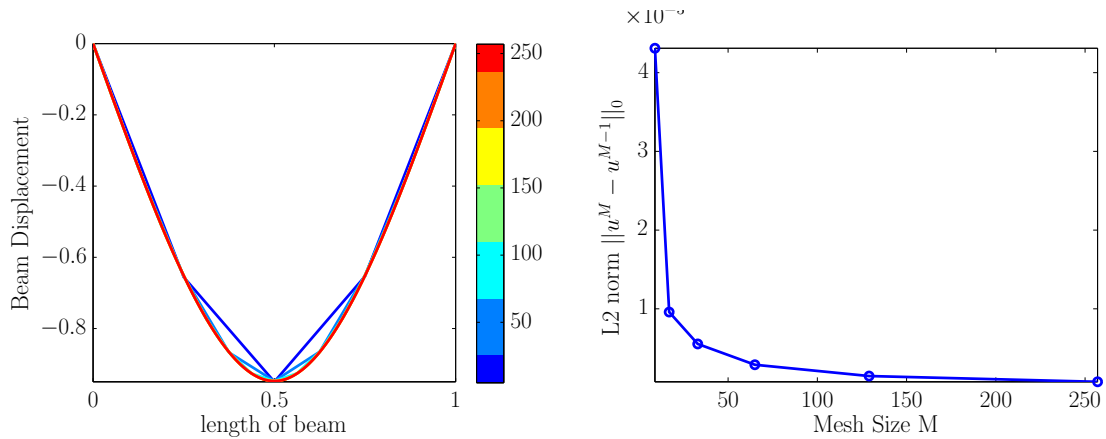
Figure 4.7: Displacement of beam for various time steps

The displacement solutions are studied for the same loading and thermal conditions of a thermoelastic beam, for different values of non-dimensional time step sizes. The convergence norm is selected as the L_2 norm of the difference between the value of the solution of the current time step size Δt_n to that of the previous time step size Δt_{n-1} as $\|e^{\Delta t_n}\|_0 = \|u^n - u^{n-1}\|_0 = \left(\int_a^b |u^n - u^{n-1}|^2 dx \right)^{1/2}$ [60]. The error norm reduces as the time step decreases, as can be seen in the displacement of the beam in Figure 4.7. The displacement converges for smaller time steps. We will restrict the desired solution convergence to an order of magnitude of 10^{-3} and select a suitable

value of time step size for this convergence factor. Since the convergence tolerance is met for solutions of time step size $\Delta t = 0.08$ and smaller, we select the time step size $\Delta t = 0.05$ considering allowable computation cost.

4.4.3 Mesh Convergence

The finite element formulation involves differential approximations of the displacements along the beam for the strains. Also, the moment generated due to plastic strain for a single node along the cross section is determined from the plastic strain distributions across the cross section. The mesh density of the beam will therefore affect these results. In this section, a uniform nested-node convergence study is carried out, i.e the mesh refinement for each iteration includes all the nodes of the previous iteration. The convergence norm is selected as the L2 norm of the difference between the value of the solution of the current mesh size M to that of the previous mesh size $M - 1$ as $\|e^M\|_0 = \|u^M - u^{M-1}\|_0 = \left(\int_a^b |u^M - u^{M-1}|^2 dx \right)^{1/2}$ [60]. This error norm for the various mesh sizes has a converging trend as can be seen from Figure 4.8b. We select a convergence criterion of 10^{-3} for the error norm. This convergence criterion gives the optimum mesh density as 17×17 or finer refinements. Considering allowable computation costs, we will select the mesh density as 65×65 .



(a) Beam displacement for various mesh refinements, as shown in color bar (b) Convergence of load point beam displacement for various mesh refinements, as shown in color bar

Figure 4.8: Displacement of beam for various mesh refinements, as shown in color bar

4.5 SMP Beam Theory Model undergoing a Thermomechanical Cycle

4.5.1 Experimental Parameters for Thermomechanical Flexural Cycle

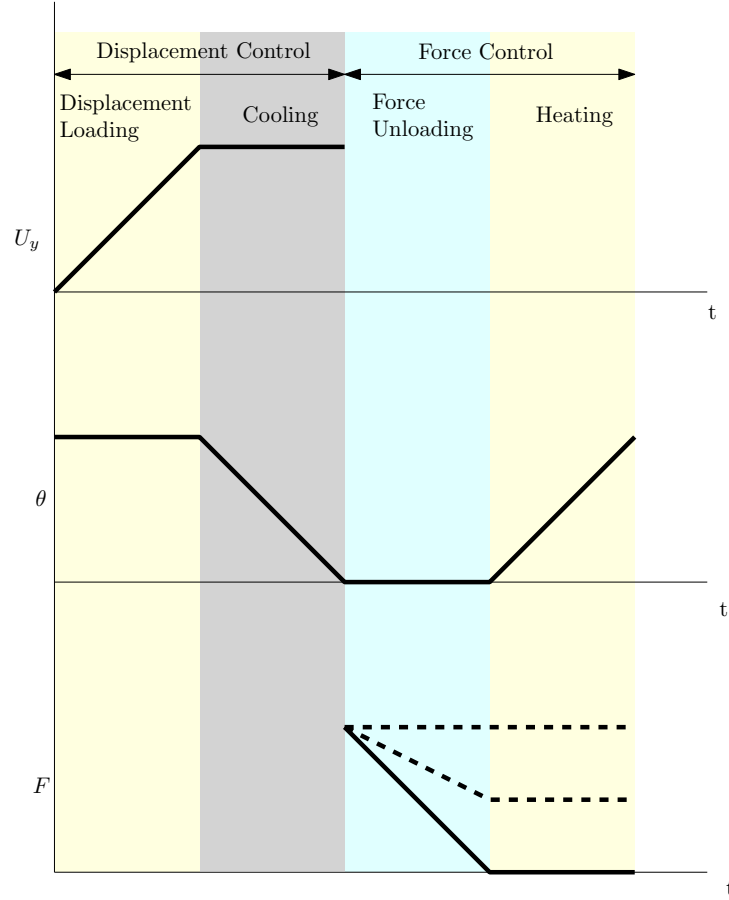


Figure 4.9: Control variables of the thermomechanical cycle: The thermomechanical cycle has three control variables: displacement U_y , temperature θ and force F , that vary with time t . The cycle can be split into displacement control and force control regimes, with subdivisions of different thermal load conditions. The resulting four ranges of the thermomechanical cycle are: (1) Displacement loading at high temperature. (2) Holding displacement constant while cooling (3) Force unloading at low temperature (4) Heating under no load condition

Control Parameters: Mechanical

- Initial condition: $[\kappa = 0, \theta_{max}, \alpha_R, \epsilon_{ve} = 0]$
- Displacement Loading: Deform upto 30% from $t = 0$ to $t = 3$
- Constant Displacement: Hold displacement constant from time step 3 to 6
- Force Unloading: Unload from time step 6 to 9
- Constant Force: Hold at constant force from time step 9 to 12

Control Parameters: Thermal

- Constant high temperature 391K from $t = 0$ to $t = 3$
- Cooling from 391K to 293K, from time step 3 to 6
- Constant low temperature 293K from time step 6 to 9
- Heating from 293K to 391K, from time step 9 to 12

Material Parameters

- Gauge dimensions: Length = 15mm; Height = 1mm; Width = 3mm;
- Glass transition temperature T_g : 90 °C
- $E_G = 886$ MPa at 26 °C
- $E_R = 8.51$ MPa at 118 °C
- $\eta_G = 116000$ MPas, $\eta_R = 2030$ MPas, $\alpha_G = 22.6 \times 10^{-5}$, $\alpha_R = 18.6 \times 10^{-5}$

Table 4.4: Control parameters for the strain recovery thermodynamic cycle

	Range 1	Range 2	Range 3	Range 4
Force(t)	NA	NA	$-g(t)$	constant
Displacement(t)	$d(t)$	constant	NA	NA
$\theta(t)$	θ_{max}	$\hat{\theta}_{cool}(t)$	θ_{min}	$\hat{\theta}_{heat}(t)$
$\kappa(t)$	κ_{max}	$\hat{\kappa}_{cool}(t)$	κ_{min}	$\hat{\kappa}_{heat}(t)$

The strain recovery thermomechanical cycle has three control variables (refer to Table 4.4 and Figure 4.9): displacement U_y , temperature θ and force F , that vary with time t . The cycle can be split into displacement control and force control regimes, with subdivisions of different thermal load conditions. The resulting four ranges of the thermomechanical cycle are: (1) Displacement loading at high temperature. (2) Holding displacement constant while cooling (3) Force unloading at low temperature (4) Heating under constant load condition.

The stress recovery thermomechanical cycle has three control variables (refer to Table

Table 4.5: Control parameters for the stress recovery thermodynamic cycle

	Range 1	Range 2	Range 3	Range 4
Force(t)	NA	NA	$-g(t)$	NA
Displacement(t)	$d(t)$	constant	NA	constant
$\theta(t)$	θ_{max}	$\hat{\theta}_{cool}(t)$	θ_{min}	$\hat{\theta}_{heat}(t)$
$\kappa(t)$	κ_{max}	$\hat{\kappa}_{cool}(t)$	κ_{min}	$\hat{\kappa}_{heat}(t)$

4.5): displacement U_y , temperature θ and force F , that vary with time t . The cycle can be split into displacement control and force control regimes, with subdivisions of different thermal load conditions. The resulting four ranges of the thermomechanical cycle are: (1) Displacement loading at high temperature. (2) Holding displacement constant while cooling (3) Force unloading at low temperature (4) Heating under constant displacement condition.

Form of the activation stress rate function

Since we are using the activation stress rate as specified in the rate form development in Chapter 3, for the beam theory, we will have to specify the activation stress for each time step. The activation stress rate form specified in Eq 3.53 in Chapter 3.

Note that for the beam bending problem, the activation stress function coefficients y_1, y_2, y_3, y_4, y_5 will be different than those specified in Chapter 3 for the uniaxial tensile extension problem. The evolution of activation stress during bending will be different than that during uniaxial extension, as the material undergoes extension in normal directions, as well shear. Although the current theory does not address these additional displacement directions, the activation stress value is ad-

justed while implementing the thermomechanical cycle so as to observe similar trends as experimental results in the work of Liu, Gall et al. [17] and Tobushi et al. [20].

For the time stepping algorithm in the beam theory implementation we have to specify the form of temperature θ_n and activation stress κ_n for the n^{th} time step.

$$\dot{\kappa} = \left(\frac{d\kappa}{d\theta} \right) \dot{\theta}$$

Therefore, $\left(\frac{\kappa_n - \kappa_{n-1}}{\Delta t} \right) = \left(\frac{d\kappa}{d\theta} \right)_n \left(\frac{\theta_n - \theta_{n-1}}{\Delta t} \right)$ (4.52)

$$\kappa_n = \kappa_{n-1} + \left(\frac{d\kappa}{d\theta} \right)_n (\theta_n - \theta_{n-1})$$
 (4.53)

The temperature specification θ_n for the cooling and heating process in the thermomechanical cycle.

$$\theta_n = \theta_{init} + (t_n - t_{init})\dot{\theta}$$
 (4.54)

where t_{init} is the starting time of the process in the thermomechanical cycle, θ_{init} and $\dot{\theta}$ are the initial temperature and cooling/heating rate depending on the process.

4.5.2 Thermomechanical Three-point Bending: Strain Recovery

In this section, the results for full unload strain recovery thermomechanical cycle are presented in Figure 4.10 which shows the control variables of the thermomechanical cycle from the code, Figure 4.11 which shows the displacement and reaction forces of the load point of beam undergoing the thermomechanical cycle, Figure 4.12 which shows the configuration of the beam through the four ranges of the thermomechanical cycle, and Figure 4.13 which shows the inelastic strain evolution in the beam through the four ranges of the strain recovery thermomechanical cycle.

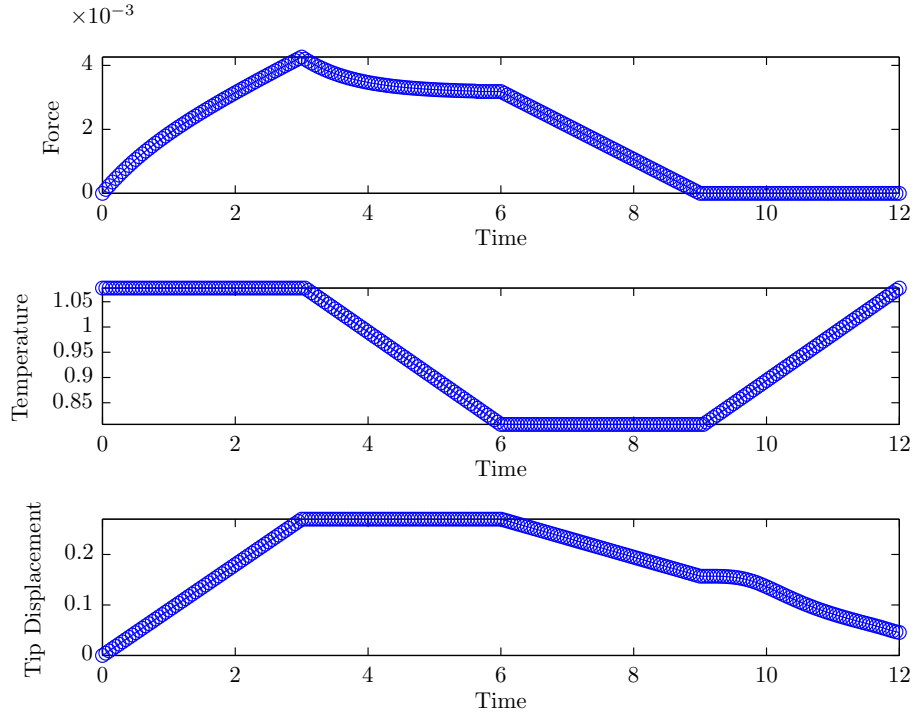


Figure 4.10: Control variables of the thermomechanical cycle from the code: The thermomechanical cycle has three control variables: displacement U_y , temperature θ and force F , that vary with time t . In the displacement control regime, the force F rises non-linearly, depending on the viscosity of the material, and then falls during cooling. In the force control regime, the displacement U_y shows a spring back behavior during unloading, and displacement recovery during heating.

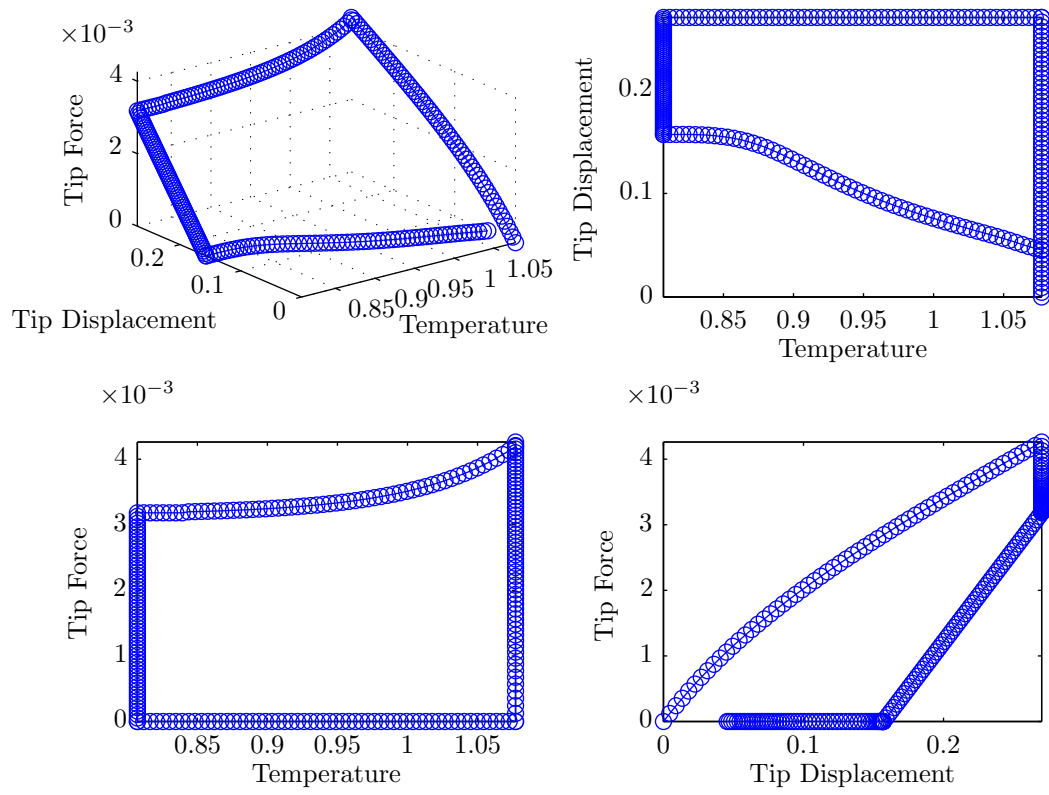


Figure 4.11: Displacement and reaction forces of the load point of beam undergoing the thermomechanical cycle.

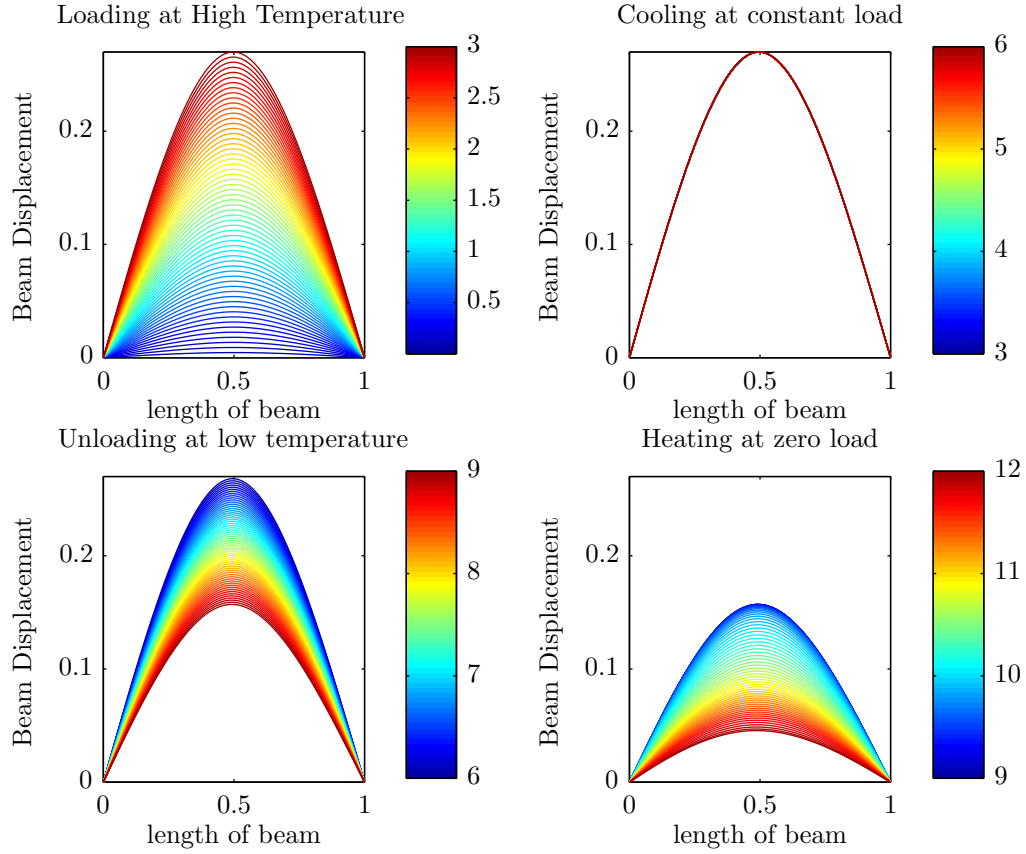


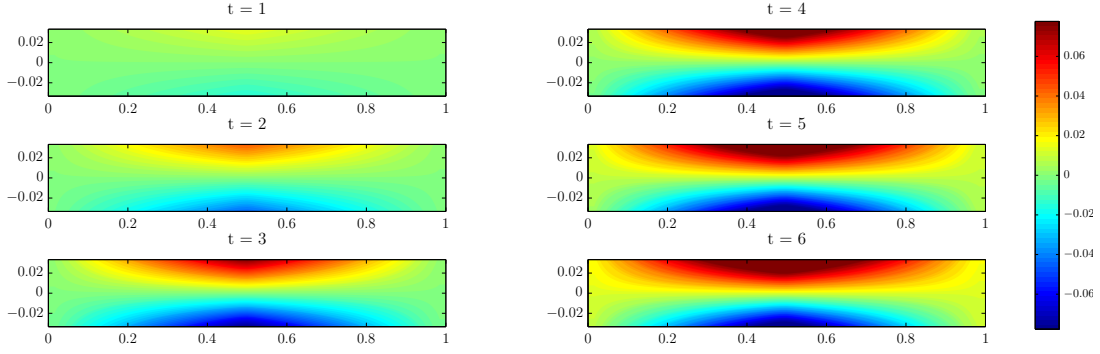
Figure 4.12: Configuration of the beam through the four ranges of the thermomechanical cycle. The time progression is shown in the colorbar beside each figure. The four figures correspond to four different ranges of the thermomechanical cycle:

Range 1 (top-left): Deforming at θ_h , force is increased with each time step and results in the deformed configuration of the beam.

Range 2 (top-right): Cooling to below θ_g at constant deformation.

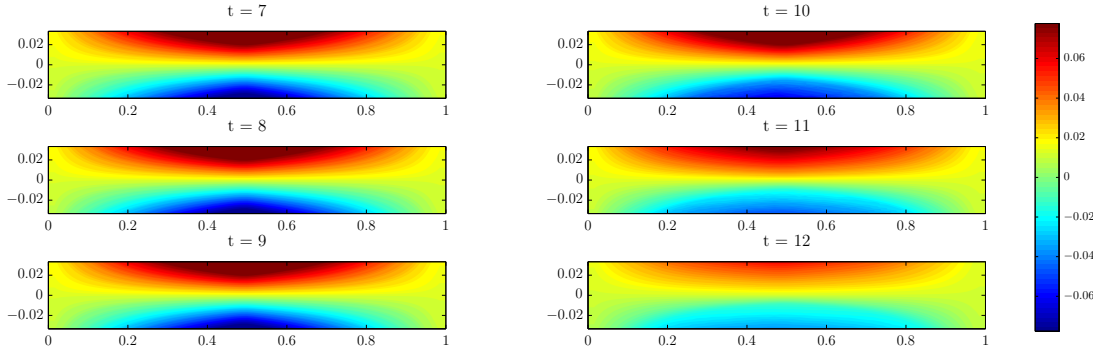
Range 3 (bottom-left): Unloading at θ_l . Force is reduced to zero with each time step, and the beam responds with some amount of spring back.

Range 4 (bottom-right): Heating to above θ_g at no load. The beam shows shape recovery during heating and recovers as time (heating) progresses.



(a) Range 1: Deforming at θ_h . Stresses developed in the beam overcome the high temperature activation stress. Inelastic strain evolves with mechanical load, zero at centerline

(b) Range 2: Cooling to below θ_g at constant deformation. Activation stress of the material rises as the material is cooled. Inelastic strain increases with reducing temperature, finite value at centerline



(c) Range 3: Unloading at θ_l . Material is at maximum activation stress value at low temperature. Inelastic strain is locked (constant) even as material is unloaded.

(d) Range 4: Heating to above θ_g at no load. Activation stress of the material reduces while heating, and stresses in the beam overcome the activation stress to unlock the inelastic strain. Inelastic strain reduces with increasing temperature

Figure 4.13: Inelastic strain evolution in the beam through the four ranges of the thermomechanical cycle. Note the comments for each range below the sub-figures

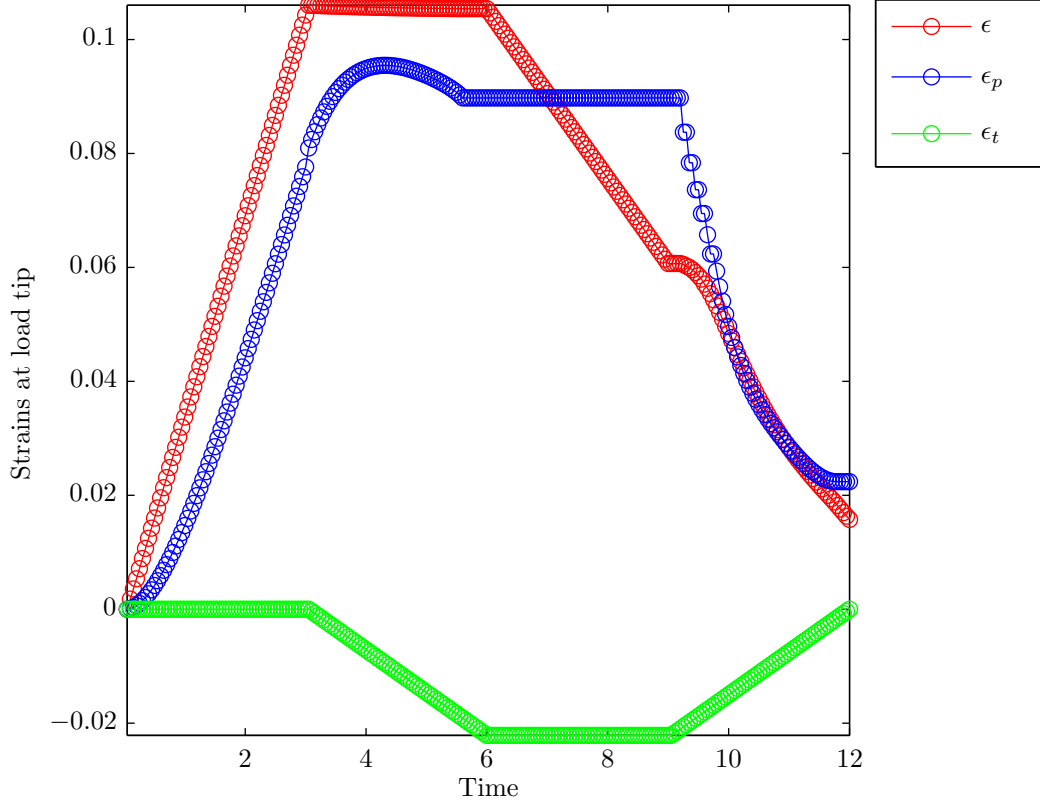


Figure 4.14: Total strain, inelastic strain and thermal strain at center of the beam through the four ranges of the thermomechanical cycle.

Range 1: ($t = 0$ to 3) Deformation at high temperature: The elastic and inelastic strain rise with deformation at constant thermal strain.

Range 2: ($t = 3$ to 6) Cooling at constant deformation: Although inelastic strains increase, they are countered with the thermal strain that is contracting. No elastic strain exists as the material is held at constant displacement, giving almost constant total strain.

Range 3: ($t = 6$ to 9) Unloading at low temperature: Inelastic strain is locked in at a constant value, but total strain reduces due to elastic spring back.

Range 4: ($t = 9$ to 12) Heating at constant load: The inelastic strain is unlocked and reduces with temperature, thermal strains increase with temperature, and their competition results in the total strain recovery.

Figure 4.15 shows the response of the center of the beam while undergoing thermomechanical strain recovery for three different unloading cases.

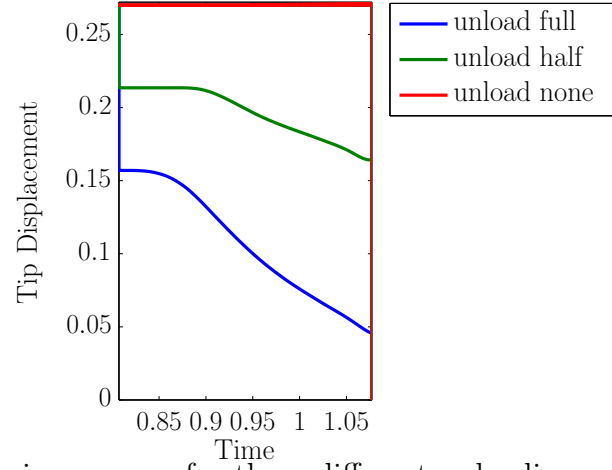


Figure 4.15: Strain recovery for three different unloading cases: 1. Full unload, 2. Half unload and 3. No unload

Figure 4.16 shows response of the center of the beam during cyclic thermomechanical loading.

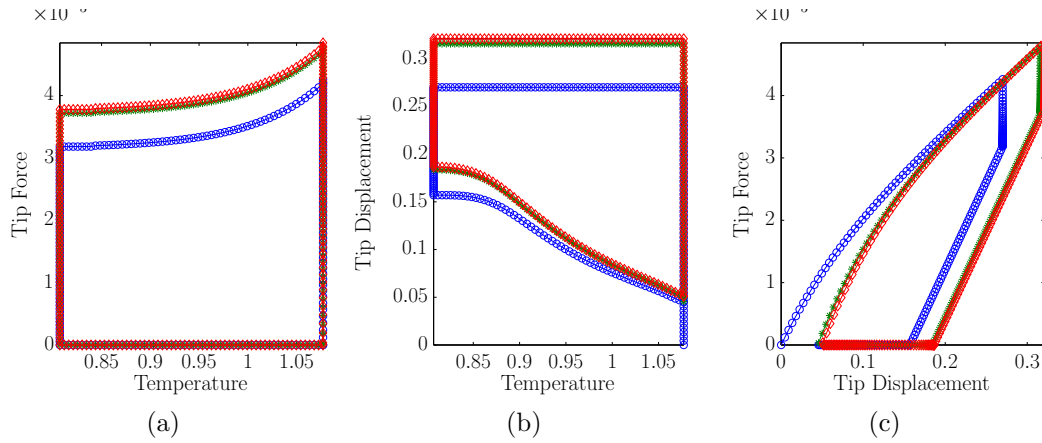


Figure 4.16: Results for three cycles of thermomechanical loading. Cycle 1: blue, Cycle 2: green, Cycle 3: red

4.5.3 Thermomechanical Three-point Bending: Stress recovery

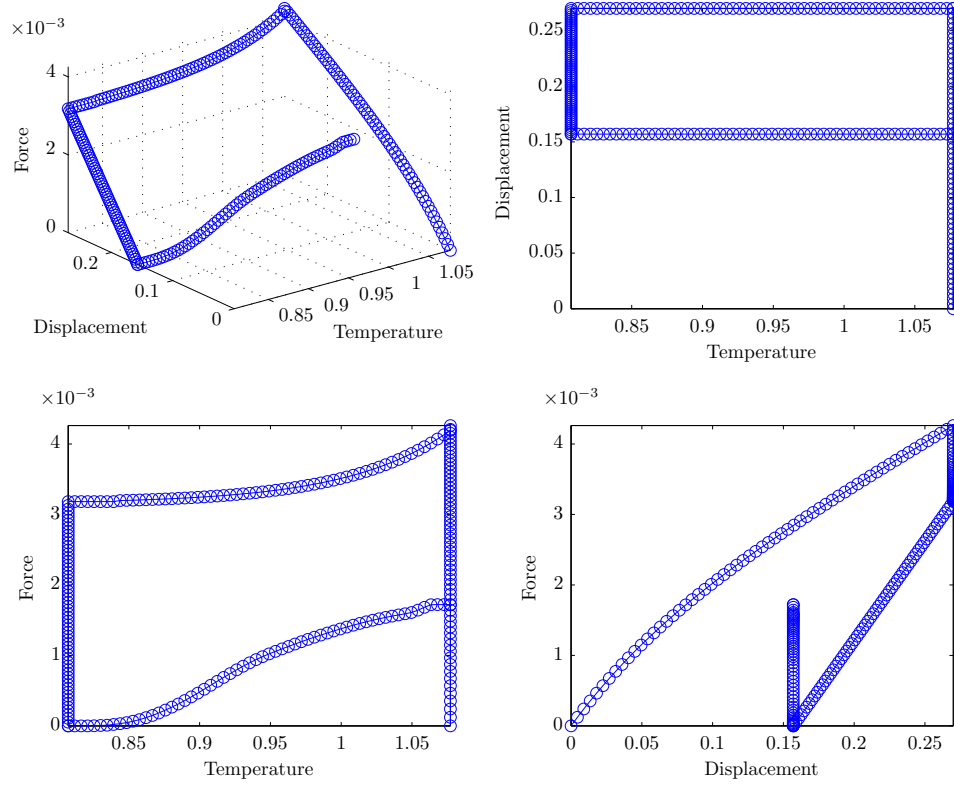
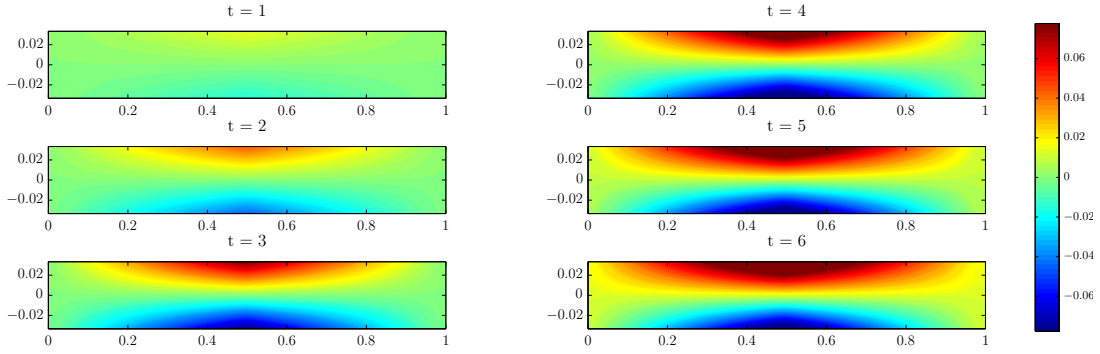


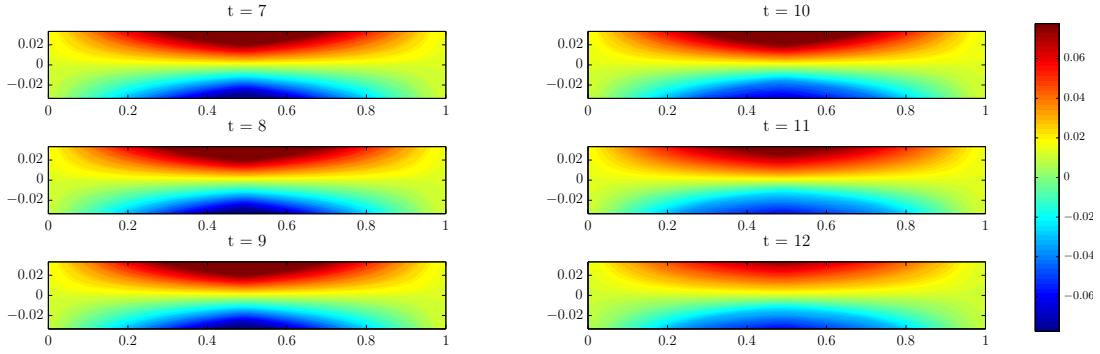
Figure 4.17: Displacement and reaction forces at the center of the beam undergoing the thermomechanical cycle

We simulate the thermomechanical stress recovery cycle for a three-point bending experiment, where the control parameters for the four ranges are as presented in Table 4.5. The response of the beam theory model can be seen in Figure 4.17 for the load point along the length of the beam. In range 1, the force F rises non-linearly with deformation, depending on the viscosity of the material, and then falls during cooling in range 2. In range 3, the displacement U_y shows a spring back behavior during unloading. The behavior in range 1, 2, and 3 is similar to that in the strain recovery cycle. In the final range 4, the displacement is held constant, and



(a) Range 1: Deforming at θ_h . Stresses developed in the beam overcome the high temperature activation stress. Inelastic strain evolves with mechanical load, zero at centerline

(b) Range 2: Cooling to below θ_g at constant deformation. Activation stress of the material rises as the material is cooled. Inelastic strain increases with reducing temperature, finite value at centerline



(c) Range 3: Unloading at θ_l . Material is at maximum activation stress value at low temperature. Inelastic strain is locked (constant) even as material is unloaded.

(d) Range 4: Heating to above θ_g at constant displacement. Activation stress of the material reduces while heating, and stresses in the beam overcome the activation stress to unlock the inelastic strain. Inelastic strain evolves with the combination of stress development under fixed displacement while heating

Figure 4.18: Inelastic strain evolution in the beam through the four ranges of the thermomechanical cycle. Note the comments for each range below the sub-figures

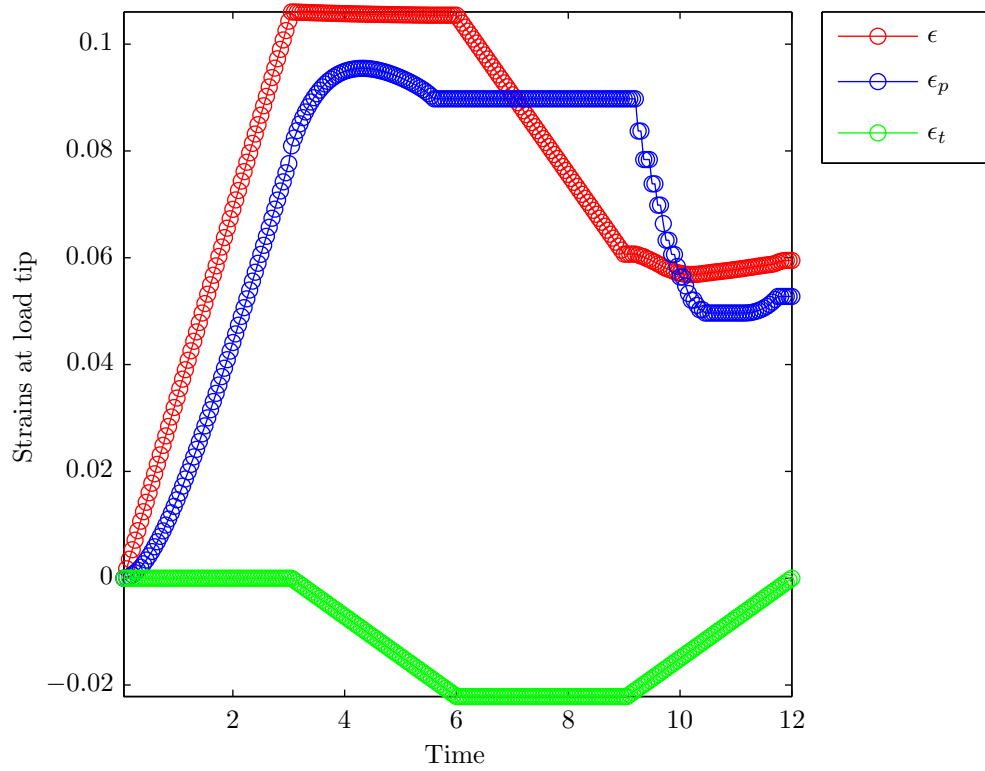


Figure 4.19: Total strain, inelastic strain and thermal strain at the center of the beam through the four ranges of the thermomechanical cycle

the material shows stress recovery during heating. The response can be explained by looking at the inelastic strain response for the four ranges of the thermomechanical cycle, as shown in Figure 4.18. The “locked in” inelastic strain behaves similar to that observed in the strain recovery cycle. On reheating, the inelastic strain is unlocked, and since the displacement is restricted, the competition between the elastic, inelastic and thermal strains as can be seen in Figure 4.19 results in the rise of stress during heating. This rise in stress during heating has been reported by Liu et al. [17] in their stress recovery thermomechanical experiments, although the trend observed by them is mostly similar to what we observe here, it involves a dip at the end of the heating cycle.

4.6 Summary

In this chapter, the Euler Bernoulli beam theory for the shape memory polymer model was developed and implemented in a finite element setup. The implementation constituted of an elastic-predictor plastic-corrector scheme, and was analysed for elastic, plastic and thermoplastic cases. The behavior of the FEM model for these cases complied with the validation for the ideal elastic case, as well as showed the different kinds of evolution of plastic strain for the plastic and thermoplastic cases. Uniformly nested mesh convergence studies showed that results converge for increasing mesh densities, but the computation time magnifies over six times after a certain limit of mesh density $N_x = N_y = 65$. Also, since this is a viscoplastic model, the size of the time step affects the plastic and thermoplastic results significantly. The time step convergence study, was therefore imperative, and showed that beyond a certain small time step $\Delta t = 0.05$ the convergence is stagnant. After testing the codes for these cases, finally we implement the thermomechanical cycle for this shape memory polymer model. This experiment has four different combinations of mechanical and thermal loading conditions, and the model behavior is similar to experiments in the literature for each of the control parameters. Since a number of important material properties such as viscosities and coefficients of thermal expansion are missing in the experimental data reported, we only limit the current study to a successful qualitative validation. We also analyze the internal variables of the model such as the plastic strain and the total strain during this cycle and provide an explanation for this behavior.

5. FINITE STRAIN MODEL USING QR DECOMPOSITION

5.1 Introduction

SMPs are capable of exhibiting large and complicated deformations. Until now we have worked with the linearized strain assumption and observed the SMP behavior only for small strains. However, SMP is primarily characterized by its non-linear behavior at large strains. Many real-world applications of SMPs exploit this ability of SMPs. Therefore it becomes important to develop a finite deformation model for SMPs and study its non-linear behavior. This chapter will focus on the development of a thermodynamically consistent finite deformation continuum model to simulate the thermomechanical response of SMPs. The SMP is modeled as a isotropic thermoviscoelastic material where thermal changes govern the evolution of the activation stress of the material, similar to a “thermal Bauschinger effect”. The response of the SMP in a thermomechanical cycle is modelled as a combination of a rubbery (viscoelastic) and a glassy (elastic) network in series. Using these assumptions, we propose a specific form for the Helmholtz potential and the rate of dissipation. In the approach presented here, the deformation gradient is multiplicatively decomposed into an instantaneous elastic part and a viscoelastic part. For the development of the finite strain model, we follow the general technique of upper triangular or **QR** decomposition [61] for deriving the constitutive equations of the SMP model. This technique involves the decomposition of a matrix into an orthogonal matrix **Q** and an upper triangular matrix **R**. We use this technique for its simpler and faster implementation benefits. The response of the model is studied for shear deformation subject to glass transition and low temperatures. We compare these results with shear experimental observations from the literature. We then explore the behaviour of the model under shear deformation at different initial temperatures, and gain a deeper insight of how the model works. This experiment is extended to cyclic shear deformation, and the results are in general agreement with those found in the literature. We also study the effect of deformation rates on the model response. Finally, we study the response of the model for a shear deformation thermomechanical cycle and compare it with the experimental findings in the literature.

5.2 Kinematics

Consider a body \mathcal{B} which at time t occupies a configuration $\kappa_t(\mathcal{B})$. The position of any particle X in κ_t is given by \mathbf{x} . The motion of the body, measure from some fixed configuration κ_r , wherein the position vector is given by \mathbf{X} , and the deformation gradient are given by the following two equations respectively.

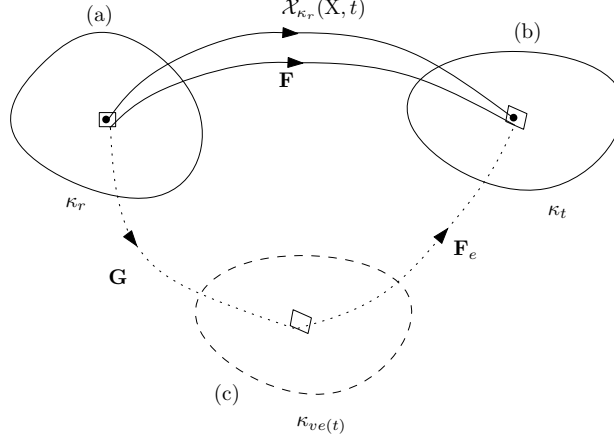


Figure 5.1: Schematic diagram to illustrate the current natural configuration of the material. Figure (a) depicts the reference configuration κ_r of the body. The motion $\mathcal{X}_{\kappa_r}(\mathbf{X}, t)$ takes the material points to their respective positions in the current configurations κ_t shown in (b). Simultaneously the material fibers are convected by the deformation gradient \mathbf{F} . The instantaneous relaxation process takes the material fibers to their natural state $\kappa_{ve(t)}$ as indicated in (c). \mathbf{F}_e^{-1} affects only the line elements and the resulting configuration is shown in dotted lines. Finally the tensor \mathbf{G} maps the reference line elements to those in $\kappa_{ve(t)}$.

$$\mathbf{x} = \mathcal{X}_{\kappa_r}(\mathbf{X}, t) \quad (5.1)$$

$$\mathbf{F} := \frac{\partial \mathcal{X}_{\kappa_r}}{\partial \mathbf{X}} \quad (5.2)$$

We consider an evolving natural configuration $\kappa_{ve(t)}$ that reflects the evolving microstructure due to network breaking and reformation as shown in Fig. (5.1). For homogeneous deformations, the gradient of mapping from κ_r to $\kappa_{ve(t)}$ is denoted by \mathbf{G} . We shall define the gradient of the mapping \mathbf{F}_e from $\kappa_{ve(t)}$ to κ_t , so that by chain

rule

$$\mathbf{F}_e = \mathbf{F}\mathbf{G}^{-1} \quad (5.3)$$

This is also known as the multiplicative decomposition of the deformation gradient into elastic and plastic components, introduced by Lee for finite deformations in 1969 [62]. This has been widely used for non-linear elasto-plastic analysis of polymers, primarily to avoid computational difficulties.

On differentiation, we get two terms, the first representing the rate of change of \mathbf{F}_e when the microstructure is fixed i.e. due to non-dissipative processes, and the second term is due to the changes in the underlying microstructure when the current configuration of the material is frozen i.e. a plastic change.

$$\dot{\mathbf{F}}_e = \mathbf{L}\mathbf{F}_e - \mathbf{F}_e\mathbf{L}_{ve} \quad (5.4)$$

where, $\mathbf{L} := \dot{\mathbf{F}}\mathbf{F}^{-1}$, $\mathbf{L}_{ve} := \dot{\mathbf{G}}\mathbf{G}^{-1}$, and $\dot{\mathbf{G}}^{-1} = -\mathbf{G}^{-1}\dot{\mathbf{G}}\mathbf{G}^{-1}$.

We can now introduce the elastic squared stretch tensor and the plastic squared stretch tensor

$$\mathbf{B}_e := \mathbf{F}_e\mathbf{F}_e^t \quad (5.5)$$

$$\mathbf{B}_{ve} := \mathbf{G}\mathbf{G}^t \quad (5.6)$$

In this development, we will use the following strain measures:

$\mathbf{e}_e := \frac{1}{2}\ln\mathbf{B}_e$, the logarithmic elastic squared right stretch tensor,

$\mathbf{B}_{ve} := \mathbf{G}\mathbf{G}^t$, the plastic squared stretch tensor,

$\mathbf{D}_{ve} := \frac{1}{2}(\mathbf{L}_{ve} + \mathbf{L}_{ve}^T)$, the plastic flow rate.

Most of the kinematics of the small strain model and the finite strain model remains the same. Refer to Table 5.1 for a comparison between their kinematic variables and form of Helmholtz potential and dissipation function. In the small strain model, we start with the state variables as the linearized strains where $\boldsymbol{\epsilon} = \frac{1}{2}(\nabla\mathbf{u} + \nabla\mathbf{u}^T) = \frac{1}{2}((\mathbf{F} - \mathbf{I}) + (\mathbf{F} - \mathbf{I})^T)$. We are thus ignoring the higher order deformation terms $\nabla\mathbf{u}\nabla\mathbf{u}^T$. In finite strain, the aim is to capture the non-linear behaviour. Therefore we start with state variables as the deformation gradients $\mathbf{F}, \mathbf{F}_e, \mathbf{G}$ directly, so that no higher order terms are lost.

The elastic strain measure used in this model is the Hencky strain measure or the logarithmic elastic squared right stretch tensor $\mathbf{e}_e := \frac{1}{2}\ln\mathbf{B}_e$. Advantages of using

Table 5.1: Comparison of the small strain model and finite strain model kinematics and constitutive approach

Variable	Small Strain Model	Finite Strain Model
Total strain	$\boldsymbol{\epsilon}$	\mathbf{F}
Glassy Network strain	$\boldsymbol{\epsilon}_e$	$\mathbf{F}_e, \mathbf{B}_e := \mathbf{F}_e \mathbf{F}_e^T$
Rubbery Network strain	$\boldsymbol{\epsilon}_{ve}$	$\mathbf{G}, \mathbf{B}_{ve} := \mathbf{G} \mathbf{G}^T$
Elastic strain	$\boldsymbol{\epsilon}_e = \boldsymbol{\epsilon} - \boldsymbol{\epsilon}_{ve}$	$\mathbf{F}_e = \mathbf{F} \mathbf{G}^{-1}$
Inelastic flow rate	$\dot{\boldsymbol{\epsilon}}_{ve}$	$\mathbf{D}_{ve} = (\dot{\mathbf{G}} \mathbf{G}^{-1})_{symm}$
Glassy Helmholtz Potential	$\psi_G(\boldsymbol{\epsilon}_e, \theta)$	$\psi_G(\mathbf{F}_e, \theta)$
Rubbery Helmholtz Potential	$\psi_R(\boldsymbol{\epsilon}_{ve})$	$\psi_R(\mathbf{G})$
Rate of Dissipation	$\xi(\dot{\boldsymbol{\epsilon}}_{ve})$	$\xi(\mathbf{D}_{ve})$
Reduced energy dissipation equation	$\boldsymbol{\sigma} \cdot \dot{\boldsymbol{\epsilon}} - \rho \dot{\psi} _\theta = \xi(\dot{\boldsymbol{\epsilon}}_{ve})$	$\mathbf{T} \cdot \mathbf{L} - \rho \dot{\psi} _\theta = \xi(\mathbf{D}_{ve})$

the Hencky strain measure include [63, 64] (1) Symmetry for inverted deformations (this is not exhibited by Lagrangian and Almansi strain), (2) Trace vanishes for isochoric deformations (3) Additivity for coaxial deformations (4) Additive separation into volumetric and isochoric deformations. Logarithmic strain allows the additive decoupling of dilation and distortion for infinitesimal engineering strain to be generalized to all strains, large or small as shown by Criscione et al. [65]. They have also noted that the principal values of Lagrangian strain are biased toward extension with the range $(-\frac{1}{2}, \infty)$ whereas those of Almansi strain are biased toward contraction with the range $(-\infty, \frac{1}{2})$. Logarithmic strain is unbiased, and the range of its principal values is $(-\infty, \infty)$. The disadvantage of the logarithmic strain measure is computational, since it needs to be based on spectral decomposition, and require computing the eigen values and eigen vectors. This is quite expensive in very large finite element models [64].

We prescribe the elastic and inelastic components of strains as additive ($\boldsymbol{\epsilon} = \boldsymbol{\epsilon}_e + \boldsymbol{\epsilon}_{ve}$) in the small strain theory, whereas we use the multiplicative decomposition of the deformation gradient into elastic and inelastic components ($\mathbf{F} = \mathbf{F}_e \mathbf{G}$) in the finite strain model. Various theories have been proposed for finite elastoplastic kinematics, primarily divided into three groups: (1) Additive decomposition of rate of deformation by Nemat-Nasser [66], (2) Additive decomposition of Lagrangian strain by Green and Naghdi [67], and (3) Multiplicative decomposition of the deformation

gradient by Lee [62]. Each theory has its own advantages and shortcomings, and have been discussed extensively in the literature. Even though there is no consensus with respect to the most favorable finite elastoplastic kinematics, in this work the multiplicative decomposition of the deformation gradient is chosen as shown in Eq. 5.4 for its computational benefits in conjunction with the definition of the elastic strain in terms of the logarithmic measures.

5.3 Constitutive Theory for Finite Deformation

The constitutive approach for the finite strain model is similar to that for the small strain model presented in Chapter 3. The two key ingredients that are required for developing a finite deformation version of the theory are (1) a form for the Helmholtz potential which involves both finite elastic and inelastic strains, and (2) a rate of dissipation function which depends on the generalization of the plastic strain rate. (3) The requirement that the rate of dissipation be maximized.

(1) Helmholtz Potential

Following the form for small deformation, we will assume that the Helmholtz potential is composed of two parts: the glassy or elastic behavior of the permanent networks $\hat{\psi}_1(\mathbf{F}_e)$ and the rubbery or transient behavior of the temporary networks $\hat{\psi}_2(\mathbf{G})$. The energy storage of the permanent network is modeled as an isotropic elastic material similar to the small strain model. The energy storage of the temporary network can be modeled as an incompressible hyperelastic material, such as the neo-Hookean model, that is often used to represent rubber-like materials.

$$\psi = \hat{\psi}_1(\mathbf{F}_e, \theta) + \hat{\psi}_2(\mathbf{G}) \quad (5.7)$$

$$\hat{\psi}_1(\mathbf{F}_e, \theta) = \frac{1}{2} \mathbf{C}_G(\mathbf{e}_e - \alpha(\theta - \theta_h) \mathbf{I}) \cdot (\mathbf{e}_e - \alpha(\theta - \theta_h) \mathbf{I}) + f(\theta) \quad (5.8)$$

$$\hat{\psi}_2(\mathbf{G}) = \frac{1}{2} \mu_R (\mathbf{I} \cdot \mathbf{B}_{ve} - 3) \quad (5.9)$$

where the glassy stiffness matrices are given as follows,

$$\begin{aligned} \mathbf{C}_G &= k_G \mathbf{I} \otimes \mathbf{I} + 2\mu_G \left(\mathbf{I} - \frac{1}{3} \mathbf{I} \otimes \mathbf{I} \right) \\ &= \left(k_G - \frac{2\mu_G}{3} \right) \mathbf{I} \otimes \mathbf{I} + 2\mu_G \mathbb{I} \end{aligned} \quad (5.10)$$

and

k_G is the glassy bulk modulus, k_R is the rubbery bulk modulus, μ_G is the glassy shear modulus, μ_R is the rubbery shear modulus, α is the thermal expansion.

(2) The Rate of Dissipation Function

Similarly a rate of dissipation similar to the small strain model can be chosen as

$$\begin{aligned}\xi &= \hat{\xi}(\mathbf{D}_{ve}) \\ &= \eta_G \mathbf{D}_{ve} \cdot \mathbf{D}_{ve} + \kappa ||\mathbf{D}_{ve}||\end{aligned}\quad (5.11)$$

where η_G is the viscosity, and κ is the network activation threshold which depends upon the temperature, stress and also the prior history of the process. It will be shown presently that until the magnitude of the deviatoric stress exceeds this threshold the shape change will be purely thermoelastic and recoverable upon unloading.

The rate of dissipation is given by the difference of the mechanical power supplied and the rate of increase of the isothermal work function:

$$\begin{aligned}\mathbf{T} \cdot \mathbf{L} - \rho \dot{\psi}|_{\theta=C} &= \xi(\mathbf{D}_{ve}) \\ \mathbf{T} \cdot \mathbf{L} - \rho \frac{\partial \psi}{\partial \mathbf{F}_e} \cdot \dot{\mathbf{F}}_e - \rho \frac{\partial \psi}{\partial \mathbf{G}} \cdot \dot{\mathbf{G}} &= \xi(\mathbf{D}_{ve})\end{aligned}\quad (5.12)$$

Now \mathbf{L} can be written in the following form:

$$\begin{aligned}\mathbf{L} &= \dot{\mathbf{F}}\mathbf{F}^{-1} \\ &= (\dot{\mathbf{F}}_e \mathbf{G})(\mathbf{F}_e \mathbf{G})^{-1} \\ &= \dot{\mathbf{F}}_e \mathbf{F}_e^{-1} + \mathbf{F}_e \dot{\mathbf{G}} \mathbf{G}^{-1} \mathbf{F}_e^{-1} \\ &= \mathbf{L}_e + \mathbf{F}_e \mathbf{L}_{ve} \mathbf{F}_e^{-1}\end{aligned}\quad (5.13)$$

where, $\mathbf{L}_e = \dot{\mathbf{F}}_e \mathbf{F}_e^{-1}$, $\mathbf{L}_{ve} = \dot{\mathbf{G}} \mathbf{G}^{-1}$.

Eq. 5.13 can be used in Eq. 5.12 as follows:

$$\begin{aligned}\mathbf{T} \cdot (\mathbf{L}_e + \mathbf{F}_e \mathbf{L}_{ve} \mathbf{F}_e^{-1}) - \rho \frac{\partial \psi}{\partial \mathbf{F}_e} \cdot \mathbf{L}_e \mathbf{F}_e - \rho \frac{\partial \psi}{\partial \mathbf{G}} \cdot \mathbf{L}_{ve} \mathbf{G} &= \hat{\xi}(\mathbf{D}_{ve}) \\ \left(\mathbf{T} - \rho \frac{\partial \psi}{\partial \mathbf{F}_e} \mathbf{F}_e^T \right) \cdot \mathbf{L}_e + \left(\mathbf{F}_e^T \mathbf{T} \mathbf{F}_e^{-T} - \rho \frac{\partial \psi}{\partial \mathbf{G}} \mathbf{G}^T \right) \cdot \mathbf{L}_{ve} &= \hat{\xi}(\mathbf{D}_{ve})\end{aligned}\quad (5.14)$$

We set the stress using the Cauchy stress definition

$$\mathbf{T} = \rho \frac{\partial \psi}{\partial \mathbf{F}_e} \mathbf{F}_e^T \quad (5.15)$$

Thus the term $\mathbf{F}_e^T \mathbf{T} \mathbf{F}_e^{-T}$ in Eq 5.14 can be written as,

$$\mathbf{F}_e^T \mathbf{T} \mathbf{F}_e^{-T} = \rho \mathbf{F}_e^T \frac{\partial \psi}{\partial \mathbf{F}_e} \quad (5.16)$$

With this definition of stress, Eq 5.14 now becomes

$$\mathbf{A}_{ve} \cdot \mathbf{L}_{ve} = \hat{\xi}(\mathbf{D}_{ve}) \quad (5.17)$$

where

$$\mathbf{A}_{ve} = \rho \left(\mathbf{F}_e^T \frac{\partial \psi}{\partial \mathbf{F}_e} - \frac{\partial \psi}{\partial \mathbf{G}} \mathbf{G}^T \right) \quad (5.18)$$

Following Zeigler[68] and Rajagopal and Srinivasa[69] we now introduce the “maximum rate of dissipation assumption” which states that the system will evolve such that the actual value of \mathbf{D}_{ve} is that which maximizes $\hat{\xi}(\mathbf{D}_{ve})$ subject to the constraint in Eq 5.17. We first form the function h in Equation 5.19.

$$h = \xi + \lambda_1(\mathbf{A}_{ve} \cdot \mathbf{L}_{ve} - \xi) + \lambda_2 \text{tr}(\mathbf{L}_{ve}) \quad (5.19)$$

We now differentiate h with \mathbf{D}_{ve} using the chosen form for ξ from Eq 5.11 and then equate it to zero.

$$\begin{aligned} \frac{\partial h}{\partial \mathbf{D}_{ve}} &= 0 \\ \frac{\partial \xi}{\partial \mathbf{D}_{ve}} + \lambda_1 \left(\frac{\partial(\mathbf{A}_{ve} \cdot \mathbf{L}_{ve})}{\partial \mathbf{D}_{ve}} - \frac{\partial \xi}{\partial \mathbf{D}_{ve}} \right) + \lambda_2 \frac{\partial \text{tr} \mathbf{L}_{ve}}{\partial \mathbf{D}_{ve}} &= 0 \\ \frac{\partial \xi}{\partial \mathbf{D}_{ve}} + \lambda_1 \left(\frac{\partial(\mathbf{A}_{ve} \cdot \mathbf{L}_{ve})}{\partial \mathbf{D}_{ve}} - \frac{\partial \xi}{\partial \mathbf{D}_{ve}} \right) + \lambda_2 \frac{\partial(\mathbf{D}_{ve} \cdot \mathbf{I})}{\partial \mathbf{D}_{ve}} &= 0 \\ \frac{\partial \xi}{\partial \mathbf{D}_{ve}} + \lambda_1 \left(\frac{\partial(\mathbf{A}_{ve} \cdot \mathbf{L}_{ve})}{\partial \mathbf{D}_{ve}} - \frac{\partial \xi}{\partial \mathbf{D}_{ve}} \right) + \lambda_2 \mathbf{I} &= 0 \end{aligned} \quad (5.20)$$

In index notation $\frac{\partial(\mathbf{A}_{ve} \cdot \mathbf{L}_{ve})}{\partial \mathbf{D}_{ve}}$ translates as:

$$\begin{aligned}
\left[\frac{\partial(\mathbf{A}_{ve} \cdot \mathbf{L}_{ve})}{\partial \mathbf{D}_{ve}} \right]^{lm} &= \frac{\partial(\mathbf{A}_{ve}^{ij} \mathbf{L}_{ve}^{ij})}{\partial \mathbf{D}_{ve}^{lm}} \\
&= \frac{1}{2}(\mathbf{A}_{ve}^{lm} + \mathbf{A}_{ve}^{ml}) \\
&= \frac{1}{2}[\mathbf{A}_{ve} + \mathbf{A}_{ve}^T]^{lm} \\
&= [\mathbf{A}_{ve}^{sym}]^{lm}
\end{aligned} \tag{5.21}$$

Thus Eq 5.20 now becomes

$$\frac{\partial \xi}{\partial \mathbf{D}_{ve}} = \frac{\lambda_1}{\lambda_1 - 1} \mathbf{A}_{ve}^{sym} + \frac{\lambda_2}{\lambda_1 - 1} \mathbf{I} \tag{5.22}$$

Using the definition of ξ from Eq 5.11, in index notation $\frac{\partial \xi}{\partial \mathbf{D}_{ve}}$ will translate as follows:

$$\begin{aligned}
\left[\frac{\partial \xi}{\partial \mathbf{D}_{ve}} \right]^{lm} &= \left[\frac{\partial}{\partial \mathbf{D}_{ve}} \left(\eta_G \mathbf{D}_{ve} \cdot \mathbf{D}_{ve} + \kappa \sqrt{\mathbf{D}_{ve} \cdot \mathbf{D}_{ve}} \right) \right]^{lm} \\
&= \frac{\partial(\eta_G \mathbf{D}_{ve}^{ij} \mathbf{D}_{ve}^{ij})}{\partial \mathbf{D}_{ve}^{lm}} + \kappa \frac{\partial(\mathbf{D}_{ve}^{ij} \mathbf{D}_{ve}^{ij})^{1/2}}{\partial \mathbf{D}_{ve}^{lm}} \\
&= 2\eta_G \mathbf{D}_{ve}^{lm} + \kappa \mathbf{D}_{ve}^{lm} (\mathbf{D}_{ve}^{ij} \mathbf{D}_{ve}^{ij})^{-1/2} \\
&= \left[2\eta_G \mathbf{D}_{ve} + \kappa \frac{\mathbf{D}_{ve}}{||\mathbf{D}_{ve}||} \right]^{lm}
\end{aligned} \tag{5.23}$$

Thus Eq 5.22 now becomes

$$\left(2\eta_G + \frac{\kappa}{||\mathbf{D}_{ve}||} \right) \mathbf{D}_{ve} = \frac{\lambda_1}{\lambda_1 - 1} \mathbf{A}_{ve}^{sym} + \frac{\lambda_2}{\lambda_1 - 1} \mathbf{I} \tag{5.24}$$

To compute the value of λ_1 , we now take a dot product of Eq 5.24 with \mathbf{D}_{ve}

$$2\eta_G \mathbf{D}_{ve} \cdot \mathbf{D}_{ve} + \kappa \frac{\mathbf{D}_{ve} \cdot \mathbf{D}_{ve}}{||\mathbf{D}_{ve}||} = \frac{\lambda_1}{\lambda_1 - 1} \mathbf{A}_{ve}^{sym} \cdot \mathbf{D}_{ve} + \frac{\lambda_2}{\lambda_1 - 1} \mathbf{I} \cdot \mathbf{D}_{ve} \tag{5.25}$$

Going back to Eq 5.17, we compare the RHS which is a function of $\xi = \hat{\xi}(\mathbf{D}_{ve})$, and

the LHS which can be split as $\mathbf{L}_{ve} = \mathbf{D}_{ve} + \mathbf{W}_{ve}$. Thus only \mathbf{D}_{ve} will contribute to $\hat{\xi}(\mathbf{D}_{ve})$, and since \mathbf{D}_{ve} is a symmetric tensor, its dot product with the antisymmetric part of \mathbf{A}_{ve} will reduce to zero. So finally Eq 5.17 will reduce to:

$$\mathbf{A}_{ve}^{sym} \cdot \mathbf{D}_{ve} = \hat{\xi}(\mathbf{D}_{ve}) \quad (5.26)$$

We can now proceed with the calculation of λ_1 in Eq. 5.25 using the above result of $\mathbf{A}_{ve}^{sym} \cdot \mathbf{D}_{ve} = \hat{\xi}(\mathbf{D}_{ve})$ in the RHS and then substituting the definition of $\hat{\xi}(\mathbf{D}_{ve})$ from Eq 5.11 in the RHS

$$\begin{aligned} 2\eta_G \mathbf{D}_{ve} \cdot \mathbf{D}_{ve} + \kappa \frac{\mathbf{D}_{ve} \cdot \mathbf{D}_{ve}}{\|\mathbf{D}_{ve}\|} &= \frac{\lambda_1}{\lambda_1 - 1} \xi + \frac{\lambda_2}{\lambda_1 - 1} \mathbf{I} \cdot \mathbf{D}_{ve} \\ \frac{\lambda_1}{\lambda_1 - 1} &= \frac{2\eta_G \|\mathbf{D}_{ve}\|^2 + \kappa \|\mathbf{D}_{ve}\|}{\eta_G \|\mathbf{D}_{ve}\|^2 + \kappa \|\mathbf{D}_{ve}\|} \end{aligned} \quad (5.27)$$

This gives

$$\lambda_1 = 2 + \frac{\kappa}{\eta_G \|\mathbf{D}_{ve}\|} \quad (5.28)$$

To compute the value of λ_2 , we now take a dot product of Eq 5.24 with \mathbf{I}

$$\begin{aligned} 2\eta_G \mathbf{D}_{ve} \cdot \mathbf{I} + \kappa \frac{\mathbf{D}_{ve} \cdot \mathbf{I}}{\|\mathbf{D}_{ve}\|} &= \frac{\lambda_1}{\lambda_1 - 1} \mathbf{A}_{ve}^{sym} \cdot \mathbf{I} + \frac{\lambda_2}{\lambda_1 - 1} \mathbf{I} \cdot \mathbf{I} \\ \lambda_2 &= -\frac{\lambda_1}{3} \text{tr} \mathbf{A}_{ve}^{sym} \end{aligned} \quad (5.29)$$

Proceeding to substitute the value of λ_1, λ_2 in Eq 5.24

$$\left(2\eta_G + \frac{\kappa}{\|\mathbf{D}_{ve}\|}\right) \mathbf{D}_{ve} = \left(\frac{2\eta_G \|\mathbf{D}_{ve}\|^2 + \kappa \|\mathbf{D}_{ve}\|}{\eta_G \|\mathbf{D}_{ve}\|^2 + \kappa \|\mathbf{D}_{ve}\|}\right) \mathbf{A}_{ve}^{dev,sym} \quad (5.30)$$

Taking norm on both sides and rearranging, we have

$$\|\mathbf{D}_{ve}\| = \frac{1}{\eta_G} \left(\|\mathbf{A}_{ve}^{dev,sym}\| - \kappa \right) \quad (5.31)$$

This gives us the following conditions:

$$\|\mathbf{A}_{ve}^{dev,sym}\| \leq \kappa \implies \|\mathbf{D}_{ve}\| \text{ set to zero} \quad (5.32)$$

$$||\mathbf{A}_{ve}^{dev,sym}|| > \kappa \implies ||\mathbf{D}_{ve}|| \text{ non-zero}$$

For the condition when $||\mathbf{D}_{ve}||$ is non-zero, substituting Eq 5.31 into the result of \mathbf{D}_{ve} in Eq 5.30:

$$\left(2\eta_G + \frac{\kappa}{||\mathbf{D}_{ve}||}\right)\mathbf{D}_{ve} = \left(\frac{2\eta_G||\mathbf{D}_{ve}||^2 + \kappa||\mathbf{D}_{ve}||}{\eta_G||\mathbf{D}_{ve}||^2 + \kappa||\mathbf{D}_{ve}||}\right)\mathbf{A}_{ve}^{dev,sym} \quad (5.33)$$

$$\mathbf{D}_{ve} = \frac{1}{\eta_G} (||\mathbf{A}_{ve}^{dev,sym}|| - \kappa) \frac{\mathbf{A}_{ve}^{dev,sym}}{||\mathbf{A}_{ve}^{dev,sym}||} \quad (5.34)$$

From the cases of $||\mathbf{D}_{ve}||$ from 5.32 we can write all the possible cases of \mathbf{D}_{ve}

$$\mathbf{D}_{ve} = \begin{cases} 0, & \forall \quad ||\mathbf{A}_{ve}^{dev,sym}|| \leq \kappa; \\ \frac{1}{\eta_G} (||\mathbf{A}_{ve}^{dev,sym}|| - \kappa) \frac{\mathbf{A}_{ve}^{dev,sym}}{||\mathbf{A}_{ve}^{dev,sym}||}, & \forall \quad ||\mathbf{A}_{ve}^{dev,sym}|| > \kappa; \end{cases} \quad (5.35)$$

5.4 QR Decomposition

Until now, we have been following the classical procedures based on the use of the multiplicative decomposition. However, when dealing with materials whose instantaneous elastic response is isotropic, there is an essential degeneracy in the relaxed configuration κ_p since isotropy demands that the constitutive response is invariant to any rotation of the configuration κ_p . This is a well known issue that has been dealt with in the plasticity literature (see e.g. Lee [62]). Two common ways of dealing with this degeneracy is to require that (1) $\mathbf{F}_e = \mathbf{V}_e$ or $\mathbf{G} = \mathbf{U}_p$, thus eliminating the redundancy. While theoretically sound, both these approaches have some severe numerical complications: When carrying out calculations with either \mathbf{V}_e or \mathbf{U}_p in a finite deformation setting, it is necessary to constantly symmetrize certain tensors (see Simo and Hughes [70] as well as Srinivasa and Srinivasan [51] for a detailed discussion).

The reasons for this difficulty lie in the fact that the set of symmetric tensors, while being closed under addition are not closed under multiplication. Recently, Srinivasa [61] has shown the efficacy of using a different decomposition of the deformation gradient. Rather than using the Polar decomposition theorem, which decomposes \mathbf{F} into a rotation \mathbf{R} and a symmetric tensor \mathbf{U} , he proposed the use of

the well known **QR** decomposition, which will decompose **F** into a rotation **Q** and an upper triangular matrix **R**. Unlike the polar decomposition, which, in general requires the use of eigenvalues and eigenvectors of **C**, the **QR** decomposition can be directly and explicitly computed (see[61]). It may also be observed that the upper triangular matrix has exactly the same number of elements as the Cauchy green stretch tensor **C** and contains the same information. Indeed they are related through a Cholesky Factorization.

The set of upper triangular matrices have a number of advantages over the the set of symmetric matrices obtained by polar decomposition. First, upper triangular matrices are closed under both addition and multiplication, so that discretizing differential equations that utilize the **QR** decomposition is simple. For example, if **G** is upper triangular so is \mathbf{G}^{-1} and \mathbf{L}_{ve} . On the other hand, if **G** is symmetric, \mathbf{L}_{ve} is not. Further, the determinant and inverse of an Upper triangular matrix are trivial to compute and hence make conditions such as incompressibility easy to enforce.

Based on this discussion, and in view of the isotropy of the elastic response, we assume without loss of generality that **G** is upper triangular. We now write **G** in **QR** decomposition form, where we decompose **G** into the product of a pure rotation and an upper triangular matrix as below.

$$\mathbf{G} = \mathbf{Q}\tilde{\mathbf{G}} \quad (5.36)$$

where **Q** is a pure rotation and $\tilde{\mathbf{G}}$ is the upper triangular form of **G**. Henceforth $\{\dot{\cdot}\}$ is the upper triangular form of $\{\cdot\}$. Therefore,

$$\dot{\mathbf{G}} = \dot{\mathbf{Q}}\tilde{\mathbf{G}} + \mathbf{Q}\dot{\tilde{\mathbf{G}}} \quad (5.37)$$

Since **Q** is an orthogonal tensor so that $\dot{\mathbf{Q}} = \Omega\mathbf{Q}$, where Ω is a skew symmetric tensor, this gives us

$$\begin{aligned} \mathbf{L}_{ve} &= \dot{\mathbf{G}}\mathbf{G}^{-1} \\ &= \Omega\mathbf{Q}\tilde{\mathbf{G}}\tilde{\mathbf{G}}^{-1}\mathbf{Q}^T + \mathbf{Q}\dot{\tilde{\mathbf{L}}}_{ve}\mathbf{Q}^T \end{aligned} \quad (5.38)$$

Also $\tilde{\mathbf{G}}^{-1}$ is triangular. This gives $\tilde{\mathbf{L}}_{ve} = \dot{\tilde{\mathbf{G}}}\tilde{\mathbf{G}}^{-1}$ as triangular.

We also have the definition $\mathbf{D}_{ve} = \mathbf{Q}\tilde{\mathbf{D}}_{ve}\mathbf{Q}^T$, and the relationship $\mathbf{D}_{ve} = \frac{1}{2}(\mathbf{L}_{ve} +$

\mathbf{L}_{ve}^T), so we can use these two alongwith the result obtained above in Eq 5.38 to find the relationship between $\tilde{\mathbf{D}}_{ve}$ and $\tilde{\mathbf{L}}_{ve}$ as follows

$$\mathbf{D}_{ve} = \frac{1}{2}(\mathbf{L}_{ve} + \mathbf{L}_{ve}^T) \quad (5.39)$$

$$\mathbf{Q}\tilde{\mathbf{D}}_{ve}\mathbf{Q}^T = \frac{1}{2}(\Omega\mathbf{Q}\tilde{\mathbf{G}}\tilde{\mathbf{G}}^{-1}\mathbf{Q}^T + \mathbf{Q}\dot{\tilde{\mathbf{G}}}\tilde{\mathbf{G}}^{-1}\mathbf{Q}^{-1} + (\Omega\mathbf{Q}\tilde{\mathbf{G}}\tilde{\mathbf{G}}^{-1}\mathbf{Q}^T + \mathbf{Q}\dot{\tilde{\mathbf{G}}}\tilde{\mathbf{G}}^{-1}\mathbf{Q}^{-1})^T) \quad (5.40)$$

$$\tilde{\mathbf{D}}_{ve} = \frac{1}{2}(\mathbf{Q}^T\Omega\mathbf{Q} - \mathbf{Q}^T\Omega\mathbf{Q} + \dot{\tilde{\mathbf{G}}}\tilde{\mathbf{G}}^{-1} + (\dot{\tilde{\mathbf{G}}}\tilde{\mathbf{G}}^{-1})^T) \quad (5.41)$$

$$\tilde{\mathbf{D}}_{ve} = \frac{1}{2}(\tilde{\mathbf{L}}_{ve} + \tilde{\mathbf{L}}_{ve}^T) \quad (5.42)$$

Since both \mathbf{A}_{ve}^{sym} and \mathbf{D}_{ve} are symmetric, we can now write it in upper triangular form for the rate of dissipation relation in Eq 5.26

$$\tilde{\mathbf{A}}_{ve}^{sym} \cdot \tilde{\mathbf{D}}_{ve} = \xi(\tilde{\mathbf{D}}_{ve}) \quad (5.43)$$

In upper triangular form we can write Eq 5.35 as

$$\tilde{\mathbf{D}}_{ve} = \frac{1}{\eta_G} \left(\|\tilde{\mathbf{A}}_{ve}^{dev,sym}\| - \kappa \right) \frac{\tilde{\mathbf{A}}_{ve}^{dev,sym}}{\|\tilde{\mathbf{A}}_{ve}^{dev,sym}\|} \quad (5.44)$$

The symmetric part of \mathbf{A}_{ve} can be derived from the relationship in Eq 5.18

$$\tilde{\mathbf{A}}_{ve}^{sym} = \left(\mathbf{F}_e^T \frac{\partial \psi}{\partial \mathbf{F}_e} - \frac{\partial \psi}{\partial \mathbf{G}} \mathbf{G}^T \right)^{sym} \quad (5.45)$$

For this we first derive the form of stress using Eq. 5.15, keeping in mind that the elastic part of the response is isotropic, i.e $\mathbf{F}_e = \mathbf{V}_e$, where \mathbf{V}_e is left stretch tensor, and $\mathbf{B}_e = \mathbf{V}_e^2$:

$$\mathbf{T} = \frac{\partial \psi}{\partial \mathbf{F}_e} \mathbf{F}_e^T \quad (5.46)$$

$$= \frac{\partial \psi}{\partial \mathbf{B}_e} \frac{\partial \mathbf{B}_e}{\partial \mathbf{V}_e} \mathbf{V}_e \quad (5.47)$$

$$= 2 \frac{\partial \psi}{\partial \mathbf{B}_e} \mathbf{B}_e \quad (5.48)$$

Consider the differentiation of ψ with respect to $\ln \mathbf{B}_e$:

$$\frac{\partial \psi}{\partial \ln \mathbf{B}_e} = \frac{\partial \psi}{\partial \mathbf{B}_e} \frac{\partial \mathbf{B}_e}{\partial \ln \mathbf{B}_e} \quad (5.49)$$

To calculate $\frac{\partial \mathbf{B}_e}{\partial \ln \mathbf{B}_e}$ we define $\ln \mathbf{B}_e$ as below

$$\mathbf{H} = \ln \mathbf{B}_e \quad (5.50)$$

$$\mathbf{f} = e^{\ln \mathbf{B}_e} = \mathbf{B}_e \quad (5.51)$$

$$\mathbf{P} = \text{arbitrary tensor} \quad (5.52)$$

We now employ the Gâteaux derivative

$$\frac{d\mathbf{f}}{d\mathbf{H}}[\mathbf{P}] = \frac{de^{\mathbf{H}}}{d\mathbf{H}}[\mathbf{P}] \quad (5.53)$$

$$= \frac{d}{d\alpha} (e^{\mathbf{H} + \alpha \mathbf{P}}) \Big|_{\alpha=0} \quad (5.54)$$

$$= \frac{d}{d\alpha} (e^{\mathbf{H}} e^{\alpha \mathbf{P}}) \Big|_{\alpha=0} \quad (5.55)$$

$$= e^{\mathbf{H}} \frac{d}{d\alpha} (e^{\alpha \mathbf{P}}) \Big|_{\alpha=0} \quad (5.56)$$

Now consider the Taylor series expansion

$$e^{\alpha \mathbf{P}} = \sum_{n=0}^{\infty} \frac{(\alpha \mathbf{P})^n}{n!} \quad (5.57)$$

$$e^{\alpha \mathbf{P}} = \mathbf{I} + \alpha \mathbf{P} + \frac{(\alpha \mathbf{P})^2}{2!} + \frac{(\alpha \mathbf{P})^3}{3!} + \dots \quad (5.58)$$

$$\frac{de^{\alpha \mathbf{P}}}{d\alpha} = \mathbf{P} + 2 \frac{(\alpha \mathbf{P}) \mathbf{P}}{2!} + \dots \quad (5.59)$$

$$\left. \frac{de^{\alpha \mathbf{P}}}{d\alpha} \right|_{\alpha=0} = \mathbf{P} \quad (5.60)$$

This now makes Eq. (5.53)

$$\frac{d\mathbf{f}}{d\mathbf{H}}[\mathbf{P}] = e^{\mathbf{H}} \mathbf{P} \quad (5.61)$$

$$\text{Thus } \frac{\partial \mathbf{B}_e}{\partial \ln \mathbf{B}_e}[\mathbf{P}] = \mathbf{B}_e \mathbf{P} \quad (5.62)$$

Since \mathbf{P} was chosen as an arbitrary tensor, we can now substitute the above result back into Eq. 5.49, to get

$$\frac{\partial \psi}{\partial \ln \mathbf{B}_e} = \frac{\partial \psi}{\partial \mathbf{B}_e} \frac{\partial \mathbf{B}_e}{\partial \ln \mathbf{B}_e} \quad (5.63)$$

$$= \frac{\partial \psi}{\partial \mathbf{B}_e} \mathbf{B}_e \quad (5.64)$$

We now have a new form for the result for stress in Eq. 5.48 from the result obtained in Eq. 5.64. We substitute this new form to get the result for stress as below, referring to the form of ψ in Eq. 5.7

$$\mathbf{T} = 2 \frac{\partial \psi}{\partial \ln \mathbf{B}_e} \quad (5.65)$$

$$= \mathbf{C}_G(\mathbf{e}_e - \alpha(\theta - \theta_h)\mathbf{I}) \quad (5.66)$$

We can substitute the result of Eq. 5.66 in Eq. 5.16 and arrive at,

$$\begin{aligned} \mathbf{F}_e^T \mathbf{T} \mathbf{F}_e^{-T} &= \mathbf{F}_e^T \frac{\partial \psi}{\partial \mathbf{F}_e} \\ &= \mathbf{F}_e^T \mathbf{C}_G(\mathbf{e}_e - \alpha(\theta - \theta_h)\mathbf{I}) \mathbf{F}_e^{-T} \end{aligned} \quad (5.67)$$

Both \mathbf{T} and $\mathbf{F}_e^T \mathbf{T} \mathbf{F}_e^{-T}$ are symmetric for isotropic materials.

Proof of symmetry for $\mathbf{F}_e^T \mathbf{T} \mathbf{F}_e^{-T}$ is derived below:

$$\begin{aligned} \mathbf{F}_e^T \mathbf{T} \mathbf{F}_e^{-T} &= \mathbf{F}_e^T \mathbf{C}_G \left(\frac{1}{2} \ln \mathbf{B}_e - \alpha(\theta - \theta_h)\mathbf{I} \right) \mathbf{F}_e^{-T} \\ &= \mathbf{F}_e^T \left[\left(k_R - \frac{2\mu_R}{3} \right) \mathbf{I} \otimes \mathbf{I} + 2\mu_R \mathbb{I} \right] \left(\frac{1}{2} \ln \mathbf{B}_e - \alpha(\theta - \theta_h)\mathbf{I} \right) \mathbf{F}_e^{-T} \\ &= \frac{1}{2} \left(k_R - \frac{2\mu_R}{3} \right) \text{tr}(\ln \mathbf{B}_e) \mathbf{I} + \mu_R \mathbf{F}_e^T (\ln \mathbf{B}_e) \mathbf{F}_e^{-T} - 3k_R \alpha(\theta - \theta_h) \mathbf{I} \end{aligned} \quad (5.68)$$

Once again we use the property of isotropic materials $\mathbf{F}_e = \mathbf{V}_e$. We know that \mathbf{V}_e is symmetric, therefore it should be sufficient to prove that the term $\mathbf{F}_e^T (\ln \mathbf{B}_e) \mathbf{F}_e^{-T}$ in Eq. 5.68 is symmetric as follows, using spectral decomposition [71]:

$$\begin{aligned} \mathbf{F}_e^T (\ln \mathbf{B}_e) \mathbf{F}_e^{-T} &= \mathbf{F}_e^T (\ln \mathbf{F}_e \mathbf{F}_e^T) \mathbf{F}_e^{-T} \\ &= \mathbf{V}_e^T (\ln \mathbf{V}_e \mathbf{V}_e^T) \mathbf{V}_e^{-T} \\ &= \mathbf{V}_e (2 \ln \mathbf{V}_e) \mathbf{V}_e^{-1} \end{aligned}$$

$$\begin{aligned}
&= 2(\lambda_p \mathbf{q}_p \otimes \mathbf{q}_p) \ln(\lambda_r \mathbf{q}_r \otimes \mathbf{q}_r) (\lambda_m^{-1} \mathbf{q}_m \otimes \mathbf{q}_m) \\
&= 2(\lambda_p \ln \lambda_r \lambda_m^{-1}) (\mathbf{q}_p \otimes \mathbf{q}_p) (\mathbf{q}_r \otimes \mathbf{q}_r) (\mathbf{q}_m \otimes \mathbf{q}_m) \\
&= 2 \ln \lambda_r \mathbf{q}_r \otimes \mathbf{q}_r
\end{aligned} \tag{5.69}$$

Thus, Eq. 5.69 is symmetric, which proves $\mathbf{F}_e^T (\ln \mathbf{B}_e) \mathbf{F}_e^{-T}$ in Eq. 5.68 is symmetric and consequently $\mathbf{F}_e^T \mathbf{T} \mathbf{F}_e^{-T}$ is symmetric.

Also we compute $\frac{\partial \psi}{\partial \mathbf{G}} \mathbf{G}^T$ as below, referring to the form of ψ in Eq 5.7

$$\frac{\partial \psi}{\partial \mathbf{G}} \mathbf{G}^T = \frac{1}{2} \mu_R \frac{\partial (\mathbf{I} \cdot \mathbf{B}_{ve} - 3)}{\partial \mathbf{G}} \mathbf{G}^T \tag{5.70}$$

$$= \frac{1}{2} \mu_R \frac{\partial (\mathbf{G} \cdot \mathbf{G} - 3)}{\partial \mathbf{G}} \mathbf{G}^T \tag{5.71}$$

$$= \mu_R \mathbf{B}_{ve} \tag{5.72}$$

Now \mathbf{B}_{ve} is symmetric, as $\mathbf{B}_{ve} = \mathbf{B}_{ve}^T = \mathbf{G} \mathbf{G}^T$.

We now have forms for both $\mathbf{F}_e^T \frac{\partial \psi}{\partial \mathbf{F}_e}$ in Eq. 5.67 and $\frac{\partial \psi}{\partial \mathbf{G}} \mathbf{G}^T$ in Eq 5.72 to find the form of \mathbf{A}_{ve} as derived in Eq. 5.18

$$\begin{aligned}
\mathbf{A}_{ve} &= \left(\mathbf{F}_e^T \frac{\partial \psi}{\partial \mathbf{F}_e} - \frac{\partial \psi}{\partial \mathbf{G}} \mathbf{G}^T \right) \\
&= (\mathbf{F}_e^T \mathbf{C}_G (\mathbf{e}_e - \alpha(\theta - \theta_h) \mathbf{I}) \mathbf{F}_e^{-T} - \mu_R \mathbf{G} \mathbf{G}^T)
\end{aligned} \tag{5.73}$$

We are mainly concerned with the symmetric part of this quantity. Both terms in \mathbf{A}_{ve} are symmetric as we observed in the comments below Eq 5.67 and 5.72. Thus we can directly write \mathbf{A}_{ve} in its upper triangular form $\tilde{\mathbf{A}}_{ve}^{sym}$.

$$\tilde{\mathbf{A}}_{ve}^{sym} = (\tilde{\mathbf{F}}_e^T \tilde{\mathbf{C}}_G (\tilde{\mathbf{e}}_e - \alpha(\theta - \theta_h) \tilde{\mathbf{I}}) \tilde{\mathbf{F}}_e^{-T} - \mu_R \tilde{\mathbf{G}} \tilde{\mathbf{G}}^T) \tag{5.74}$$

Then, to find $\tilde{\mathbf{D}}_{ve}$ derived in Eq. 5.44, we can use the deviatoric part of the above form of $\tilde{\mathbf{A}}_{ve}^{sym}$ to get the result

$$\tilde{\mathbf{D}}_{ve} = \frac{1}{\eta_G} \left(\|\tilde{\mathbf{A}}_{ve}^{dev,sym}\| - \kappa \right) \frac{\tilde{\mathbf{A}}_{ve}^{dev,sym}}{\|\tilde{\mathbf{A}}_{ve}^{dev,sym}\|} \tag{5.75}$$

Finite strain model for the SMP

1. **State Variables:** $\mathbf{F}, \mathbf{G}, \theta, \mathbf{T}$

2. **Elastic Response:**

$$\mathbf{T} = \mathbf{C}_G(\mathbf{e}_e - \alpha(\theta - \theta_h)\mathbf{I})$$

3. **Flow Rule:** $\tilde{\mathbf{D}}_{ve} = \frac{1}{\eta_G} \frac{\phi \tilde{\mathbf{A}}_{ve}^{dev,sym}}{\|\tilde{\mathbf{A}}_{ve}^{dev,sym}\|}$

4. **Activation Conditions:**

$$\phi = \begin{cases} 0, & \forall \quad \|\tilde{\mathbf{A}}_{ve}^{dev,sym}\| \leq \kappa; \\ \|\tilde{\mathbf{A}}_{ve}^{dev,sym}\| - \kappa, & \forall \quad \|\tilde{\mathbf{A}}_{ve}^{dev,sym}\| > \kappa; \end{cases} \quad (5.76)$$

5.5 Non-dimensionalization of System Equations

We select the following non-dimensionalization parameters, similar to the small strain model:

- (1) The typical rubbery modulus E_R , from experimental results.
- (2) The maximum axial strain applied ϵ_0 from experimental results.
- (3) The glass transition temperature θ_g .
- (4) The non-dimensionalization of the time, since this is connected with the kinetic response.

The non-dimensional quantities using these variables are tabulated in Table 5.2. In the current form, the constitutive equation and the kinetic equation have six

Table 5.2: Dimensional quantities and corresponding non-dimensional quantities for the finite strain model

Dim	\mathbf{T}	ϵ_e	t	θ	α	η_G	$k_{G,R}, \mu_R$
Nondim	$\bar{\mathbf{T}} = \frac{\mathbf{T}}{E_R \epsilon_0}$	$\bar{\epsilon}_e = \frac{\epsilon_e}{\epsilon_0}$	$\bar{t} = \frac{t}{t_0}$	$\bar{\theta} = \frac{\theta}{\theta_g}$	$\bar{\alpha} = \frac{\alpha \theta_g}{\epsilon_0}$	$\bar{\eta}_G = \frac{\eta_G}{E_R t_0}$	$\bar{\bullet} = \frac{\bullet}{E_R}$

dimensional parameters: $k_R, k_G, \alpha, \eta_G, \mu_R, \mu_G$.

Stress Equation:

$$\mathbf{T} = \mathbf{C}_G(\mathbf{e}_e - \alpha(\theta - \theta_h)\mathbf{I}) \quad (5.77)$$

$$= \left((k_G - \frac{2\mu_G}{3})\mathbf{I} \otimes \mathbf{I} + 2\mu_G\mathbb{I} \right) (\mathbf{e}_e - \alpha(\theta - \theta_h)\mathbf{I}) \quad (5.78)$$

Non-Dimensional form of Stress Equation:

$$\begin{aligned} \bar{\mathbf{T}}\mathbf{E}_R\epsilon_0 &= \left((\bar{k}_G\mathbf{E}_R - \frac{2\bar{\mu}_G\mathbf{E}_R}{3})\mathbf{I} \otimes \mathbf{I} + 2\bar{\mu}_G\mathbf{E}_R\mathbb{I} \right) (\bar{\epsilon}_e\epsilon_0 - \bar{\alpha}\frac{\epsilon_0}{\theta_g}(\bar{\theta} - \bar{\theta}_h)\theta_g\mathbf{I}) \\ \bar{\mathbf{T}} &= \left((\bar{k}_G - \frac{2\bar{\mu}_G}{3})\mathbf{I} \otimes \mathbf{I} + 2\bar{\mu}_G\mathbb{I} \right) (\bar{\epsilon}_e - \bar{\alpha}(\bar{\theta} - \bar{\theta}_h)\mathbf{I}) \\ \bar{\mathbf{T}} &= \bar{\mathbf{C}}_G(\bar{\epsilon}_e - \bar{\alpha}(\bar{\theta} - \bar{\theta}_h)\mathbf{I}) \end{aligned} \quad (5.79)$$

Flow Equation:

$$\tilde{\mathbf{D}}_{ve} = \frac{1}{\eta_G} (||\tilde{\mathbf{A}}_{ve}^{dev,sym}|| - \kappa) \frac{\tilde{\mathbf{A}}_{ve}^{dev,sym}}{||\tilde{\mathbf{A}}_{ve}^{dev,sym}||} \quad (5.80)$$

Non-Dimensional form of Flow Equation:

$$\bar{\mathbf{D}}_{ve} \frac{\epsilon_0}{t_0} = \frac{1}{\bar{\eta}_G\mathbf{E}_R t_0} (||\bar{\mathbf{A}}_{ve}^{dev,sym}\mathbf{E}_R\epsilon_0|| - \bar{\kappa}\mathbf{E}_R\epsilon_0) \frac{\bar{\mathbf{A}}_{ve}^{dev,sym}\mathbf{E}_R\epsilon_0}{||\bar{\mathbf{A}}_{ve}^{dev,sym}\mathbf{E}_R\epsilon_0||} \quad (5.81)$$

$$\bar{\mathbf{D}}_{ve} = \frac{1}{\bar{\eta}_G} (||\bar{\mathbf{A}}_{ve}^{dev,sym}|| - \bar{\kappa}) \frac{\bar{\mathbf{A}}_{ve}^{dev,sym}}{||\bar{\mathbf{A}}_{ve}^{dev,sym}||} \quad (5.82)$$

5.6 Implementation of the Finite Strain Model

We solve the system of ODEs for the evolution of activation stress, temperature, thermal expansion and $\tilde{\mathbf{G}}$ in mass matrix form $\mathbf{P}\dot{x} = \mathbf{r} + \mathbf{Q}x$, as described in detail in Algorithm 4, where $x = [\kappa, \theta, \alpha, \mathbf{G}_0^{6 \times 1}]$. We implement the algorithm in MATLAB using the ode45 solver, where we calculate the current value of $\tilde{\mathbf{G}}(t)$ given the input for the deformation \mathbf{F} for all time steps and the initial condition for $\tilde{\mathbf{G}}(0)$. The ODE system consists of these equations $\dot{\kappa} = f_\kappa\dot{\theta}$, $\dot{\theta} = g(t)$, $\dot{\alpha} = \frac{\partial \alpha}{\partial \theta}\dot{\theta}$, $\dot{\mathbf{G}} = \tilde{\mathbf{L}}_{ve}\tilde{\mathbf{G}}$. The

ODE system in mass matrix form $P\dot{x} = r + Qx$ looks as below

$$\begin{bmatrix} 1 & -\frac{\partial \kappa}{\partial \theta} & 0 & 0 & 0 & 0 & 0 & 0 & 0 \\ 0 & 1 & 0 & 0 & 0 & 0 & 0 & 0 & 0 \\ 0 & -\frac{\partial \alpha}{\partial \theta} & 1 & 0 & 0 & 0 & 0 & 0 & 0 \\ 0 & 0 & 0 & 1 & 0 & 0 & 0 & 0 & 0 \\ 0 & 0 & 0 & 0 & 1 & 0 & 0 & 0 & 0 \\ 0 & 0 & 0 & 0 & 0 & 1 & 0 & 0 & 0 \\ 0 & 0 & 0 & 0 & 0 & 0 & 1 & 0 & 0 \\ 0 & 0 & 0 & 0 & 0 & 0 & 0 & 1 & 0 \\ 0 & 0 & 0 & 0 & 0 & 0 & 0 & 0 & 1 \end{bmatrix} \begin{bmatrix} \dot{\kappa} \\ \dot{\theta} \\ \dot{\alpha} \\ \dot{G}_{11} \\ \dot{G}_{22} \\ \dot{G}_{33} \\ \dot{G}_{12} \\ \dot{G}_{13} \\ \dot{G}_{23} \end{bmatrix} = \begin{bmatrix} 0 \\ g \\ 0 \\ 0 \\ 0 \\ 0 \\ 0 \\ 0 \\ 0 \end{bmatrix} + \begin{bmatrix} 0 & 0 & 0 & 0 & 0 & 0 & 0 & 0 & 0 \\ 0 & 0 & 0 & 0 & 0 & 0 & 0 & 0 & 0 \\ 0 & 0 & 0 & 0 & 0 & 0 & 0 & 0 & 0 \\ 0 & 0 & 0 & 0 & 0 & 0 & 0 & 0 & 0 \\ 0 & 0 & 0 & 0 & 0 & 0 & 0 & 0 & 0 \\ 0 & 0 & 0 & 0 & 0 & 0 & 0 & 0 & 0 \\ 0 & 0 & 0 & 0 & 0 & 0 & 0 & 0 & 0 \\ 0 & 0 & 0 & 0 & 0 & 0 & 0 & 0 & 0 \\ 0 & 0 & 0 & 0 & 0 & 0 & 0 & 0 & 0 \end{bmatrix} \begin{bmatrix} \kappa \\ \theta \\ \alpha \\ G_{11} \\ G_{22} \\ G_{33} \\ G_{12} \\ G_{13} \\ G_{23} \end{bmatrix} \quad (5.83)$$

Note that for the stress control case (Algorithm 4, line 14), knowing the Cauchy stress alone is not enough to specify the deformation uniquely. We need additional assumptions about orientation. In this algorithm, we will assume wlog that $\mathbf{F}_e = \mathbf{V}_e$. If orientation information is known this can be incorporated.

5.7 Results for Shear Deformation

5.7.1 Isothermal Shear Deformation at Different Temperatures

In this section, we analyze the shear deformation behavior of the SMP model for different temperature cases, and study the normal stresses developed due to the Poynting effect in detail.

The shear deformation is controlled via the input $F = \mathbf{I} + f\mathbf{e}_1 \otimes \mathbf{e}_2$

The initial conditions are set as $\{\kappa, \theta, \alpha, \mathbf{G}_0 = \mathbf{I}\}$.

Reference temperature for this problem $\theta_{max} > \theta_g$

Activation stress: κ constant, depending on temperature case

Thermal Load: Constant, for the following temperature θ_{init} cases:

1. Greater than reference temperature: $\theta_{init} > \theta_{max}$
2. At reference temperature: $\theta_{init} = \theta_{max}$
3. At low temperature: $\theta_{init} < \theta_g$

As shown in Figure 5.2b, for large deformations, the shear deformation develops normal forces in the material. This is known as the Poynting effect. Like general trends observed in elastic-plastic materials, the Poynting effect results in strain-softening, as seen in Figure 5.2a. Even though the activation stress is kept constant in these three cases, the different strain softening trends may be attributed to the temperature at which the deformation is applied and the form of the flow potential

Algorithm 4 SMP model implementation

```

1: Input by user:
    • TimeData = [0:MaxTime], Initial Condition:  $x = [\kappa, \theta, \alpha, \mathbf{G}_0^{6 \times 1}]$ 
    • Material Parameters:  $E_G, E_R, \nu_G, \nu_R, \epsilon_0, \theta_h, \theta_l, \theta_g, \eta, t_0$ 
    • Control Parameters:  $g(t), f_\kappa, \partial\alpha/\partial\theta$ 
    • For a strain control problem, input:  $\mathbf{F}(t)$ , or for a stress control problem, input:  $\mathbf{T}(t)$ 

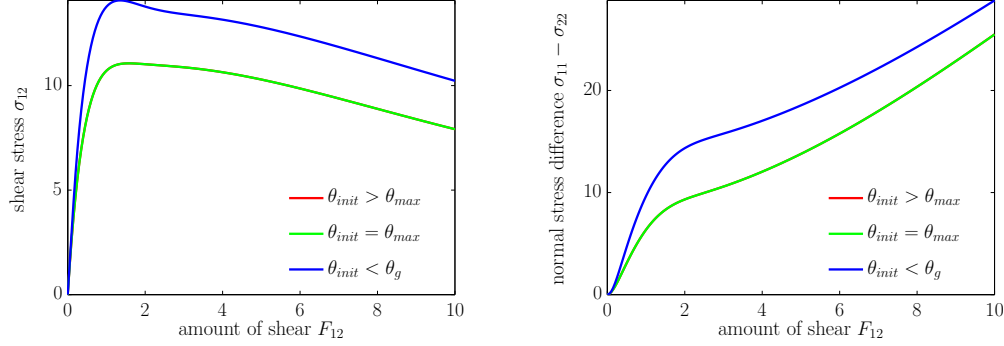
2: Calculate Non dimensional Material Parameters:  $\bar{k}_R, \bar{k}_G, \bar{\alpha}_G, \bar{\alpha}_R, \bar{\eta}_G, \bar{\mu}_R, \bar{\mu}_G$ 
3: function  $\dot{x} = \text{ODESOLVER}(t, x)$ 
4:   Assign  $\mathbf{G}_n^{6 \times 1} = \mathbf{G}_{n-1}^{6 \times 1}$  as initial approximation  $\triangleright \mathbf{G}_n^{6 \times 1}$  rearranged as upper triangular  $\mathbf{G}^{3 \times 3}$ 
5:   Call relevant function, depending on strain control (line 6) or stress control (line 14) problem:
6:   function STRAIN CONTROL(input:  $\mathbf{F}_n, \mathbf{G}_n$ , output:  $\mathbf{T}_n, \mathbf{G}_{n+1}$ )
7:      $\mathbf{F}_{e_n} = \mathbf{F}_n \mathbf{G}_n^{-1}$ 
8:      $\mathbf{B}_e = \mathbf{F}_{e_n} \mathbf{F}_{e_n}^T$ 
9:      $\ln \mathbf{B}_e = \sum_{i=1}^3 V_{Be}^i \log(\lambda_{Be}^i) (V_{Be}^i)^T$   $\triangleright \lambda_{Be}^i, V_{Be}^i$ : eigen values, vectors of  $\mathbf{B}_e$ 
10:     $\epsilon_e = \frac{1}{2} \ln \mathbf{B}_e$   $\triangleright \ln \mathbf{B}_e^{3 \times 3}$  rearranged as  $\ln \mathbf{B}_e^{6 \times 1}$ 
11:     $\mathbf{T}_n^{6 \times 1} = \mathbf{C}_G (\epsilon_e - \alpha_n (\theta_n - \theta_h) \mathbf{I})$   $\triangleright$  rearranged as upper triangular  $\mathbf{T}_n^{3 \times 3}$ 
12:    Continue to line 21
13:  end function
14:  function STRESS CONTROL(input:  $\mathbf{T}_n, \mathbf{G}_n$ , output:  $\mathbf{F}_n, \mathbf{G}_{n+1}$ )
15:     $\mathbf{M}^{6 \times 1} = 2(\mathbf{C}_G^{-1} \mathbf{T}_n^{6 \times 1} + \alpha_n (\theta_n - \theta_h) \mathbf{I})$   $\triangleright \mathbf{T}_n$  rearranged as vector  $\mathbf{T}_n^{6 \times 1}$ 
16:     $\mathbf{B}_e = e^{\mathbf{M}}$   $\triangleright \mathbf{M}^{6 \times 1}$  rearranged as upper triangular  $\mathbf{M}^{3 \times 3}$ 
17:     $\mathbf{F}_{e_n} = \mathbf{V}_e = \sqrt{\mathbf{B}_e}$   $\triangleright$  Matrix square root
18:     $\mathbf{F}_n = \mathbf{F}_{e_n} \mathbf{G}_n$ 
19:    Continue to line 21
20:  end function
21:   $\mathbf{A}_{ve_n}^{dev, sym} = dev(\mathbf{F}_{e_n}^T \mathbf{T}_n \mathbf{F}_{e_n}^{-T} - \bar{\mu}_R \mathbf{G}_n \mathbf{G}_n^T)$   $\triangleright \mathbf{A}_{ve_n}^{dev, sym}$  rearranged as  $dev \mathbf{A}_{ve_n}^{6 \times 1}$ 
22:   $\|dev \mathbf{A}_{ve_n}\| = \sqrt{|dev \mathbf{A}_{ve_n}^T dev \mathbf{A}_{ve_n}|}$   $\triangleright$  Calculating norm of  $dev \mathbf{A}_{ve_n}$ 
23:  if  $\|dev \mathbf{A}_{ve_n}\| \leq \kappa_n$  then  $\triangleright$  Activation threshold not reached
24:     $D_{ve_n}^{6 \times 1} = 0$   $\triangleright$  No update in  $\mathbf{D}_{ve}$ 
25:  else  $\|dev \mathbf{A}_{ve_n}\| > \kappa_n$   $\triangleright$  Activation threshold reached
26:     $D_{ve_n}^{6 \times 1} = \frac{1}{\eta_G} (\|dev \mathbf{A}_{ve_n}\| - \kappa_n) \frac{dev \mathbf{A}_{ve_n}}{\|dev \mathbf{A}_{ve_n}\|}$   $\triangleright$  Update  $\mathbf{D}_{ve}$ 
27:  end if
28:   $\triangleright$  Calculate  $\tilde{\mathbf{L}}_{ve}(n)$ 


$$\tilde{\mathbf{L}}_{ve}(n) = \begin{bmatrix} D_{ve_n}^{11} & 2D_{ve_n}^{41} & 2D_{ve_n}^{51} \\ 0 & D_{ve_n}^{21} & 2D_{ve_n}^{61} \\ 0 & 0 & D_{ve_n}^{31} \end{bmatrix}$$


29:    $\mathbf{P}\dot{x} = \mathbf{r} + \mathbf{Q}x$   $\triangleright$  Solve ODE system in mass matrix form (ref Eq 5.83)
30: end function

```

\mathbf{A}_{ve} (refer to equation 5.74) that competes with the activation stress. Therefore even though the activation stress is constant, the evolution of the flow potential results in strain softening behavior, as is expected in large deformation of polymers.

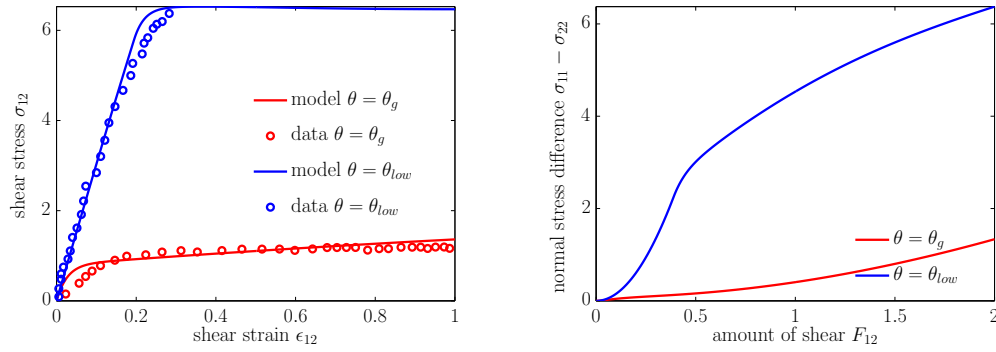


(a) Shear stress at different temperatures. Activation stress at low temperatures is high, and thus yielding at different temperatures occurs at different stress limits. (b) The trends of normal stress differences at different temperatures are similar, but the values increase with decreasing temperature.

Figure 5.2: Response for shear deformation at different temperatures

Now let us compare the isothermal shear deformation with the experimental data available in the literature. We refer to the work by Khan et. al.[19], where the shear strain is applied at glass transition and low temperatures for maximum applied shear strain of 65% on a Veriflex sample. In order to compare with the trends of the results with the experimental data, we will apply the shear deformation $F = \mathbf{I} + f\mathbf{e}_1 \otimes \mathbf{e}_2$ that is equivalent to 65% engineering strain. For this case, we define the corresponding activation stress values are kept constant at 0.1 and 4 at glass transition temperature and low temperature, respectively, to observe the relative behaviour. We set the reference temperature $\theta_{max} = \theta_g$. The initial conditions are set as $\{\kappa, \theta, \alpha, \mathbf{G}_0 = \mathbf{I}\}$. As can be seen from the shear stress response in Figure 5.3a, there is a dramatic change in the mechanical properties, when the material is subjected to the same shear deformation, depending on the temperature of the experiment. At glass transition temperature the “effective” shear modulus (42.5GPa) is lower than that at low

temperature (68GPa) as can be seen in Figure 5.3a. The trends of these results are similar to those observed by Khan et. al [19], where they carry out shear experiments at low temperature and glass transition temperature on the Veriflex sample. They also observe that the “effective” shear modulus of the sample at low temperature (60GPa) is almost four times that at glass transition temperature. During the low temperature experiment, Khan et. al observed material failure after yielding around shear strain of about 10%. Although the model does show yielding around the same shear strain, the calculated shear stresses are higher because of the assumed material properties, and the material continues the response trend beyond the yield regime.



(a) Shear stress for $\theta < \theta_g$ and $\theta = \theta_g$. The lines represent model results, while the circle represent data.

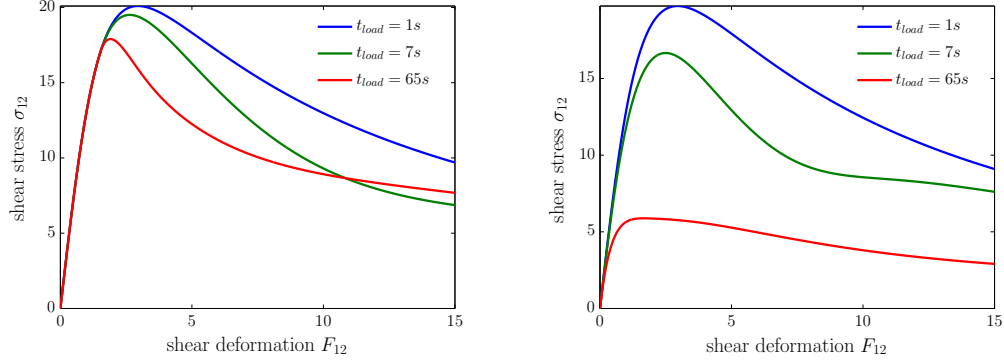
(b) Normal stress difference for $\theta < \theta_g$ and $\theta = \theta_g$. Note the different trends in the Poynting effect, depending on the temperature of deformation.

Figure 5.3: Results of the response for shear deformation at low and glass transition temperature, with respective activation stresses

5.7.2 Rate Dependent Strain Softening Behavior

Isothermal shear deformation is carried out for three different shear rates at low temperature i.e glassy state of the polymer and at high temperature i.e rubbery state of the polymer in Figure 5.4. With increasing strain rates, higher stress response levels are observed. Strain softening is observed in all three cases of strain rates, however, with increasing strain rates, the stress accumulated is higher before softening occurs. At low temperatures, the stress rise before softening is almost same

for all three shear rates (Figure 5.4a), whereas at high temperatures, the stress rise before softening, increases with increasing strain rates (Figure 5.4b).



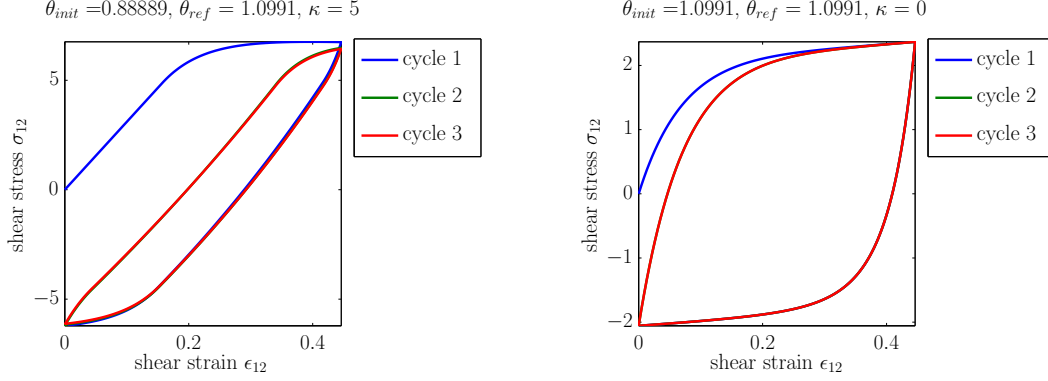
(a) Low temperature glassy case: Shear stress response for three different shear rates. Shear stress rise before softening is almost same for all three shear rates. (b) High temperature rubbery case: Shear stress response for three different shear rates. Shear stress rises with increasing shear rate.

Figure 5.4: Rate dependent strain softening behavior for low and high temperatures

5.7.3 Cyclic Isothermal Shear Deformation

Isothermal cyclic shear deformation is carried out for rubbery and glassy cases. The shear stress response for each cycle in both cases is plotted in the Figures 5.5a, 5.5b. From the characteristics of the shear stress response we observe that the shear stress versus shear strain response is repeatable after multiple cycles, and this behaviour is in agreement with the experimental observation made by McKnight et. al [72] wherein cyclic shear experiments have been carried out on a composite thermoplastic shape memory polymer (MHI Diaplex). Also, The ratio of the maximum stress rise on loading in the first cycle, to the stress rise after multiple cycles increases with temperature. In the rubbery phase (high temperature), the stress rise after multiple cycles is almost equal to that in the first cycle. In the glassy phase (low temperature), the stress rise after multiple cycles is lower than that in the first cycle. From the characteristics of the normal stress difference, we observe that the behaviour has a different trends after multiple cycles for low temperatures,

but converges rapidly for high temperature cases.



(a) Low temperature glassy case: Shear stress on loading after multiple cycles is less than the maximum shear stress attained in the first cycle (b) High temperature rubbery case: Shear stress on loading after multiple cycles is almost equal to the maximum shear stress attained in the first cycle

Figure 5.5: Results of the response for cyclic shear deformation at low and high temperature

5.7.4 Thermomechanical Shear Cycle: Stress Recovery

The experiment that we shall be considering in this work is a stress recovery thermomechanical cycle on a SMP from the work carried out on a Veriflex sample by Khan et al. [19]. The glass transition of the material is $\theta_g = 70^\circ C$. The processes involved are as listed below:

1. Initial conditions: The material is considered at a stress free state at a temperature above the glass transition temperature $\theta_{max} = \theta_g + 5$.
2. Process A: High temperature deformation: The temperature is held fixed at θ_{max} and the shear deformation is increased steadily at a constant prescribed rate to give the temporary shape to the material, where the maximum shear deformation is approximately 60% in about 50 seconds.
3. Process B: Cooling and fixing the temporary shape: The shear strain is fixed for about 100 seconds while the temperature is lowered to $\theta_{min} = \theta_g - 25$.

4. Process C: Relaxing the stress: The temperature is fixed at θ_{min} and the shear stress is gradually relaxed to zero in 3 seconds.
5. Process D: Recovering the original shape: Now the body is heated back to $\theta_{max} = \theta_g + 5$ in 500 seconds under constrained shear deformation to observe the stress recovery characteristics.

In order to implement this cycle, the model is evaluated in a strain controlled regime followed by a stress controlled regime. Both these regimes have different thermal loads which affect the evolution of the activation threshold. Depending on whether the SMP is being heated or cooled, the activation stress evolves in a hysteretic manner which is key in controlling the response of the SMP model. Since the thermomechanical cycle involved heating and cooling cycles, the rate of activation stress will evolve depending on specifics of the thermal processes, details of which can be found in the paper by Ghosh and Srinivasa [34, 73], and is summarized here for convenience.

Rate Form for the Activation Stress

The activation stress of the material is sensitive to temperature, and the material yields differently depending the current value of the temperature, the amount of strain the material is subjected to, and on whether the temperature of the material dropped or increased from the previous time-step. Thus there is a hysteresis of the activation stress from the cooling to the heating cycle, which gives the different trends of the stress-rise during cooling and the strain-recovery during heating. These considerations suggest that the rate of activation stress has the following functional form

$$\dot{\kappa} = f(\bar{\theta}, \text{sign}(\dot{\bar{\theta}}), \bar{\epsilon})\dot{\bar{\theta}}$$

$$f_{cool} = y_1(e_v + \sinh(-y_2(\theta - \theta_1)))\delta_1$$

$$f_{heat} = (-y_3e_v - y_4(1 - (y_5 \tanh(m\theta + n))^2))\delta_2$$

where, e_v is the von mises strain corresponding to the strain $(\mathbf{e}_e - \alpha(\theta - \theta_h)\mathbf{I})$. e_v is the scalar strain value selected in 3D context, such that it is affected by pure thermal strains or pure mechanical processes. Also, $m = 2/(\theta_{max} - \theta_2)$, $n = 1 - m\theta_{max}$. Here θ_1 and θ_2 are limiting values of θ until which there is no rise/fall in the stress/strain during the cooling/heating cycle.

$$\delta_1 = \begin{cases} 1, & \forall \theta \leq \theta_1; \\ 0, & \forall \theta > \theta_1; \end{cases} \quad \delta_2 = \begin{cases} 0, & \forall \theta < \theta_2; \\ 1, & \forall \theta \geq \theta_2; \end{cases}$$

Results of Stress Recovery

The results of stress recovery are shown in Figure 5.6 and 5.7.

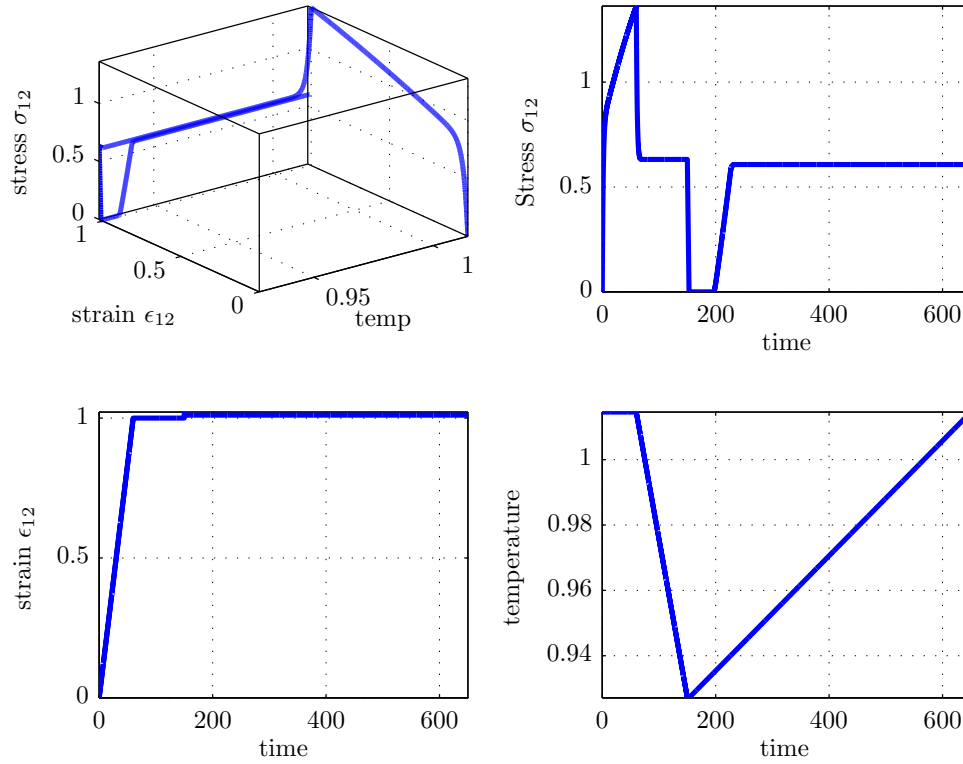


Figure 5.6: Results of the response for shear deformation thermomechanical cycle for stress recovery: Note that the stress rise during loading and stress fall during cooling is non-linear as expected from the experimental data. During unloading at low temperatures, material shows slight spring back, agreeing with experimental results. The stress recovery during heating remains near zero values for a while, as claimed by experimental data, after which it rises speedily. The experimental data for the last part of the recovery shows a decreasing trend, while the model shows almost steady or very gradual increase in stress.

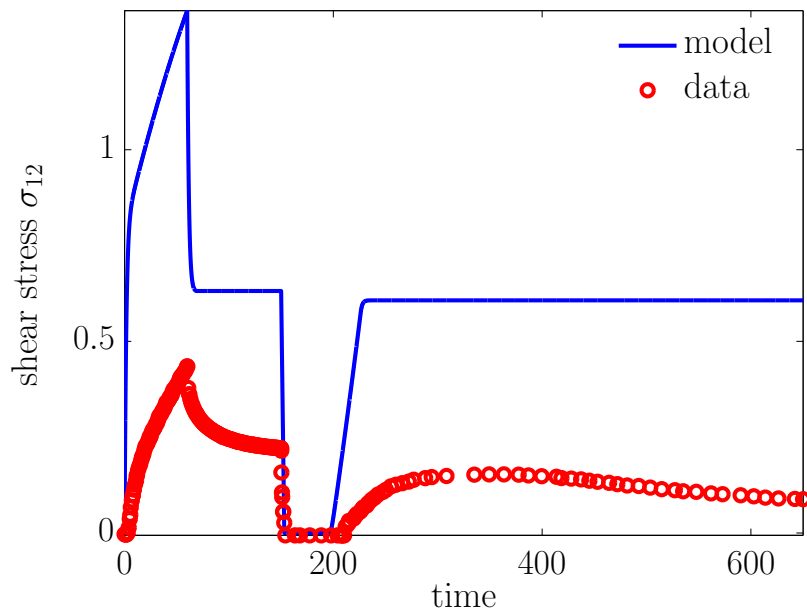


Figure 5.7: Comparison of the model response with the data for shear deformation thermomechanical cycle for stress recovery. The model is evaluated for the identified parameters in the experiment in Figure 5.3

- The behavior of the model during process A, shear deformation at high temperature and process B, cooling at constant deformation, are similar to that reported by Khan et al. [74]
 - The stress rises non-linearly during process A
 - The stress reduces during process B
 - During process C, i.e. unloading at low temperature, the material springs back slightly
- In process D, heating at constant deformation, we notice that the stress of the material falls below zero and remains at zero for a while before finally rising again, to show a stress recovery response. The experimental data reported by Khan et al. [19] for this region, notes that:

While the test does start at room temperature, some of the initial data, which only depicts a steady near zero force and steadily increasing temperature, has been omitted

We propose that this part of the response is important as the SMP model and experiment both suggest that the stress is less than zero in this region for a while, before it starts rising again. The flow potential of the material is gradually rising with temperature until it reaches a value that can compete with the activation stress, after which the stress of the material starts rising.

- As observed by Khan et al. [19] in the recovery stress and temperature of the SMP during heating, the rise in the stress begins at about 56°C, corresponding to about 0.96 non-dimensional temperature value here.
 - Around 56°C, the activation stress in the SMP model reaches a value that can now start competing with the stress developed, and results in the stress recovery response.
 - Though the stress recovery beyond θ_g , as reported by Khan et al. shows a relaxation trend, where the stress gradually diminishes towards the end of the heating process, the SMP model shows near steady values of stress until the end of the cycle.

5.7.5 Thermomechanical Shear Cycle: Shape Recovery

In Figure 5.8, the model is subjected to a shear thermomechanical cycle for the shape recovery case. The experimental and material parameters are kept the same as Section 5.7.4, except during the heating cycle, the stress is maintained at zero to study the shape recovery characteristics.

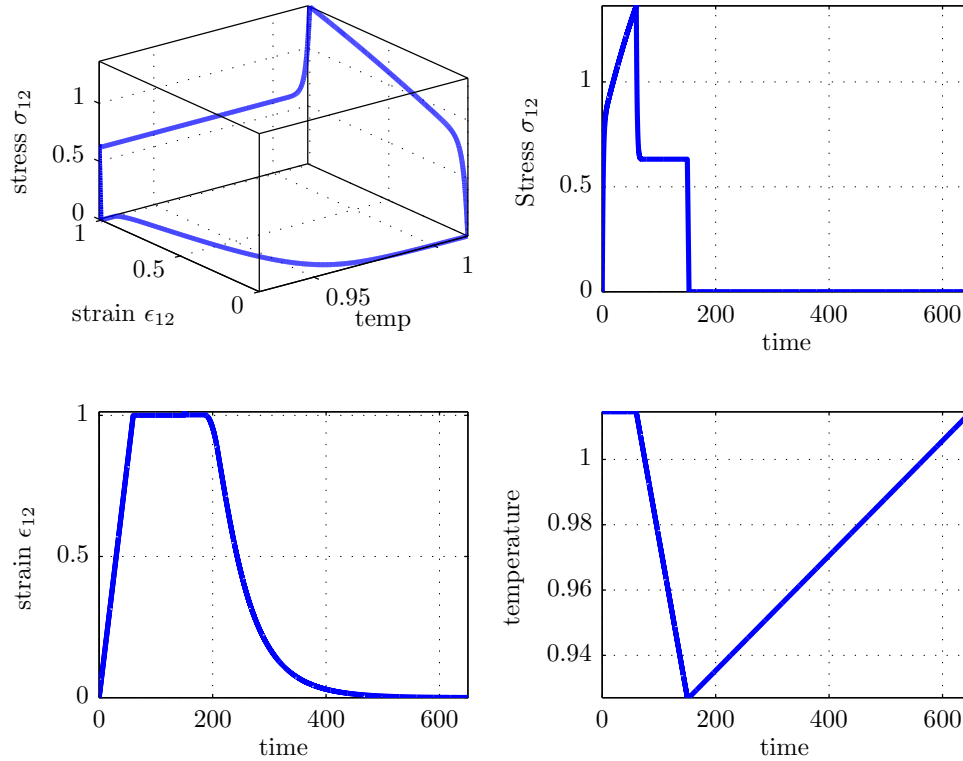


Figure 5.8: Response of the model for shear deformation thermomechanical cycle for shape recovery.

5.8 Concluding Remarks

In this chapter, the details of the development of a Helmholtz potential based 3D finite deformation constitutive model for the SMP were presented, using the QR decomposition technique. The model was set up in the form of ordinary differential equations and implemented in a suitable algorithm using an ode solver in MATLAB.

The response of the model was studied for shear deformation and the characteristics of the isothermal shear response were compared with experimental studies of Khan et al. [19] for high temperature and room temperature conditions. The model response was reasonable compared to these experimental findings. The isothermal shear deformation studies were then studied in detail for different initial temperature conditions as compared to the reference temperature of the model. The shear behaviour of the model showed similar trends at different initial temperatures. However the Poynting effect exhibited by the normal stresses at these initial conditions were radically different, and gave an insight into how the model works. We extrapolated this behaviour for cyclic shear deformation, and although the experimental data in the literature is minimum for these cases, we have made comments on related cyclic shear data for SMP composites by Mc Knight et al. [72]. We also study the model for different deformation rates in rubbery and glassy phase, and notice that the amount of stress rise before strain softening is different for these two cases, but the strain softening behaviour occurs at higher stress values with increasing shear rates. Finally we have implemented a shear deformation thermodynamic cycle for the SMP model and studied its response for the various combinations of mechanical and thermal loadings within this cycle. For the stress recovery case, the model is able to show typical data behaviour as reported by Khan et al. [19] for loading, cooling and unloading processes. However the stress recovery response for the model shows steady increase in stress till the end of the cycle, unlike the data which reports a stress relaxation kind of behavior.

6. DESIGN OF MULTI-STATE AND SMART-BIAS COMPONENTS USING SMA AND SMP COMPOSITES*

6.1 Introduction

The classical engineering approach towards building devices is to look at the macroscopic properties of the material to build components with desired functionality by employing a macroscopic assembly process. With the advent of advanced materials, whose functionalities arise from their microstructural properties, researchers began investigating how the microstructure of the material itself can be used to generate the required functionality [76]. With space and logistic limitations, replacing multi-component systems with adaptable materials that can achieve the same multiple functionalities, is now an attractive alternative [77]. With the introduction of active materials, multifunctional composites etc, researchers are now focussing on how the combined microstructural changes of such materials are able to perform multiple functions, such as integration of functions like actuation, sensing and control into a single structure using one or more material constituent[76].

Smart materials are a subgroup of such active materials, that can (1) recognize the stimulus in its surrounding environment as a signal and respond reversibly to it, and (2) be able to judge the magnitude of the signal and react with an optimal response by either changing its physical or mechanical properties [6, 7]. In Momoda's [77] review of modern technologies, she suggests that a combination of these kind of materials could integrate multiple functions within a single material system, thus reducing the overall system weight/volume, and providing an improved system performance upon demand. Such combinations can be classified as multifunctional smart material systems (MSMS), where they consist of two or more different smart material phases in the form of a hybrid system, in which every phase performs a different but necessary function. Multifunctional designs are significantly different from discrete uni-functional subsystem designs, with design methods that blend their performances in innovative ways [78]. Shape memory alloys (SMAs) and shape memory polymers (SMPs) are examples of smart materials that are gaining industrial and

*Reprinted with permission from P. Ghosh, A. Rao and A. R. Srinivasa, "Design of multi-state and smart-bias components using shape memory alloy and shape memory polymer composites", *Materials and Design*, accepted [75], Copyright [2012] by Elsevier Limited

academic popularity in terms of property investigation and product development [4]. A combination of SMA and SMP could result in a MSMS whose combined response will be different from the individual responses of SMA and SMP, as presented in this chapter.

A general idea of the properties of these two materials that will form the multi-functional system can be seen in Table 6.1. The advantages of SMPs over SMAs are evident in its lower cost, lower density, easier processing, biodegradability, lower deformation loads and larger attainable strains. SMAs rule over SMPs in their recoverable force ranges, recoverable speeds, precision control and heat conductivity.

Table 6.1: Comparison of the properties of NiTi shape memory alloys (SMAs) and shape memory polymers (SMPs) [4]

Material/ Property	NiTi SMA	SMP
Density (g/cm^3)	6-8	0.9-1.1
Typical Transformation Range ($^{\circ}C$)	-50 to 100	-10 to 150
Observed Phase Transformation	A \rightleftharpoons M, R-phase	Glass Transition
Low Temperature Modulus Range (GPa)	25 to 30	0.5 to 1
High Temperature Modulus Range (GPa)	75 to 80	0.005 to 0.01
Recovery Speed (s)	<1	1-120
Recovery Stress (MPa)	200-400	1-3
Recovery Strain	<8 %	500 %
Shaping	Difficult	Easy
Cost in \$/lb	Expensive (\sim 250)	Cheap (<10)
Heat Conductivity	Moderate	Low
Biocompatibility	-	biodegradable

In order to overcome the major drawback of SMPs i.e. their low strength and stiffness properties for practical applications, solutions have been proposed through the introduction of shape memory composites [79]. For example, Cornerstone Research Group [10] and Composite Technology Development Inc.[80] have developed fiber reinforced composites that show enhancement of rigidity and recovery force properties.

In this chapter, we discuss a method for developing SMA-SMP “smart bias systems”, that allow for the material to have different tunable characteristics in different

temperature ranges. For example it is possible to design a system with three different configurations for three different temperature ranges, as discussed later in Section 6.3. Such a multifunctional system that involves the combination of SMA and SMP not only improves these properties but also results in a MSMS with a new set of response characteristics that would be quite different than the original two materials.

There have been only a handful of attempts by researchers in the pursuit of combining SMA and SMPs to form a useful MSMS. Seward and Krulevitch [81] have presented concepts for minimally invasive microsurgery tools by utilizing combinations of SMA and SMP. The important aspect of their work was the use of bistable and reversible configuration capabilities of these SMA-SMP combinations for solving many catheter related issues in the field of microsurgery. Most of these composite structures included either SMA embedded in SMP, SMA wrapped around SMP, or SMA patterned on the surface of SMP. One of the primary ideas involved the use of variable controllable modulus of these combinations by different techniques such as stiffness scaling, combining deformation modes, or using reinforcements away from neutral axis. However, all the development in this work was focused on small scale actuation, with applications directed towards the medical industry.

Further works in the area of combining SMA and SMP's involved study of response characteristics of such systems. Sterzl et al. [82] presented a SMA thin film substrate actuator in combination with a polymer in order to achieve bistability in the composite material. The TiNiHf-Mo-Polymer bistable composite involved a polymer exhibiting a glass transition temperature between the hysteresis loop of the shape memory composite. The fabrication of this composite was discussed with emphasis on the development of suitable polymer samples.

Recovery force studies of a SMA wire embedded in SMP were carried out by Tobushi et al. [83], where they fabricated a belt using a single TiNi SMA wire embedded in a SMP polyurethane sheet matrix. The bending actuation characteristics of this belt were investigated in thermomechanical tests. As discussed in Table 6.1, the fact that the stiffness values of SMA and SMP show opposing trends at high and low temperatures provided the motivation for this work.

A two way bending property of SMA and superelastic alloy tapes sandwiched between SMP layers was discussed by Tobushi et al [84], and their recovery forces in the two shapes were investigated. The use of martensitic and austenitic SMA were chosen such that the recovery force of one was high at high temperature, and the

other was high at low temperature, so that either of the alloys would dominate the shape characteristics depending on whether the temperature was high or low.

In this chapter, thermally responsive Shape memory alloys (SMA) and Shape Memory Polymers (SMP) are combined to form a MSMS. The transformation temperatures martensitic start (M_s), martensitic finish (M_f), austenitic start (A_s) and austenitic finish (A_f) of SMA and the glass transition (T_g) for the SMP play a critical role in designing such a MSMS. Multi-state smart bias systems with varying stiffnesses can be obtained by varying the T_g of SMP between the transformation temperatures M_f and A_f of SMA. Guidelines to form such MSMS have been established by estimating the volume fractions of the individual constituents. Various ideas for “smart-bias” tools/devices have been proposed, such that they can operate under three different temperature regimes, with one material constituent being passive and the other active at a given temperature.

6.2 Smart tools: Development Details

6.2.1 MSMS Fabrication: General Considerations

Figure 6.1 refers to general considerations in designing a MSMS involving two or more smart materials. The individual constituents of the MSMS are chosen such that a few of their properties overlap depending on the application. Few examples of these properties that can be considered are response times, moduli ranges, conductivity ranges, transformation ranges etc of the individual constituents. The selected material constituents can be interfaced in different arrangements, such as micro or a macro level reinforcement, material layering, functionally grading or laminate kind of arrangements, mechanism arrangements (where one component actuates another), or structural elements like truss, frames etc, (where each material constituent could be actuated separately, to obtain a new system level response). Any of these arrangements could lead to a final MSMS, whose response could be (1) a superposition of individual component responses, or (2) competition between the individual material constituent responses or (3) structural features of one constituent, and actuation features of another combined to form a smart structural system. Care is taken in exploiting the actuation properties of these smart materials, and not allowing any material to be completely passive i.e posing only as a structural element in the system. In passive cases, the smart components may be replaced by better structural

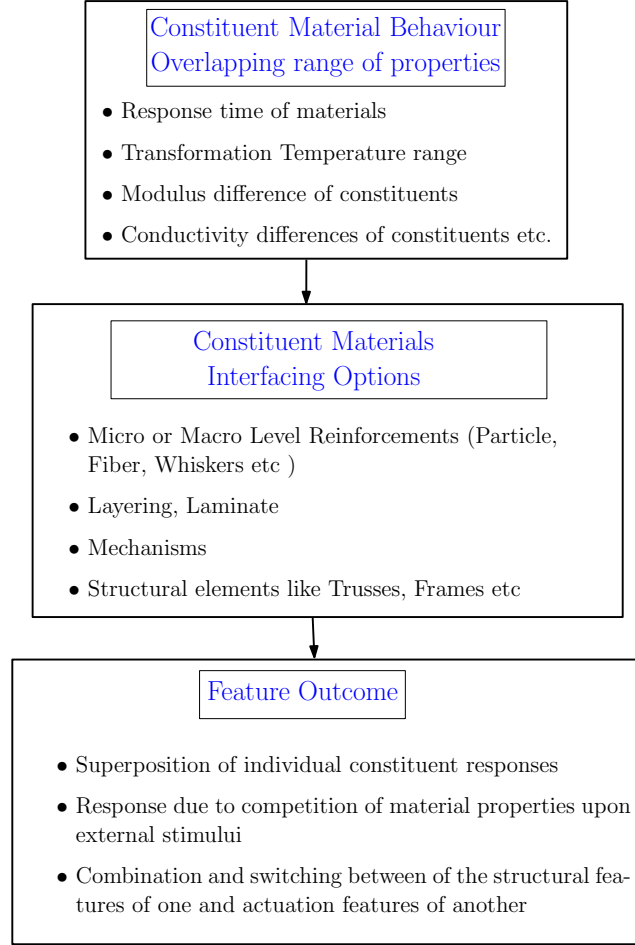


Figure 6.1: Fabrication methodology for a multifunctional smart material system

substitutes. The designs that are dealt with here however, exploit the structural properties of the smart material at one phase and the actuation properties of the same material at another phase. Details of combining SMA and SMP to form a MSMS are discussed in further sections.

6.2.2 Tuning the Glass Transition Temperature of SMP

In this work, the one-way shape memory effects in SMA and SMPs are considered, and thus both these materials work under the influence of two external agents: an applied deformation and a thermal signal. The transformation temperatures or stiffnesses of either SMA or SMP can be tuned depending on the application. The

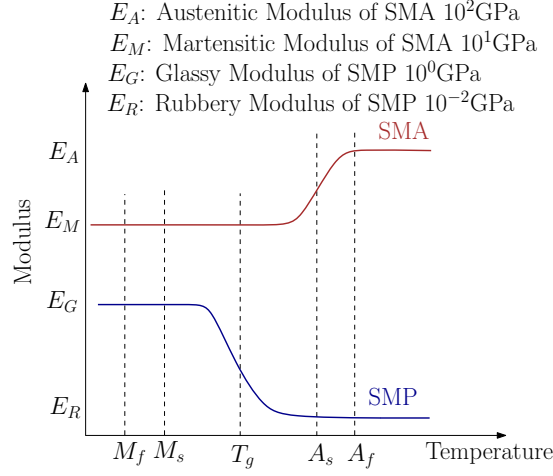


Figure 6.2: SMA vs SMP modulus comparison on a temperature scale with particular emphasis of critical transformation temperatures of SMA and SMP

transformation temperatures of concern for SMA are:

- M_f : Martensitic finish temperature
- M_s : Martensitic start temperature
- A_s : Austenitic start temperature
- A_f : Austenitic finish temperature

Below M_f , the SMA is in martensitic phase and can be easily deformed with minimal force, and above A_f it transforms to a austenitic phase which is harder to deform. The transformation temperature of concern for SMP is the glass transition temperature T_g . Below its T_g , the polymer chains are frozen and thus SMP behaves like an elastic solid and above its T_g there is onset of long range molecular motion and SMP is soft and easily deformable in this state. Figure 6.2 shows the modulus variation of SMA and SMP against a temperature scale. As seen in the figure, the T_g can be programmed between M_f and A_f transformation temperatures to observe different system stiffnesses. As also observed in the figure, the modulus variation of SMP above and below its T_g varies over two orders of magnitude. The modulus of SMA in either its martensitic or austenitic phase is two orders of magnitude greater

than that of SMP. Such a large modulus difference would indicate that the SMA volume fraction in the composite must be low. A larger volume fraction of SMA in a SMA-SMP composite would result in SMA dominating the composite response over the entire temperature range and thus debonding itself from the SMP matrix when cycled repeatedly. The issues of debonding can be reduced in some arrangements by reducing surface contact between the different material components, or matching the stiffness differences between the constituent materials as discussed further in Section 6.2.3.3.

6.2.3 Fabrication Details

We now discuss the fabrication details of a SMA-SMP based MSMS, and the organization of this section is as follows. The processing details of T_g tunable SMP are discussed in Subsection 6.2.3.1. SMA is used either in wire form or in the form of extension springs as discussed in Subsection 6.2.3.2. In Subsection 6.2.3.3 we set guidelines for selecting the volume fractions of SMA and SMP to avoid debonding issues. In Subsection 6.2.3.4 we will discuss the composite fabrication details based on the guidelines established.

6.2.3.1 SMP sample preparation

Tunable glass transition SMP samples were manufactured to attain control over the transition temperature of one of the constituents of the MSMS. Following Xie and Rousseau's approach [85], a brief description of T_g tunable SMP sample preparation is presented here. The conversion of a regular epoxy system into a T_g tunable SMP is achieved by introducing neopentyl glycol diglycidyl ether - NGDE (from TCI America) in the epoxy base diglycidyl ether of bisphenol A epoxy monomer - EPON 826 (from Hexion Specialty Chemicals, Inc.) and the curing agent poly(propylene glycol)bis(2-aminopropyl) ether - Jeffamine D230 (from Huntsman Corporation) [85]. The principle behind controlling the glass transition temperature lies in the fact that NGDE has an epoxy equivalent weight of 108 which is lower than EPON 178. On replacing the rigid aromatic epoxide EPON with the flexible aliphatic epoxide NGDE, the chain flexibility of the mixture increases, resulting in a reduction and therefore control of the transition temperature [85]. A fine variation of the ratios of these components allows the production of SMPs with a range of glass transition temperatures. The volume ratios of chemicals used in making repeatable samples of varying glass transition temperatures are enlisted in Table 6.2. Notice how the T_g reduces

as the ratio of NGDE with respect to EPON increases. Silicone molds are used for the fabrication of the SMA-SMP composite as they allow easy demolding of the prepared samples. The procedure observed in the manufacture of the SMP samples is as follows [85]. The compositions for tuning the glass transition temperature of the shape memory polymers were referred to from Table 1 in Xie et al. [85]. Multiple samples (at least eight samples) were made for each of the four cases as reported in Table 2 in this work. The photograph in Figure 6.3 shows one sample for each of these cases. The composition of sample 3 in Table 6.2 were used for the device examples discussed in Section 6.3.

1. EPON 826 is melted at 70°C for 15 minutes
2. Mixed vigorously for 10 seconds with Jeffamine D230 and NGDE
3. Mixture is poured into a silicone mold immediately
4. Thermally cured at 100°C for 1.5 hours
5. Postcured at 130°C for 1 hour
6. Demolded and ready for testing

Table 6.2: Chemical volume ratios for preparing samples with different glass transition temperatures

Sample	EPON (ml)	Jeffamine (ml)	NGDE (ml)	θ_g °C
1	10.68	2.43	1.04	60-80
2	7.12	2.43	2.08	40-60
3	3.56	2.43	3.12	20-40
4	0	2.43	4.16	0-10

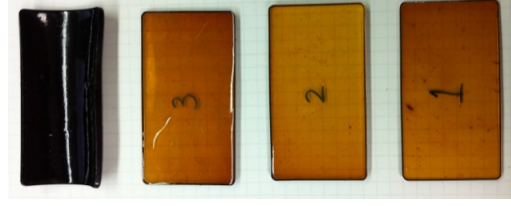


Figure 6.3: Samples prepared with volume ratios and glass transition temperatures corresponding to those enlisted in Table 6.2

6.2.3.2 SMA wires and SMA extension springs

NiTi SMA wires (Alloy type: SM495) of 0.5mm diameter were obtained from Nitinol Devices and Components (NDC). The wires were in straight annealed condition as received from the supplier. The wires were cut in specific lengths as per requirement and used as reinforcements during SMA-SMP composite fabrication. SMA extension springs were shape set as follows. SMA wires were wound around a hexagonal bolt with the ends of the wires securely held with C-clamps as seen in Figure 6.4. The entire assembly was heat treated at 500°C with 30 minutes soaking time in a resistance oven. After the heat treatment, the assembly was quickly quenched in water to shape set the SMA wire in the form of a extension spring.



Figure 6.4: Fixture to shape set SMA springs

6.2.3.3 SMA-SMP Composite Design Guidelines

As noticed from Table 6.1, the moduli difference between SMA and SMP at low and high temperature ranges are large. The ratio of volume fractions of these two components should be such that the large stiffness differences do not lead to debonding, as explained in this section.

Let,

n = number of reinforcements of SMA in the desired composite

L = Length of the resulting composite (length of the silicone mold used)

W = Width of the resulting composite (width of the silicone mold used)

H = Desired height of the composite (varied based on application/requirement)

$V_{\text{SMA}}, V_{\text{SMP}}, V_{\text{C}}$ = Volumes of the SMA, SMP and the composite respectively.

Hence,

$$V_{\text{SMA}} = n \times \left(\frac{\pi d^2}{4} \right) \times L \quad (6.1)$$

$$V_{\text{SMP}} = L \times W \times H \quad (6.2)$$

$$V_{\text{C}} = V_{\text{SMA}} + V_{\text{SMP}} \quad (6.3)$$

In order to get a rough estimate of the volume fractions, the stiffness(k) of the SMA reinforcement and the SMP matrix are considered individually. For a SMA-SMP composite, ideally the stiff configurations of SMA at a higher temperatures ($T > A_f$) and the stiff (glassy) configurations of SMP at a lower temperatures ($T < T_g$) are preferred. As discussed in Section 6.2.2, the T_g of SMP is programmed such that $M_f < T_g < A_s$. In such a case, there will be two stable stiff configurations with two distinct stiffnesses k_{SMA} and k_{SMP} , over the operational temperature range. Individually these stiffness would compare as below:

$$T < T_G \implies k_{\text{SMA}} < k_{\text{SMP}} \quad (6.4)$$

$$T_G < T < A_s \implies k_{\text{SMA}} < k_{\text{SMP}} \quad (6.5)$$

$$A_f < T \implies k_{\text{SMA}} > k_{\text{SMP}} \quad (6.6)$$

In a composite setup however, certain considerations have to be made for the individual component stiffnesses to be comparable. Since the configurations of concern correspond to temperatures in Eq 6.4 and 6.6, notice that there is a stiffness switching between these two temperature ranges, i.e stiffness of SMA switches from being lower than SMP to being higher than SMP. Ideally the stiffness inbetween these two ranges i.e Eq 6.5 should be equal for a smooth switching to take place from the low to high temperature without excessive mismatch between constituent stiffnesses that may cause debonding. The design requirement is thus that the stiffness relations of

SMA wires and SMP matrix in Eq 6.5 be adjusted so that

$$T_G < T < A_s \implies k_{SMA} \approx k_{SMP} \quad (6.7)$$

In the temperature range $T_G < T < A_s$, SMA is martensitic and SMP is rubbery. In this work, SMA wires are embedded in a SMP matrix and hence, the axial stiffness calculations would proceed as

$$T_G < T < A_s \implies k_{SMA}^{axial} \approx k_{SMP}^{axial}$$

During the heating cycle, (using martensitic moduli for SMA)

$$\frac{E_{SMA}^M \times n^M \times A_{SMA}}{L_{SMA}} = \frac{E_{SMP}^{rub} \times A_{SMP}}{L_{SMP}} \quad (6.8)$$

During the cooling cycle, (using austenitic moduli for SMA)

$$\frac{E_{SMA}^A \times n^A \times A_{SMA}}{L_{SMA}} = \frac{E_{SMP}^{rub} \times A_{SMP}}{L_{SMP}} \quad (6.9)$$

The bending stiffness calculations would proceed as

$$T_G < T < A_s \implies k_{SMA}^{bend} \approx k_{SMP}^{bend}$$

During the heating cycle,

$$\frac{E_{SMA}^M \times n^M \times I_{SMA}}{L_{SMA}^3} = \frac{E_{SMP}^{rub} \times I_{SMP}}{L_{SMP}^3} \quad (6.10)$$

During the cooling cycle,

$$\frac{E_{SMA}^A \times n^A \times I_{SMA}}{L_{SMA}^3} = \frac{E_{SMP}^{rub} \times I_{SMP}}{L_{SMP}^3} \quad (6.11)$$

L_{SMA} will depend on reinforcement orientation, in this work it is $L_{SMA} = L_{SMP} =$ Length of the mold. Also A_{SMA} is fixed with the use of SMA wires of known diameter. H_{SMP} is fixed by application requirement / mold dimensions.

Depending on the type of loading, either of the above stiffness considerations can be made, and the number of SMA reinforcements ' n^M ' or ' n^A ' can be determined in

terms of SMA and SMP moduli and SMP matrix dimensions. In addition, the lower of two estimations among ' n^M ' or ' n^A ' is assigned as the number of reinforcements for SMA ' n '. Typically from the values of E_{SMA}^A and E_{SMA}^M , it should follow that n^A would be lower of the two values and considered for the design. Hence the variables here are height for SMP i.e ' H_{SMP} ', and the number of reinforcements ' n ' for SMA. Once this estimate is made, the volume fractions of the two components can be determined resulting in the condition $V_{f_{SMA}} \ll V_{f_{SMP}}$. The volume fractions of SMA and SMP can now be obtained using the following equations.

$$V_{f_{SMA}} = \frac{V_{SMA}}{V_C} \quad (6.12)$$

$$V_{f_{SMP}} = \frac{V_{SMP}}{V_C} \quad (6.13)$$

6.2.3.4 SMA + SMP System fabrication details

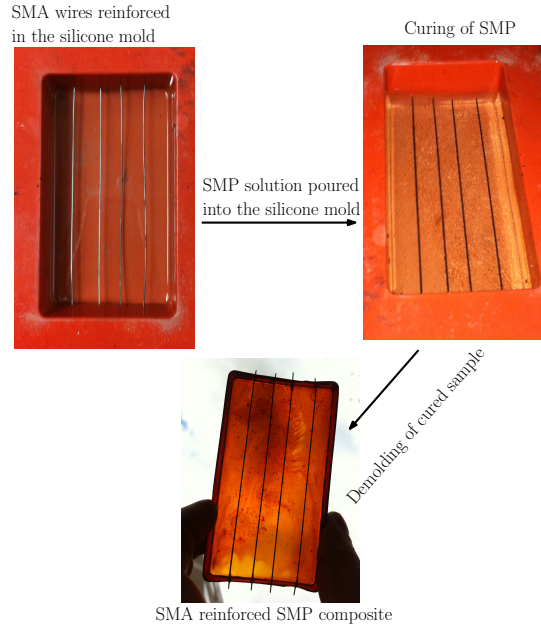


Figure 6.5: SMA and SMP composite sample preparation

The two design guidelines for a SMA - SMP based MSMS are (1) the system design criterion that the transformation temperatures of SMA and SMP are designed

such that $M_f < T_g < A_s$, and (2) the number of SMA reinforcements are determined by the criterion $k_{SMA}^{mart} = k_{SMP}^{rub}$ to prevent debonding.

SMA wires are reinforced in the silicone molds, and their position from the neutral axis are established based on the application desired, and their quantity corresponds to guideline (2). The SMP chemical solution of required volume (depending on application) is prepared, with selected ratios of chemicals to form the desired T_g , corresponding to guideline (1). This is poured into the mold that has been reinforced with SMA wires. This entire setup is then cured in an oven at 100°C for 1.5 hours and post-cured at 130°C for 1 hour more and immediately demolded. A brief view of these steps can be seen in Figure 6.5.

6.3 SMA and SMP based Multi-state and Smart-bias Components

We now discuss a few SMA-SMP based MSMS in cognizance with the design guidelines set in the earlier section.

6.3.1 Three-state Configurations

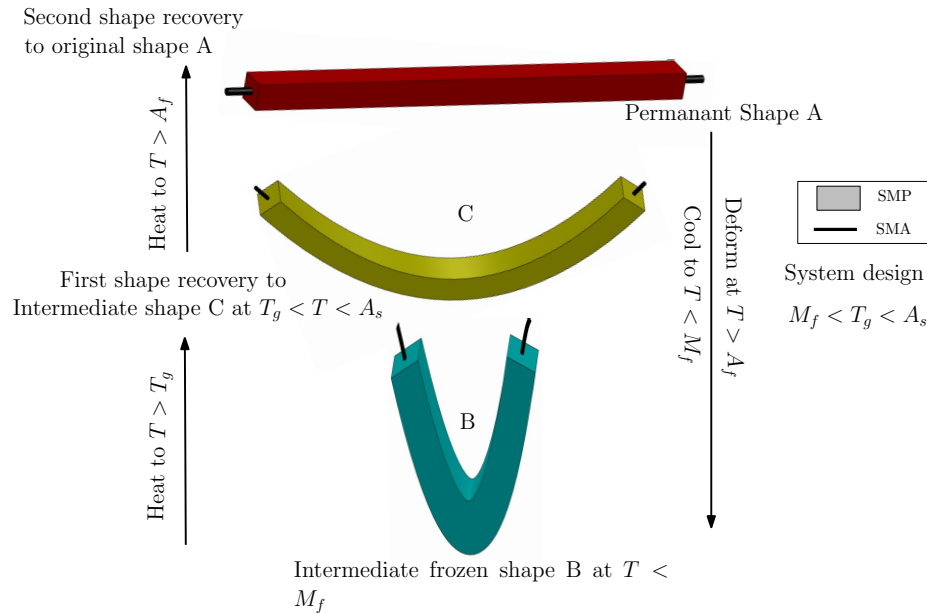


Figure 6.6: Three-state configurations obtained with SMA and SMP

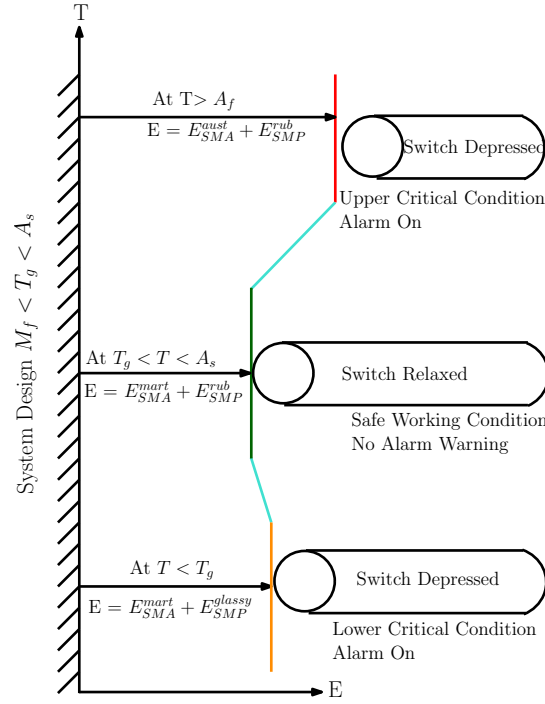


Figure 6.7: Thermally activated two - stage alarm system

Consider a system of SMP matrix with SMA reinforcement as shown in Figure 6.6, where the T_g of SMP lies between the M_s and A_s of SMA. During composite fabrication, the permanent shape of the system is set as “A” i.e the composite will always return to this shape when the temperature is greater than A_f . If the structure is now deformed at a temperature greater than A_f to a temporary shape “B” and then cooled below T_g , then the system freezes in this shape. If this frozen structure is heated to $T_g < T < A_f$, another intermediate shape “C” is attained, which is a result of the stiffness competition between SMA and SMP. This kind of a system can thus demonstrate bistable configurations “B” and “C”, and together with “A” it forms a three-state system. On proper selection of volume fractions of SMA, the modulus levels of SMA and SMP can compete resulting in a system that has three different moduli at three different temperature ranges $M_f < T_g < A_f$.

Such a system level modulus change over a temperature range can be used to design a thermally activated two - stage alarm system as shown in Figure 6.7. In such a setup, where only the modulus changes are exploited, it makes the system a completely thermally stimulated one, where external pressure is applied by the

switch as long as the modulus is $E_{SMA}^{mart} + E_{SMP}^{rub}$. This way the system can switch between states “B” and “C” reversibly by thermal stimulus, while the external pressure is provided by the switch. Whenever the system is stiffer than $E_{SMA}^{mart} + E_{SMP}^{rub}$, it can depress the switch. Thus the alarm is depressed at two temperature zones corresponding to its two stiffer configurations. This kind of an alarm system can be used to monitor a lower and an upper temperature limit by using one actuator alone.

6.3.2 Three-state Configurations with a Discontinuous SMP matrix and SMA Reinforcement

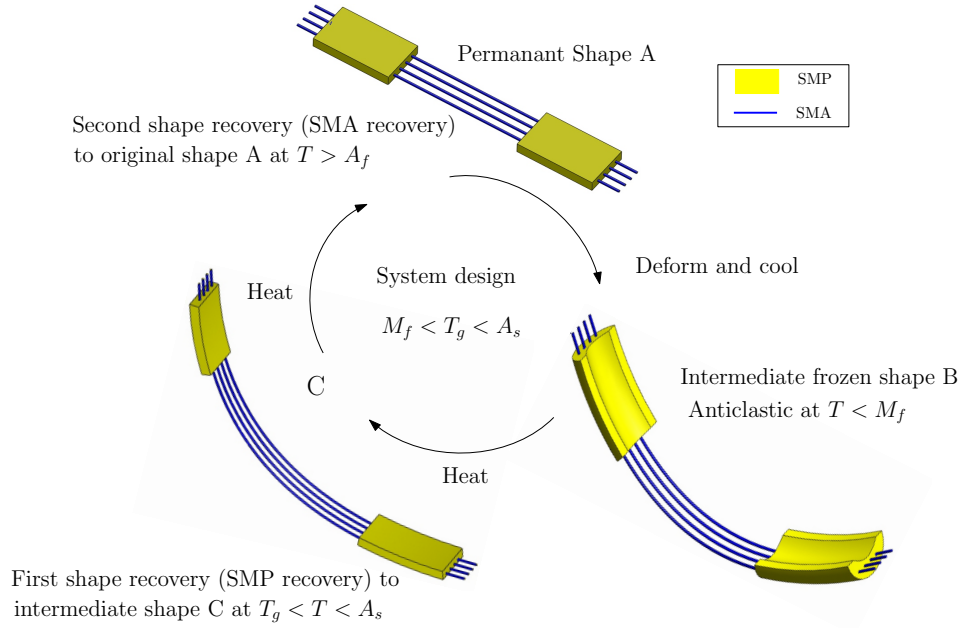


Figure 6.8: Discontinuous SMP and SMA composite showing two stage shape recovery

Using the same idea of tuning the T_g of the SMP to lie between the M_s and A_f of the SMA, consider another MSMS consisting of a discontinuous SMP matrix with SMA wire reinforcement as shown in Figure 6.8 and in the photograph in Figure 6.9.

The permanent shape is as shown in “A”. The composite is now bent along two axis (similar to anticlastic curvature) and frozen in this shape at a temperature below M_f as shown in configuration “B”. Now when the temperature is raised to $T_g < T < A_s$, the SMP recovers back to its original shape, however the SMA is

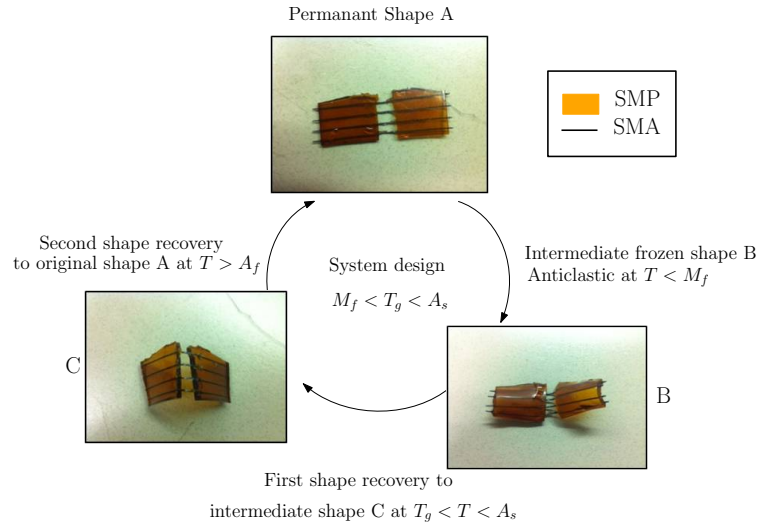


Figure 6.9: Photographs of the actual sample showing the behavior described in Figure 6.8

still in its martensitic structure and remains bent, as shown in configuration “C”. Next, when the temperature is raised above the A_f of SMA, the system returns back to its original shape “A”. This kind of a system can also demonstrate three-state configurations. This would fully exploit the SMP behavior in one temperature range and the SMA behavior in another temperature range, with one material constituent being passive and the other active at a given temperature. Such kind of a system can be used to make morphing structures, for example thermally activated locking mechanisms.

6.3.3 SMA Spring inside SMP Tube: Automatic Thermal Cycling Mechanism

On observing the deformation load required by SMP, the recovery stress generated by SMA, and the transition ranges of both, one interesting possibility comes to the fore that motivates the current idea. A system of SMA and SMP could be designed such that the recovery force generated by SMA during the end of one thermal cycle could be used to deform the SMP for the next cycle, thus forming a chain of automatic activations that is entirely thermally generated without the aid of mechanical deformation. This kind of a system can be used to make a thermally

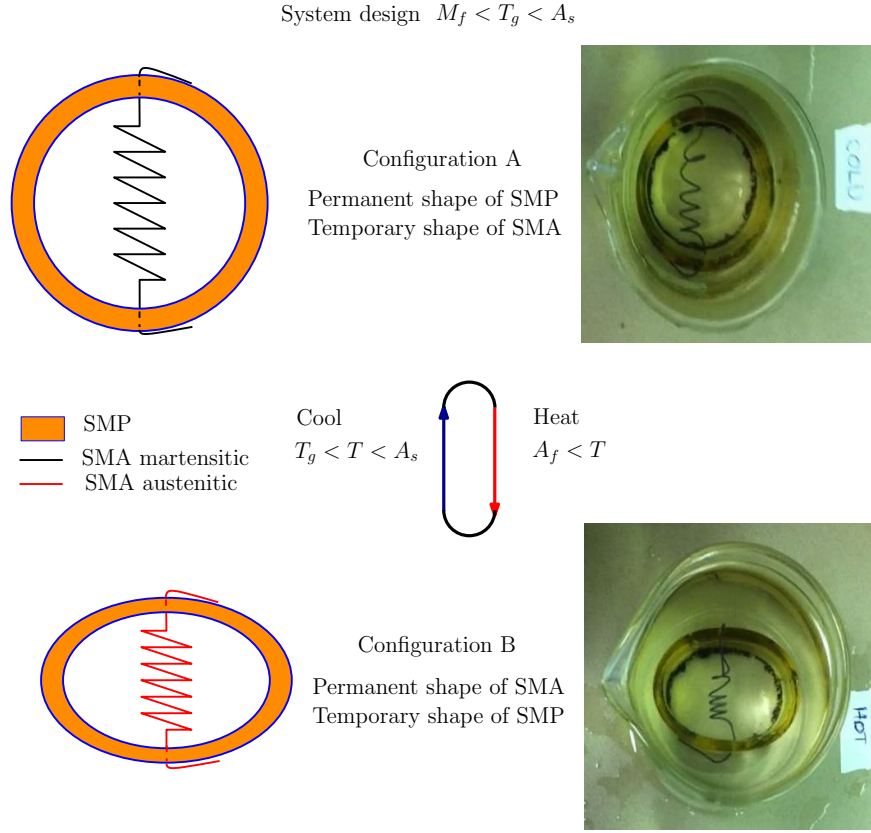


Figure 6.10: Smart valve

activated smart valve as shown in Figure 6.10. Shape set SMA extension springs are stretched and attached across the diameter of the SMP tube. At a temperature $T_g < T < A_s$, the system is in configuration “A” where the SMP is in rubbery state and the SMA in its martensitic state. When heated above A_f , the system attains configuration “B” as the SMA contracts to its permanent shape in austenitic state while the SMP is in its rubbery state. The overpowering recovery force of SMA holds the structure in “B” as long as the temperature is greater than A_f . The system relaxes back to “A” when the temperature drops to $T_g < T < A_s$. Thus, no external mechanical load is needed to observe the deformations, since the system can cycle between shape “A” and “B” with only a thermal signal, that alternates between $T_g < T < A_s$ and $T > A_f$ respectively. The shape “A” can be frozen by lowering the temperature further below $T < T_g$. Such a system can be used as a thermally activated smart valve, which has the permanent shape “A” at low working temperatures, and on exceeding a particular temperature, acts like a valve with

shape “B”. Multiple SMA springs can be connected across the SMP tube diameter which can be independently activated to obtain thermally activated differential valve openings.

6.3.4 Shape-set SMA Reinforcement in SMP Matrix: Automatic Thermal Cycling Mechanism

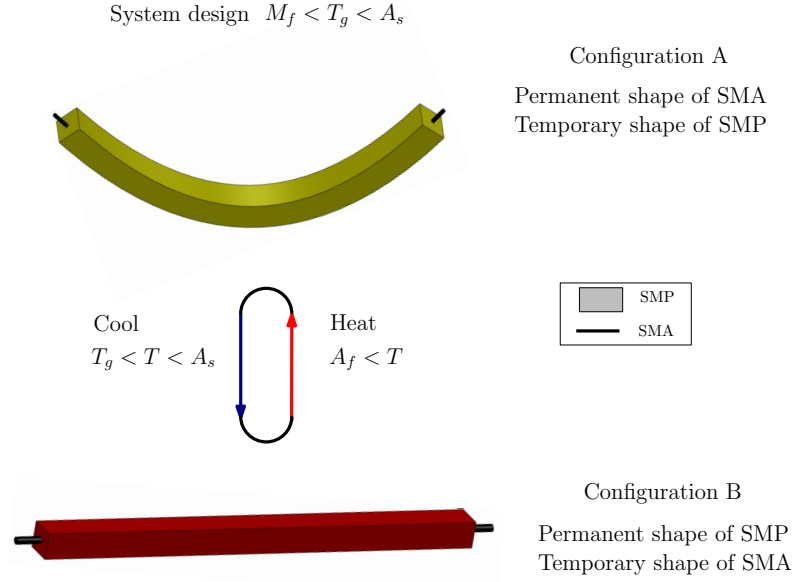


Figure 6.11: Smart tent

Configurations that can exhibit the automatic thermal cycling are not limited to mechanisms alone, but can also be performed by composite structures, as discussed in this section. In Figure 6.11, configuration “A” shows a shape set SMA wire in the form of a curve. This is embedded inside a flat SMP matrix as shown in configuration “B”, which can be as thin as membranes depending on the application desired. To fabricate such a system, SMA wires are shapese set in the form of a curve. These curved SMA wires are then straightened in its martensitic state and reinforced in the molds under external constraints. In this configuration, the chemical solution of SMP is poured into the mold as described in Section 6.2.3.4 to complete the composite fabrication process. After demolding, the system is allowed to cool down in its constrained configuration. This state is shown as configuration “B” in Figure 6.11 at a temperature $T_g < T < A_s$. When heated above A_f , the system attains

configuration “A” as the SMA attains its shape set curved shape in austenitic state while the SMP is in its rubbery state. The overpowering recovery force of SMA holds the structure in “A” as long as the temperature is greater than A_f . The system relaxes back to “B” when the temperature drops to $T_g < T < A_s$ with no external mechanical loading. The system can cycle between shape “A” and “B” with only a thermal signal, that alternates between $T > A_f$ and $T_g < T < A_s$ respectively. The shape “B” can be frozen by lowering the temperature further below $T < T_g$. Such a system may be used as thermally activated tents or umbrellas, which has a temporary shape “B” at lower temperatures, and takes on a new shape “A” at the higher working temperatures. Multiple SMA wires can be embedded inside the SMP matrix in different orientations to take on curved shape or dome shapes in configuration “A”.

6.4 Conclusions

This chapter discusses how thermally responsive Shape memory alloys (SMA) and Shape Memory Polymers (SMP) can be combined to form a Multifunctional Smart Material system (MSMS). The considerations in combining SMA and SMP to form a MSMS led to the following design guidelines (1) the transformation temperatures of SMP is programmed such that $M_f < T_g < A_s$, and (2) the number of SMA reinforcements are determined by the comparing the stiffnesses $k_{SMA}^{austenite} = k_{SMP}^{rubbery}$. Guidelines for the volume fractions of the individual constituents of such MSMS’s were established to overcome issues like debonding due to large stiffness differences between the material constituents. Using these guidelines, various SMA-SMP based MSMS’s were proposed, such that they can operate through three temperature regimes, with one material constituent being passive and the other active at a given temperature. Multi-state smart bias components such as the three-state configurations (with continuous and discontinuous SMP matrix with SMA reinforcements) showed three different moduli at three different temperature ranges $T < M_f$, $M_f < T < A_f$ and $T > A_f$. Such a system level modulus change over a temperature range can be used to design thermally activated alarm systems or morphing structures like thermally activated locking mechanisms. Shape setting of SMA in a different configuration, such that SMA is active at high temperatures and SMP is active at low temperatures can result in structures that exhibit automatic thermal cycling. Such systems can find applications as smart valves or smart tents or smart umbrellas. A SMA-SMP

based MSMS thus shows a system level response with new set of response characteristics quite different from individual constituents SMA or SMP when subjected to the same external stimuli.

7. CONCLUSIONS

7.1 Conclusions on the 1D and Small Strain 3D Model

A thermodynamically consistent 1D model and a corresponding small strain 3D model was developed simulate the gross response of a SMP undergoing a thermomechanical cycle.

1. Polymers undergo uncoiling of the polymeric chains during deformation and formation of temporary nodes because of the electrostatic attraction between the individual chains during thermal changes. A continuum model is formulated to account for these phenomena through the specification of appropriate evolution functions of the Helmholtz potential and rate of dissipation.
2. The activation stress of the material controls the gross features of the response of the model, and suggests that the material yields differently depending on not just the current value of the temperature but also on whether the temperature of the material dropped or increased from the previous time-step somewhat similar to the Bauschinger effect in plasticity, except that here the controlling parameter is the rate of temperature change rather than rate of plastic strain.
3. Quantification of the effect of thermal expansion was carried out and the model was incorporated with temperature dependent thermal expansion. Its implications were compared with the observations made by Gunes et al. [23].
4. The limited number of model parameters makes it possible to relate these parameters to response characteristics of the model. An extensive parametric study of the material parameters and their sensitive analysis showed that behavior of SMPs are complex, where each response parameter is affected by two or more material parameters simultaneously. The most influential parameters of the SMPs were rubbery modulus E_R and some of the coefficients of the activation stress function y_1, y_2 , and y_3 .
5. A similar parametric study was carried out for various loading conditions, and the results agreed with the data available in the literature.

6. A systematic parameter identification of the activation stress coefficients was carried out by performing optimization of the error between the model and the data.
7. These parameters were used for the prediction of the SMP response under different loading conditions for the experimental data obtained for uniaxial loading conditions on two different SMP samples: polyurethane and Veriflex [2, 3].

7.2 Conclusions on the Beam Theory Model

A beam theory model was developed using the continuum model described above, and a simple numerical implementation in the form of the operator-split approach was used to simulate a SMP beam undergoing a three-point bending thermomechanical cycle.

1. The model is developed for small strains based on the Euler Bernoulli beam theory. The finite element model is of the form $[\mathbf{K}^e][\Delta^e] = [\mathbf{F}^e]$, where \mathbf{K}^e is linear, developed from the constitutive equation of the model and the Hermite cubic interpolation functions, and \mathbf{F}^e contains the moment generated due to inelastic and thermal strains across the cross section of the beam.
2. The numerical solution is implemented by using an operator split technique that utilizes an elastic predictor and dissipative corrector. The key idea is that the elastic predictor is based on the solution to a beam theory boundary value problem while the dissipative corrector is entirely local (and hence can be parallelized) and is applied by considering the beam as a two or three dimensional body. This enables a very rapid solution of the problem yet maintaining fidelity of the distribution of inelastic strains across the cross-section.
3. The algorithm developed is implemented for a three-point bending test and examine the material behavior for three cases of activation stress and thermal loading conditions: elastic, plastic and thermoplastic beam. The FEM solver is validated against the ideal elastic solution. The plastic beam exhibits inelastic strains that are highest at the outer fibres, and zero at the centreline of the beam. The thermoplastic beam exhibits inelastic strains that are highest at

the outer fibres like the plastic case, but have a finite value at the centreline depending on how the inelastic zone evolves with temperature.

4. The algorithm is studied for time convergence and mesh convergence. The error norm used is the L2 norm of the displacement solution for current and previous iteration. The convergence criterion for both cases is selected as 10^{-3} . The time step size selected is $\Delta t = 0.05$, and the mesh density selected is 65×65 for allowable computation costs.
5. The beam theory model is implemented for a three-point bend thermomechanical cycle for both strain recovery and stress recovery cases. The beam response shows similar characteristics as observed in experiments, because of the evolution of the inelastic strains that is controlled by the activation stress function. Various cases are studied for the thermomechanical cycle, including different unloading cases and cyclic deformation cases.

7.3 Conclusions on the Finite Strain Model

A thermodynamically consistent finite strain 3D model was developed to simulate the gross responses of the SMP undergoing a thermomechanical shear cycle.

1. A specific form for the Helmholtz potential and the rate of dissipation is chosen from insights gained from the small strain model. The deformation gradient is multiplicatively decomposed into an instantaneous elastic part and a viscoelastic part.
2. The elastic deformation is assumed as pure stretch and the viscoelastic part of the deformation is upper triangular (based on replacing the polar decomposition with the well known QR decomposition of a matrix). This allows great simplification in the numerical methods that are used for the simulation.
3. The model which is in a state evolution form, is implemented for homogeneous deformations in an ODE solver in MATLAB, and solved for a simple shear problem. For large deformations, the shear deformation develops normal forces in the material, known as the Poynting effect. Like general trends observed in elastic-plastic materials, the Poynting effect results in strain-softening

in the SMP model. The strain softening behavior observed is different depending on the temperature of the experiment. The isothermal shear deformation response of the model is compared with shear data in the literature [19] for glass transition temperature of Veriflex and room temperature.

4. Isothermal cyclic shear deformation is carried out for three temperature cases ($\theta > \theta_{max}$, $\theta = \theta_{max}$, $\theta < \theta_{max}$), and it is observed that the behavior for different temperature cases has a similar trend after multiple cycles.
5. The finite strain SMP model is implemented for a thermomechanical shear cycle for the stress recovery case. Note that the stress rise during loading and stress fall during cooling is non-linear as expected from the experimental data. During unloading at low temperatures, material shows slight spring back, agreeing with experimental results. The stress recovery during heating remains near zero values for a while, as claimed by experimental data, after which it rises speedily. The experimental data for the last part of the recovery shows a decreasing trend, while the model shows almost steady or very gradual increase in stress.

7.4 Recommendations for Future Work

The following research topics need attention:

1. *Small Strain Model*: The extensive parametric study and sensitivity analysis in Chapter 3 can be used to develop detailed “response charts” for designers. An initial example has been shown in [75].
2. *Beam Theory Model*: For many applications, a von Kármán approximation may be more suitable in view of the large rotations. The beam formulation presented in Chapter 4 can be extended to the von Kármán beam [59]. Since this will now involve coupling between the axial and transverse displacements, a two-dimensional displacement update will be necessary for the FEM solver in the elastic predictor-dissipative corrector loop.
3. *Finite Strain Model*: The model developed in Chapter 5 can be explored for different modes of deformation and can be extended to an anisotropic model. The model can also be extended to a compressible version, by making suitable

adjustments in the Helmholtz potential, removing the incompressibility constraint and differentiating the density during the differentiation of Helmholtz potential. This is expected to show better recovery characteristics.

4. *Experimental Work*: Comprehensive data for bending and shear experiments is important for characterizing SMPs and validating the models developed in this work. Complete reporting of material properties, experimental specifications and representation of data versus time would serve as a dependable repository of bending and shear response of SMPs, especially since experimental data in these modes of deformation is limited and crucial for building better models. A few details for carrying out bending and shear experiments on SMPs are presented here for future explorations. The proposed bending experiments can be carried out on INSTRON 5567 (*Courtesy: Dr. Terry Creasy Laboratory*).

(a) *INSTRON setup*

The INSTRON 5567 is attached to INSTRON SFL Heatwave environmental chamber (Model: 3119-506 Heatwave 240) for maintaining precise air temperature throughout the length of the experiment. The Panel Controller for the environmental chamber is 2100P (modified 2132 promount hybrid). 2716 Series Mechanical Wedge-Action Grips are used to hold the attachments for the experimental setups. Fig. (7.1) shows the experimental set-up along with the mechanical grips and specimen mounting. A similar test for a four point flexure setup can be carried out. Force and tensile extension will be the parameters measured online with the help of in built 5kN capacity load cell and the crosshead displacement respectively. These parameters will be monitored and recorded as a function of time using INSTRON's customized Bluehill 2.9 software.

(b) *Temperature data*

The Vernier Surface temperature sensor can be mounted on the sample and the Logger Lite software can be used to obtain the temperature versus time data. The data acquisition sample frequency for the Logger Lite software is set to 2 samples/ second. Alternatively, the temperature versus time data can be obtained through a data acquisition system consisting of a K-type thermocouple connected a DRF-TCK-115VAC-0/150C-0/10 signal conditioner from Omega, which is connected to myDAQ from National

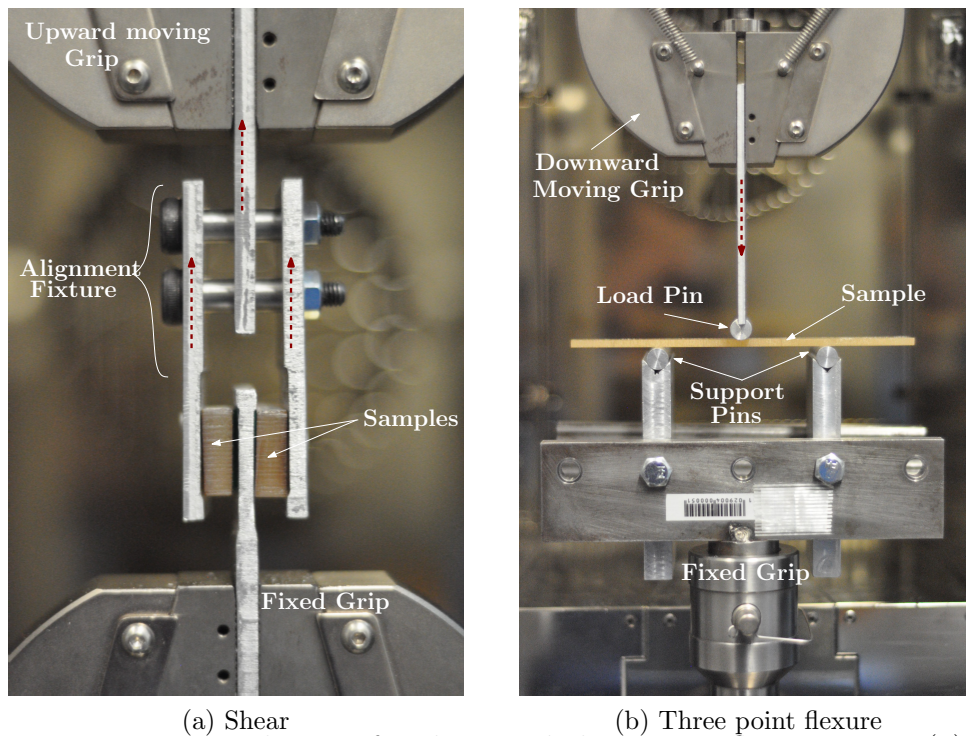
Instruments, and the temperature versus time data is obtained through LabView.

(c) *Experimental settings*

The procedure for the experiments will be for different loading conditions in a thermomechanical cycle, as explained in Chapter 2 Section 2.2. The INSTRON settings for shape recovery and stress recovery thermomechanical cycles has been recorded in Table 7.1.

(d) *Material Specifications*

The material to be used for the experiments can be either Veriflex from Cornerstone Research Group, Inc. [10] or in-house generated samples. The sample geometry is 126mm gauge length, 13 mm width and 3.5mm thickness for bending and 24mmX24mm in area and 3 mm thick for shear tests. The glass transition temperature of the Veriflex is 80 – 90°C. For in-house generated samples, the work of Xie and Rousseau [85] has been referred to, on the tuning of glass transition temperatures of epoxy polymers. The details of this have been presented in Chapter 6 Section 6.2.36.2.3.1. It is highly recommended that precise solution measures and a vacuum chamber/oven be used to synthesize samples, to exhibit repeatable response data.



(a) Shear
 (b) Three point flexure
 Figure 7.1: Experimental setup for shear and three-point flexure tests. (a) Shear: The upward moving grips will shear the symmetrically mounted glued specimens on the fixed lower grip. (b) Three point bending: The downward moving grip will apply a central load on the midpoint of the sample which rests on the fixed support pins of the lower grip.

Courtesy: INSTRON 5567 with support fixtures, Dr. Terry Creasy Laboratory.

Table 7.1: Details for INSTRON settings during a thermomechanical cycle

Experimental Process	INSTRON Settings	Thermal Chamber
To start the temperature data acquisition	Control Extension HOLD: Duration: 4 s	OP.L = 20, OP.H=100, chamber closed, constant temperature $T > T_g + 20^\circ C$
Range 1: High temp Strain:	Control Extension:- ABS RAMP: End Point = 10mm, Rate = 5mm/min	Chamber closed, constant temperature $T > T_g + 20^\circ C$
Range 2: Constant strain Cooling	Control Extension:- HOLD: Duration: 4 minutes	Chamber removed, cool down to room temp $T < T_g + 20^\circ C$
Range 3: Low Temp Unloading	Control Load:- ABS RAMP: End Point = 0 kN, Rate = 0.005kN/min	Chamber removed, maintain $T < T_g + 20^\circ C$
Range 4: Zero Load Heating (Shape recovery)	Control Load:- HOLD: Duration: 5 minutes	Chamber closed, heat to $T > T_g + 20^\circ C$
Range 4: Constant Strain Heating(Stress recovery)	Control Extension:- HOLD: Duration: 5 minutes	Chamber closed, heat to $T > T_g + 20^\circ C$

REFERENCES

- [1] W. Wagermaier, K. Kratz, M. Heuchel, and A. Lendlein, "Characterization Methods for Shape-Memory Polymers," *Shape-Memory Polymers*, vol. 226, pp. 97–145, 2010.
- [2] H. Tobushi, T. Hashimoto, S. Hayashi, and E. Yamada, "Thermomechanical Constitutive Modeling in Shape Memory Polymer of Polyurethane Series," *Journal of Intelligent Material Systems and Structures*, vol. 8, no. 8, pp. 711–718, 1997.
- [3] Y. Liu, K. Gall, M. Dunn, A. Greenberg, and J. Diani, "Thermomechanics of shape memory polymers: Uniaxial experiments and constitutive modeling," *International Journal of Plasticity*, vol. 22, no. 2, pp. 279–313, 2006.
- [4] J. Leng, X. Lan, Y. Liub, and S. Dua, "Shape-memory polymers and their composites: Stimulus methods and applications," *Progress in Materials Science*, vol. 56, no. 7, pp. 1077–1135, 2011.
- [5] E. Gil and S. Hudson, "Stimuli-reponsive polymers and their bioconjugates," *Progress in Polymer Science*, vol. 29, no. 12, pp. 1173–1222, 2004.
- [6] J. Hu, *Shape Memory Polymers and Textiles*. Woodhead Publishing Ltd., 2007.
- [7] T. Okano, "Molecular design of temperature-responsive polymers as intelligent materials," *Responsive Gels: Volume Transitions II*, pp. 179–197, 1993.
- [8] S. Kelch and A. Lendlein, "Shape memory polymers," *Angew. Chem. Int. Edn Engl*, vol. 41, pp. 2034–2057, 2002.
- [9] M. Behl, J. Zotzmann, and A. Lendlein, "Shape-Memory Polymers and Shape-Changing Polymers," *Advances in Polymer Science*, vol. 226, pp. 1–40, 2010.
- [10] C. Industries, "Morphing systems." Website. <http://http://www.crgrp.com/technology/overviews/morphing.shtml>.
- [11] A. Lendlein, M. Behl, B. Hiebl, and C. Wischke, "Shape-memory polymers as a technology platform for biomedical applications," *Expert Review of Medical Devices*, vol. 7, no. 3, pp. 357–379, 2010.

- [12] S. Reddy, E. Arzt, and A. del Campo, “Bioinspired surfaces with switchable adhesion,” *Advanced Materials*, vol. 19, no. 22, pp. 3833–3837, 2007.
- [13] T. Xie, X. Xiao, J. Li, and R. Wang, “Encoding localized strain history through wrinkle based structural colors,” *Advanced Materials*, vol. 22, no. 39, pp. 4390–4394, 2010.
- [14] T. Xie, “Recent advances in polymer shape memory,” *Polymer*, 2011.
- [15] T. Xie and X. Xiao, “Self-peeling reversible dry adhesive system,” *Chemistry of Materials*, vol. 20, no. 9, pp. 2866–2868, 2008.
- [16] S. Kim, M. Sitti, T. Xie, and X. Xiao, “Reversible dry micro-fibrillar adhesives with thermally controllable adhesion,” *Soft Matter*, vol. 5, no. 19, pp. 3689–3693, 2009.
- [17] Y. Liu, K. Gall, M. Dunn, and P. McCluskey, “Thermomechanical recovery couplings of shape memory polymers in flexure,” *Smart Materials and Structures*, vol. 12, pp. 947–954, December 2003.
- [18] G. Baer, T. Wilson, D. Matthews, and D. Maitland, “Shape-memory behavior of thermally stimulated polyurethane for medical applications,” *Journal of Applied Polymer Science*, vol. 103, no. 6, pp. 3882–3892, 2007.
- [19] F. Khan, J. Koo, D. Monk, and E. Eisbrenner, “Characterization of shear deformation and strain recovery behavior in shape memory polymers,” *Polymer Testing*, vol. 27, no. 4, pp. 498–503, 2008.
- [20] H. Tobushi, S. Hayashi, K. Hoshio, and Y. Ejiri, “Shape recovery and irrecoverable strain control in polyurethane shape-memory polymer,” *Science and Technology of Advanced Materials*, vol. 9, no. 1, p. 015009(7), 2008.
- [21] C. Buckley, C. Prisacariu, and A. Caraculacu, “Novel triol-crosslinked polyurethanes and their thermorheological characterization as shape-memory materials,” *Polymer*, vol. 48, no. 5, pp. 1388–1396, 2007.
- [22] C. Yakacki, R. Shandas, C. Lanning, B. Rech, A. Eckstein, and K. Gall, “Unconstrained recovery characterization of shape-memory polymer networks for cardiovascular applications,” *Biomaterials*, vol. 28, no. 14, pp. 2255–2263, 2007.

- [23] I. Gunes, F. Cao, and S. Jana, “Effect of thermal expansion on shape memory behavior of polyurethane and its nanocomposites,” *Journal of Polymer Science Part B: Polymer Physics*, vol. 46, no. 14, 2008.
- [24] S. M. Srinivasan, S. H. S. Kumaran, and A. P. Deshpande, “Memory characteristics of amorphous shape memory polymers and related modeling issues,” *Recent Advances in Mechanics*.
- [25] H. Tobushi, H. Hara, E. Yamada, and S. Hayashi, “Thermomechanical properties in a thin film of shape memory polymer of polyurethane series,” *Smart Materials & Structures*, vol. 5, no. 4, pp. 483–491, 1996.
- [26] H. Tobushi, T. Hashimoto, N. Ito, S. Hayashi, and E. Yamada, “Shape Fixity and Shape Recovery in a Film of Shape Memory Polymer of Polyurethane Series,” *Journal of Intelligent Material Systems and Structures*, vol. 9, no. 2, pp. 127–136, 1998.
- [27] E. Abrahamson, M. Lake, N. Munshi, and K. Gall, “Shape Memory Mechanics of an elastic memory composite resin,” *Journal of Intelligent Material Systems and Structures*, vol. 14, no. 10, pp. 623–632, 2003.
- [28] T. Takahashi, N. Hayashi, and S. Hayashi, “Structure and properties of shape-memory polyurethane block copolymers,” *Journal of Applied Polymer Science*, vol. 60, no. 7, pp. 1061–1069, 1996.
- [29] S. Lee, J. Kim, and B. Kim, “Shape memory polyurethanes having crosslinks in soft and hard segments,” *Smart Materials and Structures*, vol. 13, no. 6, pp. 1345–1350, 2004.
- [30] J. Lin and L. Chen, “Shape-memorized crosslinked ester-type polyurethane and its mechanical viscoelastic model,” *Journal of Applied Polymer Science*, vol. 73, no. 7, pp. 1305–1319, 1999.
- [31] A. Bhattacharyya and H. Tobushi, “Analysis of the isothermal mechanical response of a shape memory polymer rheological model,” *Polymer Engineering and Science*, vol. 40, no. 12, pp. 2498–2510, 2000.

- [32] S. Hong, W. Yu, and J. Youk, “Thermomechanical deformation analysis of shape memory polymers using viscoelasticity,” in *AIP Conference Proceedings*, vol. 907, pp. 853–858, AIP, 2007.
- [33] J. Diani, Y. Liu, and K. Gall, “Finite strain 3D thermoviscoelastic constitutive model for shape memory polymers,” *Polymer Engineering and Science*, vol. 46, no. 4, p. 486, 2006.
- [34] P. Ghosh and A. R. Srinivasa, “A Two-network Thermomechanical Model of a Shape Memory Polymer,” *International Journal of Engineering Science*, vol. 49, no. 9, pp. 823–838, 2011.
- [35] H. Qi, T. Nguyen, F. Castro, C. Yakacki, and R. Shandas, “Finite deformation thermo-mechanical behavior of thermally induced shape memory polymers,” *Journal of the Mechanics and Physics of Solids*, vol. 56, no. 5, pp. 1730–1751, 2008.
- [36] G. Barot, I. Rao, and K. Rajagopal, “A thermodynamic framework for the modeling of crystallizable shape memory polymers,” *International Journal of Engineering Science*, vol. 46, no. 4, pp. 325–351, 2008.
- [37] Y. Chen and D. Lagoudas, “A constitutive theory for shape memory polymers. Part I: Large deformations,” *Journal of the Mechanics and Physics of Solids*, vol. 56, no. 5, pp. 1752–1765, 2008.
- [38] J. Kim, T. Kang, and W. Yu, “Thermo-mechanical constitutive modeling of shape memory polyurethanes using a phenomenological approach,” *International Journal of Plasticity*, vol. 26, no. 2, pp. 204–218, 2010.
- [39] G. Barot and I. Rao, “Constitutive modeling of the mechanics associated with crystallizable shape memory polymers,” *Zeitschrift für Angewandte Mathematik und Physik (ZAMP)*, vol. 57, no. 4, pp. 652–681, 2006.
- [40] K. Rajagopal and A. Srinivasa, “A thermodynamic frame work for rate type fluid models,” *Journal of Non-Newtonian Fluid Mechanics*, vol. 88, no. 3, pp. 207–227, 2000.
- [41] T. Nguyen, H. Jerry Qi, F. Castro, and K. Long, “A thermoviscoelastic model for amorphous shape memory polymers: incorporating structural and stress

- relaxation,” *Journal of the Mechanics and Physics of Solids*, vol. 56, no. 9, pp. 2792–2814, 2008.
- [42] S. Reese, M. Böl, and D. Christ, “Finite element-based multi-phase modelling of shape memory polymer stents,” *Computer Methods in Applied Mechanics and Engineering*, vol. 199, no. 21, pp. 1276–1286, 2010.
 - [43] V. Srivastava, S. Chester, and L. Anand, “Thermally-actuated shape-memory polymers: Experiments, theory, and numerical simulations,” *Journal of the Mechanics and Physics of Solids*, 2010.
 - [44] J. Diani, P. Gilormini, C. Frédy, and I. Rousseau, “Predicting thermal shape memory of crosslinked polymer networks from linear viscoelasticity,” *International Journal of Solids and Structures*, 2011.
 - [45] M. Baghani, R. Naghdabadi, J. Arghavani, and S. Sohrabpour, “A constitutive model for shape memory polymers with application to torsion of prismatic bars,” *Journal of Intelligent Material Systems and Structures*, vol. 23, no. 2, pp. 107–116, 2012.
 - [46] Y. Chen and D. Lagoudas, “A constitutive theory for shape memory polymers. part ii: a linearized model for small deformations,” *Journal of the Mechanics and Physics of Solids*, vol. 56, no. 5, pp. 1766–1778, 2008.
 - [47] A. Tobolsky and R. Andrews, “Systems manifesting superposed elastic and viscous behavior,” *The Journal of Chemical Physics*, vol. 13, pp. 3–27, 1945.
 - [48] A. Tobolsky, I. Prettyman, and J. Dillon, “Stress relaxation of natural and synthetic rubber stocks,” *Journal of Applied Physics*, vol. 15, no. 4, pp. 380–395, 1944.
 - [49] K. Rajagopal and A. Wineman, “A constitutive equation for nonlinear solids which undergo deformation induced microstructural changes,” *International Journal of Plasticity*, vol. 8, no. 4, pp. 385–395, 1992.
 - [50] H. Callen, *Thermodynamics and An Introduction to Thermostatistics*. New York, John Wiley & Sons, 1985.

- [51] A. Srinivasa and S. Srinivasan, *Inelasticity of Materials: An engineering approach and practical guide*. World Scientific Pub Co Inc, 2009.
- [52] L. Segel and G. Handelman, *Mathematics Applied to Continuum Mechanics*. New York, Dover Publications, 1987.
- [53] M. Boyce, D. Parks, and A. Argon, “Large inelastic deformation of glassy polymers. part i: rate dependent constitutive model,” *Mechanics of Materials*, vol. 7, no. 1, pp. 15–33, 1988.
- [54] J. Richeton, S. Ahzi, L. Daridon, and Y. Rémond, “A formulation of the co-operative model for the yield stress of amorphous polymers for a wide range of strain rates and temperatures,” *Polymer*, vol. 46, no. 16, pp. 6035–6043, 2005.
- [55] R. Beblo and L. Weiland, “Strain induced anisotropic properties of shape memory polymer,” *Smart Materials and Structures*, vol. 17, p. 055021, 2008.
- [56] M. Behl, M. Razzaq, and A. Lendlein, “Multifunctional shape-memory polymers,” *Advanced Materials*, vol. 22, no. 31, pp. 3388–3410, 2010.
- [57] J. Simo and F. Armero, “Geometrically non-linear enhanced strain mixed methods and the method of incompatible modes,” *International Journal for Numerical Methods in Engineering*, vol. 33, no. 7, pp. 1413–1449, 1992.
- [58] J. Simo, F. Armero, and R. Taylor, “Improved versions of assumed enhanced strain tri-linear elements for 3d finite deformation problems,” *Computer Methods in Applied Mechanics and Engineering*, vol. 110, no. 3, pp. 359–386, 1993.
- [59] J. Reddy, *An Introduction to Nonlinear Finite Element Analysis*. Oxford University Press, 2004.
- [60] J. Reddy, *An Introduction to the Finite Element Method*. McGraw-Hill New York, 3rd ed., 1993.
- [61] A. R. Srinivasa, “On the use of the upper triangular (qr) decomposition for developing constitutive equations for green-elastic materials,” *International Journal of Engineering Science (in print)*, 2012.
- [62] E. H. Lee, “Elastic-plastic deformation at finite strains,” *Journal of Applied Mechanics*, vol. 36, no. 1, pp. 1–6, 1969.

- [63] H. Xiao, “Hencky strain and hencky model: Extending history and ongoing tradition,” *Multidiscipline Modeling in Materials and Structures*, vol. 1, no. 1, pp. 1–52, 2005.
- [64] Z. Bazant, “Easy-to-compute tensors with symmetric inverse approximating hencky finite strain and its rate,” *Journal of Engineering Materials and Technology*, vol. 120, pp. 131–136, 1998.
- [65] J. Criscione, J. Humphrey, A. Douglas, and W. Hunter, “An invariant basis for natural strain which yields orthogonal stress response terms in isotropic hyperelasticity,” *Journal of the Mechanics and Physics of Solids*, vol. 48, no. 12, pp. 2445–2465, 2000.
- [66] S. Nemat-Nasser, “On finite deformation elasto-plasticity,” *International Journal of Solids and Structures*, vol. 18, no. 10, pp. 857–872, 1982.
- [67] A. Green and P. Naghdi, “A general theory of an elastic-plastic continuum,” *Archive for rational mechanics and analysis*, vol. 18, no. 4, pp. 251–281, 1965.
- [68] H. Ziegler, “Some extremism principles in irreversible thermodynamics.,” *Progress in Solid Mechanics*, vol. 4, no. Chapter 2, pp. 93–193, 1963.
- [69] K. Rajagopal and A. Srinivasa, “Mechanics of the inelastic behavior of materials. part ii: Inelastic response,” *International Journal of Plasticity*, vol. 14, no. 10, pp. 969–995, 1998.
- [70] J. Simo and T. Hughes, *Computational inelasticity*, vol. 7. Springer Verlag, 1998.
- [71] R. Ogden, *Non-linear elastic deformations*. Dover Publications, 1997.
- [72] G. McKnight and C. Henry, “Large strain variable stiffness composites for shear deformations with applications to morphing aircraft skins,” in *Proceedings of SPIE, the International Society for Optical Engineering*, pp. 692919–1, Society of Photo-Optical Instrumentation Engineers, 2008.
- [73] P. Ghosh and A. R. Srinivasa, “A Two-network Thermomechanical Model and Parametric Study of the Response of Shape Memory Polymer,” *Mechanics of Materials*, In Review 2012.

- [74] F. Khan, “Regarding veriflex shearing experimental data in reference to Khan et. al. [19].” private communication, 2011.
- [75] P. Ghosh, A. Rao, and A. Srinivasa, “Design of multi-state and smart-bias components using shape memory alloy and shape memory polymer composites,” *Materials and Design*, 2012, accepted.
- [76] H. Janocha, *Adaptronics and smart structures: basics, materials, design, and applications*. Springer Verlag, 1999.
- [77] L. A. Momoda, *The Future of Engineering Materials: Multifunction for Performance- Tailored Structures*, vol. 34. The Bridge : National Academy of Engineering, 2004.
- [78] P. Matic, “Overview of multifunctional materials,” in *Proceedings of SPIE*, vol. 5053, p. 61, 2003.
- [79] C. Liang, C. Rogers, and E. Malafeew, “Investigation of shape memory polymers and their hybrid composites,” *Journal of Intelligent Material Systems And Structures*, vol. 8, no. 4, pp. 380–386, 1997.
- [80] C. materials materials materials materials, “Tembo®elastic memory composites.” Website. <http://www.ctd-materials.com/products/emc.htm>.
- [81] K. P. Seward and P. A. Krulevitch, “Shape memory alloy/shape memory polymer tools,” *US Patent 2002/0142119 A1*.
- [82] T. Sterzl, B. Winzek, M. Mennicken, R. Nagelsdiek, H. Keul, H. Hoecker, and E. Quandt, “Bistable shape memory thin film actuators,” in *Proceedings of SPIE*, vol. 5053, p. 101, 2003.
- [83] H. Tobushi, S. Hayashi, K. Hoshio, Y. Makino, and N. Miwa, “Bending actuation characteristics of shape memory composite with sma and smp,” *Journal of Intelligent Material Systems and Structures*, vol. 17, p. 1075, 2006.
- [84] H. Tobushi, S. Hayashi, and Y. Sugimoto, “Fabrication and two-way deformation of shape memory composite with sma and smp,” in *Materials Science Forum*, vol. 638, pp. 2189–2194, Trans Tech Publ, 2010.

- [85] T. Xie and I. Rousseau, “Facile tailoring of thermal transition temperatures of epoxy shape memory polymers,” *Polymer*, vol. 50, no. 8, pp. 1852–1856, 2009.

APPENDIX A

DETAILS OF PARAMETRIC STUDY OF THE SMALL STRAIN 3D MODEL

Parametric Study

The two parametric studies that were carried out were

1. Change in the order of magnitude of the parameter
2. Change in $\pm 20\%$ range of the actual value of the parameter

Thus in the tables that follow, the values of the parameters for the two studies were changed as below, using the parameter E_G as an example. We also present the graphs generated from the parametric study for the change in the order of magnitude of the parameter. The graphs generated for the change in $\pm 20\%$ range of the actual value of the parameter alongwith comments are presented in Chapter 3, Section 3.8 itself.

Table A.1: Parameter value changing details for (1) Order of magnitude and (2) $\pm 20\%$ range around actual value

E_G variation Order of magnitude	E_G variation Around exp value
$E_{G1} = E_G^{exp} \times 0.01$	$E_{G1} = E_G^{exp} + 20\% E_G^{exp}$
$E_{G2} = E_G^{exp} \times 0.1$	$E_{G1} = E_G^{exp} + 10\% E_G^{exp}$
$E_{G3} = E_G^{exp}$	$E_{G1} = E_G^{exp}$
$E_{G4} = E_G^{exp} \times 10$	$E_{G1} = E_G^{exp} - 10\% E_G^{exp}$
$E_{G5} = E_G^{exp} \times 100$	$E_{G1} = E_G^{exp} - 20\% E_G^{exp}$

Glassy Modulus

Table A.2: Glassy modulus parametric analysis: order of magnitude

Value	$\sigma_b/\sigma_b^{E_{Gexp}}$	$\sigma_{Tg}/\sigma_{Tg}^{E_{Gexp}}$	$\sigma_c/\sigma_c^{E_{Gexp}}$	$\epsilon_{cd}/\epsilon_{cd}^{E_{Gexp}}$	$\epsilon_{Tg}/\epsilon_{Tg}^{E_{Gexp}}$	$\epsilon_{ea}/\epsilon_{ea}^{E_{Gexp}}$
9	0.240815	0.246844	0.106355	10.63484	0.286057	0.877864
90	0.777587	0.783019	0.393035	3.9304	1.012478	0.998612
900	1	1	1	1	1	1
9000	1.029384	1.028489	1.167614	0.017599	0.982405	0.99979
90000	1.03241	1.031427	1.165904	-0.02256	0.981383	0.999928

Table A.3: Glassy modulus parametric analysis: around experimental data

values	$\sigma_b/\sigma_b^{E_{Gexp}}$	$\sigma_{Tg}/\sigma_{Tg}^{E_{Gexp}}$	$\sigma_c/\sigma_c^{E_{Gexp}}$	$\epsilon_{cd}/\epsilon_{cd}^{E_{Gexp}}$	$\epsilon_{Tg}/\epsilon_{Tg}^{E_{Gexp}}$	$\epsilon_{ea}/\epsilon_{ea}^{E_{Gexp}}$
1088.4	1.006278	1.006218	1.027716	0.993836	1.00051	1.000014
997.7	1.003386	1.003379	1.015508	0.996689	1.000218	1.00002
907	1	1	1	1	1	1
816.3	0.995831	0.995902	0.980876	1.002876	0.999961	0.999923
725.6	0.989832	0.990782	0.957416	1.00843	0.999851	0.999801

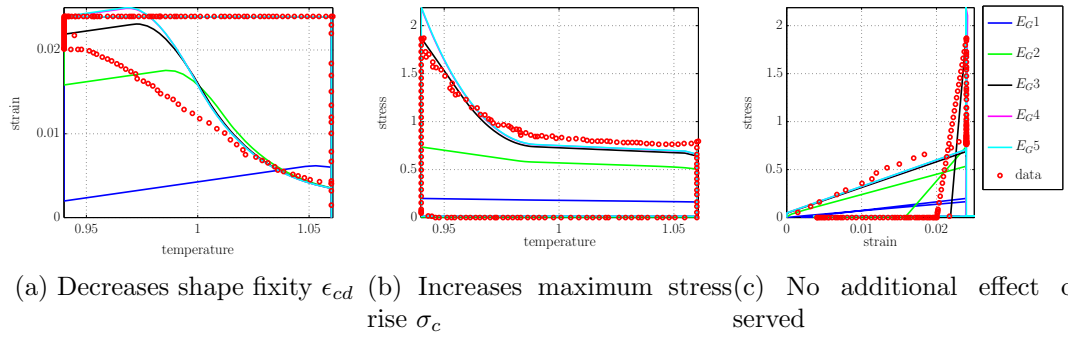


Figure A.1: Glassy modulus effect on the response for order of magnitude

Rubbery Modulus

Table A.4: Rubbery modulus parametric analysis: order of magnitude

E_R values	$\frac{\sigma_b}{\sigma_b^{E_{Rexp}}}$	$\frac{\sigma_{Tg}}{\sigma_{Tg}^{E_{Rexp}}}$	$\frac{\sigma_c}{\sigma_c^{E_{Rexp}}}$	$\frac{\epsilon_{cd}}{\epsilon_{cd}^{E_{Rexp}}}$	$\frac{\epsilon_{Tg}}{\epsilon_{Tg}^{E_{Rexp}}}$	$\frac{\epsilon_{ea}}{\epsilon_{ea}^{E_{Rexp}}}$
0.3	0.010346	0.010339	0.011963	-0.00678	0.952378	1.000184
3	0.103147	0.103069	0.11971	0.050085	0.955289	0.999904
30	1	1	1	1	1	1
300	7.660966	7.705169	3.913746	3.913957	1.088667	0.995061
3000	22.91683	23.37581	10.27342	10.2741	0.296004	0.827217

Table A.5: Rubbery modulus parametric analysis: around experimental data

E_R values	$\sigma_b/\sigma_b^{E_{Rexp}}$	$\sigma_{Tg}/\sigma_{Tg}^{E_{Rexp}}$	$\sigma_c/\sigma_c^{E_{Rexp}}$	$\epsilon_{cd}/\epsilon_{cd}^{E_{Rexp}}$	$\epsilon_{Tg}/\epsilon_{Tg}^{E_{Rexp}}$	$\epsilon_{ea}/\epsilon_{ea}^{E_{Rexp}}$
40.32	1.190917	1.191108	1.158859	1.007337	0.999474	0.99997
36.96	1.095864	1.095912	1.081012	1.003577	0.999821	0.99997
33.6	1	1	1	1	1	1
30.24	0.903409	0.903369	0.91521	0.997463	0.999987	1.000074
26.88	0.806095	0.806014	0.826072	0.993868	1.000245	1.000086

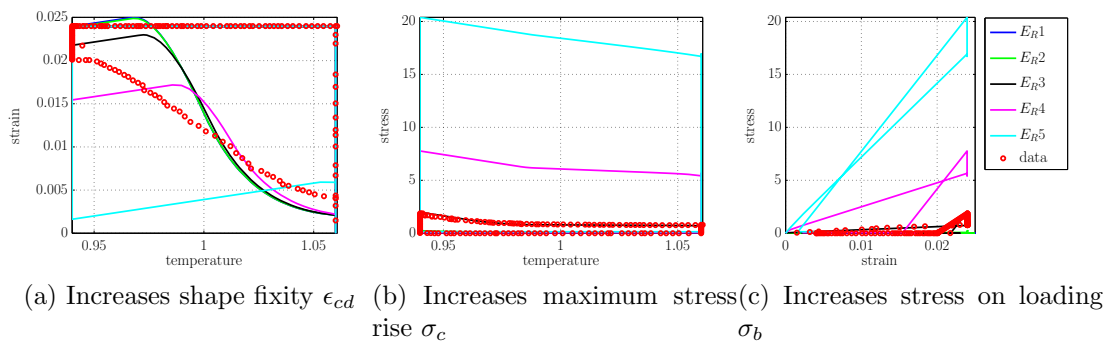


Figure A.2: Rubbery modulus effect on the response for order of magnitude

Glassy Thermal expansion

Table A.6: Glassy thermal expansion parametric analysis: order of magnitude

α_2 values	$\sigma_b/\sigma_b^{\alpha_2 exp}$	$\sigma_{Tg}/\sigma_{Tg}^{\alpha_2 exp}$	$\sigma_c/\sigma_c^{\alpha_2 exp}$	$\epsilon_{cd}/\epsilon_{cd}^{\alpha_2 exp}$	$\epsilon_{Tg}/\epsilon_{Tg}^{\alpha_2 exp}$	$\epsilon_{ea}/\epsilon_{ea}^{\alpha_2 exp}$
11.6×10^{-7}	1	0.926236	-0.14601	-0.14601	1.069844	1.02099
11.6×10^{-6}	1	0.932943	-0.02927	-0.02926	1.06417	1.018832
11.6×10^{-5}	1	1	1	1	1	1
11.6×10^{-4}	1	1.670572	1.935856	8.331518	0.306347	0.990029
11.6×10^{-3}	1	8.376358	10.16373	203.5305	-5.79981	0.801709

Table A.7: Glassy thermal expansion: around experimental data

α_2 values	$\sigma_b/\sigma_b^{\alpha_2 exp}$	$\sigma_{Tg}/\sigma_{Tg}^{\alpha_2 exp}$	$\sigma_c/\sigma_c^{\alpha_2 exp}$	$\epsilon_{cd}/\epsilon_{cd}^{\alpha_2 exp}$	$\epsilon_{Tg}/\epsilon_{Tg}^{\alpha_2 exp}$	$\epsilon_{ea}/\epsilon_{ea}^{\alpha_2 exp}$
0.000223	1	1.019987	1.064888	1.391531	0.971705	0.999828
0.000205	1	1.009992	1.039897	1.193722	0.986074	0.999883
0.000186	1	1	1	1	1	1
1.67E-04	1	0.990008	0.943235	0.810372	1.014003	1.000048
1.49E-04	1	0.980015	0.867192	0.629915	1.027439	1.000097

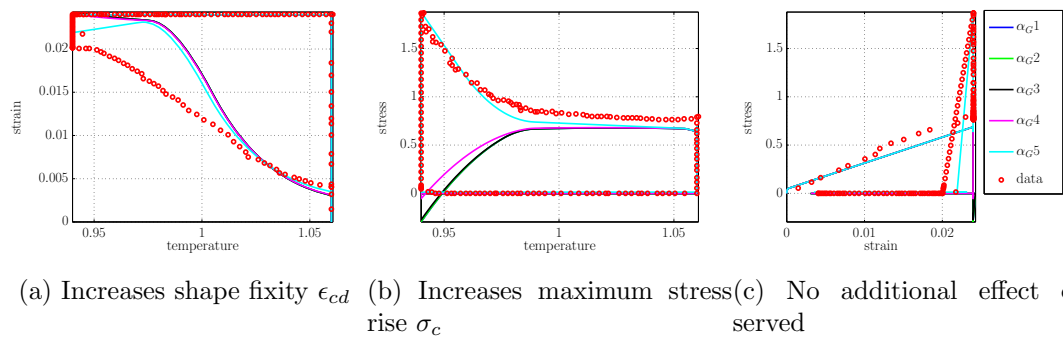


Figure A.3: Glassy thermal expansion effect on the response for order of magnitude

Rubbery Thermal expansion

Table A.8: Rubbery thermal expansion parametric analysis: order of magnitude

$\alpha 1$ values	$\sigma_b/\sigma_b^{\alpha 1_{exp}}$	$\sigma_{Tg}/\sigma_{Tg}^{\alpha 1_{exp}}$	$\sigma_c/\sigma_c^{\alpha 1_{exp}}$	$\epsilon_{cd}/\epsilon_{cd}^{\alpha 1_{exp}}$	$\epsilon_{Tg}/\epsilon_{Tg}^{\alpha 1_{exp}}$	$\epsilon_{ea}/\epsilon_{ea}^{\alpha 1_{exp}}$
11.6×10^{-7}	1	0.999564	1.000272	0.999561	1.001138	0.99992
11.6×10^{-6}	1	0.999604	1.000282	0.999575	1.001249	0.999945
11.6×10^{-5}	1	1	1	1	1	1
11.6×10^{-4}	1	1.004038	0.998967	1.004506	0.993824	1.00006
11.6×10^{-3}	1	1.044416	0.888226	0.895844	0.926763	1.003033

Table A.9: Rubbery thermal expansion: around experimental data

$\alpha 1$ values	$\sigma_b/\sigma_b^{\alpha 1_{exp}}$	$\sigma_{Tg}/\sigma_{Tg}^{\alpha 1_{exp}}$	$\sigma_c/\sigma_c^{\alpha 1_{exp}}$	$\epsilon_{cd}/\epsilon_{cd}^{\alpha 1_{exp}}$	$\epsilon_{Tg}/\epsilon_{Tg}^{\alpha 1_{exp}}$	$\epsilon_{ea}/\epsilon_{ea}^{\alpha 1_{exp}}$
0.000271	1	1.015518	0.94745	1.01099	0.960688	1.000126
0.000249	1	1.00776	0.976559	1.004597	0.980537	1.000029
0.000226	1	1	1	1	1	1
2.03E-04	1	0.99227	1.0182	0.989034	1.020925	0.999636
1.81E-04	1	0.984479	1.030254	0.994256	1.038938	0.999925

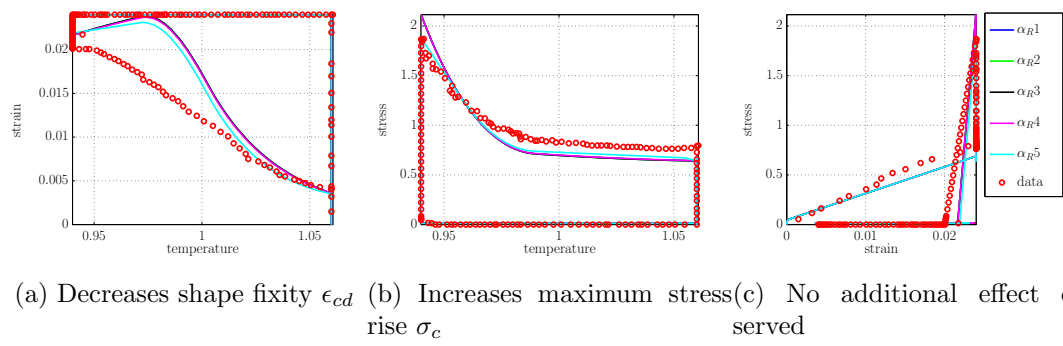


Figure A.4: Rubbery thermal expansion effect on the response for order of magnitude

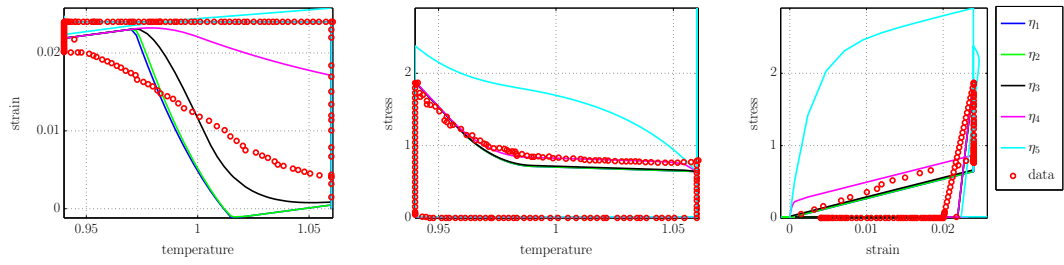
Glassy Viscosity

Table A.10: Glassy viscosity parametric analysis: order of magnitude

η_G values	$\sigma_b/\sigma_b^{\eta_{exp}}$	$\sigma_{Tg}/\sigma_{Tg}^{\eta_{exp}}$	$\sigma_c/\sigma_c^{\eta_{exp}}$	$\epsilon_{cd}/\epsilon_{cd}^{\eta_{exp}}$	$\epsilon_{Tg}/\epsilon_{Tg}^{\eta_{exp}}$	$\epsilon_{ea}/\epsilon_{ea}^{\eta_{exp}}$
10	0.966325	0.982884	0.999941	0.999935	0.374742	1.016044
100	0.969371	0.98444	0.999951	0.99995	0.402046	1.016072
1000	1	1	1	1	1	1
10000	1.306329	1.155593	1.004376	1.004377	2.097543	0.295721
100000	4.369457	2.364394	1.26744	0.7721	2.345417	-0.07864

Table A.11: Glassy viscosity parametric analysis: around experimental data

η values	$\sigma_b/\sigma_b^{\eta_{exp}}$	$\sigma_{Tg}/\sigma_{Tg}^{\eta_{exp}}$	$\sigma_c/\sigma_c^{\eta_{exp}}$	$\epsilon_{cd}/\epsilon_{cd}^{\eta_{exp}}$	$\epsilon_{Tg}/\epsilon_{Tg}^{\eta_{exp}}$	$\epsilon_{ea}/\epsilon_{ea}^{\eta_{exp}}$
1392	1.010459	1.0081	1.000236	0.977371	1.074958	0.98193
1276	1.005208	1.004046	1.000084	0.989398	1.038103	0.992052
1160	1	1	1	1	1	1
1044	0.994761	0.995958	0.999949	1.011021	0.960809	1.005985
928	0.989522	0.991914	0.999881	1.022419	0.920477	1.009918



(a) Increases strain recovery ϵ_{ea} (b) Affects the stress rise trend at beginning of cooling (c) Affects the stress rise trend at beginning of loading

Figure A.5: Viscosity effect on the response for order of magnitude

Activation Stress Coefficient y_1

Table A.12: Activation stress coefficient y_1 : order of magnitude

y_1 values	$\sigma_b/\sigma_b^{y_1}$	$\sigma_{Tg}/\sigma_{Tg}^{y_1}$	$\sigma_c/\sigma_c^{y_1}$	$\epsilon_{cd}/\epsilon_{cd}^{y_1}$	$\epsilon_{Tg}/\epsilon_{Tg}^{y_1}$	$\epsilon_{ea}/\epsilon_{ea}^{y_1}$
0.01	1	1	0.42697	13.38316	-0.12346	1.159888
0.1	1	1	0.489361	11.14937	-0.05357	1.149433
1	1	1	1	1	1	1
10	1	1	1.268637	1.268492	1.563742	-0.09575
100	1	1	1.302292	1.302293	1.559123	-0.09233

Table A.13: Activation stress coefficient y_1 : around experimental data

y_1 values	$\sigma_b/\sigma_b^{y_1}$	$\sigma_{Tg}/\sigma_{Tg}^{y_1}$	$\sigma_c/\sigma_c^{y_1}$	$\epsilon_{cd}/\epsilon_{cd}^{y_1}$	$\epsilon_{Tg}/\epsilon_{Tg}^{y_1}$	$\epsilon_{ea}/\epsilon_{ea}^{y_1}$
0.0912	1	1	1.055431	0.575498	1.318312	0.896491
0.0836	1	1	1.02904	0.561037	1.152223	0.956198
0.076	1	1	1	1	1	1
0.0684	1	1	0.967883	1.74087	0.855397	1.035748
0.0608	1	1	0.931854	2.482942	0.710527	1.071136

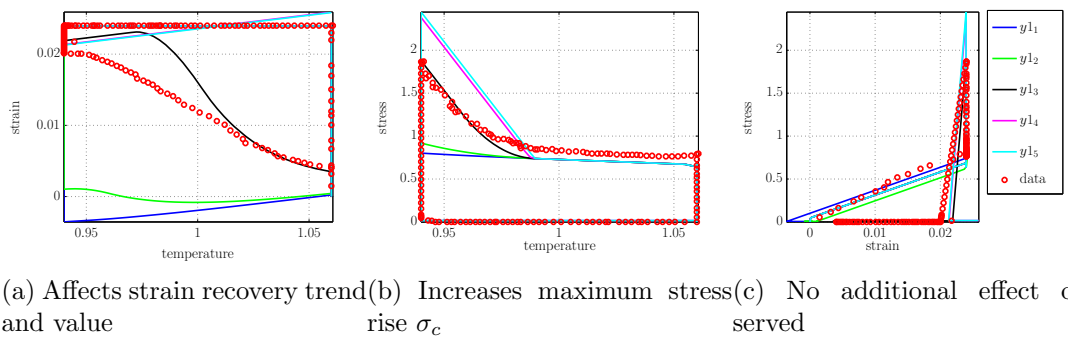


Figure A.6: Activation stress coefficient y_1 effect on the response

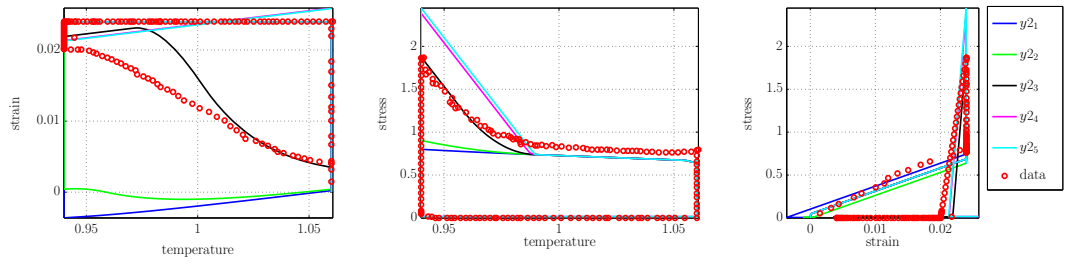
Activation Stress Coefficient y_2

Table A.14: Activation stress coefficient y_2 : order of magnitude

y_2 values	$\sigma_b/\sigma_b^{y_2}$	$\sigma_{Tg}/\sigma_{Tg}^{y_2}$	$\sigma_c/\sigma_c^{y_2}$	$\epsilon_{cd}/\epsilon_{cd}^{y_2}$	$\epsilon_{Tg}/\epsilon_{Tg}^{y_2}$	$\epsilon_{ea}/\epsilon_{ea}^{y_2}$
0.08	1	1	0.426184	13.41338	-0.12424	1.160032
0.8	1	1	0.481209	11.44879	-0.06414	1.151089
8	1	1	1	1	1	1
80	1	1	1.270674	1.270693	1.563426	-0.09552
800	1	1	1.303304	1.303241	1.559025	-0.09225

Table A.15: Activation stress coefficient y_2 : around experimental data

y_2 values	$\sigma_b/\sigma_b^{y_2}$	$\sigma_{Tg}/\sigma_{Tg}^{y_2}$	$\sigma_c/\sigma_c^{y_2}$	$\epsilon_{cd}/\epsilon_{cd}^{y_2}$	$\epsilon_{Tg}/\epsilon_{Tg}^{y_2}$	$\epsilon_{ea}/\epsilon_{ea}^{y_2}$
28.0284	1	1	1.130292	0.616317	2.133493	0.43441
25.6927	1	1	1.070386	0.583618	1.540442	0.808339
23.357	1	1	1	1	1	1
21.0213	1	1	0.916063	2.83838	0.641314	1.087
18.6856	1	1	0.832721	4.219723	0.372239	1.140133



(a) Increases strain recovery trend and value, ϵ_{Tg} and ϵ_{ea} rise σ_c
 (b) Increases maximum stress
 (c) No additional effect observed

Figure A.7: Activation stress coefficient y_2 effect on the response

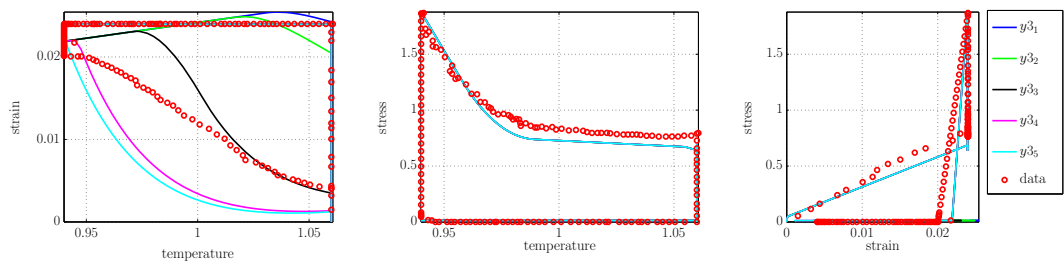
Activation Stress Coefficient y_3

Table A.16: Activation stress coefficient y_3 : order of magnitude

y_3 values	$\sigma_b/\sigma_b^{y_3}$	$\sigma_{Tg}/\sigma_{Tg}^{y_3}$	$\sigma_c/\sigma_c^{y_3}$	$\epsilon_{cd}/\epsilon_{cd}^{y_3}$	$\epsilon_{Tg}/\epsilon_{Tg}^{y_3}$	$\epsilon_{ea}/\epsilon_{ea}^{y_3}$
0.004	1	1	1	0.999762	1.600194	-0.01496
0.04	1	1	1	1.000001	1.600156	0.170456
0.4	1	1	1	1	1	1
4	1	1	1	0.999995	0.21114	1.104591
40	1	1	1	1.000002	0.163326	1.110904

Table A.17: Activation stress coefficient y_3 : around experimental data

y_3 values	$\sigma_b/\sigma_b^{y_3}$	$\sigma_{Tg}/\sigma_{Tg}^{y_3}$	$\sigma_c/\sigma_c^{y_3}$	$\epsilon_{cd}/\epsilon_{cd}^{y_3}$	$\epsilon_{Tg}/\epsilon_{Tg}^{y_3}$	$\epsilon_{ea}/\epsilon_{ea}^{y_3}$
-0.2304	1	1	1	1.000026	0.846905	1.09506
-0.2112	1	1	1	1.00001	0.922481	1.057792
-0.192	1	1	1	1	1	1
-0.1728	1	1	1	0.999994	1.079482	0.934571
-0.1536	1	1	1	1.000016	1.160979	0.863032



(a) Decreases strain recovery trend and value, ϵ_{Tg} and ϵ_{ea} served
(b) No additional effect observed
(c) No additional effect observed

Figure A.8: Activation stress coefficient y_3 effect on the response

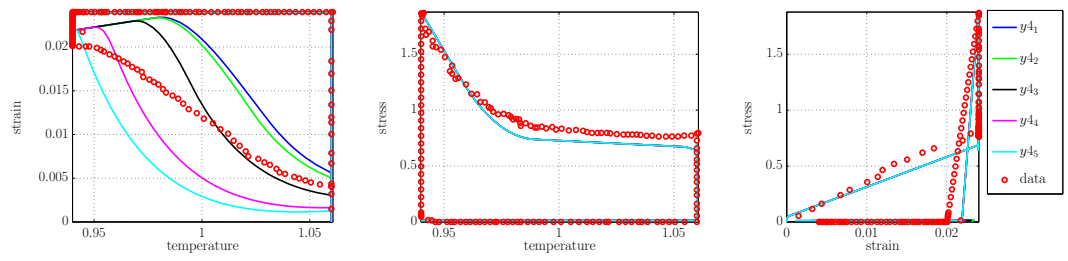
Activation Stress Coefficient y_4

Table A.18: Activation stress coefficient y_4 : order of magnitude

y_4 values	$\sigma_b/\sigma_b^{y_4}$	$\sigma_{Tg}/\sigma_{Tg}^{y_4}$	$\sigma_c/\sigma_c^{y_4}$	$\epsilon_{cd}/\epsilon_{cd}^{y_4}$	$\epsilon_{Tg}/\epsilon_{Tg}^{y_4}$	$\epsilon_{ea}/\epsilon_{ea}^{y_4}$
0.004	1	1	1	0.999997	1.615708	0.876959
0.04	1	1	1	0.999974	1.557122	0.905182
0.4	1	1	1	1	1	1
4	1	1	1	0.999998	0.373765	1.067759
40	1	1	1	0.999995	0.214832	1.084917

Table A.19: Activation stress coefficient y_4 : around experimental data

y_4 values	$\sigma_b/\sigma_b^{y_4}$	$\sigma_{Tg}/\sigma_{Tg}^{y_4}$	$\sigma_c/\sigma_c^{y_4}$	$\epsilon_{cd}/\epsilon_{cd}^{y_4}$	$\epsilon_{Tg}/\epsilon_{Tg}^{y_4}$	$\epsilon_{ea}/\epsilon_{ea}^{y_4}$
0.0348	1	1	1	1.00009	0.97669	1.026261
0.0319	1	1	1	1.000041	0.988339	1.013133
0.029	1	1	1	1	1	1
0.0261	1	1	1	1.000083	1.011823	0.986837
0.0232	1	1	1	1.00008	1.023544	0.973693



(a) Decreases strain recovery trend and value, ϵ_{Tg} and ϵ_{ea} served
 (b) No additional effect observed
 (c) No additional effect observed

Figure A.9: Activation stress coefficient y_4 effect on the response

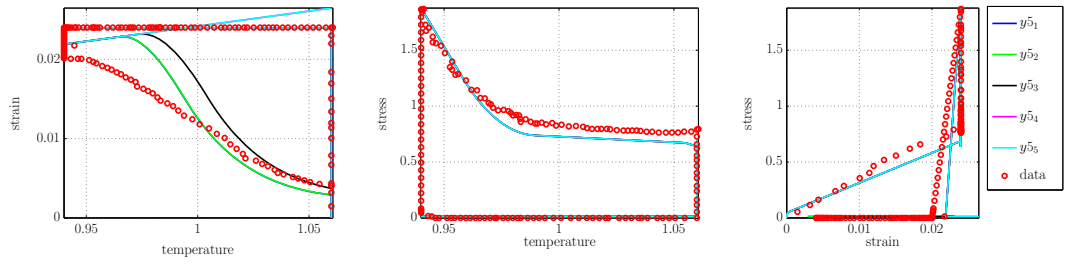
Activation Stress Coefficient y_5

Table A.20: Activation stress coefficient y_5 : order of magnitude

y_5 values	$\sigma_b/\sigma_b^{y_5}$	$\sigma_{Tg}/\sigma_{Tg}^{y_5}$	$\sigma_c/\sigma_c^{y_5}$	$\epsilon_{cd}/\epsilon_{cd}^{y_5}$	$\epsilon_{Tg}/\epsilon_{Tg}^{y_5}$	$\epsilon_{ea}/\epsilon_{ea}^{y_5}$
0.012	1	1	1	0.99998	0.721825	1.040805
0.12	1	1	1	1.000002	0.724138	1.040395
1.2	1	1	1	1	1	1
12	1	1	1	1.000004	1.485002	-0.12408
120	1	1	1	1.000004	1.485002	-0.12408

Table A.21: Activation stress coefficient y_5 : around experimental data

y_5 values	$\sigma_b/\sigma_b^{y_5}$	$\sigma_{Tg}/\sigma_{Tg}^{y_5}$	$\sigma_c/\sigma_c^{y_5}$	$\epsilon_{cd}/\epsilon_{cd}^{y_5}$	$\epsilon_{Tg}/\epsilon_{Tg}^{y_5}$	$\epsilon_{ea}/\epsilon_{ea}^{y_5}$
0.6576	1	1	1	1.000095	1.001176	0.9972
0.6028	1	1	1	1.000083	1.000634	0.99865
0.548	1	1	1	1	1	1
0.4932	1	1	1	1.000049	0.999621	1.001185
0.4384	1	1	1	1.000073	0.99927	1.002247



(a) Increases strain recovery trend and value, ϵ_{Tg} and ϵ_{ea} served
 (b) No additional effect observed
 (c) No additional effect observed

Figure A.10: Activation stress coefficient y_5 effect on the response